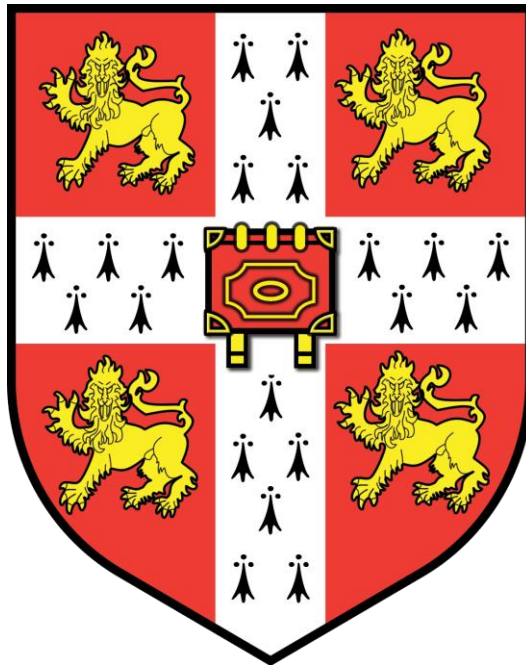


Development of an ultrafast laser ultra-precision machining platform



Christopher Wright

Hughes Hall

University of Cambridge

This dissertation is submitted for the degree of

Doctor of Philosophy

December 2020

Declaration

This dissertation is the result of my own work and includes nothing which is the outcome of work done in collaboration. It is not substantially the same as any that I have submitted, or, is being concurrently submitted for a degree or diploma or other qualification at the University of Cambridge or any other University or similar institution. I further state that no substantial part of my dissertation has already been submitted, or, is being concurrently submitted for any such degree, diploma or other qualification at the University of Cambridge or any other University or similar institution. It does not exceed the prescribed 65,000 words and 150 figures of the Engineering Degree Committee.

Christopher Wright

21/12/2020

Development of an ultrafast laser ultra-precision machining platform

Christopher Wright

Abstract

Ultra-precision manufacturing is commonplace in today's society. It is used in a huge number of applications from electronics, medical devices to energy devices. Most devices manufactured using ultra-precision methods are made in high quantities where the volume of the components is required to outweigh the cost of the production equipment. However, there are few technologies targeting the manufacture of prototypes or small batches and those that are costly in terms of time or resources. Thus, there is a demand for a high speed, flexible manufacturing platform that is capable of ultra-precise manufacture. Currently, manufacturing techniques using ultrafast lasers are limited with regards to accuracy and repeatability. This body of work investigates how to develop an ultra-precision ultrafast laser manufacturing platform.

From literature it was found that there are a significant number of avenues that could be investigated to improve the precision of an ultrafast laser machining process. This included the integration of metrology to perform closed-loop processing, studies of laser stability, new machining strategies and the effect of processing on plume formation.

A significant proportion of the research presented was focused on the development of the ultra-precision platform. This work was carried out to provide a basis for this research but also for those that will use the platform in the future. One of the key outputs from this development was a graphical user interface that integrated with the range of devices on the platform such as the laser, 5-axis stage and beam diagnostic tools. This interface provides methods for automatic tilt correction, autofocus for the laser, angular ablation machining methods and other diagnostic tools. The interface is setup to capture the required data to provide traceability and diagnostics on the laser machining process. This aided the research carried out into improving the accuracy and repeatability of the laser-based process.

First, an investigation into the characteristics of the laser installed on the ultra-precision platform was undertaken to determine the long-term stability of the laser with regards to the pointing stability, power stability and beam diameter stability. These characteristics are significant because they all affect the fluence at the focal spot which is responsible for ablating material. Variance in any of those parameters can have an effect and therefore influence the accuracy and repeatability of the process. The effect of duty cycle on power repeatability and the implications of this on machining was examined. Finally, a simulation was created to demonstrate the effect of laser stability on quality of machining.

The ability to machine on angled planes enabled an investigation of the effect of angle on plume formation and the ablation threshold of the material. The ablation threshold for silicon was found at angles between normal and 45 degrees. It was found that the threshold could not be correlated with change of incident angle on the area of the focal spot. A range of different powers and angles were captured using the holographic camera and the effect on plume development was assessed.

Overall, a range of tasks was completed which enabled several developments of the ultra-precision platform. These included in-process monitoring, the establishment of a novel machining strategy, and the capture of the effect of angular ablation on plume formation using a holographic camera.

The platform is now placed to continue further development and integrate with other metrology technologies to provide closed-loop machining capabilities which will lead into a laser-based process which will be used for MEMS and similar device manufacture.

Acknowledgements

Some say it takes a village to raise a child, I would say it has taken a town to raise this thesis.

Firstly, I would like to thank my supervisor Prof. Bill O'Neill. I don't think either of us knew the journey that I was about to embark on when I walked into O6 in Downing aged 17 for my undergrad interview. Thank you for multiple chances that you have given me, and I am sorry that I fallen short of expectations so many times. Hopefully when this is all done and dusted, we can go to the pub and reminisce about the rollercoaster that the last 10 years has been.

I would like to thank Dr Martin Sparkes for his daily input and attempting to keep me on the straight and narrow. Also, thanks to Sophie Fuller and Alison Gregory who helped me out many a time with things outside of the lab.

Special thanks to the EPSRC for funding both my PhD, but also the amazing piece of equipment I worked on to develop.

To Dr Carole Sargent, your assistance and support throughout this process has been amazing throughout and I couldn't have asked for a better college tutor.

Dr Anthanasios Kolios, I am so glad we met. Without your guidance at Cranfield, I would never have continued in academia, let alone return to Cambridge to pursue a PhD.

I was extremely lucky to return to Cambridge with such great people in my cohort; Sam Brown, Dr Clare Collins, Dr Jason Ten, Dr Yoanna Shams. I have always been so appreciative that we could always help each other out, both in and out of the lab. It made the whole experience better.

To the wider CIP group: Dr Krste Pangovski, Dr Andrew Payne, Dr Andrew Cockburn, Dr David Hopkins, Dr Francisco Orozco, Dr Katjana Lange, Nadeem Gabbini, Diego Punin and Franco Ussi. Thank you for all your assistance and insight throughout my four years in the lab.

Through my Cambridge experience, I have met some of the best people I know. Many of whom I have stepped out onto a rugby pitch with come wind, rain, or shine. A special mention goes to Toby Salisbury, Oli Holmes, Elliot Ryan, Dr Matt Raven and the wider

Eddies-Hughes rugby club, my post-grad life would not have been the same without them. Dr Jason Olsthoorn, thanks for being a great friend and housemate.

I have been fortunate that I have met some great friends prior to starting my PhD and they have always kept me grounded. My home friends: Josh Keegan, Ben Smith, Tom Walsh, Alex Foster, Richard Gayton, Andrew Forbes, and Alex Appleton have always been on the other end of the phone whenever needed. Robin McGrath was great company whilst at Cranfield, which made being there so much better than I ever thought it was going to be. Dr John Lacy, who has always been in my corner inside or outside of the ring.

Uncle Peter, thank you for all your support and ensuring that every comma, hyphen, and 'whether' is in the correct place.

To Dad and Katie, thank you for always believing in me and pushing me on to not accept defeat, I am so lucky to have you both.

To Mum and Aunty Julie, which none of this would have been possible without. Thank you for always being there, no matter what.

Table of Contents

Abstract.....	i
Acknowledgements.....	iii
Table of Contents.....	v
List of Figures.....	ix
List of Tables.....	xv
1 Introduction.....	1
1.1 Background.....	1
1.2 Research Aim and Question.....	3
2 Review of Precision Manufacturing Technologies and Laser Matter Interaction.....	5
2.1 Applications.....	5
2.1.1 MEMS.....	5
2.1.2 Microfluidic Devices.....	6
2.1.3 Optical Microcavities.....	8
2.1.4 Carbon-based devices.....	9
2.1.5 Review of Applications.....	10
2.2 Competing Technologies.....	11
2.2.1 Photolithography.....	11
2.2.2 Micromachining.....	12
2.2.3 FIB Processing.....	14
2.3 Laser Sources and Parameters.....	20
2.3.1 Basic Components and Types of Laser.....	20
2.3.2 Laser focal spot parameters.....	22
2.3.3 Laser beam parameters.....	24
2.3.4 Measurement techniques for beam parameters.....	26
2.3.5 Devices for laser control.....	29
2.4 Models and Phenomenology in Ultrafast Laser-Matter Interactions.....	30
2.4.1 Overview of Mechanism timescales.....	30
2.4.2 Laser Beam Delivery and Scanning Methods.....	31
2.4.3 Light Absorption.....	36
2.5 Optical Properties of Materials.....	45
2.5.1 Coherence of multiple internal reflections.....	46
2.5.2 Optical penetration depth.....	47
2.5.3 Effect of Temperature on Optical Properties.....	48
2.6 Metrology Methods for Laser Machining.....	49
2.6.1 Off-line.....	49
2.6.2 In-process.....	50
2.7 Ultrafast Laser Ablation at an Angle.....	56
2.7.1 Pulsed Laser Deposition.....	56
2.7.2 Angled ablation for machining.....	57
2.8 Laser Plume Imaging Techniques.....	63
2.8.1 Spectroscopic Techniques.....	63
2.8.2 Shadowgraph and Related Techniques.....	63
2.8.3 High speed imaging.....	64

2.8.4	Digital holographic interferometry	65
2.8.5	Review of Laser-Matter Interaction Diagnostics	68
2.9	Summary	69
3	Experimental System and Measurement Tools.....	71
3.1	Ultra-Precision Laser Platform	71
3.1.1	Overview	71
3.1.2	Ultrafast stage performance	75
3.1.3	Optical Layout	76
3.1.4	Laser source, Control, and Diagnostic Equipment	79
3.2	System Development	85
3.2.1	System Interfaces.....	85
3.2.2	Control of laser parameters	86
3.2.3	In-process power logging.....	87
3.2.4	Autofocus for microscope	88
3.2.5	Laser Alignment	98
3.2.6	Autofocus of laser.....	101
3.2.7	Tilt correction methodology.....	107
3.2.8	Microscope-Laser alignment.....	112
3.2.9	Determining relative centre of rotary axis position	114
3.2.10	Machining on an angled plane	116
3.2.11	Screenshot of Ultra-Precision Platform Control GUI	121
3.3	Tools for in-process and post-process analysis.....	125
3.3.1	In-process Analysis	125
3.3.2	Post Processing Analysis	131
3.4	Summary	132
4	Effect of Laser Stability on ultra-precision laser machining	133
4.1	Equipment selection.....	134
4.2	Experimental Setup.....	135
4.3	Measurement procedure	137
4.4	Talisker Laser 1 Hour Stability	139
4.4.1	1064 nm 1 hour Stability Results	139
4.4.2	532 nm 1 hour Stability Results	143
4.4.3	355 nm 1 hour Stability Results	147
4.4.4	Analysis and Discussion.....	151
4.5	Repeatability of Talisker Laser Power	155
4.5.1	Interval Exposure Measurements	156
4.6	Modelling of Stability Effects on Track Machining.....	160
4.6.1	Simulation Results.....	161
4.7	Summary	165
5	Laser ablation of silicon at varying incident angles	167
5.1	Effect of angle on ablation threshold	168
5.1.1	Material Used	168
5.1.2	Experimental Method.....	168
5.1.3	Experimental Results.....	170
5.1.4	Analysis.....	172

5.1.5 Discussion.....	177
5.2 Effect of Angle on Track Fidelity	178
5.2.1 Experimental Results	178
5.2.2 Analysis	180
5.2.3 Discussion.....	181
5.3 Plume Formation for Varying Incident Angles and Laser Parameters	182
5.3.1 Experimental Setup.....	182
5.3.2 Methodology	183
5.3.3 Limitations.....	185
5.3.4 Holographic Images of Plume Development.....	186
5.3.5 Comparison of Plume Development at Same Power and Varying Angle	190
5.3.6 Plume Angle at Varying Incident Angles.....	194
5.3.7 Analysis Method.....	195
5.3.8 Plume Evolution Analysis	196
5.3.9 Plume Evolution Discussion	202
5.3.10 Improvements to Experimental Method	202
5.4 Summary	204
6 Conclusions and Future Work	205
6.1 Platform Development	205
6.1.1 Designs and Methods Implemented	205
6.1.2 Summary	206
6.2 Beam Stability Investigation.....	206
6.3 Ablation at Varying Incident Angles	207
6.4 Future Work.....	209
6.4.1 Ultra-Precision Platform Development.....	209
6.4.2 Experimental work.....	214
6.5 Conclusion.....	215
REFERENCES	217
APPENDICES.....	227

List of Figures

Figure 1-1 Graph showing achievable resolution against scalability for current ultra-precision manufacturing techniques and the ultra-precision ultrafast laser platform.....	1
Figure 2-1 Schematic of typical dimensions for a MEMS accelerometer [10]	5
Figure 2-2 Procedure of fabrication of CaF ₂ microdisk by femtosecond laser and FIB milling [19]	8
Figure 2-3 Different allotropes of carbon [21]. Left: Fullerene. Centre: Carbon nanotube. Right: Graphene.	9
Figure 2-4 Basic representation of photolithography process [2]	12
Figure 2-5 Precision machining systems a) Kern Evo [27] b) Nanoform 250 [28]	13
Figure 2-6 Left: Interaction of ion with material [30] Right: Beam profile of FIB [31]..	14
Figure 2-7 Relationship between dose, time and area for FIB machining [31]	15
Figure 2-8 Comparison between FIB and FIB plasma removal rates [32].....	15
Figure 2-9 Zeiss Auriga with laser attachment [35].....	17
Figure 2-10 TriBeam system arrangement [36]	18
Figure 2-11 Difference between Gaussian and top-hat beam profiles [41]	25
Figure 2-12 Schematic of knife edge technique [43].....	26
Figure 2-13 Scanning slit beam profiling [45].....	27
Figure 2-14 Schematic of quadrant sensor.....	28
Figure 2-15 Example of camera arrangement for measuring pointing stability [47]...	28
Figure 2-16 Typical timescales and intensity ranges of laser phenomena [49]	31
Figure 2-17 Cylindrical transverse mode patterns TEM(<i>pl</i>) [51].....	33
Figure 2-18 π Shaper [52].....	33
Figure 2-19 Linear, circular and elliptical polarisation orientations of lasers [57].....	34
Figure 2-20 SEM photo of Laser Induced Periodic Surface Structures (LIPSS): capillary waves (periodicity 800 nm, centre) and beads (about 2 μ m, right) on silicon [60]	34
Figure 2-21 Left: Effect of threshold fluences on the modification of silicon with femtosecond laser pulses. Right: Optical micrograph of the silicon sample surface treated with a single laser pulse. [65]	41
Figure 2-22 Differences in interaction with substrate for long pulses and short pulses [25]	43
Figure 2-23 Left: Image of laser ablation with a pulse width of 10 ⁻⁹ s Right: Image of laser ablation with a pulse width of 10 ⁻¹⁵ s [67].....	44

Figure 2-24 Optical absorption depths for several materials from 0 nm to 2000 nm wavelength. [73]	47
Figure 2-25 Ablation threshold for silicon at different temperatures with wavelengths 343, 515, and 1030nm, 3 ps pulse duration. [74].....	48
Figure 2-26 Michelson interferometer for digital holographic microscopy of reflective specimen. [89].....	53
Figure 2-27 Left: Change in Raman shift due to number of layers of graphene for 514 nm and 633 nm Right: Change in Raman shift at edge of bulk graphene for 514 and 633 nm [93]	54
Figure 2-28 Dual comb interferometer schematic [97]	55
Figure 2-29 Pulse laser deposition experimental setup [98].....	56
Figure 2-30 Experimental set-up used for investigating angular dependence of ablation rate [108].....	59
Figure 2-31 Normally incident ablation curve measurements for PC and SU8 at 248nm and 193 nm wavelengths. Solid lines are cubic regression fit [108]	60
Figure 2-32 Geometry of oblique irradiation [109].....	61
Figure 2-33 Ablation depth per pulse versus angle of incidence. Left: Polycarbonate at 193 nm and fluences of 50, 150, and 350 mJ cm ⁻² . Right: SU8 at 248 nm and fluences of 250, 700, and 1075 mJ cm ⁻² . [109].....	62
Figure 2-34 An example of an experimental setup for digital holographic interferometry	65
Figure 3-1 Top: 3D model of source side of platform. Bottom: Source side of platform with equipment installed.	73
Figure 3-2 Top: 3D model of processing side of platform. Bottom: Processing side of platform with equipment installed.	74
Figure 3-3 Optical train design for ultra-precision platform.....	77
Figure 3-4 Graphs showing desired transmission characteristics for each dichroic mirror.....	78
Figure 3-5 Optical arrangement for beam control	81
Figure 3-6 Power meter placement.....	87
Figure 3-7 Sequence for finding image focus using the Laplace transform	89
Figure 3-8 Test sequence of images used to develop autofocus method. These are tiled in order from top left to bottom right.	90
Figure 3-9 Plot of Laplace variance for image scan sequence	91
Figure 3-10 a) raw image b) Threshold level = 0.06 c) Threshold level = 0.27 d) Threshold level = 0.45	92
Figure 3-11 Connected pixel area for image scan sequence	93

Figure 3-12 Demonstration of image focusing algorithm centring feature and achieving focus.....	93
Figure 3-13 Methodology for connected pixel algorithm	94
Figure 3-14 Implementation of methods for different scan lengths	95
Figure 3-15 Arrangement for precise laser alignment.....	98
Figure 3-16 Adjustment mirrors for precise laser alignment.....	99
Figure 3-17 Effect of Gaussian optic on beam diameter and intensity [123]	101
Figure 3-18 Layout of focus grid. Horizontal red lines indicate ablated tracks.	103
Figure 3-19 Methodology for finding focus of laser on sample.....	105
Figure 3-20 Implementation of plane fitting to perform tilt correction. Blue plane is initial data points. Green plane is after tilt correction transformation.....	109
Figure 3-21 Experimental setup to measure tilt correction method.....	110
Figure 3-22 Comparison of before and after tilt correction applied	111
Figure 3-23 Diagram of Silicon Sample. Red crosses indicate raw corner positions. The sample is purposefully drawn not to be square.	112
Figure 3-24 Blue region indicates maximum working area. Orange crosses indicate fiducial markers.....	113
Figure 3-25 Sample holder and alignment to axis.	114
Figure 3-26 Demonstration of effect of axis offset on uncertainty of focal point position after rotation.....	114
Figure 3-27 Geometric representation of distances	115
Figure 3-28 Layout of angled plane test. Stars indicates start of machined line	116
Figure 3-29 Result of machining on angle plane test.....	117
Figure 3-30 Code to test stage repeatability.....	118
Figure 3-31 Test showing three iterations of the same procedure giving inconsistent results	119
Figure 3-32 Comparison of angled machining trials before and after reconditioning of Y-axis.....	120
Figure 3-33 Ultra-Precision Platform GUI	121
Figure 3-34 Schematic of arrangement for holographic camera trials.....	126
Figure 3-35 Representation of oscilloscope output for measuring time difference from start of laser machining and captured image. Blue is processing laser pulses. Red is holographic camera laser.....	127
Figure 3-36 Method for automated holographic camera captures	128

Figure 3-37 Sample of processed images produced by holographic camera for ultrafast ablation of target. Time is the difference from processing beginning and frame captured.	130
Figure 4-1 Examples of beam profile at maximum power	135
Figure 4-2 Ideal beam diagnostic layout	135
Figure 4-3 Left: Dichroic mirror mount Right: Redesigned mount	136
Figure 4-4 Interim beam diagnostics layout	136
Figure 4-5 Effect of entry angle on focal spot position for different types of lenses [124]	137
Figure 4-6 Beam stability testing interface	138
Figure 4-7 Variation in centroid position for 100% power at 1064 nm	139
Figure 4-8 Variation of centroid position in X for 1 hour	139
Figure 4-9 Variation of centroid position in Y for 1 hour	140
Figure 4-10 Variation of diameter in X (1064 nm)	141
Figure 4-11 Variation of diameter in Y (1064 nm)	141
Figure 4-12 Power variation for test period normalised to mean value (1064 nm)...	142
Figure 4-13 Variation in centroid position at max power (532 nm)	143
Figure 4-14 Variation of centroid position in X (532 nm)	143
Figure 4-15 Variation of centroid position in Y (532 nm)	144
Figure 4-16 Variation of diameter in X (532 nm)	145
Figure 4-17 Variation of diameter in Y (532 nm)	145
Figure 4-18 Power variation for test period normalised to mean value (532 nm) ...	146
Figure 4-19 Variation in centroid position at max power (355 nm)	147
Figure 4-20 Variation of centroid position in X (355 nm)	147
Figure 4-21 Variation of centroid position in Y (355 nm)	148
Figure 4-22 Variation of diameter in X (355 nm)	149
Figure 4-23 Variation of diameter in Y (355 nm)	149
Figure 4-24 Power variation for test period normalised to mean value (355 nm) ...	150
Figure 4-25 20-40 minutes section of variation of centroid position in X with polynomial regression	152
Figure 4-26 Diagram showing relationship between position of camera, measured deviation and angle deviation. Diagram not to scale.....	153
Figure 4-27 Trial of 10 seconds burst with 10 seconds rest. Red: First trial. Blue: Second trial with 15 minutes wait from previous trial. Green: Third trial with 30 mins wait from previous trial	156

Figure 4-28 Plot of variation in power output for different duty cycles.	157
Figure 4-29 Plot showing variation in power rise from source after triggering.	158
Figure 4-30 Plot showing different warm up strategies and the effect on power output. Red: Three minute warm up. Blue: Immediate use.	159
Figure 4-31 3D representation of simulated machining.	161
Figure 4-32 Variation in track depth of simulated machining. Red line: Smoothed average of raw data.	162
Figure 4-33 Top down view of simulated trench. Blue: Data points above ablation threshold. Red: Data points below ablation threshold. Green: smoothed average of the above threshold points.	163
Figure 4-34 Macro view of the edge of simulated trench.	164
Figure 5-1 Examples of machined tracks captured with BX51 microscope. All tracks are at normal incidence – 0 degrees. Incident powers for tracks are a) 84.1 mW b) 70.2 mW c) 52.4 mW d) 36.3 mW.	170
Figure 5-2 Plots of measured track width squared versus focal spot fluence. a) 0 degrees b) 15 degrees c) 30 degrees d) 45 degrees	171
Figure 5-3 Plot of track width against laser fluence at different angles	172
Figure 5-4 Visualization of the effect of sample angle on focal spot cross section. Blue Line shows focusing beam profile. Red Line indicates intersection with sample. Left: Overall view. Right: Zoom view.	174
Figure 5-5 Left: Simulation of the effect of angle on Gaussian intensity profile. Right: Plot of focal spot radius versus incidence angle.	174
Figure 5-6 Left: Overview of Reflectance versus incident angle for 0 to 90 Degrees Right: Zoomed in to show change in reflectance for 0 to 45 Degrees.	175
Figure 5-7 Left: Plot of track width squared corrected versus fluence. Right: Plot of adjusted threshold fluence versus angle.	176
Figure 5-8 Nominal 27 μm Track at 45 degrees. Left: Microscope Image Centre: Threshold Image Right: Plot of horizontal sum of pixels. Red lines indicate maximum width. Green lines indicate minimum width.	179
Figure 5-9 Threshold Images for ablated tracks	179
Figure 5-10 Plot of minimum-maximum track width ratio versus angle	180
Figure 5-11 Schematic of arrangement for holographic camera trials.	182
Figure 5-12 Schematic of laser and FOV orientation for holographic camera trails	183
Figure 5-13 Incident angle from normal = 0 Degrees	186
Figure 5-14 Incident angle from normal = 15 Degrees	187
Figure 5-15 Incident angle from normal = 30 Degrees	188
Figure 5-16 Incident angle from normal = 45 Degrees	189

Figure 5-17 Power Values – a) 0 Degrees = 1.3275 W b) 15 Degrees = 1.628 W c) 30 Degrees = 1.67 W d) 45 Degrees = 1.558 W.....	190
Figure 5-18 Power Values – a) 0 Degrees = 3.98 W b) 15 Degrees = 4.07 W c) 30 Degrees = 4.125 W d) 45 Degrees = 3.895 W.....	191
Figure 5-19 Power Values – a) 0 Degrees = 5.77 W b) 45 Degrees = 5.77 W	192
Figure 5-20 Power Values –a) 15 Degrees = 11.6 W b) 30 Degrees = 11.6 W c) 45 Degrees = 11.6 W	193
Figure 5-21 Measurement of plume angle from normal after 20 pulses.	194
Figure 5-22 Holographic camera measurements and regions of interest.	195
Figure 5-23 Plot of plume height versus time at 0 degrees incident angle.	196
Figure 5-24 Composition of plume changes in refractive index along centroid at different incident angles. Scale indicates refractive index.	197
Figure 5-25 Holograms showing examples of shockwaves. Left 5.77 W at 6.74 μ s. Right: 5.77 W at 14.16 μ s. Scale indicates refractive index	198
Figure 5-26 Plot of plume height versus time at 15 degrees incident angle.	199
Figure 5-27 Plot of plume height versus time at 30 degrees incident angle.	200
Figure 5-28 Plot of plume height versus time at 45 degrees incident angle.	201
Figure 5-29 Green dotted line shows the field of view of the holographic camera. Blue line shows the edge of the plume. Red arrow indicates incident laser.	203
Figure 5-30 Design of fixturing for holographic camera on the ultra-precision platform	203
Figure 6-1 Schematic of future developments on the ultra-precision platform.....	209
Figure 6-2 SEM of ablated region.....	214
Figure 6-3 Left: EDX of region outside ablated region. Right: EDX of ablated region.	214

List of Tables

Table 2-1 Examples of microfluidic devices (Adapted from [14])	7
Table 2-2 FEI Helios NanoLab G3 Stage Data [33]	16
Table 2-3 Gas mixtures with corresponding wavelengths for gas lasers [37].....	20
Table 2-4 Gain medium with corresponding wavelength for solid state lasers [37] ...	21
Table 2-5 Beam control	29
Table 2-6 Different temporal regimes with conditions and appropriate model.....	39
Table 2-7 Definitions of symbols used in section 2.7.2	61
Table 2-8 Values used for holographic calculations.	67
Table 2-9 Summary of laser-matter interaction diagnostics	68
Table 3-1 Devices with corresponding wavelengths	76
Table 3-2 Specifications of Talisker Ultra laser system.	79
Table 3-3 Specifications of Qioptiq Linos beam expander.....	80
Table 3-4 Specifications of Watt Pilot variable attenuator.....	81
Table 3-5 Specifications of LMH-5X-1064 focusing objective.	82
Table 3-6 High Power Meter - Specifications of Ophir 30A-BB-18.....	82
Table 3-7 Low Power Meter - Specifications of Ophir PD300R-3W	83
Table 3-8 Energy Sensor - Specifications of Ophir PD10-pJ-C	83
Table 3-9 Beam Profiler - Specifications of Ophir SP300	83
Table 3-10 Specifications of Qioptiq Motorised Zoom Microscope	84
Table 3-11 Breakdown of components, functions and interfaces for ultra- precision platform.....	85
Table 3-12 Breakdown of devices which affect laser parameters.	86
Table 3-13 Scan ranges for 20x zoom.	95
Table 3-14 Scan ranges for 200x zoom.....	95
Table 3-15 Measuring variation in centroid of beam over 25mm sweep	100
Table 3-16 Angle of beam over sweep.....	100
Table 3-17 Visualisation of recording presence of tracks to find focus. Green indicates track present.	106
Table 3-18 Track machining paths.	116
Table 3-19 Recorded centroid of machined path for three iterations	119
Table 3-20 Devices used for automated holographic camera capture.	129

Table 4-1 Talisker Ultra specifications	133
Table 4-2 Ophir Sp300 Spiricon camera specifications.....	134
Table 4-3 Ophir 30A-BB-18 specifications	134
Table 4-4 Results from pointing stability test (1064 nm)	140
Table 4-5 Variation of beam diameter (1064 nm).....	142
Table 4-6 Average power output (1064 nm)	142
Table 4-7 Results from pointing stability test (532 nm)	144
Table 4-8 Variation of beam diameter (532 nm).....	145
Table 4-9 Average power output (532 nm)	146
Table 4-10 Results from pointing stability test (355 nm)	148
Table 4-11 Variation of beam diameter (355 nm).....	149
Table 4-12 Average power output (355 nm)	150
Table 4-13 Comparison of angular stability between two camera positions for 1064 nm	153
Table 4-14 Different duty cycles tested.....	157
Table 5-1 Specifications of LMH-5X-1064 Objective.....	169
Table 5-2 Ablation threshold at different incident angles.....	172
Table 5-3 Focal spot area, reflectance, ablation threshold and adjusted ablation threshold for different incident angles	176
Table 5-4 Values for calculated minimum-maximum track width ratio.....	180
Table 5-5 Different angle and power combinations captured.	185

1 Introduction

1.1 Background

'Ultra-precision technologies include machine, process and metrology technologies that enable the manufacture or function of parts having nanometre tolerance surfaces or features applied to artefacts of differing scale.' – Shore and Morantz [1]

The demand for ultra-precision devices is continuously increasing due to ever expanding applications in electronics, bio-medical, optical and energy devices. The term 'ultra-precision' will be used in this context to refer to geometrical feature of the order of 10 μm or smaller. Ultra-precision devices are typically manufactured using techniques such as photolithography which are economical when producing a large quantity of the same component [2]. For this type of manufacture a large initial capital outlay is subsidised by the high throughput to give a low final cost per device. However, for prototypes or small batches of devices this approach has a large associated cost and long lead time from concept to functioning device. Therefore, there is a demand for a processing method which is capable of prototyping and creating small batch quantities with a short lead time and low cost. The landscape for where the ultra-precision ultrafast laser platform fits into current ultra-precision manufacturing techniques is shown in Figure 1-1.

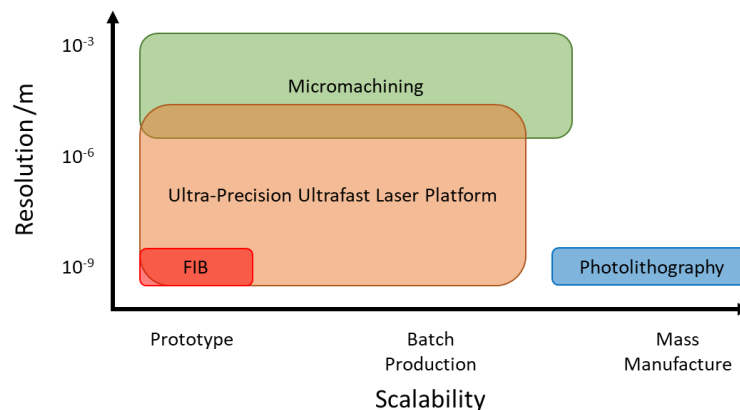


Figure 1-1 Graph showing achievable resolution against scalability for current ultra-precision manufacturing techniques and the ultra-precision ultrafast laser platform

Many new developments in manufacturing platforms have come from the optimisation and hybridisation of different manufacturing techniques in order to improve performance, whether in terms of throughput, surface finish or another property [3].

This has led to the diversification of manufacturing methods from traditional or established platforms.

A proposed solution to the small batch production of ultra-precision devices is the use of ultrafast laser processing. There are several advantages of using this machining method:

- A higher degree of flexibility than established technologies.
- Reduced production time for device prototyping, continuous customisation or low volume devices.
 - Capable of a large range in feature sizes from nm to mm.
 - Removal of ion milling processing reduces material degradation caused by ion implantation.

An ultra-fast laser process is a direct-write technology. This removes the need for an intermediate stage such as mask manufacture, which offers a clear advantage over lithography-based processes. Masks used in photolithography to pattern the substrate can be costly and time-intensive to make, and a single device may require several masks. At high production volumes masks become cost effective however for prototypes and low batch volumes they can be prohibitively expensive.

This key issue of this type of approach is that currently tolerances of parts machined using laser-based sources are limited to the open-loop feedback performance of the process which has a significant impact when functional features require nanoscale accuracy. Open-loop performance of ultrafast machining is limited by the inherent instability of the laser [4] which varies in beam position, power and diameter, affecting the characteristics of the focal spot. This can lead to geometrical errors which traditionally can only be evaluated by removing the part from the platform and evaluating using other metrology equipment which limits the ability to rework the part. Therefore, for this to be an effective processing route, an in depth understanding of the influence of these factors should be gained to produce ultra-precision parts. This includes identifying parameters which give desirable characteristics with regards to form, surface roughness, recast and heat affected zone. Therefore, a greater understanding of light-material interaction is required to find an optimal production route.

1.2 Research Aim and Question

The central aim in this work is to gain a better understanding of ultrafast laser processing to manufacture ultra-precision devices such as MEMS:

How does laser incident angle affect the light-matter interaction of an ultrafast laser pulse with silicon - to what degree can this knowledge be used to develop an optimised ultra-precision laser-based production route?

This can be broken down into the following questions:

- How can mechanical, optical and software design be used to improve the accuracy and repeatability of the ultra-precision platform?
- How stable is the laser and does this influence the process stability?
- Does changing the laser incident angle influence the plume which could correlate to a change in processing?

To answer the research question, the following objectives need to be tackled:

Objective 1: Identify, design, and implement equipment and methodologies to improve the accuracy and repeatability of the ultra-precision platform.

- The system should be designed to allow the development of other closed-loop metrology methods.
- Procedures should be developed to improve on current methods for sample alignment and machining.
- The platform should have the ability to monitor laser characteristics whilst performing machining.

Objective 2: Investigate the characteristics of the picosecond laser installed on the ultra-precision platform and the effect this can have on machining.

- Measure the point stability, beam diameter and power stability of the laser system.
- Identify the effects of duty cycle on beam stability.
- Simulate the effect of beam stability on machining accuracy.

Objective 3: Investigate how changing incident angle affects laser ablation at an angle.

- Determine the result of changing the incident angle on the ablation threshold for silicon.
- Measure the effect of incident angle on laser generated plume dynamics.

The proposed hypothesis of this work is that by moving to a greater incident angle this will reduce or negate the pulse plume interaction which will intern lead to a machining process with improved accuracy and repeatability.

2 Review of Precision Manufacturing Technologies and Laser Matter Interaction

2.1 Applications

In order to determine the requirements for the ultrafast laser processing route it is necessary to determine the types of devices the platform will be tailored to manufacture. Two very large markets are MEMS and microfluidic devices which had a combined value of \$13 billion in 2014 [5] and require features at the micron scale. A new area of development for the direct three-dimensional creation of features is optical microcavities which are typically produced using lithography techniques.

2.1.1 MEMS

Microelectromechanical systems (MEMS) are becoming widely used in numerous different applications and technologies [6]. MEMS development came about from the miniaturisation of mechanical and electromechanical systems. The initial concept was to manufacture mechanical systems using techniques typically used for electronic devices [7]. MEMS devices can have a wide range of applications including; gyroscopes, comb drives and sensors [8]. Traditional MEMS are silicon based but, as the platform has developed, other materials are now being used such as plastics and ceramics [9]. The geometry of MEMS can vary greatly depending on the device, the overall device can vary from a millimetre to a couple of microns. For example, an accelerometer requires multiple fingers with a separation of 1.3 μm with 1.6 μm gap from the base substrate material as shown in Figure 2-1.

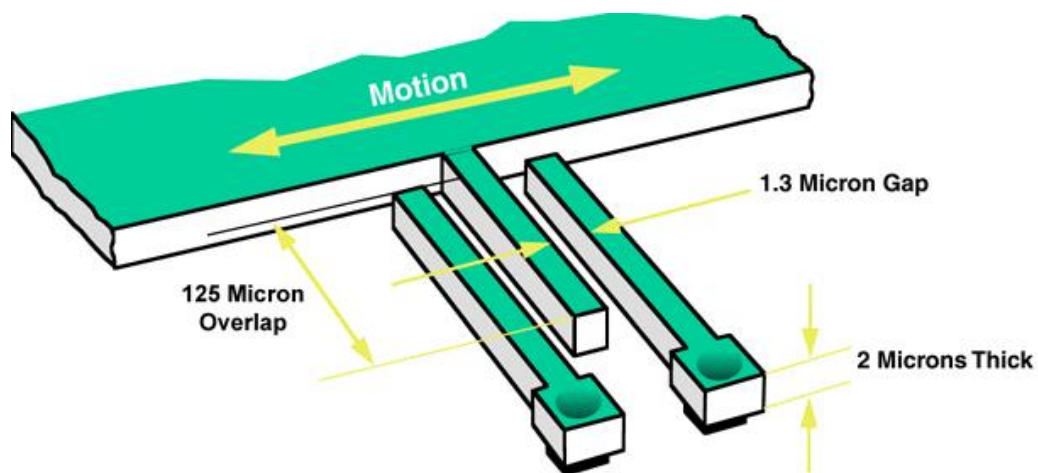


Figure 2-1 Schematic of typical dimensions for a MEMS accelerometer [10]

This example demonstrates the scale and geometry that are required to produce a functioning device. MEMS technology is being further developed to increase the level of miniaturisation which is leading to the term nanoelectromechanical systems (NEMS).

2.1.2 Microfluidic Devices

Microfluidics refers to the precise control and manipulation of fluids within confined channels which are within the micron or tens of microns scale [11]. A microfluidic chip is a set of micro-channels which are either etched or moulded into a substrate material such as glass, silicon or PolyDimethylSiloxane (PDMS) [12]. Microfluidic devices have several advantages which include:

- Reduction in fluid volumes and reagents required.
- Faster analysis of samples due to reduced diffusion times.
- Reduction of overall system size.

Examples of the areas of development for microfluidics are summarised in Table 2-1.

A significant effort is being put into developing 'lab-on-a-chip' (LOC) devices which is the integration of a single or multiple laboratory tests into a single device [13]. LOC demonstrates the integration of MEMS and microfluidic technology to provide a single self-contained device.

Another area of development in microfluidics worthy of consideration is the production of inkjet nozzles which are being developed into an additive manufacturing method. The size and topology of the inkjet nozzle have a significant effect on the droplet size, which in turn affects the minimum feature size that can be created.

As with MEMS, the envelope is being pushed toward nanofluidic devices the required precision for the device should be considered when developing a manufacturing platform.

Table 2-1 Examples of microfluidic devices (Adapted from [14])

Example	Components	Features	Aspects
Mixing analysis chip	Dye laser. Waveguides. Fluid network. Photodetectors	Mixers. Channels. Inlet/Outlet ports	Mixing length. Alignment of waveguides.
DNA Sequencer	Pumps. Valves. Control/flow network	Channels. Reservoirs. Inlet/Outlet ports	Interlayer thickness. Cross-section geometry
Oxygenation device	Blood, O ₂ network. O ₂ sensor	Channels. Junctions. Inlet/Outlet ports	Alignment. Interlayer thickness Bonding
Electrophoresis chip	Electrodes. Fluid network	Channels. Junctions. Reservoirs. Inlet/Outlet ports	Channel length. Alignment. Cross-section geometry
Microlens	Silicon base Fluidic cell PDMS cover	Channels. Layer. Inlet/Outlet ports	Surface roughness. Bonding
Microfuel cell	Electrodes Fuel, O ₂ source. Fluid network.	Channels. Junctions.	Channel length. Bonding.

2.1.3 Optical Microcavities

Optical microcavities are used to confine light to small volumes by resonant recirculation [15]. Microcavities are used to control transmission of data over optical fibres, and allow for a narrow spot size for devices such as DVD players.

Traditionally these devices are manufactured using planar lithography devices which has been shown to be rapid and cost-effective but doesn't give the ability to form three-dimensional cavities directly. Currently most high-Q crystal whispering-gallery-mode (WGM) microcavities are fabricated by mechanical polishing [16].

Developments have been made in the fabrication of microcavities using different processes including ultrafast ablation [17] and Focused Ion Beam (FIB) milling [18]. Lin et al [19] discuss multiple alternative methods for the production of microcavities from crystalline materials using a femtosecond laser and focused ion beam. The target diameter for the microdisk is a few microns to tens of microns depending on the application. The outline for the procedure is detailed below:

1. Femtosecond laser ablation of the CaF_2 substrate which is immersed in water to form the free standing disk-shaped structure. As seen in Figure 2-2 (a).
2. Smoothing of the side wall of the disk-shaped structure using FIB milling to create an ultra-smooth side wall. As seen in Figure 2-2 (c).

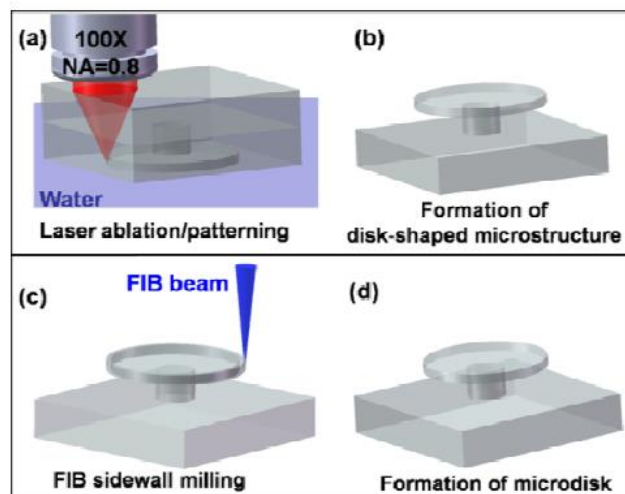


Figure 2-2 Procedure of fabrication of CaF_2 microdisk by femtosecond laser and FIB milling [19]

The microdisk created in this paper had a diameter of $79\ \mu\text{m}$ but the paper doesn't provide data on the surface roughness of the sidewall. Lin et al conclude that the technique was successful but the performance of the device was limited by the taper

applied to the sidewall due to the beam profile and the inaccessibility of the underside of the microdisk to the FIB. A 5-axes stage would give the ability to access this face which will lead to better feature production.

2.1.4 Carbon-based devices

The functionalisation of carbon-based structures is an area which is currently being intensively studied [20]. These structures are carbon nanotubes and graphene which are both members of the fullerene structural family. Graphene is the term used to refer to a two-dimensional, honey-comb structure formed from only carbon atoms. A carbon nanotube is a cylindrical structure where the walls are formed from sheets of graphene [21]. Carbon nanotubes and graphene's electronic and mechanical properties are ideal for micro and nano mechanical systems, electron field emitters, thin-filmed transistors, and conductive composites.

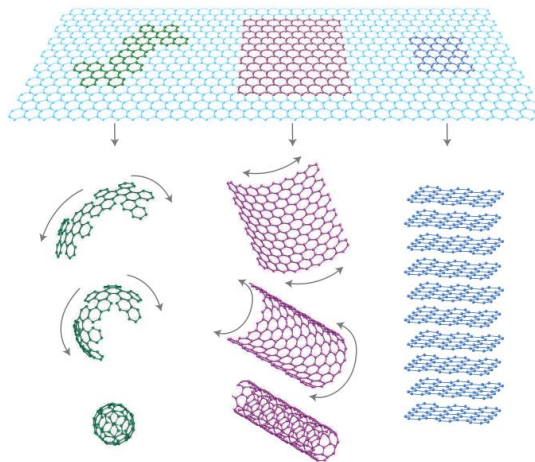


Figure 2-3 Different allotropes of carbon [21]. Left: Fullerene. Centre: Carbon nanotube. Right: Graphene.

A major focus has been to take raw graphene or carbon nanotubes and develop effective techniques to form functional devices. Work has been carried out with respect to the use of ultrafast lasers to pattern these materials however the current processing method is limited to a make and test strategy. Therefore, as the geometry and structure are unknown until the end of the process with time and capital having already been invested, this can lead to a very low-yield process which, in turn, increases the costs of manufacturing.

2.1.5 Review of Applications

From reviewing the types of devices that could be manufactured by this processing route, it appears that the geometries of MEMS, microfluidic devices, and optical microcavities are similar such that, when broken down, they are generated from simple trenches with varying depths, widths and lengths. This provides an initial geometry to target for the processing route. When creating a, the following characteristics must be considered:

- Accuracy of trench width
- Consistency of trench width
- Accuracy of trench depth
- Consistency of trench depth
- Vertical walls
- Flatness of base of trench
- Square corners

The challenge is to determine the limit of the accuracy that can be achieved by an ultrafast laser approach and whether this acceptable for the manufacture of the devices which have been identified.

For carbon-based devices there is the opportunity to develop a precise manufacturing platform capable of inspecting the raw sample before manufacturing using on platform metrology, then machine the raw material, and assess afterwards using the platforms metrology to increase process yield. However, this integration maybe beyond the scope of this research.

2.2 Competing Technologies

An assessment of the viability of the proposed processing route requires a review of existing competing manufacturing methods. These have been identified as being:

- Photolithography
- Micro-machining
- FIB Processing

Each of these techniques can be used to achieve sub-micrometre features however they are targeted to different materials, production routes and products.

2.2.1 Photolithography

Lithography techniques have made a significant contribution to the manufacture of integrated circuits (IC), microchips and semiconductor-based devices [2]. Lithography techniques have a broad range of feature sizes from tens of nanometres (current minimum feature size is 14 nm) to tens of millimetres and can be used for both subtractive and additive manufacture.

The demand for faster, smaller and power-efficient microprocessors has led to an increase in the number of transistors per chip and a decrease in feature size which has allowed microprocessors to advance in line with Moore's law. A photolithography fabrication plant is capable of meeting the high accuracies required for microprocessors and is capable of processing 50,000 300mm wafers per month [22]. This approach allows for low per-unit costs [23] and very low failure rates [24].

Photolithography functions by using ultra-violet light to transfer a geometric pattern from a mask to a light-sensitive photoresist on the substrate. This process can be repeated numerous times on the same sample to build up multiple layers to form a functional device. Photolithography is used because it is possible to produce accurate repeatable features to within tens of nanometres [25].

The basic photolithography method proceeds as follows:

1. Photoresist application – A photoresist is applied by spin coating to form a thin layer across the wafer.
2. Exposure – The photoresist is cured by ultra-violet light through a photomask forming the required pattern on the top layer of the wafer.

3. Etching – This process removes material on the uppermost layer of the substrate which has not been protected by the photoresist.

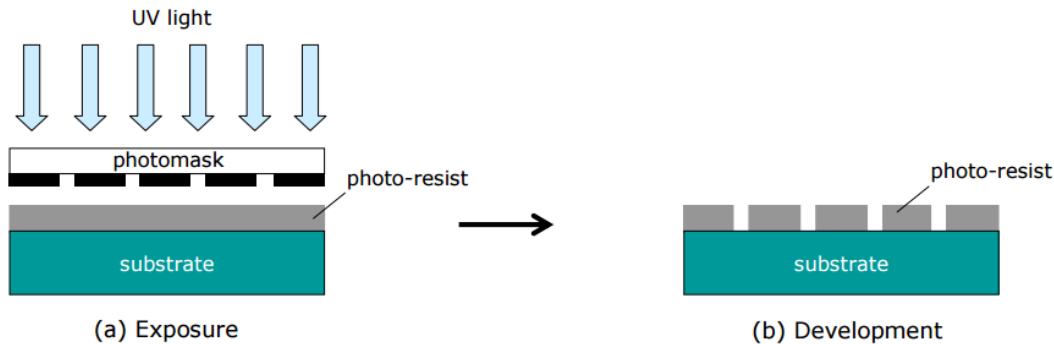


Figure 2-4 Basic representation of photolithography process [2]

A significant disadvantage of photolithography, rendering it less suitable for batch production, arises from the costs of the equipment, maintenance and masks. After a large number of exposures, the masks can become worn which leads to less accurate feature generation. An advantage of the laser processing route is due to the fact that the material is directly machined. In contrast to photolithography, there is no need for the use of chemicals which are hazardous to the environment.

2.2.2 Micromachining

Micro-machining is a traditional manufacturing platform and involves the removal of material. Ultra-precise machining is capable of producing complex three-dimensional shapes with good dimensional control and good surface finishes [25].

Machining can be broken down into four typical processes: milling, turning, drilling and grinding. Milling is a common process, where the part is held stationary whilst a rotating cutting blade moves around the part to give the required physical features. The part is mounted on a bed that can move in the x-y plane and depending on the model either the cutting head moves vertically up and down or the bed does to allow all three dimensions of motion. Turning takes place on a lathe where the part is rotated whilst a stationary blade cuts in parallel to the axis of rotation of the part. The parts selected for this process are usually cylindrical to prevent imbalance when rotating at high speeds. With this process it is possible to cut into and along the part to change its physical features. Drilling only involves the machining of holes into the workpiece. Grinding is used to provide the final finish to the part and has the lowest material removal rate of the four processes.

Ultra-precision machining is capable of achieving form accuracies of ± 50 nm and surface roughness (Ra) of 5 nm depending on the process [26]. Typically, these levels of precision are achieved during turning operations rather than milling operations, due to the simpler geometries involved. Examples of precision machines are the Kern Evo and the Nanoform 250.



Figure 2-5 Precision machining systems a) Kern Evo [27] b) Nanoform 250 [28]

2.2.3 FIB Processing

Focused ion beams (FIB) can be used for imaging, deposition and ablation of materials. FIB involves using an ion source, such as gallium, which is controlled by electric fields to collide with a substrate. This substrate will then sputter emitting secondary ions, neutral atoms and secondary electrons. Depending on the beam dosage, this collision will have different effects on the substrate. There are several factors to consider to ensure that this method works appropriately and effectively. An important area for milling is the characterisation of the beam profile as this will affect the quality of the sample after processing. The predicted limits of FIB milling using helium ions is the production of a 0.25 nm focal spot [29] although, this is subject to a number of factors such as sample material, chamber vacuum and beam current.

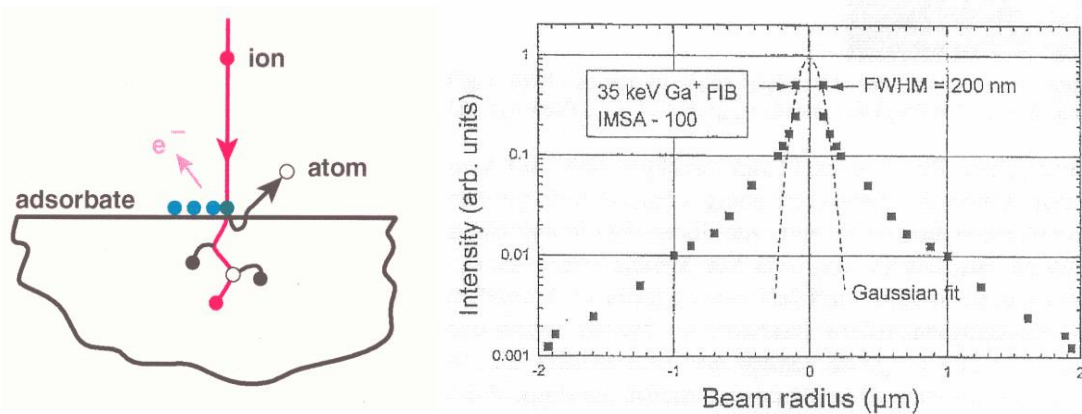


Figure 2-6 Left: Interaction of ion with material [30] Right: Beam profile of FIB [31]

2.2.3.1 Gallium ion machining

To ensure clean edges at the milling sites the beam energy needs to be set correctly to avoid sputtering and implantation of Gallium ions on the sample. This would necessitate a trade-off against processing time.

There are two different mechanisms for controlling the beam spot on the sample, the moveable stage, and controlling the beam direction. The stage is used for gross movements over 20 μm, whilst the beam direction would be used for milling fine features.

During machining of the features on the FIB the accuracy of the features produced can be monitored with a SEM to ensure that they meet the specification. This could be carried out in line with the manufacturing process causing little time overhead for the overall process. Figure 2-7 shows how the material removal rate is affected by the

dose. It indicates that as the dose increases the machining time for comparable areas reduces.

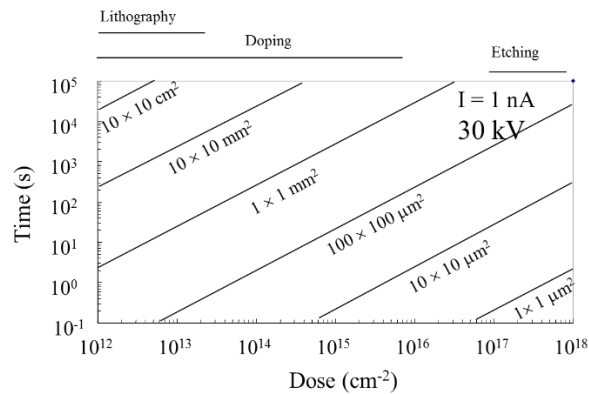


Figure 2-7 Relationship between dose, time and area for FIB machining [31]

2.2.3.2 Plasma ion machining

Plasma ion is a development of focused ion beam machining. Plasma ion uses significantly larger xenon ions in place of gallium ions to carry out machining. This means that up to 50 times higher material removal rates can be achieved. Secondly, for the same beam current, there is reduced ion implantation in the specimen reducing amorphisation within the sample. While ion-based, this method carries the disadvantage of being unable to achieve similar resolutions to FIB due to the use of larger ions. However, due to the commonality with FIB the two processes can run on a hybrid platform. Figure 2-8 shows a comparison of the material removal rates between gallium ion milling and plasma ion milling.

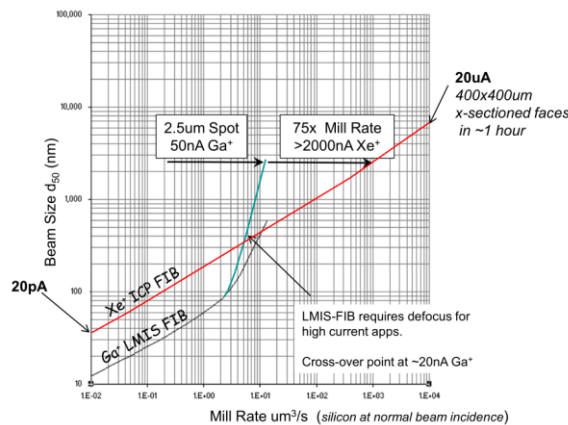


Figure 2-8 Comparison between FIB and FIB plasma removal rates [32]

There are a number of plasma FIB systems in developed such as those made by Oregon Physics and Tescan. These are additional columns that can be added to existing FIB-SEM platforms meaning they suffer from the same control issues.

2.2.3.3 Commercial Ion Systems

2.2.3.3.1 FEI Helios NanoLab G3

The FEI Helios is a FIB-SEM platform which is intended for sub-nm resolution imaging along with the ability to produce ultrathin samples for S/TEM. The system is capable of achieving a resolution of 0.6 nm when using the electron beam at 15 kV. The ion beam column can achieve a resolution of 4 nm at 30 kV [33]. The specification of the stages are as follows:

Table 2-2 FEI Helios NanoLab G3 Stage Data [33]

Property	Value
Stage Type	5-Axis
XY Travel	110 mm
Z-axis	10 mm
Rotation around Z Axis	Endless
Rotation around Y axis	-10° to +60°
XY Repeatability	1µm

As seen in Table 2-2, the available data only shows the repeatability of the X-Y axes. This causes issues regarding using a FIB-SEM platform as a machining tool. In order for the platform to be used as an ultra-precision manufacturing tool further detail is required which includes:

- Accuracy of the axes
- Repeatability of the axes
- Resolution
- Straightness of axes
- Perpendicularity

The FEI Helios is capable of milling features to within tens of nanometres when selecting the correct parameters and using beam steering. However, a method of

validating the geometry of the milled part whilst the sample is on the system is not currently available. The option to remove the part from the system for measurement exists but carries with it a significant challenge to achieve identical re-positioning for any corrective work.

2.2.3.3.2 Zeiss AURIGA

The Zeiss AURIGA is a Zeiss Crossbeam system with a laser processing chamber attached.

The Zeiss Crossbeam is a dual beam platform which has both a FIB column and a Scanning Electron Microscope (SEM) column. This allows the sample to be imaged by both columns with the advantage of the SEM being a non-destructive imaging method in contrast to FIB.

The Zeiss Crossbeam is capable of an imaging resolution of 0.7 nm using the electron column and 4 nm using the gallium FIB column. Stage data for the Zeiss Crossbeam only provides travel limits and no performance data [34].

The Zeiss AURIGA uses a nanosecond pulsed, diode-pumped solid-state laser operating at 355 nm provided by TRUMPF AG. The platform uses two stages to use the different processing techniques. The laser is kept in a separate chamber from the FIB-SEM because deposition of material generated from ablating the sample would be detrimental to the functionality of the FIB-SEM.



Figure 2-9 Zeiss Auriga with laser attachment [35]

This platform is targeted at analysing existing samples rather than a manufacturing platform. The laser appears to be a Galvoscaner arrangement and is only capable of top-down material removal aimed at sectioning samples. The laser system is mainly used to remove material of the order of several 10 mm³ within minutes, and is attached

to a load-lock chamber. This process is followed by FIB preparation and SEM analysis, which can be carried out in the same instrument. This reduces the preparation time of samples by 2000% compared with a single FIB process [35]. The accuracy and repeatability of machining on this platform are not considerations due to the intended use.

2.2.3.3.3 TriBeam System

The details of this section are from “A new TriBeam system for three-dimensional multimodal materials analysis” [36].

The TriBeam system is a FIB-SEM platform with a femtosecond laser (150 fs, 780 nm) into a single platform. This system has been developed for material analysis. The platform incorporates the femtosecond laser to increase the rate of material removal which allows for an increased throughput of serial sectioning of samples for three-dimensional datasets.

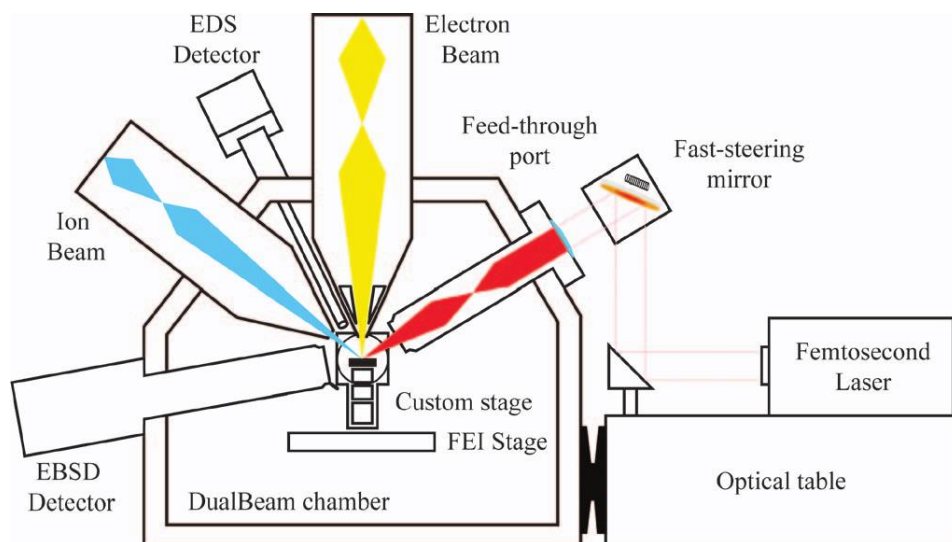


Figure 2-10 TriBeam system arrangement [36]

The system designed in the paper is based upon a FEI Strata™ DB 235 which is a previous version of the FEI Helios evaluated previously in this report. The arrangement of the system is designed to place the sample at the eucentric point of all three beams. The laser system is a Clark-MXR™ CPA-2110 which has an average power of 1.2 w, 1 kHz repetition rate and a wavelength if 780 nm.

Due to the stock stage not meeting the system requirements for the system a new micro stage was designed and attached to the existing stage. The micro stage uses Attocube micro positioners which have a sub-1 nm resolution and rotator resolution of

~1 μ degree. From testing, the femtosecond laser significantly increased the material removal rate from $0.5 \mu\text{m}^3/\text{s}$ for FIB milling to $1.4 \times 10^3 \mu\text{m}^3/\text{s}$.

The system demonstrates that there is a significant benefit of combining the FIB-SEM with an ultrafast laser to achieve greater material removal rates. The paper doesn't outline the accuracy or repeatability of the system which is a key detail for a manufacturing platform. Another problem may be that, for samples which require larger volumes to be ablated, contamination of the vacuum chamber and focusing optics of the FIB-SEM column may become an issue. The paper doesn't identify how they have verified the depth they have milled down too with this system, which adds uncertainty to the measured geometry reported. .

2.3 Laser Sources and Parameters

2.3.1 Basic Components and Types of Laser

There are several different types of laser which use different types of approaches and gain mediums. The wavelength of the laser is defined by the energy states of the gain medium. Common gain mediums include ruby, Nd:YAG, He-Ne, and CO₂. An energy source is used to pump the gain medium, sources include flash lamps, lasers, electrons, chemical reactions, ion beams and X-ray sources. Power of the laser can be controlled by changing the power supplied to the pumping source but also the quantity of the active medium. An optical resonator is used to amplify the light generated by the gain medium to reach the threshold for lasing. The optical resonator is constructed of a fully reflective mirror at one end and a partially reflective mirror at the other.

2.3.1.1 Gas Lasers

Gas lasers use a gas, either confined or flowing, as the gain medium. A common gas laser uses carbon dioxide for the gain medium with an operating wavelength of 10.6 μm . Carbon dioxide lasers have been used for a wide range of applications including cutting, welding, alloying, cladding, and heat treatment.

Excimer lasers are another form of gas laser. There are several gas mixtures used which are usually from the noble gas halides. An advantage of these types of laser is that short wavelengths can be achieved without the need for additional optics.

Table 2-3 Gas mixtures with corresponding wavelengths for gas lasers [37]

Gas Mixture	Wavelength (nm)	Power (W)
ArF	193	0.3-100
KrCl	222	2-4
KrF	248	2-100
XeCl	308	0.02-150

2.3.1.2 Solid State Lasers

Solid state lasers are built from either an insulated dielectric crystal or amorphous glass which hold an active medium. The active medium is a rare earth ion or a transition ion which have discrete electronic levels to perform the lasing action. An advantage of solid-state lasers is the relatively long lifetimes for the excited states which enables higher energy storage than are achievable with gas lasers.

Table 2-4 Gain medium with corresponding wavelength for solid state lasers [37]

Solid State	Wavelength (μm)	Power (W)
Ruby	0.694	10-20
Nd:YAG	1.06	0.04-800
Yb:fibre	1.03-1.1	0.01-20000
Er:fibre	1.5-1.6	0.01-500

Solid-state lasers through the use of Q-switching allows high peak powers in short pulses. A Q-switch allows for rapid shuttering of the optical cavity to generate fast, short pulses of power. Q-switches are available in multiple configurations, mechanical chopper, optoelectronic shutter or acousto-optic switch. The device allows energy to build up in the cavity and then when the shutter is opened a large amount of energy can be released in a short period of time.

The use of nonlinear optical devices such as lithium niobite crystal allow the transmitted frequency to be doubled thereby halving the wavelength. Therefore, from a 1064 nm source 532 nm can be achieved. The addition of a second stage of frequency doubling allows 355 nm to be transmitted.

Diode-pumped solid state (DPSS) lasers are a significant improvement over flash lamp pumped lasers as they allow for an improved energy efficiency due to the diode exposure being centred on a strong absorption line. Diodes produce a reduced heat output which means less energy is used in cooling the laser. This also allows for improved beam quality and improved pulse-to-pulse consistency [38].

Fibre lasers are the latest development of solid-state lasers. Fibre lasers use a double clad fibre where the internal active medium is pumped by the external cladding. Fibre lasers allow for small beam diameters, improved beam quality and require less cooling.

2.3.2 Laser focal spot parameters

To achieve high-quality laser machining, suitable operating parameters should be selected to achieve the accuracy required. This is determined by the fluence at the focal spot. The laser fluence or the energy density of the beam is determined by [39]:

$$F_{Abs} = \frac{P/r}{\pi * w_0^2} \quad (2-1)$$

$P = Power$, $r = repetition\ rate$, $w_0 = focal\ spot\ radius$

The focal spot diameter is determined by the following equation:

$$2w_0 = \left(\frac{4\lambda}{\pi}\right) \left(\frac{f}{D}\right) \quad (2-2)$$

$\lambda = wavelength$, $f = Focal\ Length$, $D = Raw\ Beam\ Diameter$

Each of these laser parameters is defined below, together with its effect on the focal spot characteristics.

Laser wavelength:

The wavelength of the laser sets the minimum focal spot diameter as it is diffraction limited. Also, materials have different absorption characteristics at different wavelengths which changes the pulse energy for ablation to occur.

Repetition rate:

This is the number of pulses per second and determines the volumetric material removal rate. However, depending on the type of target material, the repetition rate can affect whether mechanisms such as plasma drilling occur.

Average power:

Depending on the laser platform, the pulse energy remains constant for any laser platform and is then multiplied by the repetition rate. Some systems allow for higher pulse fluence by reducing the repetition rate but maintaining the average power.

Pulse energy:

The pulse energy directly affects the fluence at the focal spot. Fluctuations in pulse energy can change the interaction with the material and can cause the region within

the focal spot to have a fluence greater than the threshold fluence of the material, subsequently changing the width of the region ablated.

Pulse duration:

The pulse duration affects the regime which occurs and is explained in further detail in section 2.4.

Raw beam diameter:

This affects the focal spot diameter as noted in the focal spot diameter equation causing a deviation in fluence and the same effects as variation in pulse energy. For example, as the raw beam diameter increases, the focal spot radius decreases.

Focal spot velocity:

This is significant when milling tracks as it will determine the rate at which new material is presented per pulse. This typically isn't included in models for laser ablation.

2.3.2.1 Analysis

Laser fluence has direct relation to the ablation depth. Therefore, we can determine that variation in the pulse energy and raw beam diameter can cause a significant difference in the ablation depth and track-width milled by the laser. These are interlinked by equation (2-3) shown below and demonstrates the need for control of pulse energy and raw beam diameter to achieve precise machining.

$$F_{Abs} = \frac{E}{\pi * w_0^2} = \frac{P/r}{\pi \left[\left(\frac{2\lambda}{\pi} \right) \left(\frac{f}{D} \right) \right]^2} \quad (2-3)$$

2.3.3 Laser beam parameters

When considering using lasers for manufacturing it is a requirement to know the profile of the beam at the machining point. The beam profile will be characterised by the following parameters:

Quality

The beam quality and divergence are quantified using the parameter M^2 . If a beam is truly Gaussian then the M^2 value is 1, unfortunately for a real beam the M^2 value tends to be between 1.1 and 1.3 for ultrafast lasers [40]. The larger the M^2 value the greater deviation of the beam profile from Gaussian.

Divergence

This is the increase in beam diameter as distance from the aperture increases causing a reduction in the fluence of the beam.

Shape

The shape of the beam is significant to the effectiveness of using a laser for machining. The two typical beam shapes are Gaussian and top-hat.

The Gaussian has the advantage that the power at the centre of the beam can be controlled to give the required threshold fluence at a precise point. However, the edge of the beam can cause undesirable effects such as melting or phase changing. In contrast, the top-hat or flat-top beam shape gives a uniform beam profile across the focal spot reducing edge effects [41].

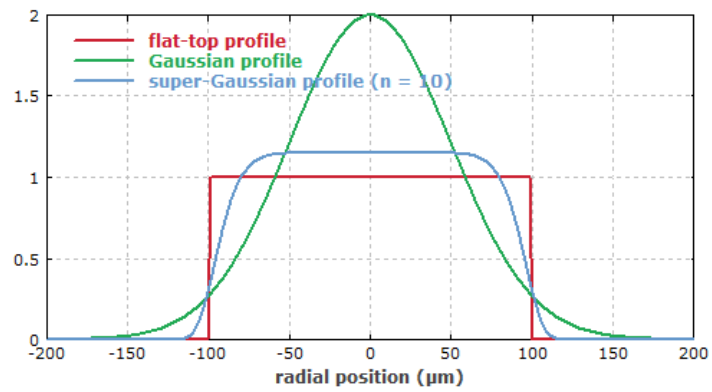


Figure 2-11 Difference between Gaussian and top-hat beam profiles [41]

Stigmatism

This term is used to describe the power density distribution of the beam. A beam which when focused through a focusing object has focal points where the vertical and horizontal directions do not coincide is called astigmatic.

Pointing stability

This is used to characterise the translational stability and the angular stability [42].

The pointing stability of the laser has a great significance on the precision that can be achieved with ultrafast lasers. Any variation in position of the beam affects the position of the focal spot on the target. This can lead to the machining of tracks which deviate from the intended straight path.

2.3.4 Measurement techniques for beam parameters

Beam parameters should be measured in accordance with ISO standards 11670, 11146, 11145, 13694 which define the experimental setup and procedure for performing beam diagnostics. These should be referred to for a thorough methodology for beam testing [42].

There are a number of different methods that can be used to characterise the properties of a laser beam. These have been reviewed with regards to attaining accurate results and the scope for implementation as an in-process solution.

2.3.4.1 Beam diameter measurement

Knife-edge technique

The knife-edge technique involves using a single edge razor blade and a translational stage. The beam is incident on a device which is capable of measuring beam intensity. The blade is advanced through the beam at equal increments and the measured intensity is recorded.

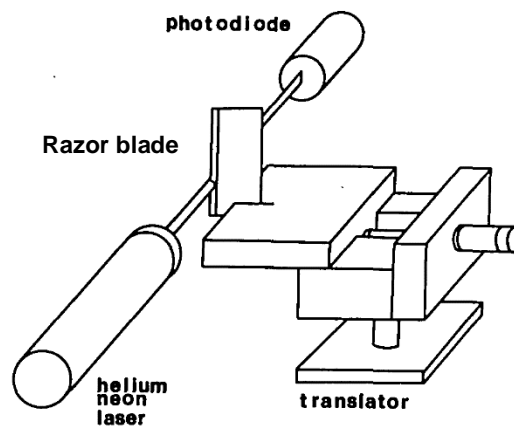


Figure 2-12 Schematic of knife edge technique [43]

This method is limited in the rate at which the beam diameter can be acquired by the speed of the stage [44]. Due to the occlusion of the beam whilst undertaking measurement, this method can be carried out during processing but requires the use of a beam splitter, and a detector of greater sensitivity is required due to the drop in power.

Scanning slit optical beam profiler & aperture method

This method is similar to the knife-edge technique by occluding the beam and detecting the difference in intensity. A plate with a slit is translated through the beam and the change of intensity is measured for the position of the slit and the overall beam profile is interpolated.

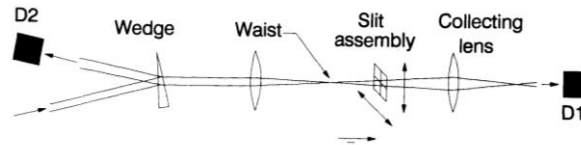


Figure 2-13 Scanning slit beam profiling [45]

Camera beam profiler

A camera beam profiler requires the beam to be incident on the camera. The advantage of this method is that the overall beam profile can be viewed which allows for the deviation in X & Y diameter to be measured simultaneously. The camera will also give detail on the centroid position and beam shape by analysing the intensity measured by each pixel. The increase in the resolution of the camera and decrease in the pixel pitch allows for measurements to be taken in the sub 5 micrometre domain. The camera-based setup carries a built-in limitation from the maximum rate of data acquisition set by the frames-per-second capability of the camera (typically of the order of 20-30 FPS), which can miss higher-frequency changes.

2.3.4.2 Power measurement

Thermopile

A thermopile operates by measuring the voltage generated by the temperature difference between two dissimilar materials [46]. This type of power meter has the disadvantage of being susceptible to environmental changes, has a slow response rate and usually used for CW lasers.

Pyrometer

This sensor operates by measuring the voltage generated by a temperature change of a single material [46]. Pyrometers have a non-linear response to changes in power making reliable measurements difficult.

Photodiode

A photodiode is a solid state device which converts incident light into electrical current [46]. This type of sensor has a linear response to the change in power and is capable of a wide range of measurements. Consequently, it is the method of choice for measuring laser power reliably.

2.3.4.3 Pointing Stability

Quadrant sensors

A quadrant sensor is made up of four separate photodiodes which have small gaps between them. The difference of the intensity measured by each photodiode can be used to calculate the position of the beam centroid.

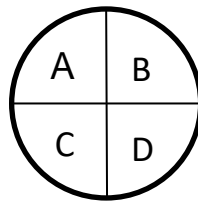


Figure 2-14 Schematic of quadrant sensor

The position of the centroid of the beam is calculated using:

$$X = \frac{(B + D) - (A + C)}{A + B + C + D} \quad Y = \frac{(A + B) - (C + D)}{A + B + C + D} \quad (2-4)$$

Quadrant sensors are capable of very quick responses due to the linearity of the photodiode.

Camera beam profiler

The data captured and limitations are identified in the beam diameter measurement.

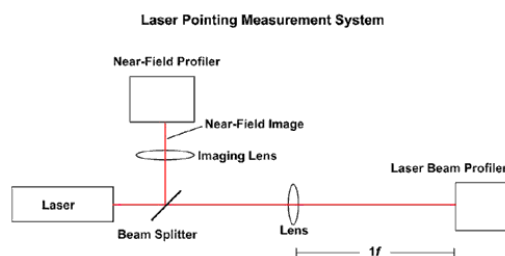


Figure 2-15 Example of camera arrangement for measuring pointing stability [47]

2.3.5 Devices for laser control

In order to counter the change in these parameters during processing allowing precise machining with the laser it is necessary to implement control solutions to reduce the deviation from the desired value.

Table 2-5 Beam control

Parameter	Solution	Explanation
Beam diameter	Motorised beam expanders	This device allows for the beam diameter to be changed dynamically.
Power	Motorised attenuators	This allows for a requested power level to be maintained however this requires the raw beam power to be consistently greater than the power level requested.
Pointing stability	Beam steering using piezo mirrors	This system uses a set of actuated mirrors to correct the position of the beam. Piezo actuated mirrors are usually selected as they can introduce small displacements at very high frequencies.

2.4 Models and Phenomenology in Ultrafast Laser-Matter Interactions

There has been a significant volume of research into the application and theory of pulsed lasers since their development. A key reason for such a large number of research papers is the number and range of parameters that can be varied which include pulse energy, pulse duration, wavelength, repetition rate and material to name a few [48]. Most theoretical models are based around the application of the two-temperature model and rely on experimental values for material properties such as reflectivity and absorption depth. An issue with laser-based research papers is that results are difficult to repeat due to the high number of variables affecting the outcome a significant number of which are not documented. Therefore, it is best to review these papers for guidance and suitable research methods rather than seeking a 'how to' guide. In this section a focus has been made on the application of picosecond laser ablation of silicon at 1064 nm and oblique angles ablation.

One of the best overall reviews for ultrafast laser ablation is "Modelling ultrafast ablation" by Rethfeld and Ivanov [49].

2.4.1 Overview of Mechanism timescales

The response of a material to an ultrafast laser pulse is very complex and can include a range of phenomena from material excitation to ablation. Figure 2-16 gives the different possible pathways for different materials when exposed to a 100 fs laser pulse. Typically, the pulse energy is absorbed to the electron-lattice structure during the range of femtoseconds. If melting is to occur this happens within the picosecond domain and ablation can last into the nanosecond domain [50]. All of these timescales are affected by material properties such as electron-lattice transfer time and laser properties like pulse duration. For picosecond laser pulses it can be considered that evaporation is a direct solid-vapor transition.

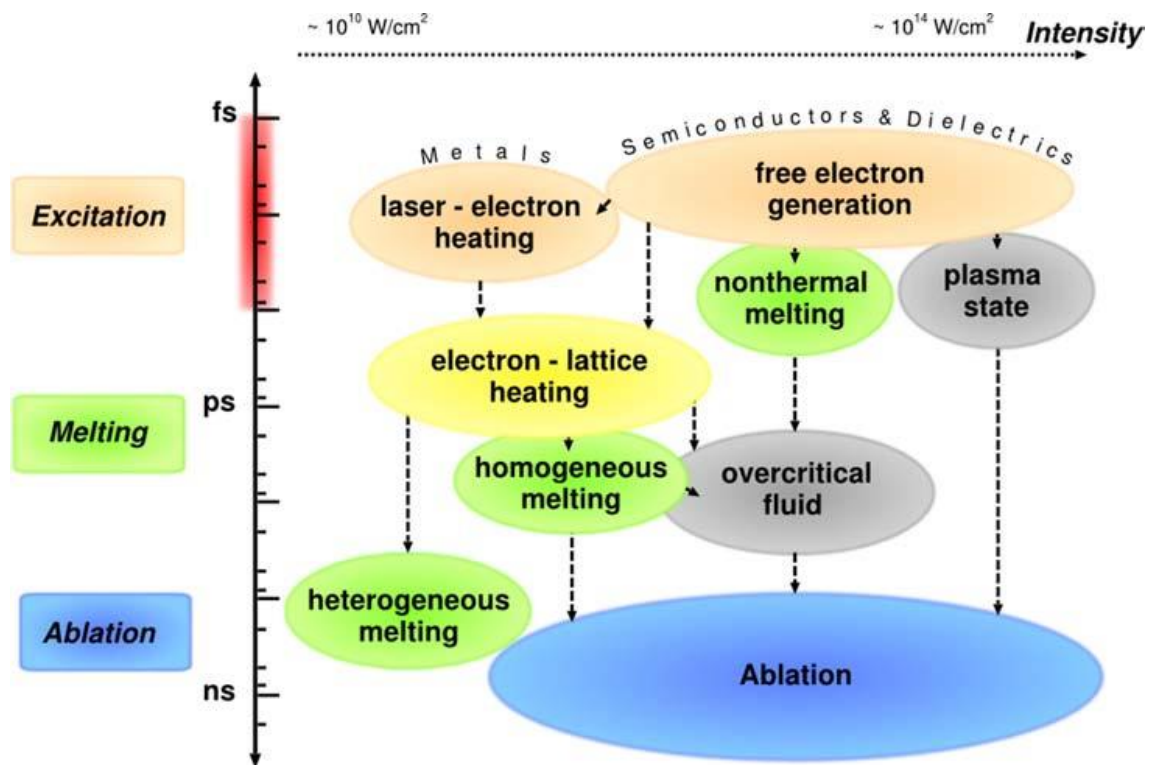


Figure 2-16 Typical timescales and intensity ranges of laser phenomena [49]

2.4.2 Laser Beam Delivery and Scanning Methods

There are a number of different properties which affect the focal spot of the laser that can be manipulated to give different desired outcomes. These can come from the original wavelength of the laser, the spatial energy distribution at the focal spot, the delivery of the energy with respect to time, the polarisation of the incident light and scanning strategies.

2.4.2.1 Wavelength

The wavelength of the incident light can have significant implications on the outcome of the exposure. Every material has a different absorption spectrum which means that incident wavelength selection can be important in achieving a desirable outcome.

A secondary implication of the wavelength is the limitation on the minimum focal spot dimension due to the Rayleigh criterion. The shorter the wavelength the narrower the focal spot can be achieved. Therefore, the required feature size may dictate the necessary wavelength range.

The wavelength also determines the method in which the photon energy couples into the material. For direct photon-electron coupling the wavelength of the photon must

match a band gap in the material. The transition energy of the photon is calculated by the following equation:

$$\Delta E = \frac{hc}{\lambda} \quad (2-5)$$

ΔE is the photon energy, h is Planck's constant, c is the speed of light and λ is the photon wavelength.

In the event that the photon energy does not match the band gap in the material, coupling can still occur through phonon-assisted coupling or multi-photon absorption. Due to the negligible momentum of a photon the difference in wave vector must be supplied by a phonon.

2.4.2.2 Spatial Energy Distribution

Changing the spatial energy distribution at the focal spot can be desirable depending on the intended patterning required. Typical spatial profiles used are Gaussian, top-hat and 'donut'. There are two key methods in which the spatial energy distribution at the focal spot can be modified. This can be done through the geometry and dimensions of the gain medium within the laser or using external optics such as a ' π Shaper'.

The transverse electromagnetic modes (TEM) can be used to describe the spatial energy distribution of a laser. TEM₀₀ is the lowest order mode and corresponds to a Gaussian profile. The modes are denoted by TEM_{PL} where P and L are integers labelling the radial and angular mode orders, respectively. In real applications it is difficult to achieve a true Gaussian beam profile therefore most laser manufacturers provide a beam quality factor or M² value. A perfect Gaussian beam has an M² = 1 as the beam deviates from a Gaussian profile causing a reduction in beam quality the M² value increases. The beam quality affects the quality of focus that can be achieved.

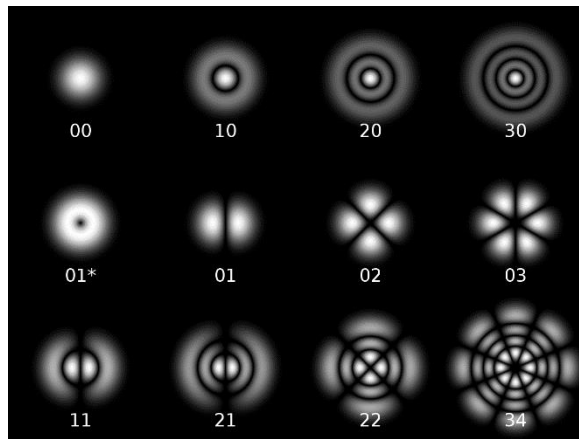


Figure 2-17 Cylindrical transverse mode patterns TEM(p,l) [51]

Another method of changing the spatial energy is to use optics to change the wave front of the beam. A common conversion used in research is to change from a Gaussian profile to top-hat. This can be done using a propriety device such as a ‘πShaper’ or a different arrangement of lenses. The advantage of a top-hat profile is a uniform intensity across the diameter of the beam.



Figure 2-18 πShaper [52]

The spatial-temporal profile general case can be defined as:

$$I(r, t)|_{\Delta\lambda} = I(t)e^{-\frac{2r^2}{D^2}} \quad (2-6)$$

2.4.2.3 Temporal Energy Distribution

When considering pulsed lasers, the delivery of energy over time for that pulse needs to be considered; this is often called the pulse shape. Although a pulse can have a defined energy and duration there can be a difference with how the energy is delivered within the pulse envelope. Pulsed lasers are typically broken down into three regimes, nanosecond, picosecond and femtosecond. A wide number of studies on the effect of pulse duration and pulse shape have been carried out for silicon [53] [54] [55] [56].

2.4.2.4 Polarisation Orientation

Laser-generated light has a linear polarisation when emitted. Polarisation refers to the electric field vector of the light relative to the direction of propagation.

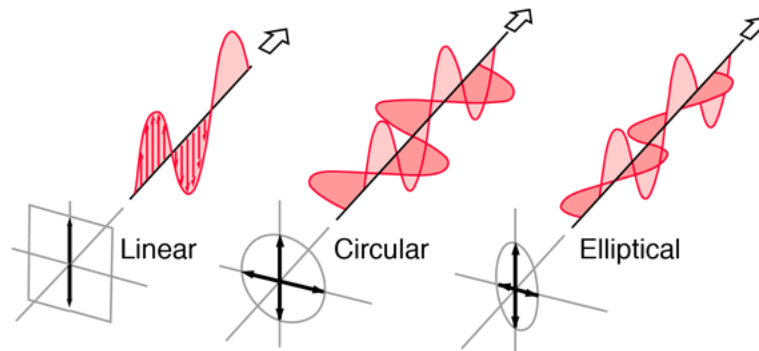


Figure 2-19 Linear, circular and elliptical polarisation orientations of lasers [57]

The polarisation of the light can be changed using quarter and half-waveplates. Waveplates are constructed out of a birefringent material which has two different refractive indexes which are perpendicular to each other. This allows the introduction of a controlled phase shift between the two polarisation components of the light wave.

One effect that can be caused by linearly polarised light is laser-induced periodic surface structures (LIPSS) [58] [59]. When the fluence is close to the ablation threshold a standing wave pattern is produced on the surface of the substrate. The periodicity of the structures is typically close to the wavelength of the incident light. The orientation of the LIPSS is dependent on the polarisation of the light, pulse overlap, and pulse energy.

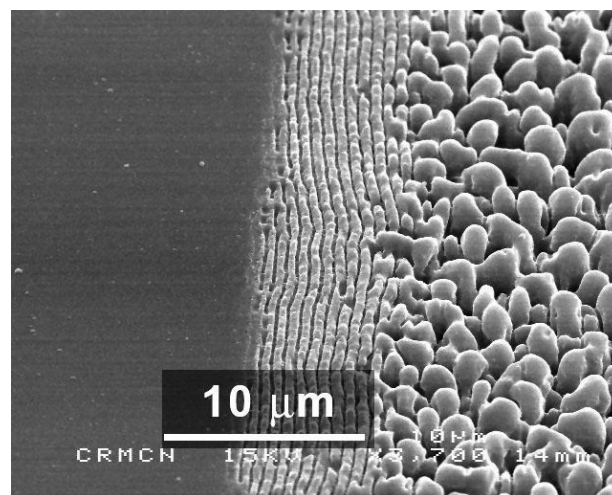


Figure 2-20 SEM photo of Laser Induced Periodic Surface Structures (LIPSS): capillary waves (periodicity 800 nm, centre) and beads (about 2 µm, right) on silicon [60]

It can be advantageous to use circularly polarised light to avoid effects such as LIPSS and some materials, such as silicon, can exhibit different absorption characteristics dependent on focal spot movement relative to crystal orientation.

2.4.2.5 Scanning Methods

For laser machining there are three main methods for moving the focal spot relative to the sample. By far the fastest is the use of a galvo-scanner which uses two perpendicular mirrors attached to piezo actuators for fast focal spot movement in the order of 1000 mm/s. One disadvantage of this method is a reduction in positional accuracy. Also, long focal-length objectives are typically used, which cause a larger focal spot diameter. The other two methods use motorised stages to either move the focal spot around the sample or the sample around the focal spot. These methods provide the highest level of accuracy however the stage speed is significantly limited.

When it comes to scanning strategy there are two dominant methods, vector scanning and raster scanning. Vector scanning takes the exact path required whereas raster scanning is similar to an inkjet printer and breaks the pattern into discrete units and then moves line by line over the whole grid.

2.4.3 Light Absorption

2.4.3.1 Two Temperature Model

Laser ablation is the process of removing material from a substrate by irradiating it with a laser beam.

Pulsed lasers can have pulse lengths from nanoseconds to attoseconds [61]. The term ultrafast laser refers to lasers with a pulse durations shorter than picoseconds [62]. The duration of the pulse affects the type of interaction with the target material.

For the interaction of low intensity pulses with metal targets the laser is absorbed by the free electrons due to the inverse Bremsstrahlung effect [63]. This forms a nonequilibrium of the electron gas with the lattice. During a short period of a few picoseconds or less the lattice maintains its low temperature.

The absorbed energy is transferred to the lattice structure and these can be characterised by their temperatures. This relationship can be described by the following one-dimensional two temperature model as reported in [63]. The energy exchange between electrons and the lattice can be described by the following equation.

$$C_i \frac{\delta T_i}{\delta t} = -C_e \frac{\delta T_e}{\delta t} = \text{div}(k_i \nabla T_i) - \gamma_{e-l}(T_e - T_i) \quad (2-7)$$

The specific heats of the electrons and lattice are denoted by C_e and C_i . T_e and T_i are the electron and lattice temperatures respectively. The energy exchange between the two subsystems is defined by γ_{e-l} . To account for energy transport from the hot surface layer to the bulk of the material, the effect of lattice heat conduction should be included. This is accounted for in the divergence term where k_i is the thermal conductivity of the lattice.

A similar equation for the electron temperatures can be formed:

$$C_e \frac{\delta T_e}{\delta t} = k_e \frac{\delta^2 T_e}{\delta z^2} - \gamma_{e-l}(T_e - T_i) + S(z, t) \quad (2-8)$$

The energy released into the electron subsystem by the laser is covered by S . k_e is the thermal conductivity of the electrons.

The two-temperature model which is formed from these two equations allows for theoretical predictions on the process which will occur for a given pulse energy and pulse duration such as melting threshold or heating rates [64] [63].

This model does have limitations such as when applied to the femtosecond timescale as the pulse duration is close to at which electron-electron collisions typically occur therefore the application to determine temperature is questionable. A further assumption is that the electron and phonon energy transfer mechanisms adhere to Fourier's law. Finally, it is assumed that the material properties remain unchanged during the process.

In order to simplify the application of the two-temperature model it is assumed that thermal conduction into the bulk of the material is negligible. From this the characteristic time of electron gas cooling due to energy exchange with the lattice is:

$$\tau_e = \frac{C_e}{\gamma_{e-l}} \quad (2-9)$$

And lattice heating is:

$$\tau_i = \frac{C_i}{\gamma_{e-l}} \quad (2-10)$$

For the case of electron cooling in laser-irradiated metals $C_e \ll C_i$ and it is assumed that the lattice temperature is constant as long as $T_e \gg T_i$. This leads to the relaxation temperature being described by:

$$\tau_{relax} = \frac{C_e C_i}{(C_e + C_i) \gamma_{e-l}} \quad (2-11)$$

Since $C_e \ll C_i$ this can be approximated to:

$$\tau_{relax} \simeq \frac{C_e}{\gamma_{e-l}} \quad (2-12)$$

There are multiple suggested methods for the calculation of the energy exchange rate, γ_{e-l} . A common method relates the material resistivity ρ , the effective mass m^* , and the carrier concentration, n , by:

$$\gamma_{e-l} \simeq \frac{C_e n e^2 \rho_{res}}{m^*} \quad (2-13)$$

The interaction between the target and laser pulse is determined by three characteristic timescales:

- τ_e = Electron cooling time.
- τ_i = Lattice heating time.
- τ_L = Laser pulse duration.

When the pulse duration is typically shorter than the electron cooling time, $\tau_L \ll \tau_e$. Therefore, the assumption can be made that electron heat conduction can be neglected. For evaporation to occur the absorbed laser fluence, F_a , needs to be greater than the threshold fluence, F_{th} . The absorption coefficient of the material is identified by α . Assuming the laser fluence is greater than the threshold fluence, the ablation depth per pulse, L , is:

$$L \cong \alpha^{-1} \ln \left(\frac{F_a}{F_{th}} \right) \quad (2-14)$$

This relationship between laser fluence and ablation depth allows for precise laser-processing of metals using picosecond lasers.

The threshold fluence, F_{th} , is the laser fluence required for ablation and is calculated by equation (2-15) where L_v is the latent heat of vaporisation.

$$F_{th} \cong \frac{\rho L_v}{\alpha} \quad (2-15)$$

From this the electron and lattice temperatures immediately after a pulse can be calculated by:

$$T_e \cong \left(\frac{2F_a\alpha}{C_e} \right)^{1/2} e^{-\alpha z/2} \quad (2-16)$$

$$T_i \cong \left(\frac{F_a\alpha}{C_i} \right) e^{-\alpha z} \quad (2-17)$$

Picosecond lasers operate in the regime where the pulse length is longer than the electron heating time but shorter than the lattice heating time, $\tau_e \ll \tau_L \ll \tau_i$. Approximations lead to the same relationship between laser fluence and ablation depth as femtosecond lasers however this is an oversimplification of the real interaction for

picosecond lasers. The relationship for lattice temperature remains the same however the electron temperature is:

$$T_e \cong \left(\frac{F_a \alpha}{\tau_L \gamma_{e-l}} \right) e^{-\alpha z} \quad (2-18)$$

Nanosecond pulses give a significantly greater time period to transfer heat to the target. This means that the target is heated to the melting point and then to the vaporisation temperature. As the evaporation of material from the melted material occurs, it becomes significantly more complicated to perform accurate machining using nanosecond pulses. In this condition the $T = T_i = T_e$ which suggests that the bulk values of the material can be used for heat capacity, C_p , thermal diffusivity, D_{th} , and conductivity, k_T . The thermal penetration depth is given as:

$$l_T = 2 \left(\frac{k_T \tau_L}{\rho C_p} \right)^{1/2} \quad (2-19)$$

The thermal diffusivity is defined as:

$$D_{th} = \frac{k_T}{\rho C_p} \quad (2-20)$$

For all of the scenarios mentioned above there are limitations which determine the thermodynamic conditions due to temporal constraints. These are outline in Table 2-6.

Table 2-6 Different temporal regimes with conditions and appropriate model.

Regime	Condition	1-D Model
$\tau_L \ll \tau_e \ll \tau_i$.	$\frac{C_e T_e}{t} \gg \gamma_{e-l} T_e$	$C_e \frac{\delta T_e}{\delta t} = 2 \frac{F_a}{\tau_L} \alpha e^{-\alpha z}$
$\tau_e \ll \tau_L \ll \tau_i$.	$\frac{C_e T_e}{t} \ll \gamma_{e-l} T_e$	$k_e \frac{\delta^2 T_e}{\delta z^2} - \gamma_{e-l} (T_e - T_i) = \frac{F_a}{\tau_L} \alpha e^{-\alpha z}$
$\tau_e \ll \tau_i \ll \tau_L$	$D_{th} \tau_L \alpha^2 \gg 1$	$C_p \frac{\delta T}{\delta t} = k_T \frac{\delta^2 T}{\delta z^2} + S(z, t)$

2.4.3.2 Thermodynamic Response

Energy transfer to the lattice by electron-phonon interaction is usually much slower than the characteristic relaxation time for electrons which is in the order of $\tau_e = 100$ fs. Only when the timescales involved are significantly greater than the electron-phonon relaxation time τ_{ph} , can the system be described by one temperature. For time periods shorter than this each system needs to be considered independently.

Fourier heat conduction can be applied to time periods greater than 100 ps as an equilibrium is reached between electrons and phonons.

The surface temperature can be calculated from equation (2-21). The regime applied depends on the ratio of the thermal, l_T , and optical penetration depths, l_α , where T_∞ is the ambient temperature of the system.

$$T_s(t) = \begin{cases} T_\infty + \frac{2(1-R)I_0}{k_T} \left(\frac{D_{th}t}{\pi} \right)^{1/2} & \text{for } l_T \gg l_\alpha \\ T_\infty + \frac{\alpha(1-R)I_0}{\rho C_p} t & \text{for } l_T \ll l_\alpha \end{cases} \quad (2-21)$$

Typically, a Gaussian spatial profile is used for the laser beam which means that equation (2-21) has to be solved to include lateral heat losses as shown in equation (2-22).

$$T_s^{Gauss}(x, y) = T_\infty + \frac{(1-R)D_{min}I_0(x, y)}{k_T\sqrt{2\pi}} \tan^{-1} \left(\frac{2\sqrt{D_{th}t}}{D_{min}} \right) \quad (2-22)$$

2.4.3.3 Laser Modification Thresholds

The level of fluence of the laser spot can cause many different material effects. When considering laser ablation for machining there are two key thresholds that need to be considered, the ablation threshold and the melting threshold.

Fluences below the threshold of melting can enhance diffusion rates promoting impurity doping, a change in crystal structure or the sintering of porous materials. The increased temperature of the substrate from the laser fluence can also cause chemical reactions such as oxidation which wouldn't have occurred at ambient temperature.

When the laser fluence is greater than the threshold of melting this can cause the formation of melt pools on the substrate. Due to the liquid nature of the melt pool this allows for higher atomic mobilities and solubilities causing rapid material

homogenization. By changing the fluence of the laser spot the cooling rate can be controlled to change the properties of the solidified material.

For laser ablation to occur the fluence of the focal spot must be greater than the ablation threshold of the material. The ablation threshold is defined as the minimum fluence required for strong evaporation of the substrate material to occur. Ablation can occur with both constant wave and ultrafast pulsed lasers. The pulsed laser offers the advantage of delivering a pulse whose duration is shorter than the thermal diffusion time as discussed in section 2.4.3.1 with the result that the heat affected zone is significantly reduced.

One factor to consider is how the spatial energy profile of the focal spot relates to the region exposed. Ultrafast laser ablation typically performed with a Gaussian beam profile, where the fluence across the focal spot varies significantly as the intensity reduces from the centre of the spot outwards. However, different beam profiles can be used which can have advantages over a Gaussian beam profile. From Figure 2-21 it is apparent that the region at the centre which experiences the greatest intensity undergoes ablation and the regions further from the centre experience other thermal processes such as melting, annealing and oxidation. As the overall focal spot fluence increases the central region of ablation increases in diameter.

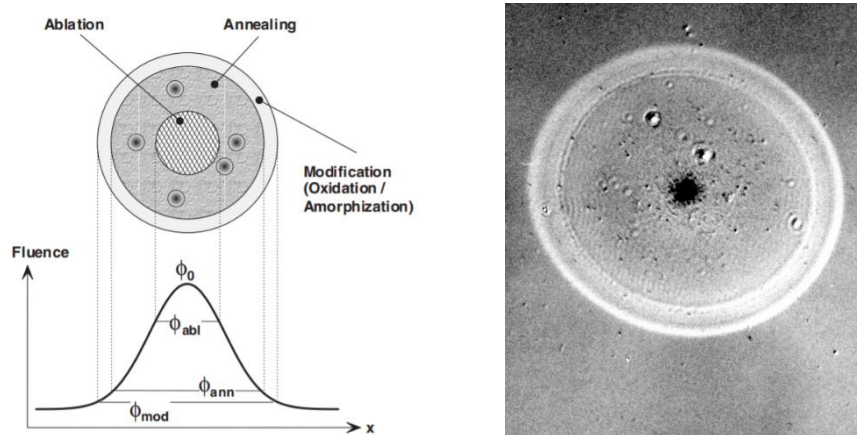


Figure 2-21 Left: Effect of threshold fluences on the modification of silicon with femtosecond laser pulses. Right: Optical micrograph of the silicon sample surface treated with a single laser pulse. [65]

The Gaussian intensity profile can be used to produce sub-wavelength features through spatial profile and precise power control.

The spatial energy distribution is given by equation (2-23). Equation (2-24) is obtained by taking the natural logarithm of equation (2-23) and delivers a linear relationship between ablated radius and focal spot fluence. By taking experimental data and applying a linear regression the ablation threshold fluence can be calculated.

$$F_{th} = F_0 \exp\left(-\frac{2r^2}{w^2}\right) \quad (2-23)$$

$$\ln(F_0) = \frac{1}{2w^2} (2r)^2 + \ln(F_{th}) \quad (2-24)$$

2.4.3.4 Summary

In summary the following properties need to be determined to predict the regime which should be used to predict the outcome of laser machining:

- Laser fluence – This is the energy per unit area for the beam.
- Absorption coefficient – Determines the distance light of a given wavelength can penetrate the material before being absorbed.
- Optical penetration depth – This is the reciprocal of the absorption coefficient.
- Thermal penetration depth – The distance heat will transfer by thermal conductivity through the sample.
- Electron cooling time – Time taken for electrons to return to state prior to the laser pulse.
- Lattice heating time – Time taken for the energy from the pulse to be transferred to the lattice.
- Pulse duration – Length of time for a single pulse of the laser.
- Threshold fluence – energy per unit area to cause ablation of the substrate.

The following figure gives a visual representation of the difference in material interaction to a short and long pulses [66].

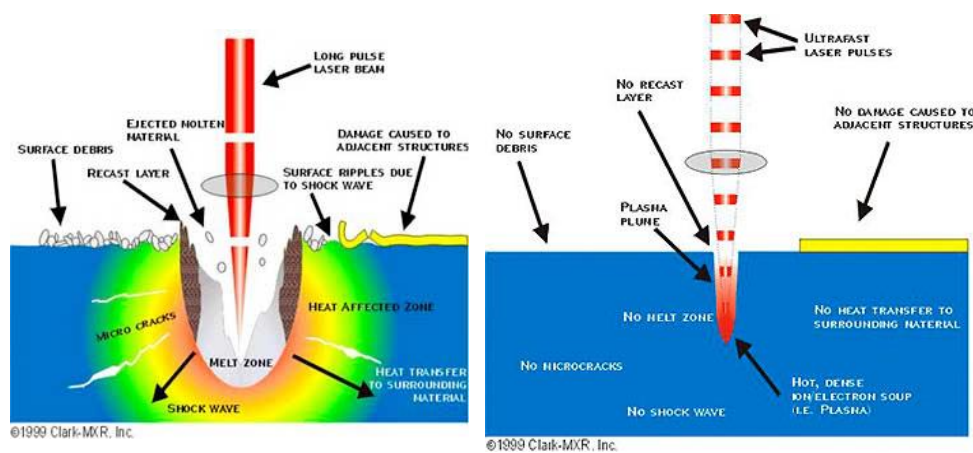
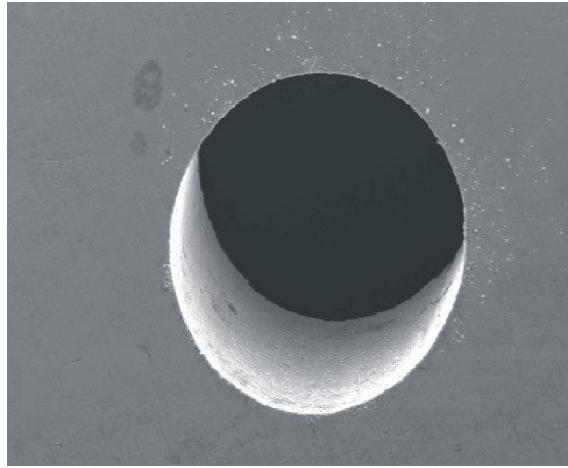
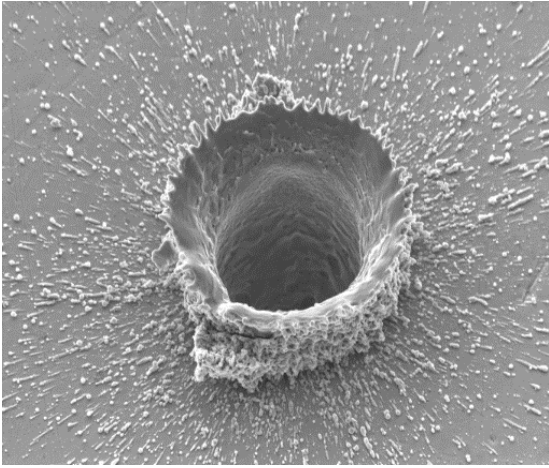


Figure 2-22 Differences in interaction with substrate for long pulses and short pulses [25]



**Figure 2-23 Left: Image of laser ablation with a pulse width of 10^{-9} s
Right: Image of laser ablation with a pulse width of 10^{-15} s [67]**

2.5 Optical Properties of Materials

Snell's law describes the relationship between the angle of incidence and the angle of reflection for light passing between two isotropic materials. Snell's law is defined as follows:

$$\frac{\sin \theta_2}{\sin \theta_1} = \frac{v_2}{v_1} = \frac{n_2}{n_1} \quad (2-25)$$

For this equation θ is the angle measured from the normal of the boundary, v is the velocity of light through the respective medium and n is the refractive index of the specific material [68] [69].

The refractive index can also be defined as the relationship between the speed of light in the material and the speed of light in a vacuum, c .

$$n = \frac{c}{v} \quad (2-26)$$

For most materials there are two optical properties to observe, namely the reflection, R , and transmission, T , of the material. These two properties are conserved thus:

$$1 = R + T \quad (2-27)$$

To include this material property the complex refractive index is used:

$$\tilde{n} = n + ik \quad (2-28)$$

The extinction coefficient, k , is related to the absorption coefficient, α , where λ_0 is the wavelength of the incident light:

$$\alpha = \frac{4\pi k}{\lambda_0} \quad (2-29)$$

For a two-material interface the reflectivity is defined as:

$$R = \left| \frac{\tilde{n}_2 - \tilde{n}_1}{\tilde{n}_2 + \tilde{n}_1} \right|^2 \quad (2-30)$$

The reflectivity is dependent on the polarisation of the incident light relative to the surface. As the light can be polarised parallel or perpendicular to the surface the reflectivity is as follows:

$$R_{\parallel} = \frac{(n \cos \theta - 1)^2 + k^2 \cos^2 \theta}{(n \cos \theta + 1)^2 + k^2 \cos^2 \theta} \quad (2-31)$$

$$R_{\perp} = \frac{(n \cos \theta + 1)^2 + k^2}{(n \cos \theta - 1)^2 + k^2} \quad (2-32)$$

2.5.1 Coherence of multiple internal reflections

When considering substrates of a finite thickness it is necessary to consider the reflectance deviations between the front and rear surface. For wideband uncollimated radiation these deviations cancel each other out and the energy of the reflected beams can be summed. However, for monochromatic light, interference can be observed from reflections from the front and rear surfaces.

Equation (2-33) is the coherent mathematical expression for determination of total fringe amplitude with highly collimated narrow bandwidth radiation on parallel substrates:

$$T = \frac{(1 - R)^2 e^{-\alpha t}}{1 - 2R e^{-\alpha t} \cos \varphi + R^2 e^{-2\alpha t}} \quad (2-33)$$

Where α is the absorption coefficient, t is the distance of the substrate the incident radiation is attenuated by and φ is the reflection phase shift. From this the effect of incoherent light, high absorption and finite substrate depth can be calculated.

2.5.2 Optical penetration depth

The absorption of a material varies with the wavelength of the incident light. A high absorption is beneficial as it means the total incident laser power can be reduced for ablation to occur [70]. High absorption means that the optical penetration depth is reduced, and heating of the substrate is concentrated in the top surface. Thus, the volumetric heating is reduced which reduces the size of the heat affected zone of the substrate [71].

The Beer-Lambert Law relates the attenuation of light to the properties of the material that it is travelling through. The optical penetration depth is given by equation (2-34) where α_{ext} is the absorption coefficient.

$$l = \frac{1}{\alpha_{ext}} \quad (2-34)$$

The intensity of the incident light at a given depth within the material is:

$$I(z) = I_0 e^{-\alpha_{ext}z} \quad (2-35)$$

Each material has a different absorption spectrum and reflectivity spectrum [72]. Below is a plot of absorption depth against wavelength for multiple materials.

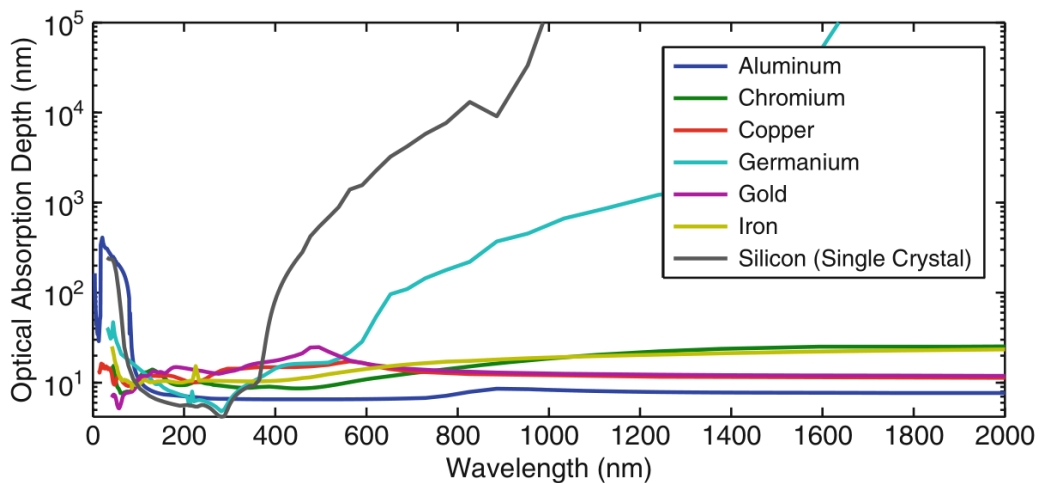


Figure 2-24 Optical absorption depths for several materials from 0 nm to 2000 nm wavelength. [73]

For high-energy laser pulses these relationships do not hold true due to the rapidly changing environment and complexity of energy coupling into the material. Therefore, these values are usually found experimentally which can be a challenging process.

2.5.3 Effect of Temperature on Optical Properties

As already discussed the absorption and reflectivity of a material can change with wavelength. However, it has been found experimentally that the ablation threshold of silicon can change with respect to temperature. Figure 2-25 shows that substrate heating can be used as a technique to lower the ablation threshold of silicon when processing using ultrafast lasers within the infra-red domain.

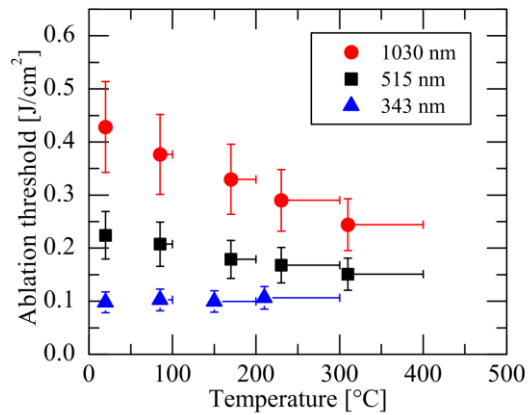


Figure 2-25 Ablation threshold for silicon at different temperatures with wavelengths 343, 515, and 1030nm,3 ps pulse duration. [74]

An in-depth analysis and simulation model has been carried out by J. Thorstensen and S. E. Foss [74]. The authors suggest that the temperature-ablation threshold relationship is related to the critical electron density rather than vaporisation of the lattice.

2.6 Metrology Methods for Laser Machining

For laser ablation to be used as an ultra-precision machining method the ability to assess the accuracy and repeatability of the features machined is required. The standard approach is to use 'off-line' metrology techniques which review the open-loop machining process and have a high level of precision. However, the need to remove the part from the machining platform renders reworking problematic as it is virtually impossible to achieve the identical positioning upon part replacement. One answer to this is the use of 'online' metrology methods which allow for closed-loop feedback and active adjustment of the machined features on the machining platform. This section looks at the current technologies used in laser machining metrology and future avenues for closed-loop machine development.

2.6.1 Off-line

2.6.1.1 Atomic Force Microscopy

Atomic force microscopy (AFM) is a contact method of measurement where a very small stylus attached to a cantilever is dragged across a sample. As the topology of the sample changes the position of the stylus changes deflecting the cantilever. The deflection of the cantilever is measured using a laser and a sensor [75]. This data can be collated to form a three-dimensional topology of the measured sample. The resolution of the AFM is limited by the size of the tip rather than diffraction limited like optical methods. Typical resolutions of an AFM is around 10 nm but sub-nanometre resolutions are possible [76]. When measuring a sample using AFM a consideration should be made when selecting a probe. If the probe tip is too large detail can be lost on high aspect features [77].

2.6.1.2 Electron Microscopy

Scanning (SEM) and tunnelling (TEM) electron microscopy are widely-used by the scientific community. These systems are capable of achieving resolutions below 1 nm due to the short de Broglie wavelength of electrons.

SEM has the following benefits over optical microscopy. SEM has a greater depth of field allowing for surface topology to be in focus; significantly higher magnifications are achievable with a resolution of <1 nm; composition of samples can be determined [78].

For a SEM, electrons are produced using a tungsten filament within an electron gun which form a beam that is controlled using multiple condenser and objective lenses

and scanning coils. The electron beam interacts with the sample and produces secondary electrons, backscattered electrons, and x-rays. These outputs are collected by different detectors and converted to give a live image of the sample. Secondary electrons are electrons which have been released from the surface of the sample with energies below 50 eV and give a higher resolution than backscattered electrons. Backscattered electrons tend to provide more chemical composition data on the sample. The x-rays generated can be used to find the chemical composition of the sample.

The principle of TEM has been explained previously but the main contrast to SEM is that the sample is required to be very thin to allow electrons to pass through them.

Electron microscopy systems image samples in a two-dimensional plane limiting the information which can be gained from the sample. However, the sample stage can be rotated to view the sample from different orientations. There have been developments to generate three-dimensional reconstructions of sample using SEM [79].

2.6.1.3 White Light Interferometer

White light interferometry uses a polychromatic light source, instead of a laser, to create a separate set of interference fringes for each wavelength of light is present. The intensity at any point in the image plane is the summation of the different fringe sets. In order to attain the highest contrast fringe pattern, the optical path difference should be zero. The most common white light interferometer techniques used are diffraction grating interferometers, vertical scanning or coherence probe interferometers, and white light scatter-plate interferometers. White light interferometry allows surface topology to be captured extremely accurately.

2.6.2 In-process

There are a number of in-process technologies which will aid the development of the system. These have been identified and the potential for implementation on the ultrafast platform and are outlined in the following section.

2.6.2.1 Machine Vision

Machine vision is the term used for systems used to provide visual inspection and analysis for a wide range of tasks including PCB inspection and part identification. This technology is widely used in industry to automate repetitive and intensive tasks.

Machine vision systems usually use an imaging device (e.g. camera) to capture an image which can be processed to provide feedback to the manufacturing tool.

Machine vision has been used in a wide variety of real-world applications, which include[80]:

- Optical character recognition – reading handwritten postal codes on letters and automatic number plate recognition.
- Machine parts inspection – rapid inspection of parts for quality assurance.
- 3D model building – Fully automated construction of 3D models.
- Dimensional analysis – Checks part geometry matches the required tolerances.

Machine vision can be incorporated into many different control systems and is usually implemented in either feedforward control or feedback control. A feedforward solution could be a method in which quality control is implemented and defective parts are removed during manufacture. A feedback implementation would be the reporting of statistical data to the manufacturing process on the defect rate [81].

For measurement applications it is recommended that a high resolution camera is used as it more effective for feedback control as high resolution images reduce errors in the results from processing the images [82]. A factor to consider is that the microscope objective is diffraction limited for the lateral resolution which needs to be considered when decided the features which are to be measured.

An advantage of using a machine vision system is that it is a non-contact method of measurement therefore the property being measured isn't modified or degraded. This is particularly key when measuring fine geometry or surface finish which would be affected by a contact probe.

OpenCV (Open Source Computer Vision Library) is an open source computer vision and machine learning software library [83]. OpenCV provides a library of over 2500 optimized algorithms for a wide variety of uses and can be used to implement the examples given above. This software package provides a wide scope of different control solutions that could be implemented on the hybrid laser-FIB platform.

Machine vision provides a number of development avenues to be pursued for integration with the hybrid laser-FIB platform. The first initial application would be the integration of a fiducial marker arrangement for alignment on both systems and the cross-platform transfer.

2.6.2.2 Optical Coherence Tomography

Optical coherence tomography (OCT) in its most basic form is a Michelson interferometer. A Michelson interferometer involves a low temporal coherence light source with a reference path and path to the sample. The difference in the path length between the reference and the sample path can be used to collect depth information.

Within OCT there are two different procedures required to collect three-dimensional data from the sample. The first is the depth-scan which is performed by the reference mirror. The second the lateral OCT scan which involves moving the sample or by scanning the probe beam illuminating the sample [84]

There are two main types of OCT which are time domain and Fourier domain (FD-OCT). Time domain OCT allows for imaging with a large axial field but at the cost of a reduced scanning speed. Fourier-domain OCT has a significant advantage over time domain as only the lateral scan needs to be performed. Depth information is determined using the inverse Fourier transform of the backscattered light. There are two methods for implementing FD-OCT which are swept source (SS-OCT) and spectral-domain OCT (SD-OCT). SS-OCT involves using a laser which is tuneable to a wide number of wavelength and a single photodiode, whereas SD-OCT uses a broadband light source and a spectrometer detects the interference pattern. OCT is capable of producing two-dimensional and three-dimensional information by using the positional information from the stage and depth information from the system.

Commercial OCT systems are capable of resolutions smaller than 5 μm axially and laterally [85]. Systems with even smaller axial resolutions are in development by various research groups. An advantage of OCT is the system's ability to carry out in-situ monitoring of the process. This allows for closed-loop control methods to mill to depth when coupled with an ultrafast laser platform. A disadvantage of coupling OCT and an ultrafast laser to provide a closed-loop milling system lies in OCT's inability to evaluate the change of depth per pulse which is in the order of 50 nm [86] [87].

An 'inline coherent imaging and galvo-telecentric beam delivery system' [88] has been developed which combines laser machining and OCT with scanning optics. The galvo-based process is capable of significantly higher scanning velocities than those achievable by stage-based systems. A performance comparison to a high precision stage would offer an interesting bench mark to determine the limit of the OCT system.

2.6.2.3 Digital Holographic Microscopy

Digital holographic microscopy (DHM) is a method of carrying out high resolution three-dimensional measurements. A typical system requires the following: an illumination source, interferometer, digital camera, and a computer [89]. A wide range of lasers can be used as the illumination source depending on the wavelength required. As with OCT the system relies on a reference path and a sample path. The waves both arrive at the digital sensor with the same waveform curvature.

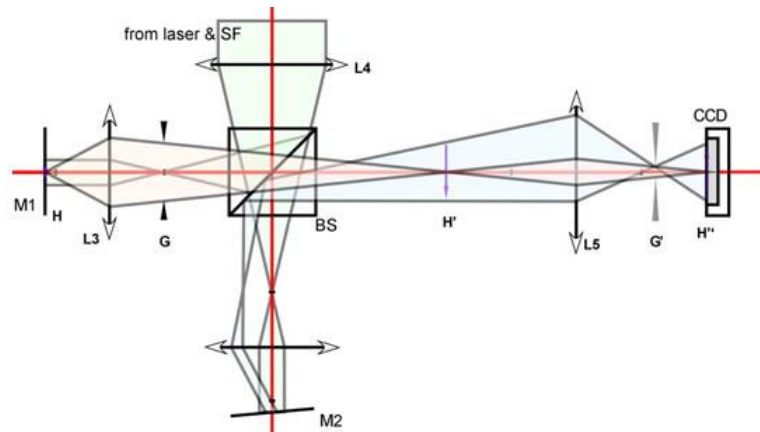


Figure 2-26 Michelson interferometer for digital holographic microscopy of reflective specimen. [89]

Commercial systems are capable of an accuracy of 0.15 nm [90]. With a single wavelength source the system resolution is limited to half the imaging wavelength for axial field of view. In current systems the resolution is limited by the pixel count of the camera used.

2.6.2.4 Raman spectroscopy

Raman spectroscopy uses the inelastic scattering of monochromatic light to perform chemical analysis. Inelastic scattering is the term used to describe when the photons from the monochromatic light source change upon interacting with the sample. The photons are absorbed by the sample then reemitted. The Raman effect is the shift in the frequency of the reemitted photons from the photons produced by the monochromatic source. This shift can be used to determine vibrational, rotational and low frequency transitions in molecules. In turn, this can be used to study solid, liquid and gas samples [91].

The most common form of Raman scattering is Stokes Raman, which occurs when the photon energy is reduced by the vibrational energy quantum of the scattering molecule.

Raman emission is normally weak but it can be enhanced by several orders of magnitude when the laser wavelength is close to the electronic absorption band of the sample. This is known as resonance Raman spectroscopy [92].

The use of Raman spectroscopy has recently been a useful tool for the identification of graphene. When carrying out Raman spectroscopy of graphene care is required to prevent sample damage or heating occurs from the laser source. Raman spectroscopy allows the identification of single and multiple layers of graphene which was previously only possible using transmission electron microscopy. Atomic force microscopy was only capable of measuring folds of wrinkles in graphene as this causes a change in the measured spectra [93]. Raman spectroscopy can also be applied to carbon nanotubes to identify whether the carbon nanotube is single-walled or multi-walled structure or any defects [94].

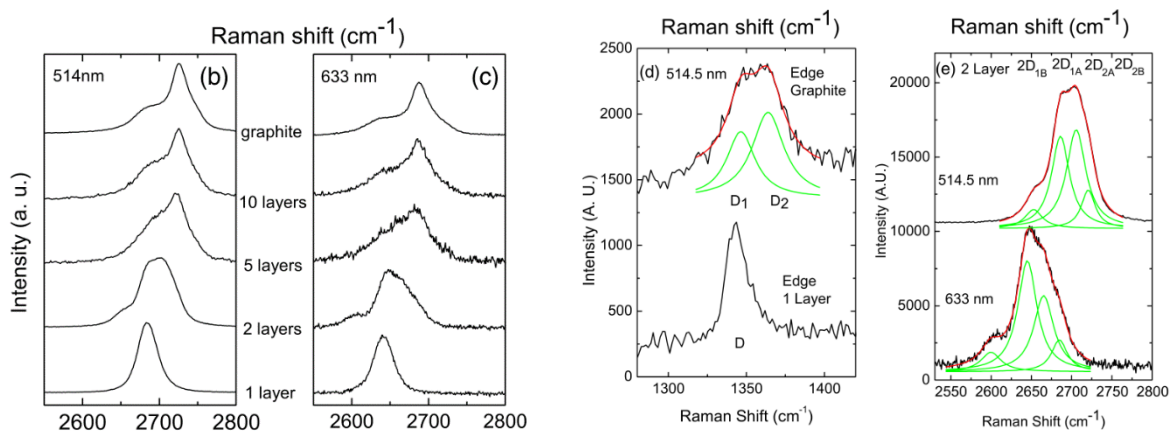


Figure 2-27 Left: Change in Raman shift due to number of layers of graphene for 514 nm and 633 nm

Right: Change in Raman shift at edge of bulk graphene for 514 and 633 nm [93]

Raman spectroscopy could be used to scan a sample of graphene or carbon nanotubes creating a map of the properties of the sample. This data could then be used to cleave a sample with the required properties using the ultrafast laser. After cleaving the sample the Raman spectroscopy could perform a second scan for any defects created after which the laser could be used to correct the defects. A platform with both Raman spectroscopy and ultrafast ultra precise laser to form closed-loop in-situ fullerene machining has not been previously attempted.

2.6.2.5 Dual comb interferometer

The typical approach to laser ranging is to measure the time for a pulse to leave the laser and return to the detector. Shorter wavelength signals can be used to improve the resolution of the measurement but this approach is limited. Laser interferometry measures the phase of optical wavelengths to achieve sub-nanometre resolution [95]. However, this only allows for measurement of relative range changes rather than an absolute value.

A frequency comb is a phase-stable mode locked laser. This comb is capable of sending pulses with a large number of modes at repetition rates in the hundreds of megahertz [96].

A dual comb is built from two frequency combs which have slightly different repetition rates. This allows the second comb to gate the first comb which causes a Vernier scale between the pulses. The Vernier scale provides the absolute distance whereas the phase difference between the two combs provides sub-wavelength resolution.

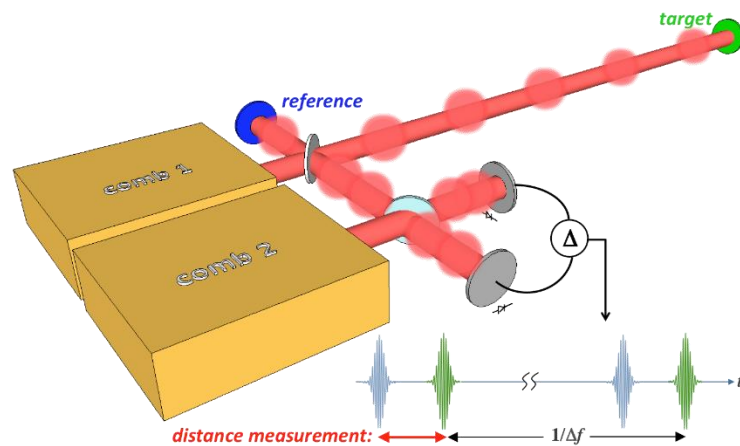


Figure 2-28 Dual comb interferometer schematic [97]

2.7 Ultrafast Laser Ablation at an Angle

Focused laser ablation has traditionally been performed at a normal angle of incidence. However, by performing ablation at an oblique angle can have advantages and be used for different techniques. The most common current use for oblique angle ablation is for Pulsed Laser Deposition (PLD) and there have been some applications for direct-write ablation.

2.7.1 Pulsed Laser Deposition

Pulsed laser deposition (PLD) is used in the production of thin films on to a substrate. Pulsed laser deposition is similar to sputter deposition in that it is a physical vapour deposition technique carried out within a vacuum. For PLD, a pulsed laser is focused onto a target which is the material that is to be deposited on the desired substrate [98]. When ablation occurs a plume is formed made up of a small amount of material from the substrate. The ablated material is ejected towards the substrate and provides the material flux for film growth. The ejected material absorbs part of the incoming pulse energy to form a plasma. Ablation conditions are chosen so that the plume consists of low mass species such as atomic and diatomic particles [99]. The wavelength of the laser and the pulse width can be tuned to allow for the desired plume conditions depending on the target material.

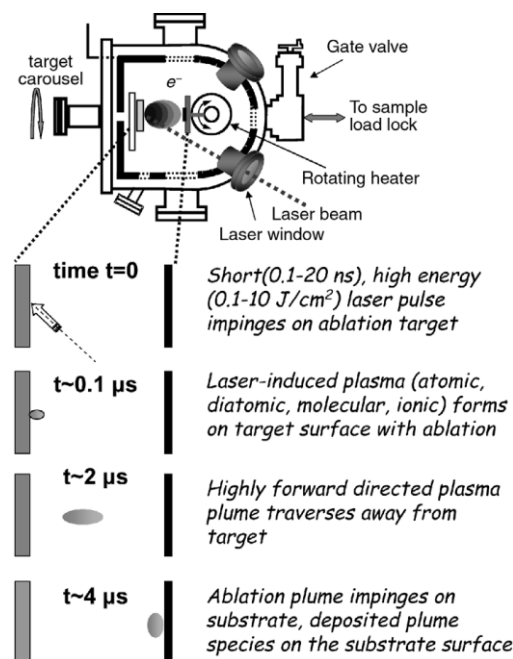


Figure 2-29 Pulse laser deposition experimental setup [98]

PLD is an attractive method of deposition of complex films for several reasons. The process can be performed at a range of vacuum pressures from ultrahigh vacuum to 1 Torr. PLD also allows for stoichiometric transfer of material from the target, hyperthermal reaction between the ablated material and the background gas, and the generation of energetic species. By using multiple different targets, films of different species can be deposited. An issue with PLD is the non-uniformity of the distribution thickness from a stationary plume. This can be mitigated through raster scanning the ablation beam over the target or moving the substrate relative to the laser focal spot [100] [101].

Plume dynamics for PLD have been investigated using both experimental and theoretical models to predict and evaluated [102]. Using techniques such as ICCD photography, mass spectrometry and emission spectroscopy [103]. Theoretical models have been built upon Monte Carlo simulations, shock layer models and fluid dynamic models [104]. However, there is still work to be done with respect to pulse-plume interaction and the effect of incident angle on plume shape and direction.

2.7.2 Angled ablation for machining

The majority of research into ablation rate and the application of laser ablation for machining has been concerned with normally incident radiation. However, there is a small body of research that covers the introduction of a change of incident angle for laser ablation machining [105][106][107].

Initial models for angular ablation rates assumed that the ablation rate for a given wavelength and temporal pulse profile for ablation carried out a given fluence at normal can be transposed as a function of incident angle. The initial model is given in equation (2-36) where R is the ablation depth per pulse, F is fluence and θ is angle of incidence and R_θ is the angle dependent reflectivity of the surface for the given material. When θ is zero $R(F, 0) = f(F)$ which is the typical ablation depth per pulse for the material when carried out at a normal incidence [108].

$$R(F, \theta) = f\left(F \cos \theta \left(\frac{1 - R_\theta}{1 - R_0}\right)\right), \text{ with } R \rightarrow f(F \cos \theta) \text{ as } R_\theta \rightarrow 0 \quad (2-36)$$

This has been used to explain the geometrical effects of changing the angle of incidence such as the variation in side-wall angle with changes in fluence and illumination. The simplicity of the model assumption that the ablation process is

photothermal which is compatible with the nanosecond pulse regime appears to be reasonable. However, to believe that the fluence at the focal spot is the only factor which contributes to variation in ablation characteristics is potentially insufficient. Optical penetration depth, as previously identified in section 2.5.2, is a key material property affecting ablation. This property varies with a change in incident angle and therefore can be an important contributor to variation in ablation when compared to thermal penetration depth. This may well explain the significant variance observed when comparing experimental results to the predictions to this model.

A secondary model has been proposed to introduce the effect of light absorption into the material using the Beer-Lambert law. This model uses the relation that ablation only occurs when fluence at the focal spot is greater than the threshold fluence, F_T , of the material. For this model the normal incidence ablation curve is defined as:

$$f = \alpha^{-1} \ln\left(\frac{F}{F_T}\right) \quad (2-37)$$

In equation (2-38) θ' is used to denote the propagation of the refracted light inside the material. This model proposes that the ablation depth along the direction of light propagation is constant with respect to a correction in fluence due to reflection and refraction. The model gives the ablation depth normal to the surface and not the direction of propagation.

$$R(F, \theta) \approx \cos \theta' f \left(F \frac{(1 - R_\theta) \cos \theta}{(1 - R_\theta) \cos \theta'} \right), \text{ with } R \rightarrow f(F \cos \theta) \text{ as } R_\theta \rightarrow 0 \quad (2-38)$$

Investigation into the accuracy of these models has been performed through experiments comparing ablation depth, angle of incidence and fluence. These experiments tested two materials, polycarbonate and SU8 photoresist, at two different wavelengths, 193 nm and 248 nm, using nanosecond pulses. A chuck arrangement was used to change the angle of incidence as shown in Figure 2-30 to ensure that laser focus was maintained on the top surface of the substrate.

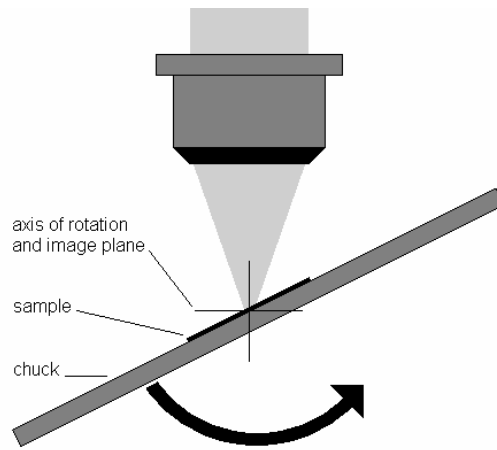


Figure 2-30 Experimental set-up used for investigating angular dependence of ablation rate [108]

Figure 2-31 shows the results of the trials performed above. The author concludes that the ability of each model to make an accurate prediction is dependent on the regime applied. The second model provides more accurate results when applied to the highest fluence levels except at high angles of incidence. Whereas the first model predicts more accurately at the lowest fluence levels. The author provides no explanation or speculation for this disagreement.

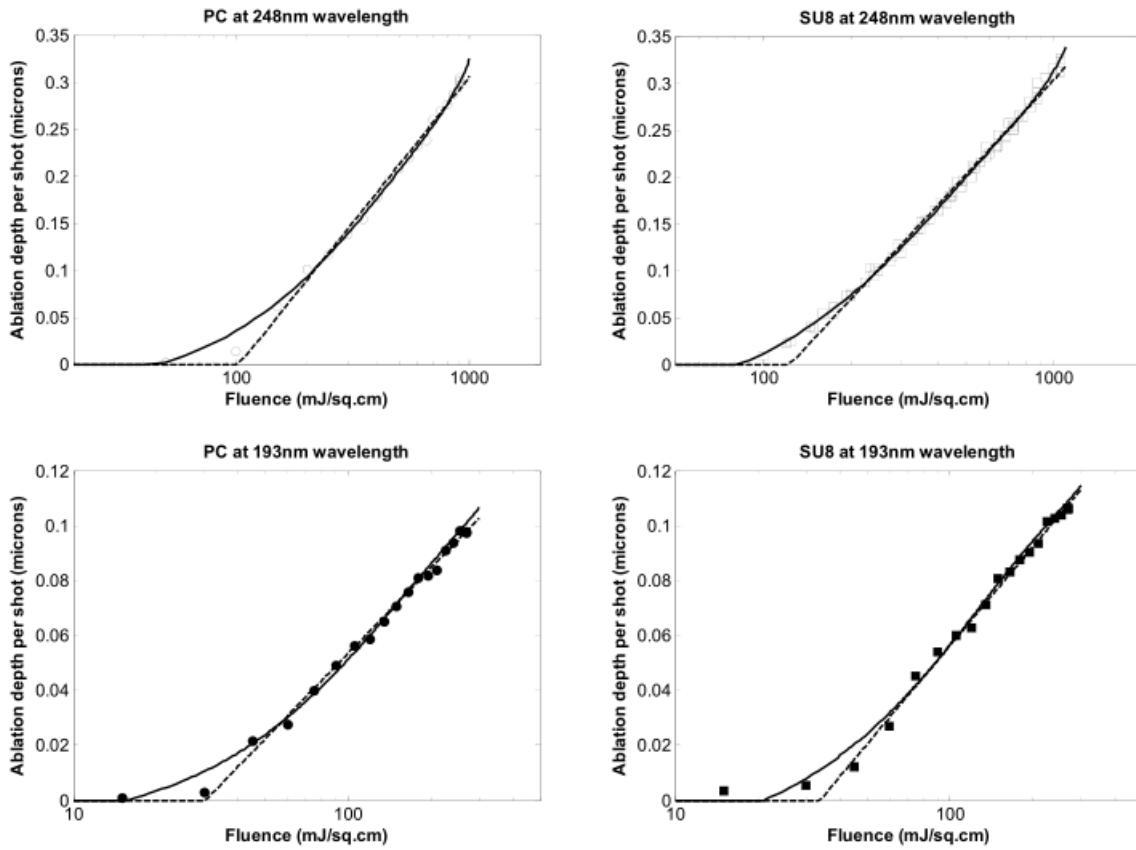


Figure 2-31 Normally incident ablation curve measurements for PC and SU8 at 248nm and 193 nm wavelengths. Solid lines are cubic regression fit [108]

A further advancement of the model suggest that plume absorption of the laser pulse can contribute to the changes in ablation depth at oblique angles. From this a mass absorption coefficient for both the solid polymer, μ , and the plume, μ_p is introduced. The mass absorption coefficient is dependent on the absorption coefficient, α , and density, ρ and these are linked by the following equation. The variable x is defined in Figure 2-32.

$$\text{Solid Polymer} - \mu = \frac{\alpha}{\rho} \quad \text{Plume} - \mu_p(x) = \frac{\alpha_p(x)}{\rho_p(x)} \quad (2-39)$$

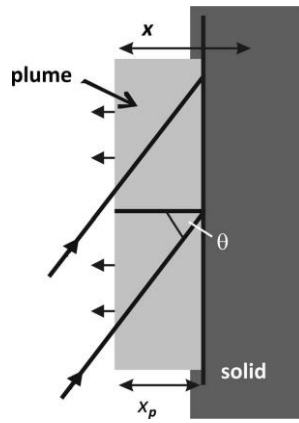


Figure 2-32 Geometry of oblique irradiation [109]

The improved model for ablation depth at oblique angles takes the form shown below [109]:

$$x_d = \frac{\mu \cos \theta}{\mu_p \alpha_0} \ln \left[1 + \frac{\mu_p (1 - R_\theta) F}{\mu (1 - R_0) F_{T0}} - \frac{\mu_p \alpha_0}{\mu \alpha_\theta \cos \theta} \right] \quad (2-40)$$

Table 2-7 Definitions of symbols used in section 2.7.2

Symbol	Definition
x_d	Ablation Depth
F	Focal Spot Fluence
F_{T0}	Ablation Threshold Fluence at Normal ($\theta = 0$)
θ	Incident Angle
μ	Solid Mass Absorption Coefficient
μ_p	Plume Mass Absorption Coefficient
ρ	Solid Density
ρ_p	Plume Density
α	Solid Absorption Coefficient
α_p	Plume Absorption Coefficient
R_0	Reflection Coefficient at Normal
R_θ	Reflection Coefficient at Incident Angle

This model demonstrates a notable improvement over previous models when compared to experimental data as shown in Figure 2-33.

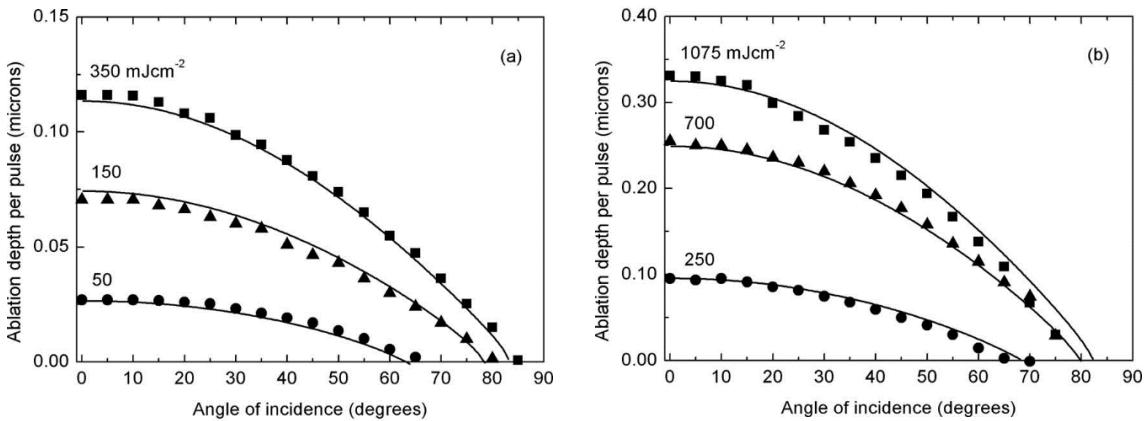


Figure 2-33 Ablation depth per pulse versus angle of incidence.

Left: Polycarbonate at 193 nm and fluences of 50, 150, and 350 mJ cm⁻².

Right: SU8 at 248 nm and fluences of 250, 700, and 1075 mJ cm⁻². [109]

Despite the model taking a singular value for the plume mass absorption coefficient independent of the position of the plume, the model provides a high level of confidence for the prediction of ablation depth. Two other simplifications are the discounting of any refractive effects caused by the plume or an increase in the energy deposition zone due to thermal diffusion within the pulse.

2.8 Laser Plume Imaging Techniques

Laser plume imaging techniques are vital to the understanding of laser-matter interactions. Although the mechanisms involved can be explained by the equations identified above, the range and complexity of the interaction observation of the event make it necessary to fully understand laser-matter interaction.

The wide availability of digital capture methods has allowed for high resolution digital imaging at high frame rates with instantaneous delivery of results, enabling researchers to gain insights into laser-matter interactions. These have made it possible to explain the phenomena occurring in pulsed laser ablation of matter such as the kinetics, composition and dynamics of shockwaves, plumes and plasmas.

Laser ablation processes have been investigated using different techniques which include; spectroscopy, shadowgraphs, schlieren and interferograms.

2.8.1 Spectroscopic Techniques

Spectroscopy techniques allow accurate temporal interrogation of plasmas however they are limited in the spatial domain [110]. The emission spectra of the laser-induced plasma can be observed over the duration of the event. From this the peak emission intensity can be used to record the electron density and plasma temperature at different times [54].

By using an external light source this technique can be used to identify the different species present within the plasma by inspecting the absorption spectra. By tuning the external light source wavelength this can be matched to a specific atomic or molecular absorption line [111].

2.8.2 Shadowgraph and Related Techniques

Shadowgraphs, schlieren, and interferograms give the ability to identify the relative difference in density within the field of view which can be applied to laser-generated plasmas [112][113]. A light source such as a laser can be passed through the plume to provide a source of illumination so that a CCD sensor can be used to detect the different regions of refractive disturbance.

Shadowgraphs can be used for particle ejection as these are opaque hence blocking light to the CCD. However, it is not possible to determine absolute particle position and

sizing due to attenuation effects and diffraction rings caused by the particle [114]. These issues can be solved using interferometric methods.

A key use of shadowgraphs is shockwave detection, and this has been widely applied to high power ablation [115][116]. Unfortunately, when applied to low power ablation the relative change in refractive index is smaller and therefore harder to detect. Sub-nanosecond temporal resolutions can be achieved through the use of short pulse laser sources and active shutter cameras.

2.8.3 High speed imaging

High speed imaging uses the emission from the laser-matter interaction as the light source. This can be used to determine the source of emission within the event from which the temperature of regions can be calculated [117]. The temporal resolution of this method is limited by the exposure time of the camera, if the event is shorter than this the image may not be captured.

2.8.4 Digital holographic interferometry

Digital holographic interferometry (DHI) has been shown to be one of the most useful techniques for the investigation of high power laser-matter interactions [118]. DHI observes the interference fringes created by a diffracted wave field. From the interference pattern the phase and amplitude of the wave field can be extracted [119].

The basic optical arrangement for DHI is shown in Figure 2-34. A coherent beam is split into a reference arm and an object arm and then recombined to form an interference pattern. The interference pattern can be recorded using photographic film or a CCD [120].

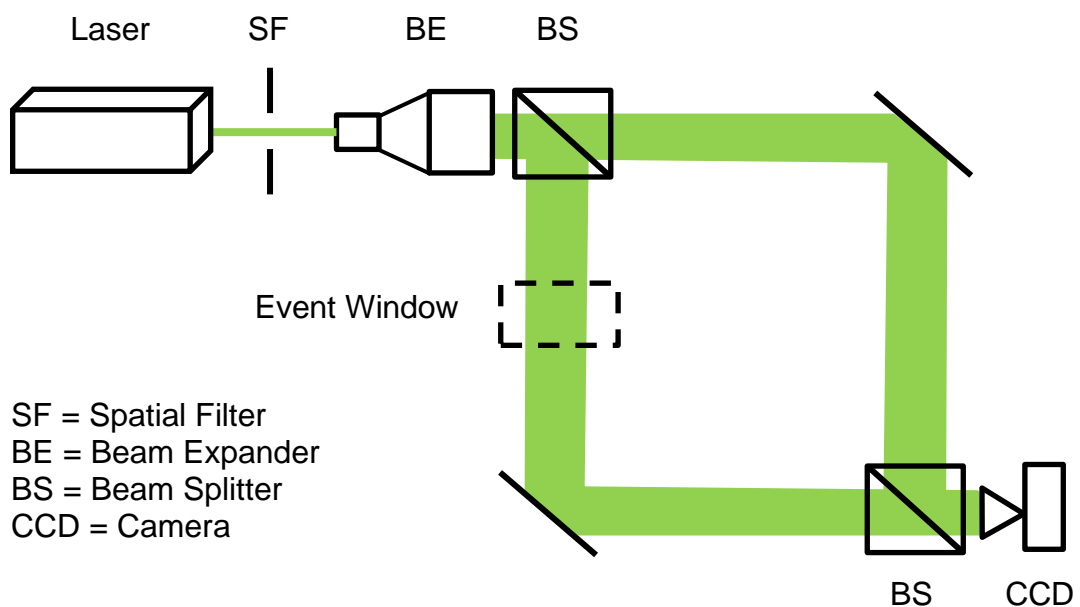


Figure 2-34 An example of an experimental setup for digital holographic interferometry

Two optical arrangements of DHI can be performed which are in-line and off-axis. The off-axis arrangement provides a number of advantages over in-line arrangement which is the spatial separation of the direct current noise term. This allows for an improved identification of the side order terms which include the information for the object under examination.

As this body of research is interested in the application of DHI to laser-matter interactions the details regarding holographic reconstruction, phase reconstruction, and phase unwrapping will not be discussed within this work.

2.8.4.1 Determining Plasma Properties from DHI

DHI can be used to determine the absorption regions and the mechanisms of absorption involved during ablation. This method uses the relationship between variations in the refractive index and free electron density [113].

$$(n - 1) = -\frac{e_0^2}{8\pi^2 \varepsilon_0 m_e c^2} \lambda^2 N_e + \sum_i \left(A_i + \frac{B_i}{\lambda^2} \right) \frac{N_i}{N_A} \quad (2-41)$$

The probe laser wavelength is λ . The electron mass and charge are m_e & e_0 , the dielectric constant is ε_0 , c is the speed of light in a vacuum. and N_A the is Avogadro constant. N_A and N_i are the number densities of the free electrons and of particles of kind i , respectively, and A_i and B_i denote gas-specific constants for these particles.

From inspecting equation (2-41) it is apparent that, if the probing wavelength is sufficiently far away from the absorption lines for the plasma, the summation term can be ignored. Therefore, the electron density can be calculated by equation (2-42) for a refractive index at a single probing wavelength [110][111]:

$$N_e = \frac{8\pi^2 \varepsilon_0 m_e c^2}{e_0^2 \lambda^2} (n(\lambda) - 1) \quad (2-42)$$

This can be approximated as:

$$N_e \approx 10^{21} \lambda^{-2} (1 - n^2) \quad (2-43)$$

The refractive index of the plasma can be related to the plasma frequency by equation (2-44) where ω_{pl} is the frequency of the plasma and ω is the probe frequency:

$$n_0 + \Delta n = \left(1 - \frac{\omega_{pl}^2}{\omega^2} \right)^{1/2} \quad (2-44)$$

2.8.4.2 Calculating Plume Temperature from DHI

From the ideal gas law, the relationship between temperature and volume is well understood.

The relationship between shockwave temperature and shockwave pressure is related by equation (2-45) as discussed in section 2.8.4.1.

$$T_{sh} = \frac{P_{sh}}{R_c \rho_{sh}} \quad (2-45)$$

The Gladstone-Dale formula can be used to calculate the refractive index of a gas for a given density [121].

$$(n - 1) = \rho_n C_{GD} \quad (2-46)$$

Where n is the refractive index, ρ_n is the local density and C_{GD} is the Gladstone-Dale constant. The change in pressure can be calculated using [122]:

$$\frac{P}{P_0} = \left(1 + \frac{n - n_{air}}{n - 1}\right) \quad (2-47)$$

For this body of work the following values will be used:

Table 2-8 Values used for holographic calculations.

Constant	Value
Probe Wavelength - λ	532 nm
Refractive index of air - n_{air}	1.000277
Gladstone-Dale constant - C_{GD}	$0.227 \times 10^{-3} \text{m}^3 \text{kg}^{-1}$
Ambient Pressure - P_0	101.3 kPa

2.8.5 Review of Laser-Matter Interaction Diagnostics

It has been shown that there are several different methods that have been used to observe the different properties of laser-matter interactions. The uses of each method have been summarised in Table 2-9.

Table 2-9 Summary of laser-matter interaction diagnostics

Technique	Observable Property			
	Plume Velocity	Plume Temperature	Electron Density	Particle Field
Absorption spectroscopy	X	X	X	
Emission Spectroscopy	X	X	X	
High Speed Photography	X	X	X	
Shadowgraph	X			X
DHI	X	X	X	X

Whilst the other techniques have shown that they are useful for observing laser-matter interactions, it is apparent that DHI is best suited as it is capable of capturing all the necessary properties in a single exposure. By using a stop motion method, multiple exposures can be collected to form a time-lapse of the laser-matter interaction.

2.9 Summary

This chapter gives an overview of the targets, tools and theory for ultra-precise laser manufacturing. A number of key applications have been identified to which ultrafast ultra-precision laser manufacturing could be applied and compared to the current competing technologies.

The fundamentals of laser optics and parameters are covered and how these can be measured and controlled to increase the precision of ultrafast laser processing. Suitable techniques have been identified along with the types of equipment required to collect beam data.

A review was completed of laser-matter interaction and the optical properties of materials. This demonstrates that laser ablation is a complex process and one that cannot be fully explained by widely applied models such as the two-temperature model. One factor to consider is the change in optical characteristics of materials with respect to temperature and how this can affect the processing of materials.

Metrology methods were identified which could be used in-process or off-line to measure the features machined by the ultrafast laser. In-process metrology will not be performed within this body of work but knowledge of the technologies available is required for the development of the platform. The off-line techniques which include, optical microscopy, SEM and WLI are commonplace in ultra-precision manufacture and will be used to evaluate experimental results.

It has been found that there has been little investigation into the application of non-normal to surface laser machining. Laser ablation at an angle is commonly used for pulsed laser deposition. It is of interest to see whether changing the machining strategy could lead to improved performance. One assessment that could be used is imaging of the plume at varying angles and observing its evolution.

An assessment of different plume imaging techniques has been performed and it has been determined that digital holographic interferometry (DHI) provides the most flexible solution which gives significant detail of the plume. The use of DHI allows a comparison to theoretical models and can be used to form informed judgements on the ablation occurring. DHI gives the ability to build detail of the plume with a timescale and see how it evolves.

3 Experimental System and Measurement Tools

To develop a laser-based manufacturing technique capable of competing with current ultra-precision technologies such as photolithography, a laser platform needed to be designed from the ground up. This required the design of a platform that would be thermally stable and unaffected by external vibrations and movements. Sourcing components which allow for accurate and repeatable stage movements along with fine laser control was required. Finally, integration of in-process and post-process inspection methods for sample verification was required.

3.1 Ultra-Precision Laser Platform

3.1.1 Overview

A key design element of the platform is the implementation of active feedback control and automatic recording of data to allow long-term stability and quality assurance for manufacturing.

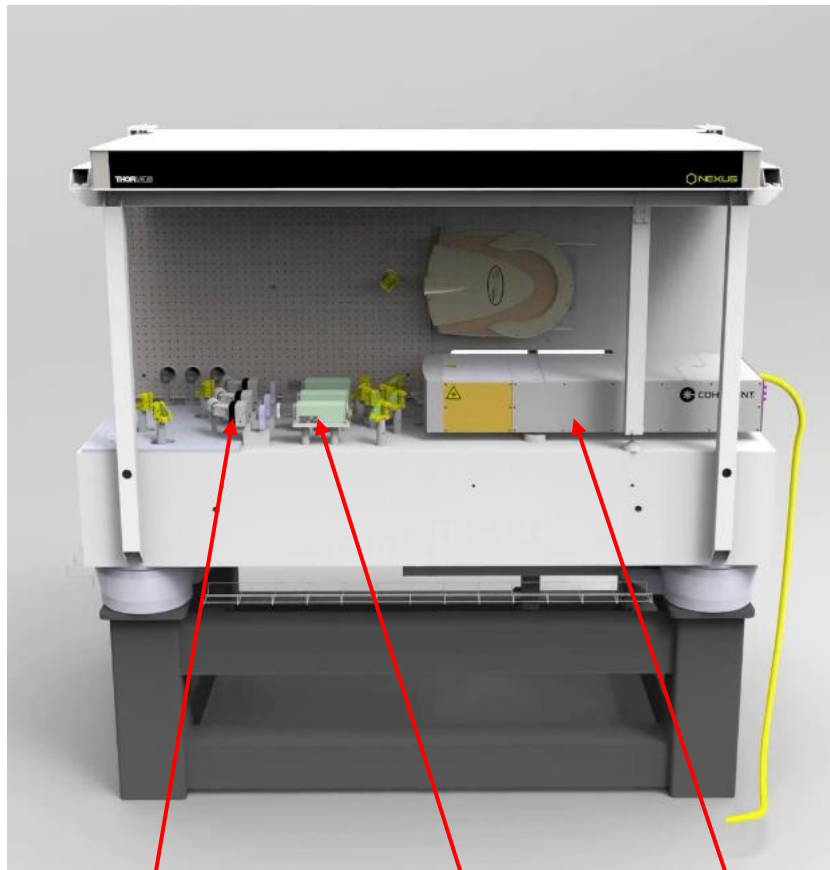
In order to implement this within the design the platform is built on a granite table with a granite bridge which divides the two sides of the platform. The table sits on a steel frame with dampers with air isolators. The isolators function to self level the table and reduce the transfer of any local vibrations to the platform. The low thermal conductivity of granite, at 1.73-3.98 W/(mK) combined with the large mass of the granite table and the attached steel frame all aid in making the platform thermally stable by producing a significantly long 'thermal soak' time.

A consideration throughout the design of the platform is the selection of material with a similar coefficient of thermal expansion for critical mechanical mounts. Therefore all permanently installed equipment is mounted directly to the granite table on stainless steel fixtures using threaded inserts. This includes beam expanders, attenuators, laser sources and the majority of the mirrors. Granite and stainless steel have a similar coefficient of thermal expansion, $7.9 - 8.4 \times 10^{-6} \text{m}/(\text{mK})$ for granite and $9.9 \times 10^{-6} \text{m}/(\text{mK})$ for ferritic stainless steel. This reduces the effect of changes in ambient temperature on beam and stage position.

To allow flexibility in possible setups and optical arrangements on the platform suitable surfaces are covered by aluminium breadboards mounted on floating holes suitable for thermal expansion. The breadboards have a square grid of M6 holes spaced at 25mm.

To ensure safe use of the platform a light tight enclosure is placed around the platform fitted with safety interlocks for the lasers to protect against accidental exposure.

The processing side has access to the processing optics, 5-axis stage and beam diagnostic devices. The laser source side houses the lasers, beam expanders and attenuators as shown in Figure 3-1 and Figure 3-2.



Motorized Attenuators

Beam Expanders

Talisker Laser

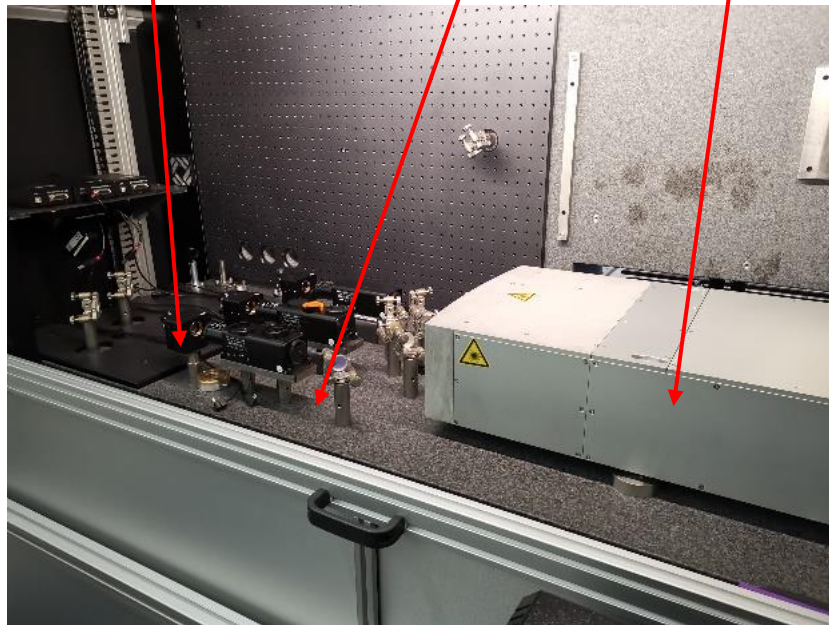


**Figure 3-1 Top: 3D model of source side of platform.
Bottom: Source side of platform with equipment installed.**

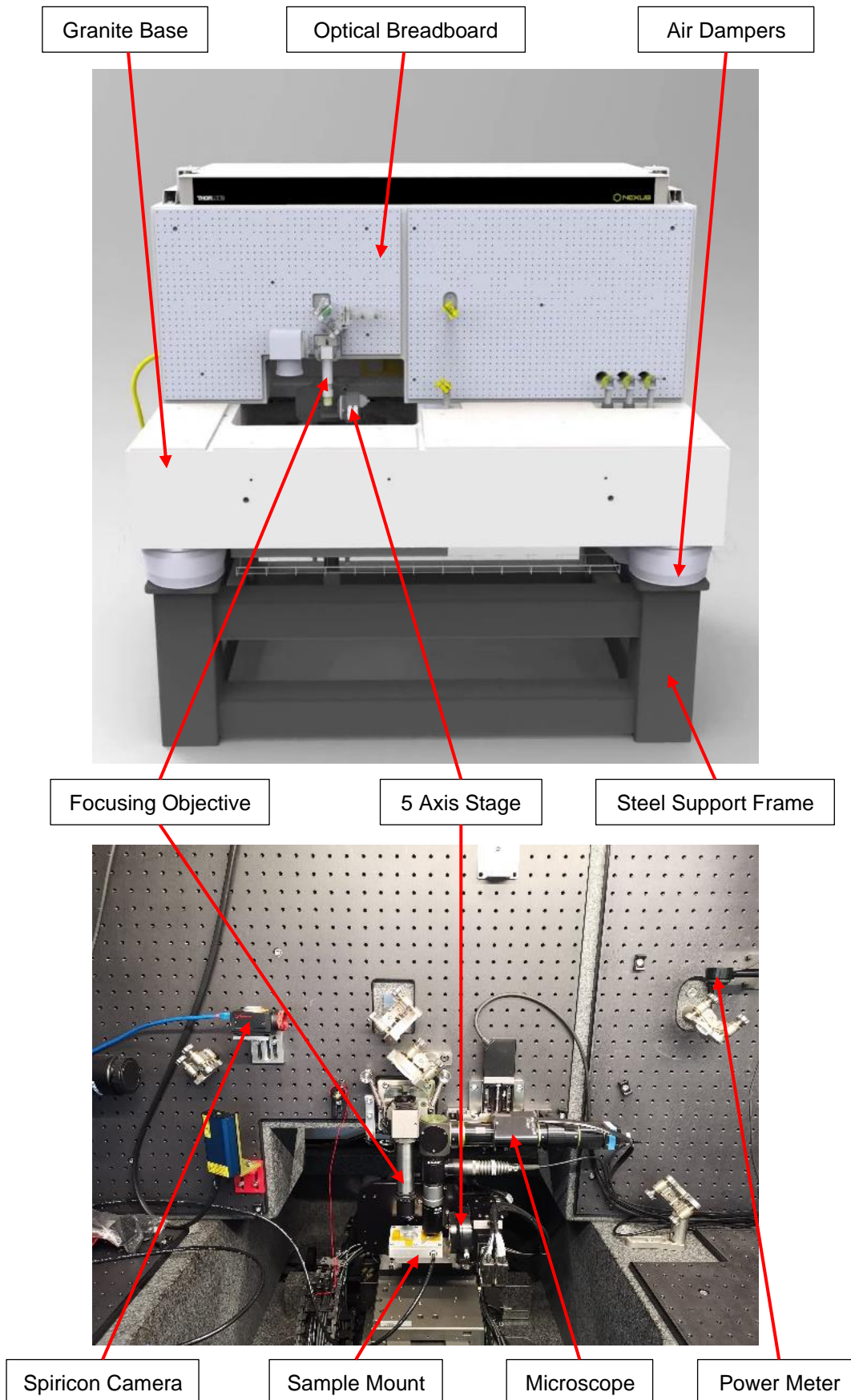


**Figure 3-2 Top: 3D model of processing side of platform.
Bottom: Processing side of platform with equipment installed.**

3.1.2 Ultrafast stage performance

Aerotech, the manufacturer of the 5 axis stage, have provided the 'Acceptance Test Procedure' for the ultrafast platform stage, which provided the methodology and equipment used for testing the stage. A key detail is that the stage was tested and calibrated with a sample holder mass of 0.5 kg which may mean performance will change depending on the sample holder installed. The following tables give the key information for the stage:

Single Axis Accuracy

Axis Name	Test Interval	Verification Interval	Specification	Test Result	Pass/Fail
Z	2 mm	5 mm	2.0 μm	1.080 μm	Pass
A	10 degree	10 degree	6 arc sec	3.1 arc sec	Pass
B	10 degree	10 degree	6 arc sec	4.8 arc sec	Pass

Calibrated 2D Accuracy

Axes	Test Interval	Verify Interval	Spec	Test Result	Pass/ Fail
X/XX	10 mm	10 mm	1 μm	0.28 μm	Pass
Y	5 mm	10 mm	1 μm	0.36 μm	Pass

The 2D accuracy appears to be the greatest performance limiter of this platform.

Axis Repeatability:

Axis Name	Test Interval	Specification	Test Result	Pass/Fail
X/XX	15 mm	200 nm Bi-directional	133 nm	Pass
Y	5 mm	100 nm Bi-directional	74 nm	Pass
Z	5 mm	200 nm Bi-directional	158 nm	Pass
A	10 degree	3 arc sec Bi-directional	0.9 arc sec	Pass
B	10 degree	3 arc sec Bi-directional	0.8 arc sec	Pass

System Repeatability:

(3 different locations with compound movements)

Axis Name	Test Position	Specification	Test Result	Pass/Fail
X/XX	#1	300 nm Uni-directional	9 nm	Pass
Y	#1	300 nm Uni-directional	23 nm	Pass
Z	#1	300 nm Uni-directional	69 nm	Pass
X/XX	#2	300 nm Uni-directional	78 nm	Pass
Y	#2	300 nm Uni-directional	12 nm	Pass
Z	#2	300 nm Uni-directional	27 nm	Pass
X/XX	#3	300 nm Uni-directional	10 nm	Pass
Y	#3	300 nm Uni-directional	2 nm	Pass
Z	#3	300 nm Uni-directional	140 nm	Pass

3.1.3 Optical Layout

As part of the commissioning of the stage of the platform a new optical train needed to be designed. There were several requirements to bring the optical layout in line with targets of the platform. The optical train had to be compatible with the following systems:

Table 3-1 Devices with corresponding wavelengths

Device	Wavelength /nm
Processing laser	1064
OCT system	1250-1350
Raman System	638-1000
Inline Optical Microscope	400-700
Spiricon Camera	1064
Quadrant sensors	1064

Below is the finalised optical train design for the platform along with the profiles of the dichroic mirrors which are used as band-pass and notch filters and had to be custom made for the platform. Further optical arrangements were designed for the systems to be compatible with 355 & 532 nm processing wavelengths.

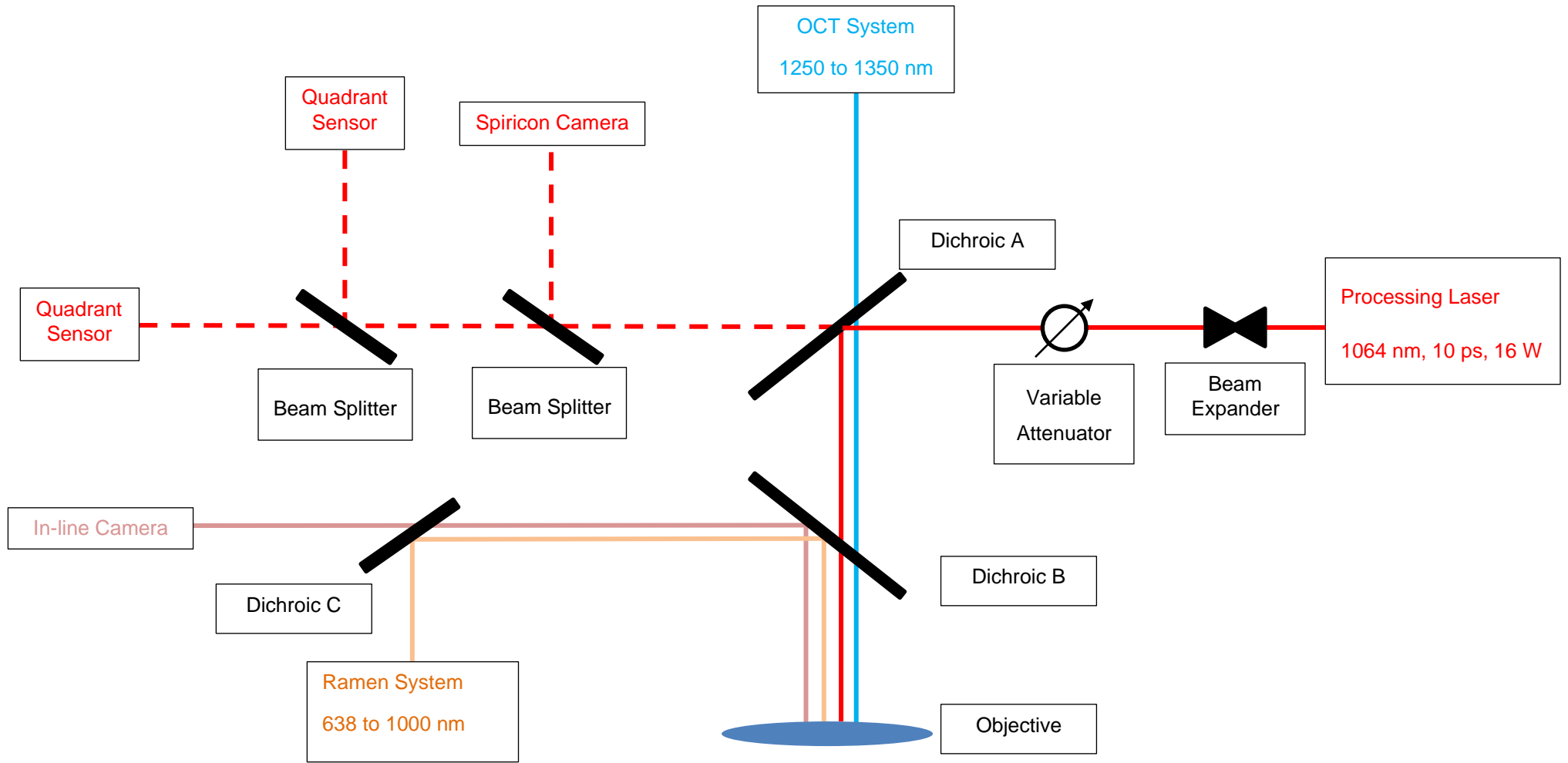


Figure 3-3 Optical train design for ultra-precision platform

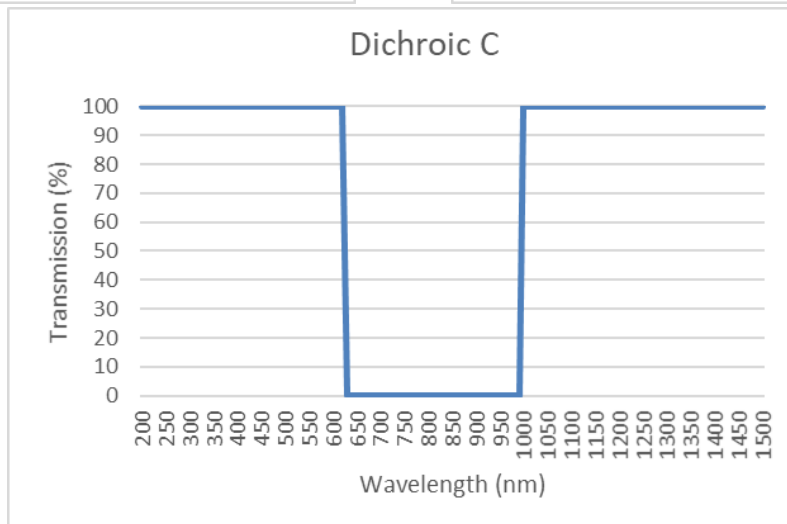
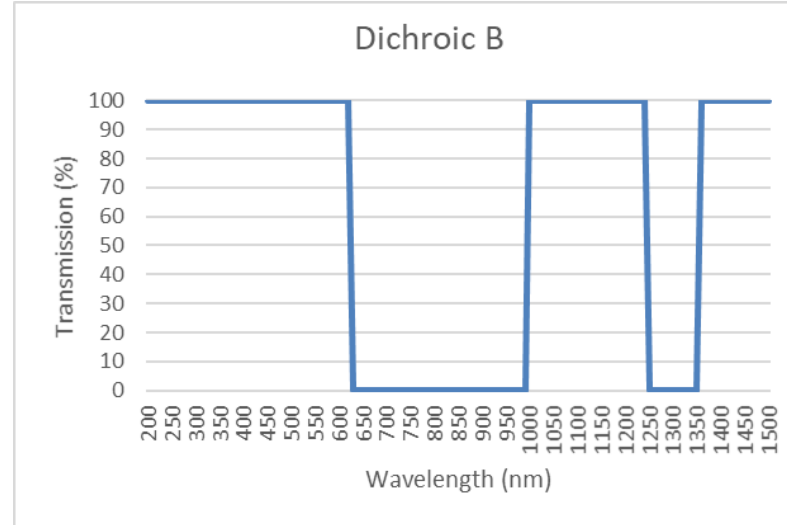
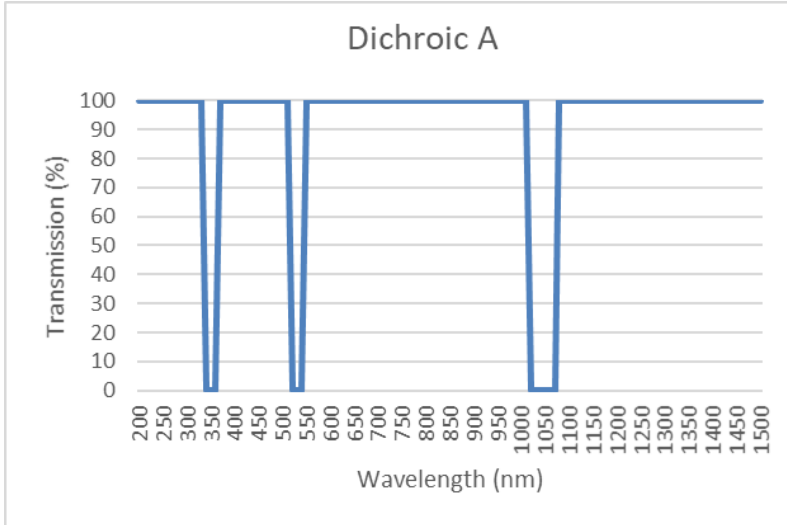


Figure 3-4 Graphs showing desired transmission characteristics for each dichroic mirror

3.1.4 Laser source, Control, and Diagnostic Equipment

The primary laser source for the Ultra Precision platform is a three-wavelength Talisker Ultra laser system. This is a picosecond, diode-pumped solid state (DPSS) laser with first and second order frequency doubling to achieve shorter wavelengths from the same source. The laser uses an Acoustic Optic Modulator (AOM) which is used for repetition rate and single pulse picking control. The laser has a built-in optical attenuator which uses a polariser arrangement. For safety there is a shutter within the optical cavity which has been wired into the enclosure interlocks to stop any uncontrolled exposure.

Table 3-2 Specifications of Talisker Ultra laser system.

Property	Value		
Output Wavelength (nm)	1064	532	355
Average power output (W)	>16	>8	>4
Repetition Rate Range (kHz)	Single pulse to 200		
Pulse width (ps)	<15		
Pulse to Pulse Stability (%)	<2	<2	<5
Average Power Stability (%)	<2		
1/e ² Beam Diameter (mm)	2.0±0.5	1.4±0.3	1.3±0.3
Beam Circularity (%)	>85		

3.1.4.1 Beam Expander – QIOPTIQ Linos Beam Expander

A motorised beam expander with a Galilean arrangement was selected. This model has a sufficiently high laser induced damage threshold so that over the lifetime of the platform the optics don't degrade over time. The fixed-body motorised beam expander requires no further physical interaction after alignment, thereby avoiding the risk of causing misalignment of the entire optical train.

Table 3-3 Specifications of Qioptiq Linos beam expander.

Property	Value
Compatible Wavelength	1030 to 1080 nm
Magnification	2x to 8x
Material Optics	Fused silica
Entrance Diameter	8 mm
Exit Diameter	31 mm
Laser Induced Damage Threshold	20J/cm ² @ 1064 nm for 12s
% Transmission	97
Pointing Stability	<0.5 mrad

An alignment process was developed to ensure coaxial alignment of the processing beam and the beam expander optics. The process uses two mirrors near to the entrance aperture to steer the beam with a front and rear iris mounted on the beam expander. The beam is imaged using the Spiricon beam profiler, using an iterative method of reducing the iris apertures and then adjusting the mirror positions and viewing the profile on the Spiricon. When the beam is aligned correctly the profile should remain centred on the camera independent of magnification or iris position.

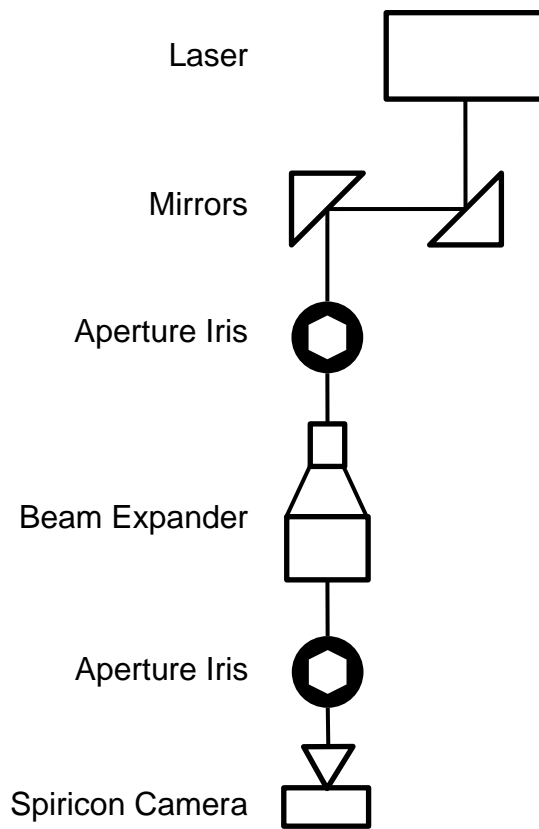


Figure 3-5 Optical arrangement for beam control

3.1.4.2 Variable Attenuator – Watt Pilot

The Watt Pilot attenuator is a polarisation-based attenuator. This attenuator uses a half waveplate to change the throughput of the P and S polarisations of the laser. The polariser transmits the P-polarisation and reflects the S-polarisation into a beam dump. A small DC motor is used to rotate the half waveplate. The maximum and minimum output laser power is limited by the initial polarisation ratio of the beam.

Table 3-4 Specifications of Watt Pilot variable attenuator.

Property	Value
Clear Aperture	18 mm
Maximum Input Beam Diameter	12 mm
Attenuation Range	Up to 0.3-99%
Step Increments	3900
Resolution	<42 arcsec/step

3.1.4.3 Focusing Objective

Several focusing objectives were tested however, due to a concern in the early development of the platform that collisions between the stage and objective might occur. A relatively long focal length lens was chosen with the view that shorter focal length lenses could be used in the future. The lens used was a Thorlabs LMH-5X-1064.

Table 3-5 Specifications of LMH-5X-1064 focusing objective.

Property	Value
Magnification	5X
Working Distance	35 mm
Effective Focal Length	40 mm
Numerical Aperture	0.13
Minimum Spot Size	7.8 μm

3.1.4.4 Beam diagnostic equipment

Four different beam diagnostic devices were employed: a high and low power meters, pulse energy meter and beam profiling camera. Below are all the specifications for this equipment.

Table 3-6 High Power Meter - Specifications of Ophir 30A-BB-18

Property	Value
Aperture (mm)	Φ 17.5
Power Range	20mW – 30W
Power Noise Level	1mW
Power Accuracy $\pm\%$	3
Linearity with Power $\pm\%$	1

Table 3-7 Low Power Meter - Specifications of Ophir PD300R-3W

Property	Value		
Aperture (mm)	Φ 10		
Power Range	5 nW – 3 W (Changes with filter)		
Resolution (nW)	0.1		
Power Noise Level (pW)	200		
Power Accuracy ±% vs wavelength	Filter out	Filter in	
	10	NA	360-400 nm
	3	5	400–950 nm
	5	7	950-1100 nm

Table 3-8 Energy Sensor - Specifications of Ophir PD10-pJ-C

Property	Value
Aperture (mm)	Φ 10
Energy Scale	200nJ – 200pJ
Resolution (nJ)	0.1 at 900 nm
Energy Noise Level (nJ)	0.0001
Calibration Accuracy ±%	5

Table 3-9 Beam Profiler - Specifications of Ophir SP300

Property	Value
Active Area	7.1mm x 5.3mm
Pixel Spacing	3.69μm x 3.69μm
Number of Effective Pixels	1928 x 1448
Frame Rate	26 FPS at full resolution

3.1.4.5 Platform Analysis Tools

3.1.4.5.1 Microscope – Qioptiq Motorised Zoom Microscope

The microscope is from Qioptic and is part of a modular ecosystem. The microscope installed on the platform has interchangeable focus objectives, motorised zoom and software-controlled illumination. This solution was selected for the possibility to automate capture processes and for integration with the platform. A 20x fixed objective has been installed to provide an adequate resolution and field of view.

Table 3-10 Specifications of Qioptiq Motorised Zoom Microscope

Property	Value
Resolution	560 nm to 1.9 μ m
Magnification	20X to 100X
Sensor Resolution	2592x1944 pixels

3.2 System Development

To achieve accurate laser machining on an angled surface. Several systems need to communicate and work together cohesively to form an automated repeatable and adaptive manufacturing route.

This section outlines and details the methodologies required, how they are implemented on the platform and whether they meet the desired function.

3.2.1 System Interfaces

The table below outlines the components used in development of the platform, the function and the different methods of communication which are supported.

Table 3-11 Breakdown of components, functions and interfaces for ultra-precision platform

Component	Function	Interface
Aerotech 5-axis Stage	Stage Movement	Aerobasic Software TCP/IP API (using DLL)
Talisker Ultra	Laser Source Power Control Repetition Rate Shutter AOM control	Talisker Control RS232 (serial) Pulse Picking using 5-volt input
Beam Expander	Beam Diameter	Linos Software RS232 (serial)
Watt Pilot	Power Control	Watt Pilot Software RS232 (serial)
Spiricon SP300	Record Beam Profile	Beamgauge Software API (using DLL)
Ophir Power Meters	Record measured beam power	Starlab Software API (using DLL)
Microscope	Capture Images Illumination Control Zoom Control	For Camera - ICMeasure, API (using DLL) For Zoom lens – RS232 (serial) For Illumination – RS232 (serial)

From reviewing the above table, it is apparent that each device can be controlled by third party software. Consequently, bespoke software will be developed in C# which will centralise all control of the platform and be used to record all relevant data during processing and post-processing.

3.2.2 Control of laser parameters

All of the key laser parameters identified in section 2.3.3.

Table 3-12 Breakdown of devices which affect laser parameters.

Parameter	Device
Power	Talisker Attenuator Watt Pilot Attenuator Diffractive Attenuator
Repetition Rate	Talisker Pulse Picker
Beam Diameter	Motorised Beam Expanders
Triggering	Shutter Talisker Acoustic Optical Modulator

3.2.3 In-process power logging

The traditional method for laser machining trials is to setup the equipment, turn on the laser, measure the laser power, turn off the laser then turn the laser back on to perform the trial. A significant flaw in this method is the assumption that the laser power has remain invariant in this process. To achieve ultra-precision manufacturing a source of variance such as this must necessarily to be removed.

A solution to this problem was the integration of a power meter into the machining platform and routine to allow for real-time logging of the power of the laser for each test as shown in Figure 3-6. The power meter was aligned to measure the transmitted beam by means of a dichroic mirror. The power to the focusing objective could then be determined by placing another power meter in the post dichroic mirror path and correlating the reflected laser power with the to the transmitted laser power.

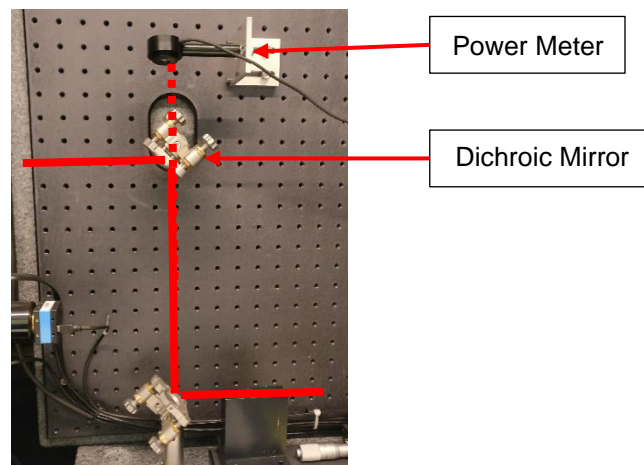


Figure 3-6 Power meter placement

This presented a couple of challenges the greatest of which is the development of the software, given an initial unfamiliarity with the C# programming language. The second arose from a ramping of the power meter reading which may cause an issue if the laser is only on for a short period of time such that the sensor was unable to settle on a value.

A future development would be an automated procedure where a power level would be requested, and the attenuators would be set automatically to achieve this.

3.2.4 Autofocus for microscope

To automate the ability to capture images using the microscope installed on the system, it is necessary to create a method that captures the images in focus failing which the images would be of no use. An auto focus method is necessary due to the high level of precision required and the short working distance of the microscope focal objective.

There are many different ways of the level of focus of an image. A selection of the most common methods is outlined below:

- Standard deviation of neighbouring pixels
 - Generally, images that are in focus have a greater difference in neighbouring pixel values and therefore, the larger the standard deviation of the neighbouring pixels, the more in focus the image.
- Canny edge detection
 - Canny edge detection is used widely in machine vision applications and is regarded as one of the most reliable methods for edge detection. Canny edge detection is performed by the 5 following steps:
 1. Apply Gaussian filter to smooth image and remove noise.
 2. Find intensity gradients of image.
 3. Apply non-maximum suppression to get rid of spurious response to edge detection
 4. Apply double threshold to determine potential edges
 5. Track edge by hysteresis: Finalize the detection of edges by suppressing all the other edges that are weak and not connected to strong edges.
- Frequency domain analysis
 - Images that are out of focus have low frequency signals whereas images that are in focus have high frequencies due to the increased sharpness of edges. By taking the Laplacian of the image further derivatives can be calculated to determine the relative focus of the image.
- JPEG file size
 - When developing an autofocus algorithm for the Curiosity Mars rover it was found that the focus of the image correlated with the file size of the JPEG image. The closer to focus the image the larger the file size.

The following method was chosen to determine focus for the samples measured on the platform. The method must meet a few criteria which are: repeatability, time, memory/computational overhead and programming simplicity.

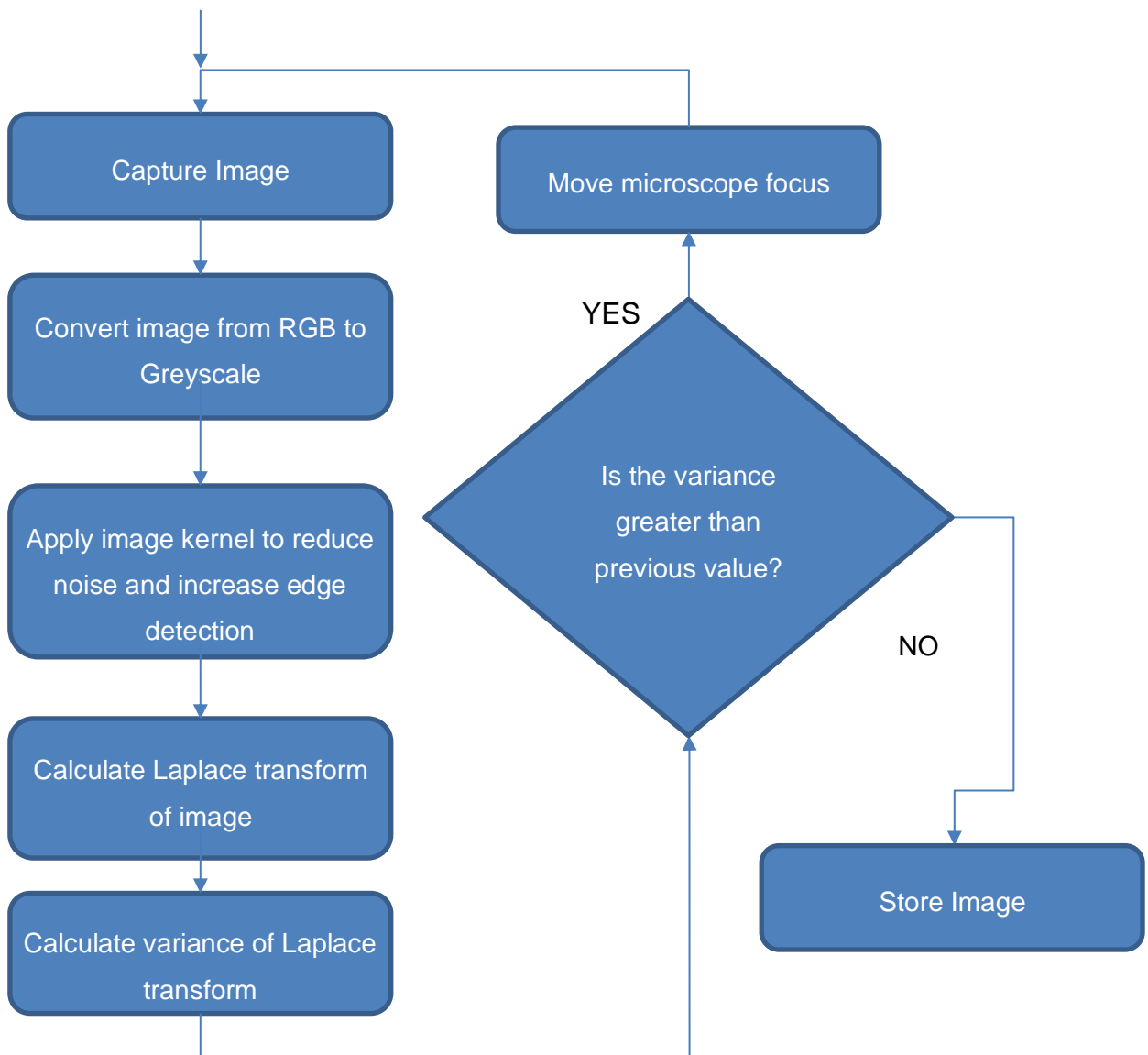


Figure 3-7 Sequence for finding image focus using the Laplace transform

A test set of images was produced to test the autofocus methodology. Figure 3-8 is a sample of the sequence of images used to test and develop an autofocus algorithm.

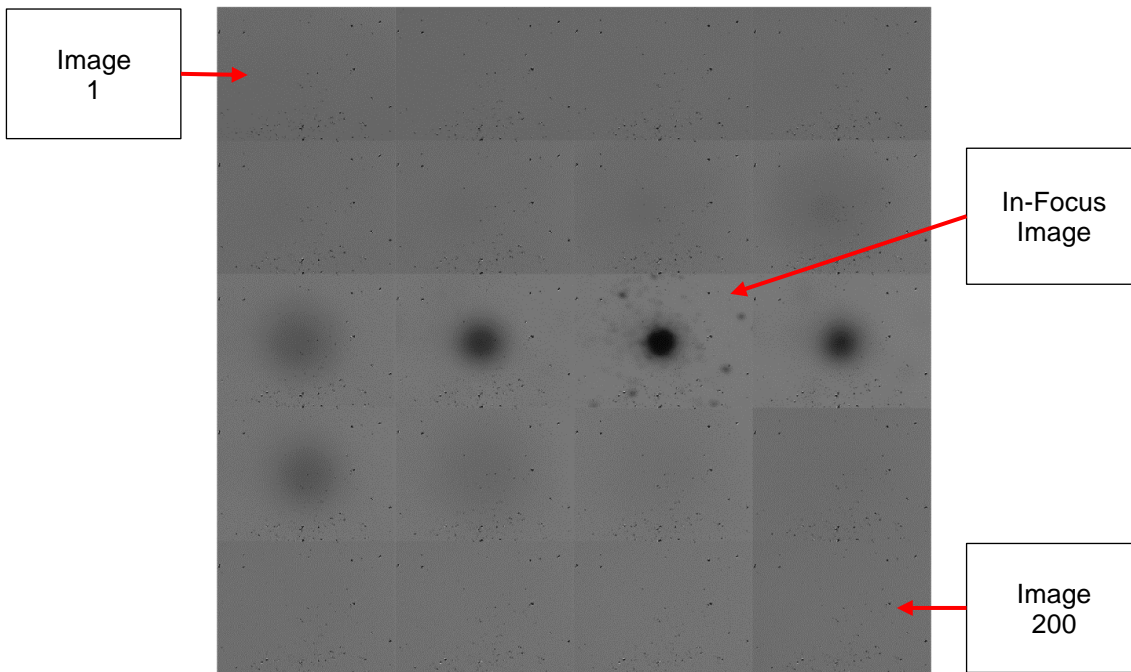


Figure 3-8 Test sequence of images used to develop autofocus method. These are tiled in order from top left to bottom right.

In this test sequence 200 images were captured over a range of 0.4 mm at increments of 2 μm . This was designed to ensure that the feature would move through and focus sufficiently as well as verifying whether dust on the lens or the substrate would cause issues for the algorithm.

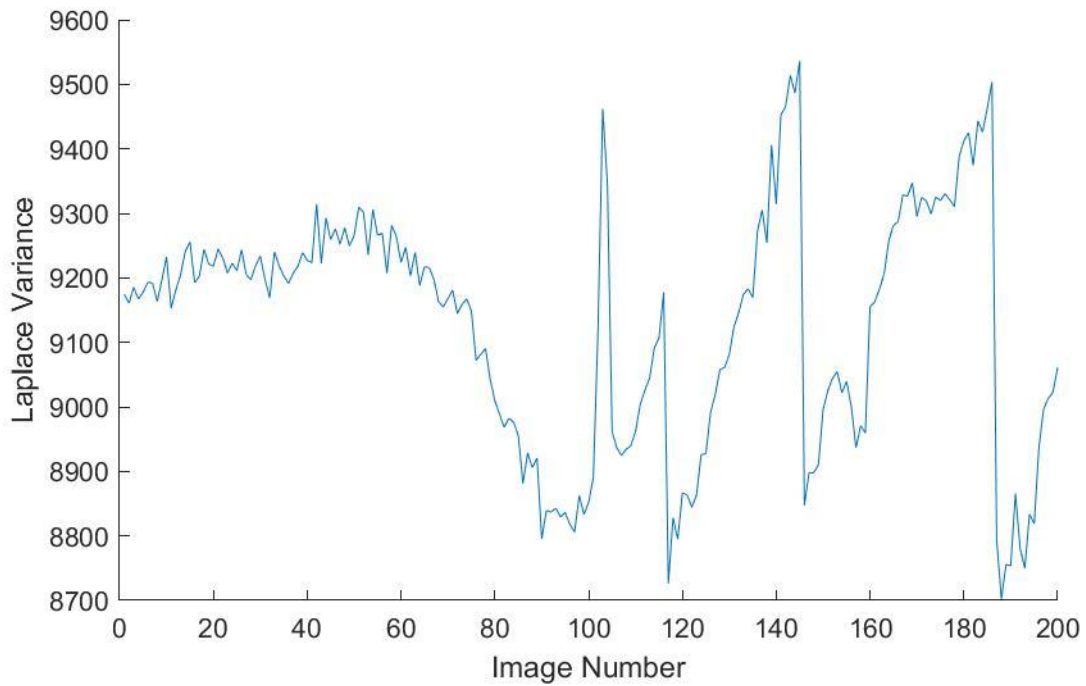
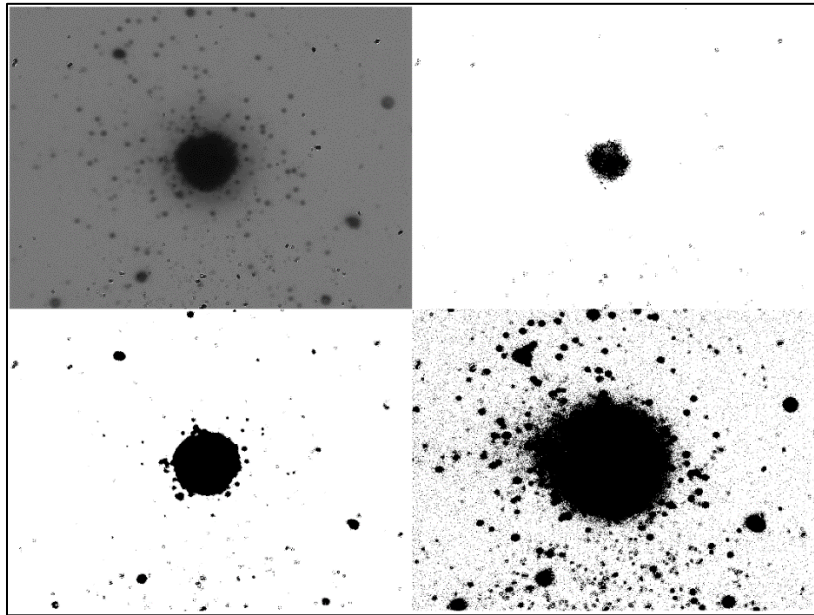


Figure 3-9 Plot of Laplace variance for image scan sequence

Figure 3-9 is a plot of the Laplace transform variance for the test images. The in-focus image is at image 102 out of the data set of 199. It is apparent that the algorithm is not robust for general usage due to the significant number of localised peaks which can provide false positives. This is notable within the region of images 120-146. These false positive results can be generated from dust on the lens, dark pixels on the sensor etc. Therefore, further development was required to discriminate between real and spurious effects. Secondly, this method is only effective if the feature is in the centre of the field of view, so active feature finding would be advantageous.

Fortunately, due to the limited application of this algorithm, we can implement a priori knowledge to improve the accuracy of the process. 'a priori' knowledge refers to information about the image which is gathered from other sources than the image itself. In this case we know that we are looking to identify simple geometry such as, rectangle, circle and cross on a silicon substrate with consistent brightness, exposure and contrast settings within data sets. This allows for two further analysis tools to be implemented. The first is to threshold the greyscale image and then implement a connected pixels analysis. From viewing the raw images, we can determine that the machined areas are darker than the unprocessed substrate. A binary threshold can be applied on the image where the level can be determined experimentally to determine the closest match to the machined area. The threshold limit is defined by a percentage

relative to the intensity of each individual pixel. The individual intensity of the pixel determines whether it is recorded as 1 or 0. The effect of different threshold levels is shown in Figure 3-10.



**Figure 3-10 a) raw image b) Threshold level = 0.06
c) Threshold level = 0.27 d) Theshold level = 0.45**

The threshold limit is fixed at the same value across data sets to allow for direct comparison. This method works by taking advantage of the fact that, as the image comes into focus, the contrast between the feature and the substrate increases. The size of the threshold area is measured using the connected pixel algorithm. For images that are in focus the connected pixel area is greater and therefore indicates the correct position to achieve focus. Below is a plot of the connected pixel area for the sample data set used.

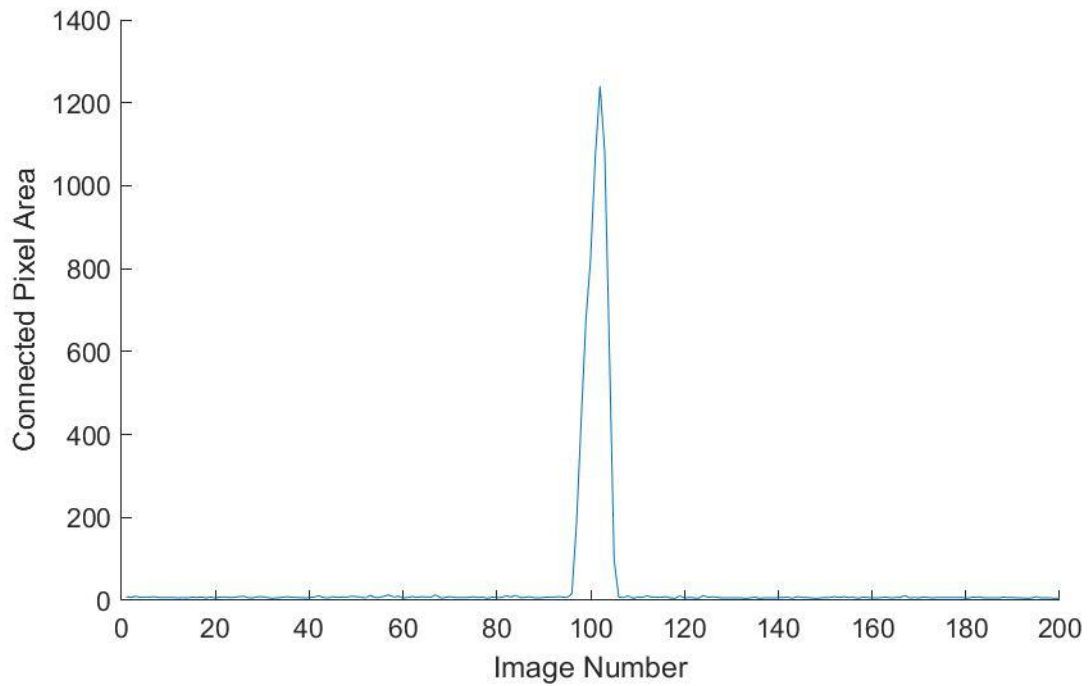


Figure 3-11 Connected pixel area for image scan sequence

A property of the connected pixel algorithm is a calculation of the centre of mass of the connected. This can be used to determine whether the mass is at the centre of the field of view of the camera. By determining the effective pixel widths through calibration of the camera sensor using a traceable reference, the geometric difference of the centre of mass of the connected pixels and the centre of the sensor can be calculated, following which a movement of the stage can be applied to bring the feature into alignment. This can be done per frame in real time.

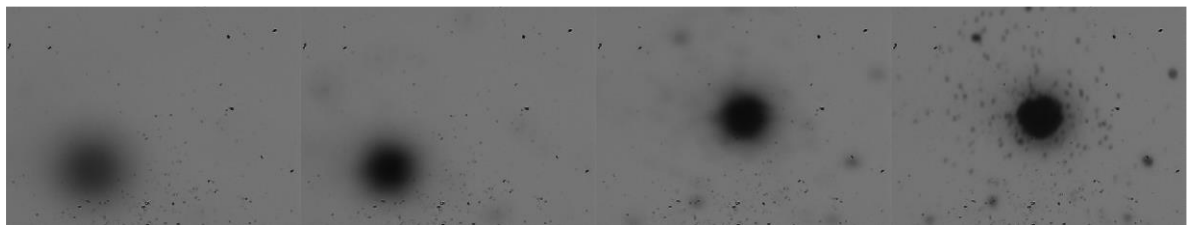


Figure 3-12 Demonstration of image focusing algorithm centring feature and achieving focus.

Using the connected pixel area methodology and Laplace transform algorithm, the limitation of achieving a high accuracy and repeatable auto-focus process is limited by the repeatability of the 5-axis stage as stated in section 3.1.2.

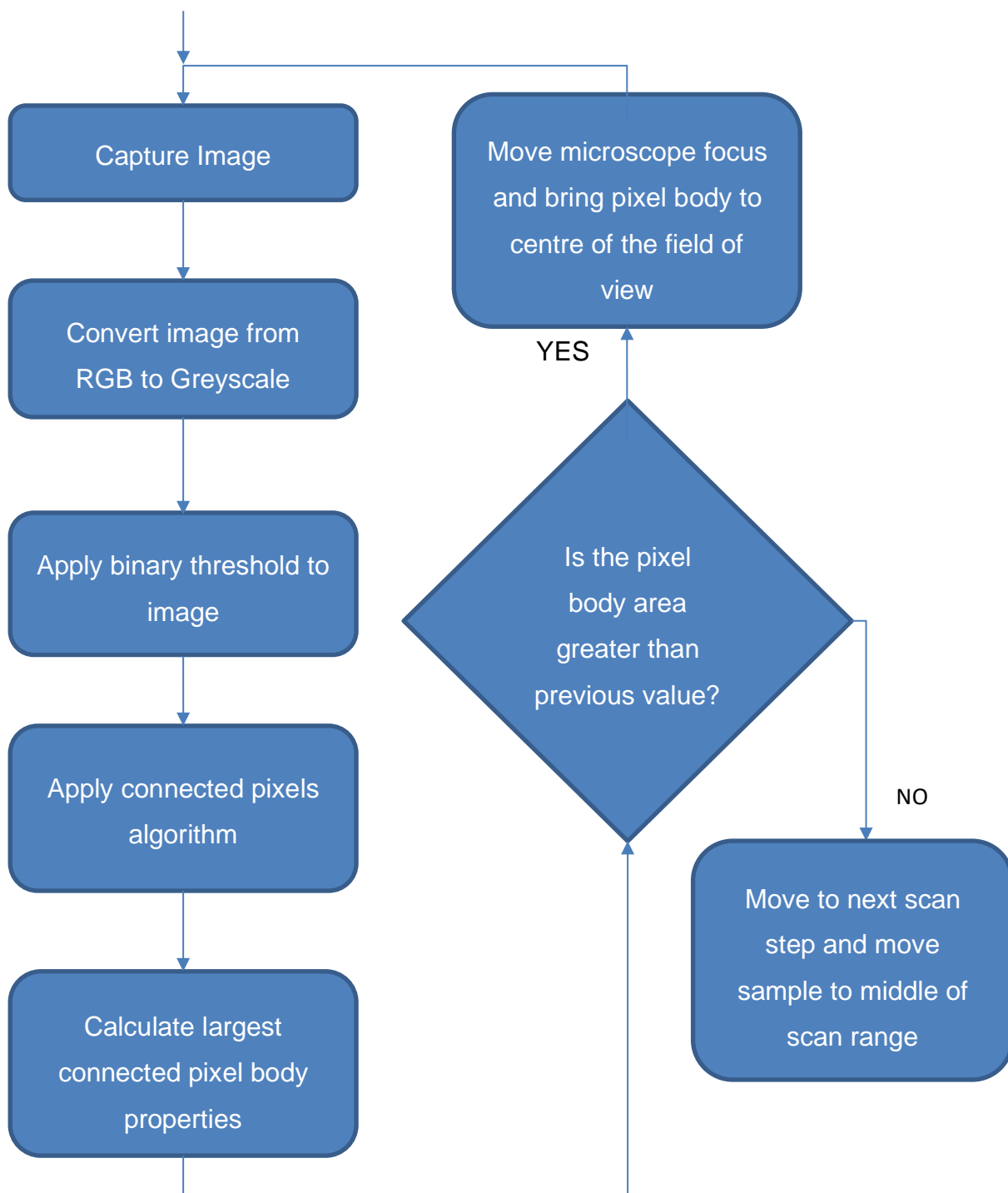


Figure 3-13 Methodology for connected pixel algorithm

The final method is the incorporation of the Laplace method initially identified and the connected pixel method. The connected pixel method is applied in two stages with reducing scan lengths and finer sampling increments then the Laplace method is used to capture an in-focus image of the feature. Figure 3-14 illustrates this process:

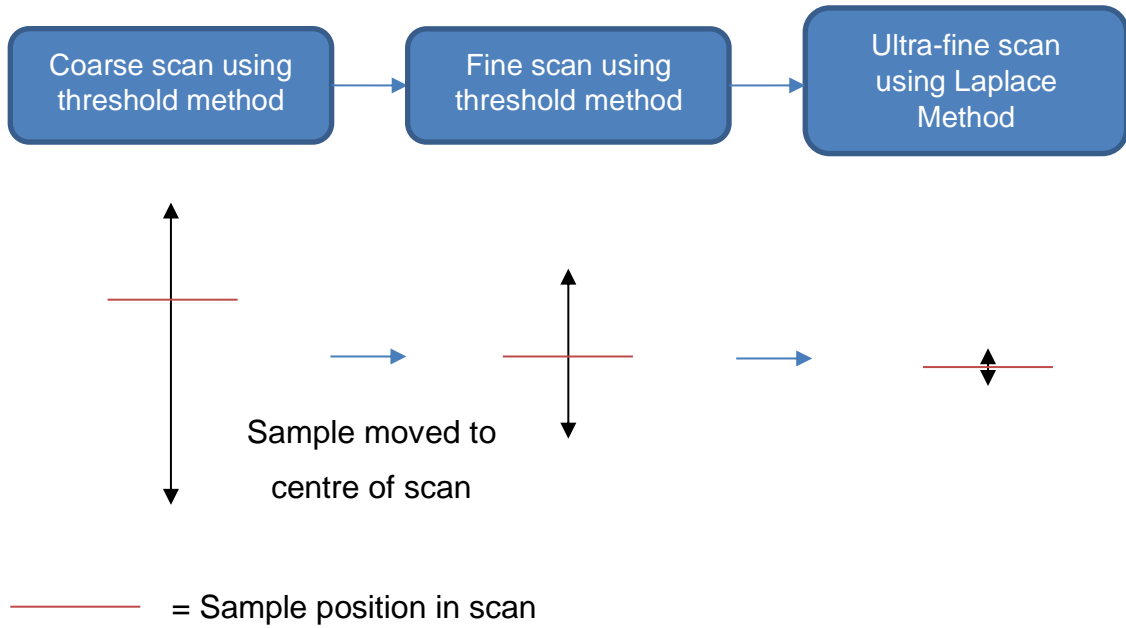


Figure 3-14 Implementation of methods for different scan lengths

The scan ranges are as follows:

Table 3-13 Scan ranges for 20x zoom.

Scan	Range / μm
Coarse	500
Fine	100
Ultra-fine	10

Table 3-14 Scan ranges for 200x zoom

Scan	Range / μm
Coarse	300
Fine	20
Ultra-fine	5

The depth of focus for the objective was used to define the range for the ultra-fine scan. The depth of focus at 20x zoom was <2 μm and the 200x zoom was <0.2 μm. Step increments were made at 0.1 x scan range for the ultra-fine pass.

Basic optimisations have been implemented such as detecting when the image has gone out of focus so that the scan stops and moves to the next scan level.

This method reduces the time taken to find focus of the feature in the field of view from approximately 5 minutes when done manually to less than 30 seconds when automated. A significant advantage of this method is that it can be left to run unattended. Secondly this method achieves the peak level of focus and is not affected by user preference or interpretation. When using the 20x zoom lens the method is accurate to +/- 0.1 μm of peak achievable focus.

Post Processing

To aid in improving the accuracy of the measurement of features in the captured data sets there are two additional sets of images which are recorded to remove artefacts from the image.

- Dark image

This is a singular image that is taken to remove the effect of bad pixels which return a fixed value. This dark field image is subtracted from each captured image to remove this effect. This is taken with zero illumination so that only faulty pixels produce a value, and this allows them to be mapped out.

- Flat Field

Microscope lens are prone to artefacts whether this is dust on the lens or distortions in the optical path. Collection of an array of images which are then averaged to produce a flat field can be applied to the raw image to remove these artefacts.

These two image sources are used to produce the corrected image, C, from the raw image, R, dark field, D, flat field, F, and image average value of (F-D), m, using the following equation:

$$C = \frac{(R - D) \times m}{(F - D)} \quad (3-1)$$

Summary

An automated method has been implemented which allows for auto-focus image capture which can then be used for feature identification in process or data capture for analysis of sample post process. This method uses two algorithms, one based on connected pixels and the other using the variance of the Laplace transform of image.

3.2.5 Laser Alignment

Alignment of the 1064 nm laser to the beam tube was achieved using the following arrangement shown in Figure 3-15.

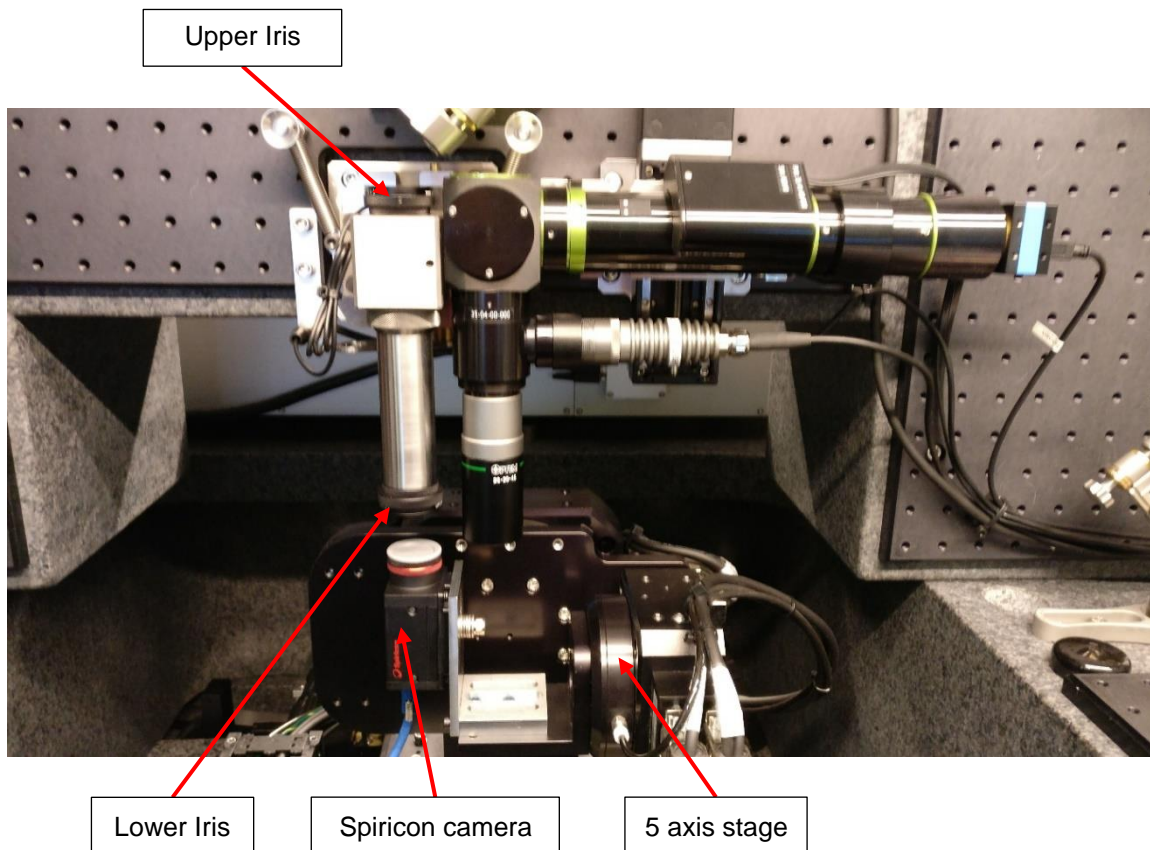


Figure 3-15 Arrangement for precise laser alignment

The Spiricon was mounted on the 5-axis stage using the mount shown. The beam power was attenuated to minimal power levels, <0.5 W, using the Talisker attenuator, motorised attenuators and neutral density filters.

A rough alignment was performed using the indicator card and IR camera to position the beam central to the top iris. The beam tube has a top and bottom iris which can be used to aid in achieving alignment.

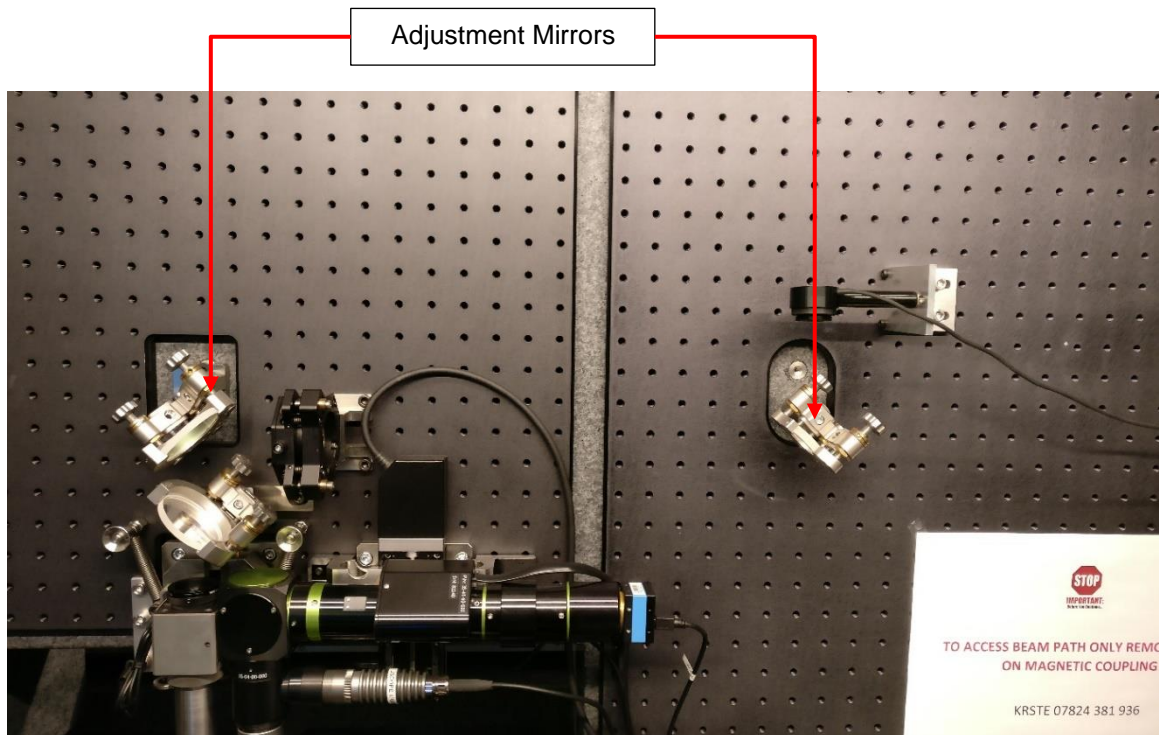


Figure 3-16 Adjustment mirrors for precise laser alignment

The final two mirrors, shown in Figure 3-16, were used to carry out adjustment whilst the other mirrors were locked in position.

With the iris fully open small adjustments were made with the mirrors to get part of the beam to pass through the beam tube. The Spiricon camera was then moved to view the partial beam.

An iterative process was implemented as follows:

- Reduce the diameter of the top iris.
- Looking at the direction of clipping to the beam.
- Adjust using both mirrors.
- Move Spiricon to improve view of beam.
- Reduce the diameter of bottom iris.
- Repeat stages 2-4.
- Repeat stages 1-6.
- Finish when closing either iris clips the beam equally in all directions.

To ensure that the beam is central to the beam tube and coaxial to the Z-axis of the platform measurements of the beam centroid can be taken at different Z heights with the camera.

A sweep over 25 mm recording at 5 mm intervals was performed.

Table 3-15 Measuring variation in centroid of beam over 25mm sweep

Position /mm	Centroid X /μm	Centroid Y /μm
0	3.47E+03	2.59E+03
5	3.49E+03	2.56E+03
10	3.47E+03	2.56E+03
15	3.46E+03	2.55E+03
20	3.44E+03	2.54E+03
25	3.45E+03	2.53E+03

This gives the following angles to the normal:

Table 3-16 Angle of beam over sweep.

Θ_x/deg	Θ_y /deg
0.0378	0.1175

This is towards the limit of the accuracy of this setup as the beam is moving in real time. The use of piezo mirror controllers and quadrant sensors would improve the alignment accuracy.

3.2.6 Autofocus of laser

Ensuring that a sample is at the focus to the machining objective is a necessary condition for precise machining using an ultrafast laser. To achieve precise machining using an ultrafast laser. There are several advantages of being at focus for machining materials, and these include:

- At focus the laser fluence covers the smallest area for that possible objective such that finer features can be machined.
- For Gaussian beams the heat affected zone is reduced
- At focus less energy is required for ablation as this is a function of fluence, which is determined by energy over focal spot area.

Typically, Gaussian optics are used for machining therefore characteristics of the beam from passing through a focusing objective can be used to form a method to focus the laser on the substrate. Figure 3-17 shows how a movement of the substrate through the focusing path of the laser alters the apparent focal spot diameter. The laser is at focus when the focal spot diameter is at a minimum. A secondary consequence of the focal spot diameter increasing a reduction in focal spot fluence for identical beam power.

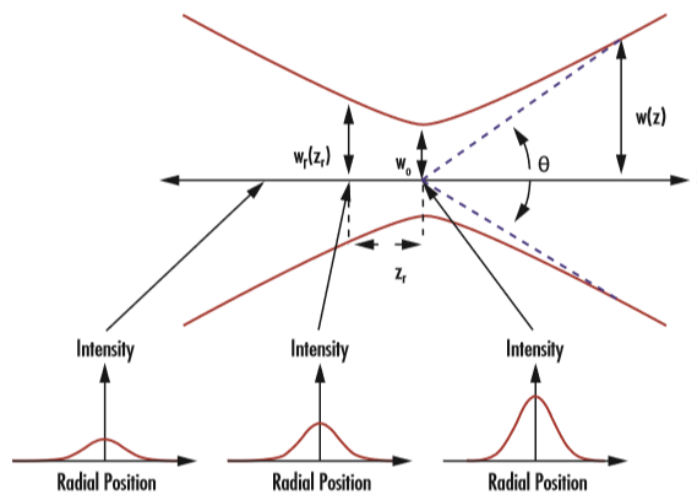


Figure 3-17 Effect of Gaussian optic on beam diameter and intensity [123]

There are different methods for determining whether the laser is at focus on the substrate. Two methods that have been identified are as follows:

- Use of in-line camera

Using the optical arrangement shown in Figure 3-17 a reflection of the focal spot on the substrate can be viewed. When the laser is at focus the focal spot is at a diameter minimum.

- Machining a test grid on the substrate

This is a destructive method in which the substrate is machined at different positions in the focus beam path which determines two factors. Firstly, whether there is presence of a track, assuming the fluence is greater than the ablation fluence for that objective. Secondly, the track width reduces closer to the ablation threshold.

These two methods were used for different setups due to the advantages for different applications. The in-line camera method requires the user to estimate the reflected beam diameter, the test grid method was preferred as measurement is carried out at a higher level of precision. The test-grid method was therefore integrated method was integrated into the automated processes for the Ultra Precision platform.

Test Grid Machining Method

This method was designed to be flexible, accurate and repeatable which are all requirements for an ultra-precision laser-based machine tool. The method needs to be suitable for use with different materials, different focusing objects and even different types of laser.

A test grid which was compatible with these requirements needed to be developed. This necessitated marking tracks in an array at different Z heights in each corner of the sample as shown in Figure 3-18. This grid was chosen for the following reasons:

- Variable range and accuracy through changing Z scan range and marking interval.
- Compact in using a small area of the sample.
- The result allows for averaging and can be used to improve tilt correction on the sample.
- Can be automated using feature recognition methods that have been developed.

- A track shares many of the features used in machining trials.

For this method to be effective two pieces of a priori knowledge are required:

- Estimated focal spot position.
- Estimated ablation threshold for lens when sample is at focus.

The estimated focal spot position can be calculated from comparing the difference in sample thickness between the two samples and using the previous focal spot position.

The ablation threshold estimation should be found from literature and the required fluence for ablation at focus then calculated.

Before finding focus for the laser, a tilt correction is performed using the optical microscope, to bring the sample close to normal of the machining laser.

The ablation method uses the following parameters to define the geometric pattern used to find focus:

- Z scan length
- Number of sampling marks
- Mark length
- Mark spacing
- Refined corner positions

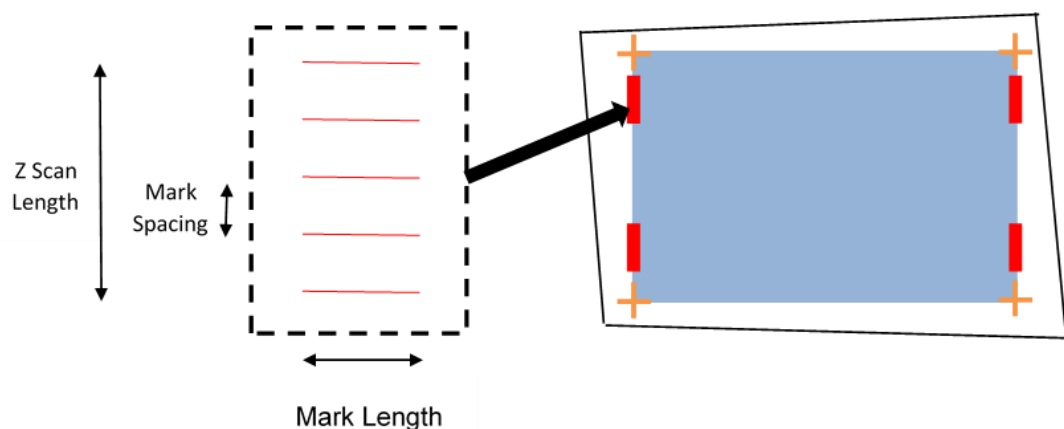


Figure 3-18 Layout of focus grid. Horizontal red lines indicate ablated tracks.

The pattern is repeated at each corner of the sample to determine the focus at each corner. The pattern machines tracks at different Z heights. The aim of the pattern is to have the beam power sufficiently low that as moving through the different Z heights the pattern starts with no ablation, then ablation, then no ablation again.

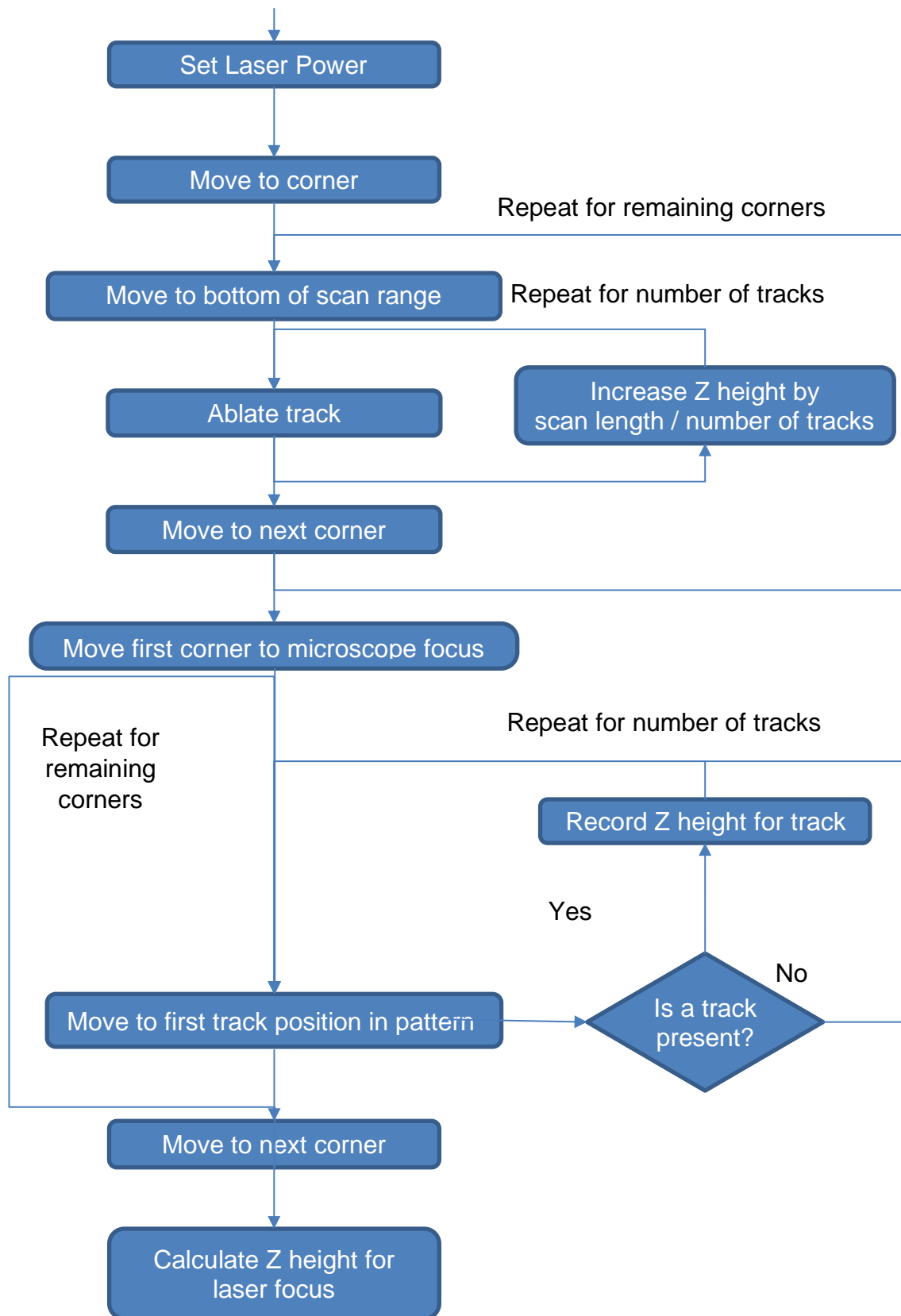


Figure 3-19 Methodology for finding focus of laser on sample

The data is recorded in a table like this, where F is the estimated focal position:

Table 3-17 Visualisation of recording presence of tracks to find focus. Green indicates track present.

Z Height / μm	F - 0.3	F - 0.2	F - 0.1	F	F + 0.1	F + 0.2	F + 0.3
Corner A							
Corner B							
Corner C							
Corner D							

Linear interpolation can be used to find the correct Z height for focus on the substrate. Depending on the variance in the Z height between each corner a further tilt correction can be applied.

The above method has been automated into a turnkey solution and integrated into the main control software for the platform. The software uses the feature detection method outlined in Section 3.2.6 to detect the presence of a machined track and record the coordinates at which the track was machined.

3.2.7 Tilt correction methodology

Ensuring that a sample is kept at the focal spot of the laser is a requirement for repeatable machining. Any variation in the position of the sample in the focal envelope of the laser affects the fluence of the focal spot on the sample, which affects the machining.

Two possible methods are suggested:

- “Seesaw” Method

This is an iterative method which inspects two opposite points. A small correction being applied to the relevant rotary axis to bring the points both into focus without adjusting the Z axis. This is then repeated for the perpendicular axis until the sample can be moved in the X-Y plane without any Z axis correction. After each axis correction the other axis correction must be checked.

- Plane fitting

This method requires at least three points where the sample is at focus and the coordinates of each point recorded in X, Y and Z. A plane can then be fitted to the points and the angular corrections for the rotary axis can be calculated.

The “seesaw” method is simple to implement but can require a large number of iterations and checking to ensure that the applied tilt correction is correct. Mathematically and computationally, the plane fitting method is more involved but it has a number of advantages which are: compatible with three points or more; the exact solution is calculated; and less overall time is required to perform the tilt correction.

3.2.7.1 Implementation of plane fitting tilt correction

This method involves finding more than three regions which are on the same plane on the sample and bringing them to the focus and recording the X, Y and machined Z height of the feature. This produces a point cloud of regions which were in focus. Then a plane can be fitted to the point cloud. The plane can then be used to find the suitable rotations to bring the sample to a plane which is in focus across the sample. The mathematical implementation of the plane fitting method is outlined below.

Plane Fitting Mathematical Implementation

The equation of a plane is defined as:

$$z = a_0 + a_1x + a_2y \quad (3-2)$$

This equation for the given points can be calculated using a method of multiple regression and solving this matrix to find a_0 , a_1 , a_2 .

$$\begin{pmatrix} n & \sum x & \sum y \\ \sum x & \sum x^2 & \sum xy \\ \sum y & \sum xy & \sum y^2 \end{pmatrix} \begin{pmatrix} a_0 \\ a_1 \\ a_2 \end{pmatrix} = \begin{pmatrix} \sum z \\ \sum xz \\ \sum yz \end{pmatrix} \quad (3-3)$$

QR decomposition is used to find these values. The detail of QR decomposition is beyond the scope of this work.

With the equation of the interpolated plane the normal vector of the plane can be found.

$$InterpPlane = \begin{pmatrix} -a_1 \\ a_2 \\ 1 \end{pmatrix} \quad (3-4)$$

This allows for the first angle to be calculated to transform the normal of the plane to (0,0,1):

$$\theta = -1 * \left(\arctan \left(-\frac{a_1}{1} \right) \right) \quad (3-5)$$

The normal vector can be rotated using the rotation around Y matrix:

$$\begin{pmatrix} \cos \theta & 1 & \sin \theta \\ 0 & 1 & 0 \\ -\sin \theta & 0 & \cos \theta \end{pmatrix} \begin{pmatrix} -a_1 \\ a_2 \\ 1 \end{pmatrix} = YR \quad Y \text{ Rotated Vector} \quad (3-6)$$

Using the same trigonometric method, the second angle, φ , can be calculated and the final plane normal vector can be found using the rotation around X matrix:

$$\begin{pmatrix} 1 & 0 & 0 \\ 0 & \cos \varphi & -\sin \varphi \\ 0 & \sin \varphi & \cos \varphi \end{pmatrix} YR = XR \quad X \text{ Rotated Vector} \quad (3-7)$$

This method is demonstrated using 4 points collected using the optical microscope in section 3.2.8. The blue stars are the raw data points, the purple square is the interpolated plane and the green plane is the result of the calculation of the angles and transformations applied to the plane as shown in Figure 3-20.

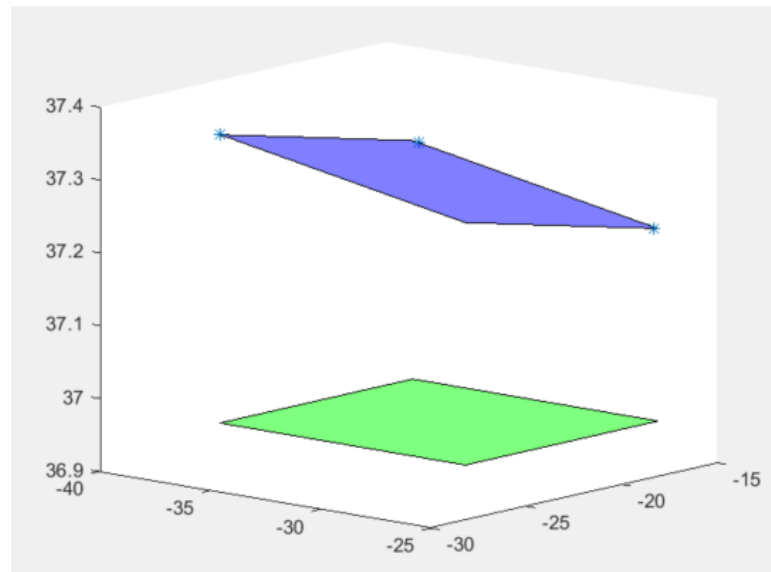


Figure 3-20 Implementation of plane fitting to perform tilt correction.

Blue plane is initial data points. Green plane is after tilt correction transformation.

This method is scalable to as many data points as the user decides to record.

This method has been developed so that multiple iterations of this procedure could be performed for cases where a rough tilt correction could be desirable, followed by a fine correction and then a fine correction carried out using focus find regions. This could be an initial correction carried out using the microscope followed by an application of the laser focus positions.

After this tilt procedure a final laser focus scan would be required due to the rotation of the stages potentially causing a variance in Z for the sample.

3.2.7.2 Testing of tilt correction

An arrangement to test that the dial gauge was coaxial to the Z axis of the stage is shown in Figure 3-21. The stage was jogged at 10 μm intervals which is the resolution of the dial gauge. There was no discernible difference in the requested increment and the reading on the dial gauge.

The stage was moved a span of 10 mm in both X and Y recording the measured value from the dial gauge and output of the Z axis on the Aerotech software.

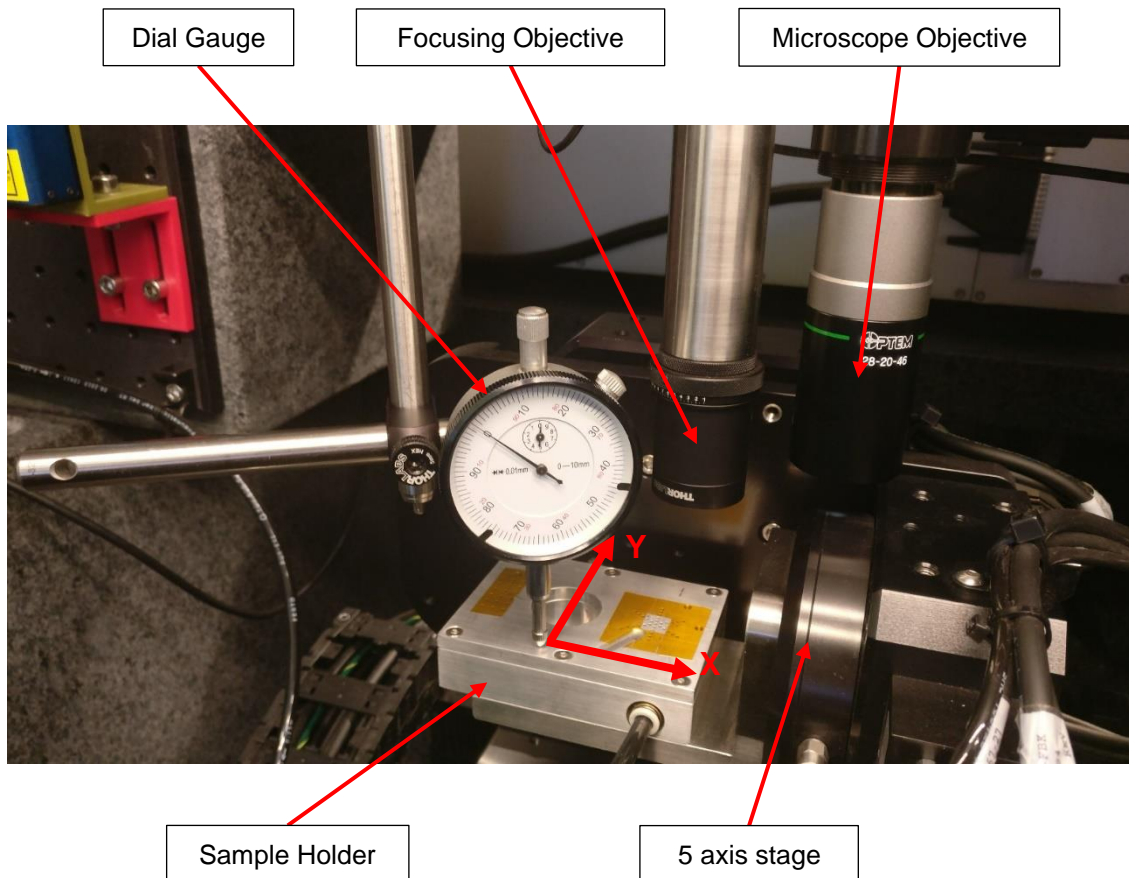


Figure 3-21 Experimental setup to measure tilt correction method

For the X axis the variation in Z over 10mm was $<10 \mu\text{m}$ for both the raw and tilt corrected measurements over the 10 mm travel.

For the Y axis the following result was recorded and shown in Figure 3-22:

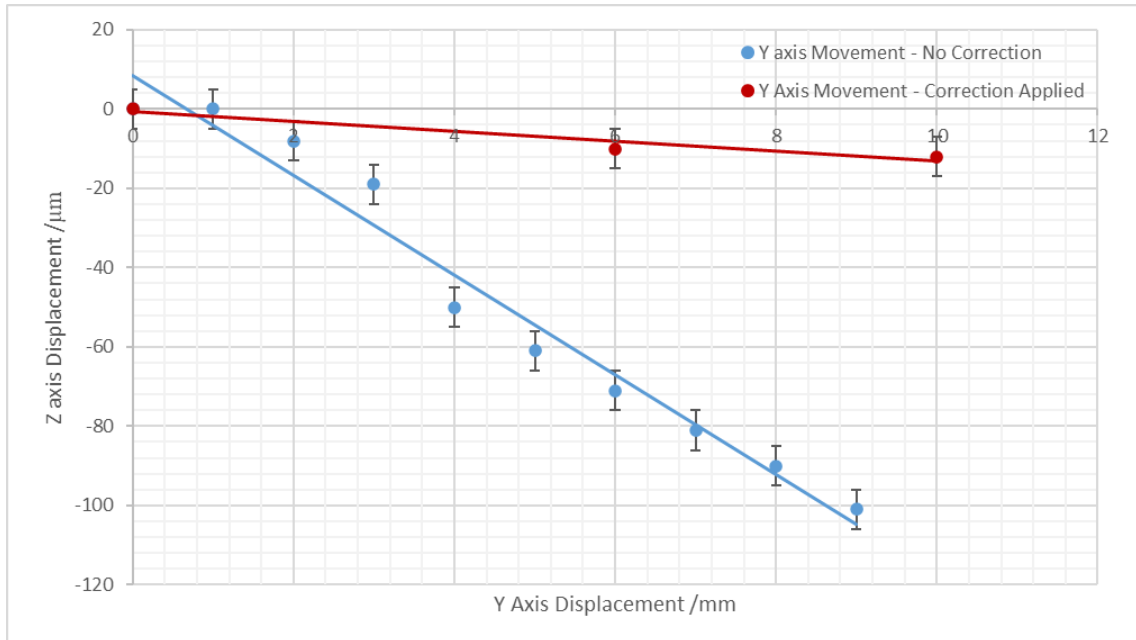


Figure 3-22 Comparison of before and after tilt correction applied

Therefore, within the normal 10 x 10 mm working region of the stage, the maximum compound displacement in Z from movement in the X and Y stages was 12 µm.

The following issues with this result are:

- Insufficient stiffness of the fixturing holding the dial gauge.
- The measured surface is not that of the stage but the sample holder meaning the result is the compound error of the stage but also the sample holder.
- The resolution of the dial gauge is too coarse to provide accurate readings.

Implications to silicon machining

With the beam expander installed the measured raw beam diameter is 4.55 mm. With the 50 mm focal length lens installed the focal spot has a diameter of 14.88 µm and a working distance of 327 µm. Therefore, the process instability previously found appears unlikely to have been caused by the stage moving out of focus when processing.

3.2.8 Microscope-Laser alignment

The ability to precisely machine using any method requires the ability to set datums and how the tooling relates to the datum. For a laser-based approach this requires identifying the site using a microscope, machining a marker followed by measurement of the correct offset between the two focal points.

Due to changing sample sizes, sample positions and thermal effects, it is beneficial to recalibrate the offset for each machining trial rather than relying on a historical value. As with all procedures developed for the platform, the intention is for the process to be automated, compatible with a range of samples and having a high level of accuracy and repeatability.

The most precise method of alignment is a destructive approach where a defined marker is machined and can then be compared to the reference image for the marker.

The following procedure was developed:

- Find position of the four corners of the sample using the optical microscope ensuring that the corners of the sample are in focus, and record the X, Y, Z coordinates.

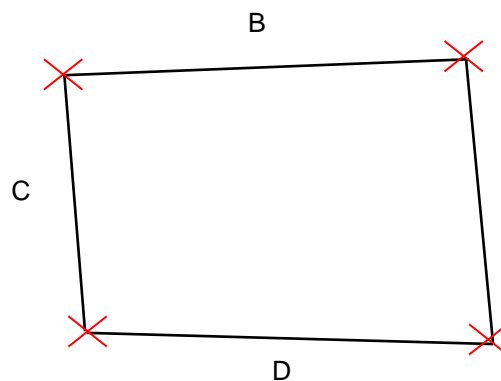


Figure 3-23 Diagram of Silicon Sample. Red crosses indicate raw corner positions. The sample is purposefully drawn not to be square.

- Calculate tilt correction as outlined in Section 3.2.7 and apply correction to A and B axis.
- Check tilt correction and refine sample corner positions.
- The maximum viable working area is then calculated using these refined corner positions and giving a 0.25 mm margin from the perimeter of the sample.

- Using the previous offset values for the relative position of the microscope focus point and laser objective points, four fiducial markers are machined at the corners of the working area.

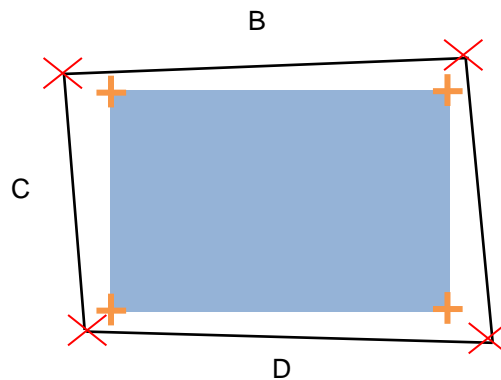


Figure 3-24 Blue region indicates maximum working area.

Orange crosses indicate fiducial markers.

- The fiducial markers are then inspected by the microscope and the new offset values for this test are calculated.

Four markers are used to ensure the offset is accurate for the whole working area of the sample by comparing the value at each corner and taking the average.

3.2.9 Determining relative centre of rotary axis position

A key advantage of the ultra-precision platform is the two rotary axes allowing for the ablation of samples at an angle, which opens new machining strategies. Although the two centres of rotation for the rotary axes intersect, when a sample is installed the physical arrangement of the platform with a sample mounted stops the user from being able to simply rotate the stage when focus has been found to perform angular ablation.

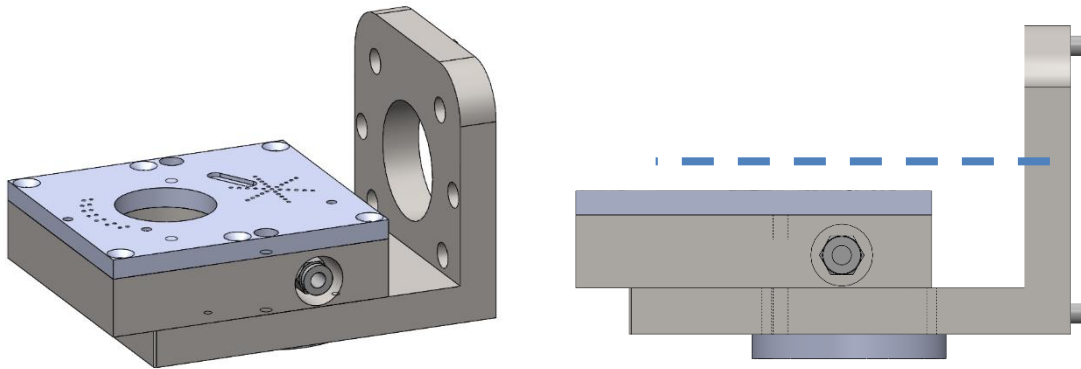


Figure 3-25 Sample holder and alignment to axis.

The rotational axis of the platform is higher than the top surface of the sample holder which causes issues upon rotating the sample holder. This is shown in Figure 3-25. The offset means that focal spot no longer remains on the surface of the silicon sample. This can be accounted using trigonometry if the centre of rotation and focal point of the laser are known.

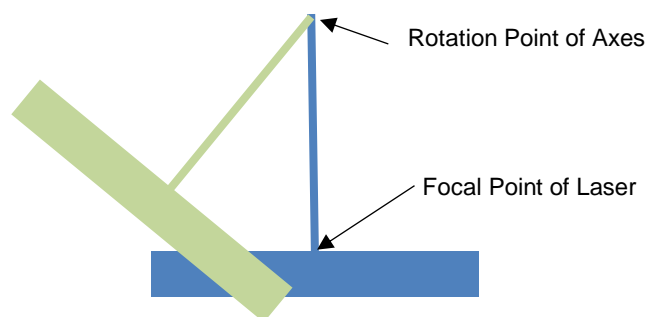


Figure 3-26 Demonstration of effect of axis offset on uncertainty of focal point position after rotation.

The following procedure has been developed:

1. Decide on a marker on the substrate and record the D coordinate for the microscope.

2. Rotate the sample by +10 degrees (absolute) and find the marker on the substrate using the optical microscope; then record the X, Y, D.
3. Solve to find centre of rotation.

These coordinates can be inserted into a set of linear equations to find the rotational point of the axes, allowing for the axis offset to be calculated.

Figure 3-27 shows the geometry involved to calculate the X axis offset and the Z axis offset. The offsets are the distance of the point P from the centre of rotation, R. P⁰ is the initial recorded position and P¹ is the position of the same point of the sample once it has been rotated.

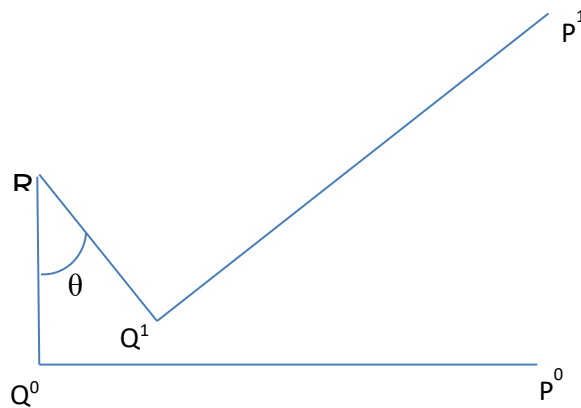


Figure 3-27 Geometric representation of distances

$$\overrightarrow{Q^0P^0} = X_{off} \quad \overrightarrow{Q^0R} = Z_{off} \quad (3-8)$$

$$X_{off} = \frac{1}{2} \left[(P_x^1 - P_x^0) - (P_z^1 - P_z^0) \frac{(1 + \cos \theta)}{\sin \theta} \right] \quad (3-9)$$

$$Z_{off} = \frac{1}{2} \left[(P_x^1 - P_x^0) \frac{\sin \theta}{(1 - \cos \theta)} - (P_z^1 - P_z^0) \right] \quad (3-10)$$

With the correct offsets for the sample found this allows for angular ablation on the sample. This method has been automated and is compatible with samples where the surface to be machined is below or above the axis of rotation.

3.2.10 Machining on an angled plane

A method to test the stage accuracy is to use compound movements which requires the sample to be moved along all three linear axes simultaneously. This test also uses the two rotary axes to initially perform tilt correction to place the sample normal to the focusing objective prior to rotation to change the incident angle of the laser to the sample.

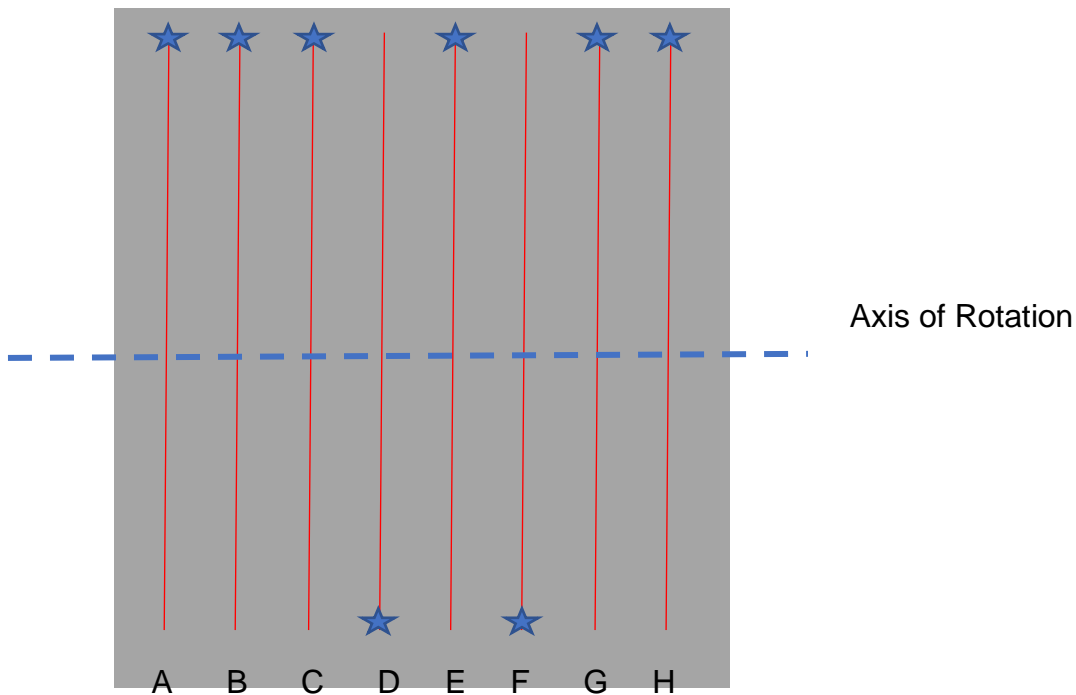


Figure 3-28 Layout of angled plane test. Stars indicates start of machined line

Table 3-18 Track machining paths.

Letter	Machining Path
A	Flat
B	+30 Degrees Downhill
C	Flat
D	+30 Degrees Uphill
E	Flat
F	-30 Degrees Downhill
G	Flat
H	-30 Degrees Uphill

Test Sequence Results

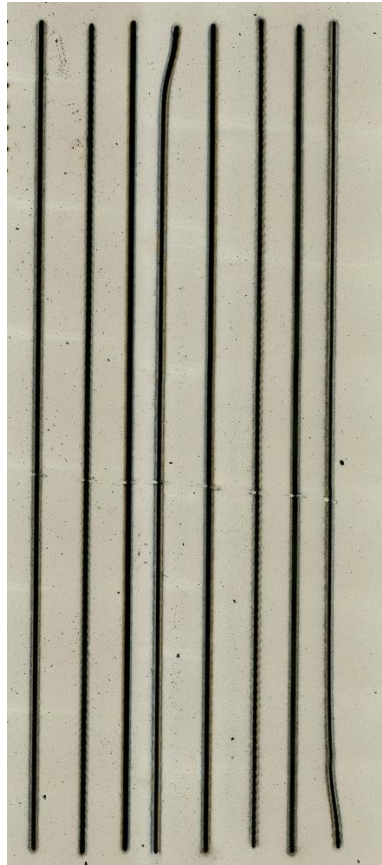


Figure 3-29 Result of machining on angle plane test

On the test pattern shown in Figure 3-29 the defined spacing between each track was 0.5 mm. It is visible that the spacing changes irregularly and that some tracks have a 'hockey stick' shape rather than a straight line.

Investigation of Irregularities

The written code shown in Figure 3-30 was reviewed to determine whether this was the cause of the irregularities in the spacing and path of the test grid. It was found that there was no obvious error and, upon repeating the sequence the imperfections were not repeated in the same areas.

```

1. for (int i = 0; i < 3; a++)
2. {
3.     shutter_open();
4.     double a, b;
5.
6.     // Record Axis Positions
7.     a = myController.Commands.Status.AxisStatus("X", AxisStatusSignal.ProgramPositionFeedback);
8.     b = myController.Commands.Status.AxisStatus("Y", AxisStatusSignal.ProgramPositionFeedback);
9.     microscope_focus = myController.Commands.Status.AxisStatus("D", AxisStatusSignal.ProgramPositionFeedback);
10.
11.    // Move sample to laser focus and ablate cross
12.    Movement_3D_ablation(a, b, 0, 5); // Includes set offset distance
13.    MarkCross(0.25);
14.
15.    // Move sample back to uScope
16.    Movement_3D_uScope(a, b, 0, false);
17.
18.    shutter_closed();
19. }

```

Figure 3-30 Code to test stage repeatability

Initially it was thought that thermal effects of the laser on the optics could be causing the irregularity. Different duty cycles of the platform were tested to see if this was the case. Unfortunately, the non-repeatable error remained.

Finally, it was determined that the stage must be a fault, despite being delivered with a guaranteed calibration report. In order to test this a simple iterative method was constructed. This involved the following steps:

- Identify a suitable sample site using the microscope.
- Machine a cross on the site and record coordinates of the centre of the cross.
- Return sample to microscope field of view.
- Capture field of view of microscope.
- Repeat two more times without moving the stage starting position or changing any parameters.

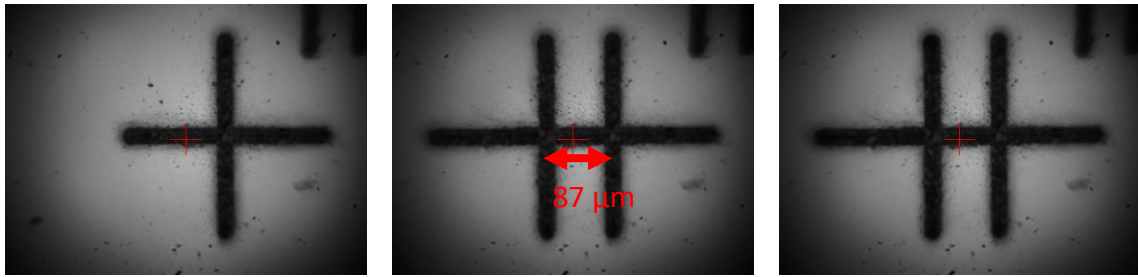


Figure 3-31 Test showing three iterations of the same procedure giving inconsistent results

Figure 3-31 shows that although the procedure hasn't changed, the machined position of the cross is different between iterations. To check for the presence of a procedural error, the recorded values for the cross can be compared in Table 3-19.

Table 3-19 Recorded centroid of machined path for three iterations

	Iteration 1	Iteration 2	Iteration 3
X /mm	-77.6257873517101	-77.6258127420381	-77.6258830697969
Y /mm	-25.9256127521119	-25.9253066744348	-25.9252691072962

These are the values recorded directly from the controller and not those that are calculated from user-generated code. The controller is recording less than a 1 μm variation in either axis between iterations. Therefore, the conclusion must be that there is a discrepancy between the encoder value and the real position of the axis.

Eventually it was found that the bearings in the Y-axis had some slack which was causing an irregular deflection in the axis when momentum or an external force is applied. For this to be resolved, the stage had to be disassembled for the axis to be reconditioned.

Recommissioning of Stage

To determine whether the reconditioned axis has solved the task, the same angled ablation test pattern was machined.

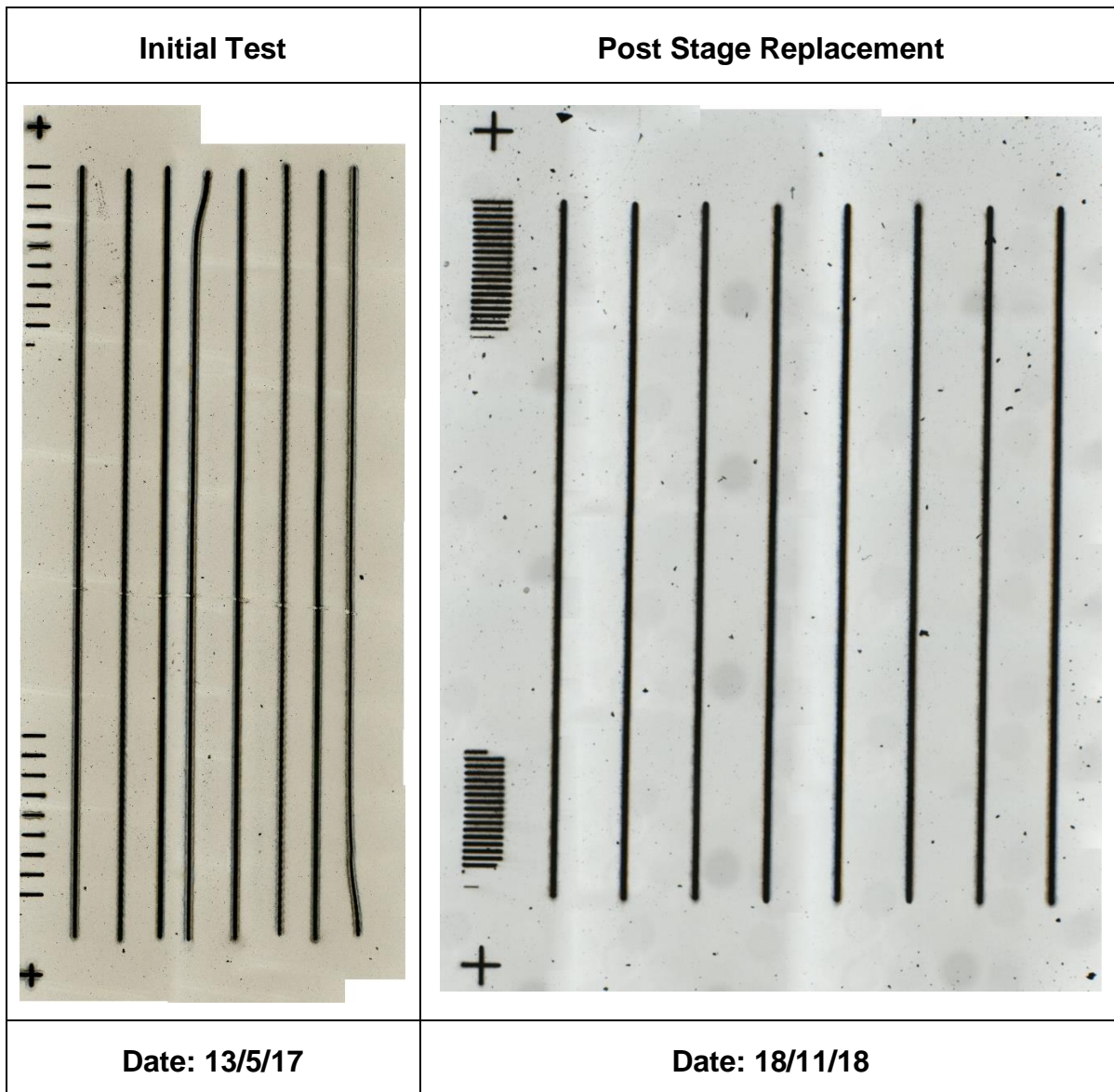


Figure 3-32 Comparison of angled machining trials before and after reconditioning of Y-axis

In Figure 3-32, in the right-hand picture the spacing is regular and the lines are straight compared to the first recorded sample of this type. Therefore this confirms that slippage in the bearings of the Z-axis was the cause of issues with regards to stage repeatability that were seen on other samples at the beginning of working on the platform.

3.2.11 Screenshot of Ultra-Precision Platform Control GUI

The screenshot displays the Aerotech Control GUI, which is divided into several functional panels:

- Stage Control:** Located at the top left, it features a grid of control buttons for X, Y, Z, D, A, and B axes, each with a green power icon and a blue home icon.
- Stage Read Out:** Located at the top center, it displays real-time position and velocity data for the X, Y, Z, D, A, and B axes.
- Microscope Control:** Located at the top right, it includes controls for Save Bitmap, Min Zoom, Max Zoom, Min Intensity, Max Intensity, Intensity, and Moving Zoom.
- Microscope Viewer:** A large grayscale image on the right side of the interface showing a crosshair target with a red crosshair overlay.
- Sample Alignment and Machining Procedures:** Located in the bottom left, it contains various buttons for alignment and machining, such as Start Alignment, Perform Tilt Correction, Set uScope Focus, and Find Rotational Centre.
- Power Meter Control and Readout:** Located in the bottom center, it displays a large 'Value' field and includes buttons for Auto Align and Auto Focus.
- Laser and Attenuator Control:** Located in the bottom right, it features controls for Talisker Laser, including Open Shutter, Shutter Status, and various attenuation settings.

Red arrows point from the callout boxes to their respective panels in the GUI. A vertical label '121' is positioned on the left side of the image.

121

Figure 3-33 Ultra-Precision Platform GUI

Below is an outline of the functions of each part of the software labelled in Figure 3-33.

Stage Control

This covers the 'Home Procedure' for the stage and the ability to move the stage manually.

The 'Home Procedure' is a sequence of movements which allows each axis to find the homing marker on the encoder for the axis. The homing marker is used as a datum for the axis and every movement after homing is done relative to the datum. Due to the complexity of the platform and the number of axes, the procedure had to be designed to prevent any of the stages colliding with other parts of the platform.

The buttons labelled with a positive or negative sign and an axis letter e.g. '+X' or '-Y' can be used to jog the stage in the required direction. The jog increment can either be changed using the predefined intervals or by manually typing in a required increment.

Stage Read Out

This region gives real-time information about the current status of each axis on the stage which includes:

- Stage status – Enabled or Disabled
- Homing status – Homed or Floating
- Current axis position – mm or degrees depending on type of axis
- Current axis velocity – mm/s or degrees/s depending on type of axis
- Microscope Control

This area allows for manual control of the microscope for example when initial alignment of samples is necessary.

Two zoom levels are programmed, maximum and minimum; the microscope is capable of increments between these, but experience showed that access to these was not necessary.

The microscope features a built-in light source whose intensity can be changed. This is useful when changing between samples to ensure that adequate lighting is used, and the image is neither under- nor over-exposed.

The ability to save the image viewed on the microscope manually is also available.

Microscope Viewer

This gives the live view of the camera and the image viewed is the same as what will be saved without any pre- or post-processing.

A red cross overlay has been applied to assist with sample alignment.

Sample Alignment and Machining Procedures

This region is the implementation of all of the methods and algorithms mentioned in the afore-mentioned sections. The order they need to be implemented is from top to bottom. The function of each button is outlined below:

- Start Alignment – Brings the sample to an approximate position using historical data to view the sample with the microscope. Buttons A, B, C and D are used to record the corner positions of the sample.
- Perform Tilt Correction – This is the implementation of the method outlined in section 3.2.7. The ‘Update Coords’ button is used to update the sample corner positions stored in memory for access later.
- Set uScope Focus (1) – Allows the user to move the stage and bring the sample into focus for the microscope.
- Align laser and uScope – Targets are marked on the sample using historical data for the focal position of the sample on the stage. The relative position of the marker to the microscope is then found to improve future alignment.
- Find Focus – The method outlined in section 3.2.5 is implemented and the true position of the focal spot is found and recorded.
- Set uScope Focus (2) – This refocuses the microscope on the sample now that the correct Z axis position is found for machining.
- Find Rotational Centre – This implements the method in section 3.2.9. There is also the ability to check that the method has worked correctly using the ‘rot test’ button. Any angle between 0 and 45 degrees can be tested.
- Move Zoom – In some trials the zoom function of the microscope is required to capture the machined pattern. This checks whether any adjustments are required when using a high magnification.
- Ablate Test Pattern – This performs the required trial and is configured in code to machine, record and capture the required data.

Power Meter Control and Readout

This region is used to setup and view the live read-out from the power meter. If more than one power meter is attached to the system, the one required can be selected using the 'Scan USB' button.

Laser and Attenuator Control

This gives the status and full control of the laser parameters for the system through control of the Talisker laser interface and Watt Pilot Attenuators. This includes:

- Shutter position – Open/Closed
- Laser mode – Continuous/Divided/Burst
- Laser repetition rate
- Talisker attenuation level
- Watt Pilot attenuation level
- AOM Gate – High/Low

3.3 Tools for in-process and post-process analysis

3.3.1 In-process Analysis

3.3.1.1 Ultrafast Pulsed Digital Holographic Interferometry

Digital holography of plasma plumes generated by ultrafast pulses is a technique that the research group is familiar with. Up until this point this has been performed with the laser focused normal to the surface of the sample. Determining the effect of changing the incident angle of the laser to the sample on the plume creation is of interest.

The technique measures the relative change in refractive index of the medium in the field of view. This requires taking a reference image and an event image. Image processing methods are then applied to unwrap the phase map of the image.

Although the technique has been developed, a single frame takes a significant amount of time to produce and doesn't lend itself to the production of large data sets or capturing different parameter combinations. Therefore, to accomplish this goal, the task of automating the data capture was undertaken.

3.3.1.1.1 System overview

The system used was designed and built by Dr Pangovski of the Centre for Industrial Photonics. Full detail and explanation of the system is available in their thesis. Below is a summary of the system.

The holographic system uses a 400 ps pulsed 532 nm imaging laser triggered by a Stanford Research Systems DG353 digital pulse generator. The imaging laser is split to form an object arm and a reference arm. The object arm is expanded and propagates through the laser event and then is projected onto the surface of the CCD. The reference arm is also projected onto the CCD to form the interference pattern. A narrow bandpass filter is used to suppress emissions from the laser event reaching the CCD.

Passing the imaging laser through a laser-induced event such as a plume causes a phase change on the wave front. The field of view (FOV) of the imaging laser is arranged so that the substrate is just out of view and the focal spot is centred in the FOV. Static objects in the FOV can cause issues when processing the interferograms.

3.3.1.1.2 Hologram acquisition and automation

Experimental arrangement

Due to the level of precision required two photodiodes are used to measure the true time-interval between the rising edge of the machining period and the rising edge of the imaging laser. The optical layout for the holographic camera trials is shown in Figure 3-34. Figure 3-35 shows the typical output from the oscilloscope. Delta, Δ , is the measured offset between the ultrafast laser and the imaging laser in the camera. Delta is varied to capture the event at different stages of evolution.

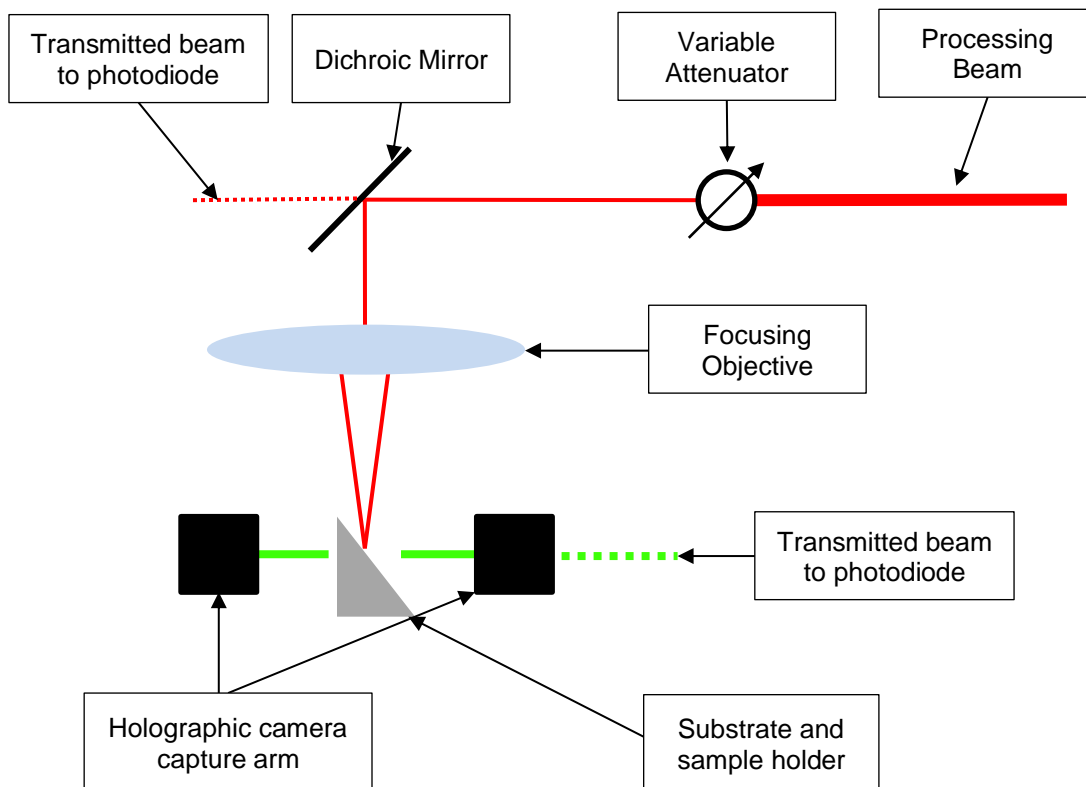


Figure 3-34 Schematic of arrangement for holographic camera trials.

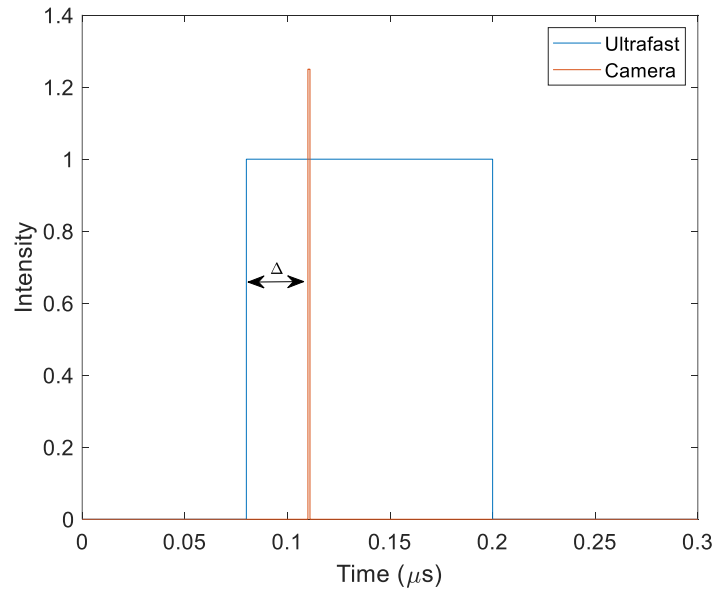


Figure 3-35 Representation of oscilloscope output for measuring time difference from start of laser machining and captured image. Blue is processing laser pulses. Red is holographic camera laser.

3.3.1.1.3 Capture method

When inspecting plume formation, it is important to see the development over time. Unfortunately, a limitation of the technology is that, although the frame capture time is instantaneous, the captured frames per second is very slow which means that to attain a video rather than a still of the evolution the same event needs to be imaged at multiple delta values.

Due to the number of operations required to reset the experiment, the acquisition of a single frame can take approximately 5 minutes, it can take over 16 hours to produce a 200 frame video of a single 1 millisecond event. Therefore, for this method to be effective in capturing different events in a reasonable time frame, reducing the time taken to capture a single frame needs to be reduced and automated.

The method for capturing an event either manually or automated is illustrated:

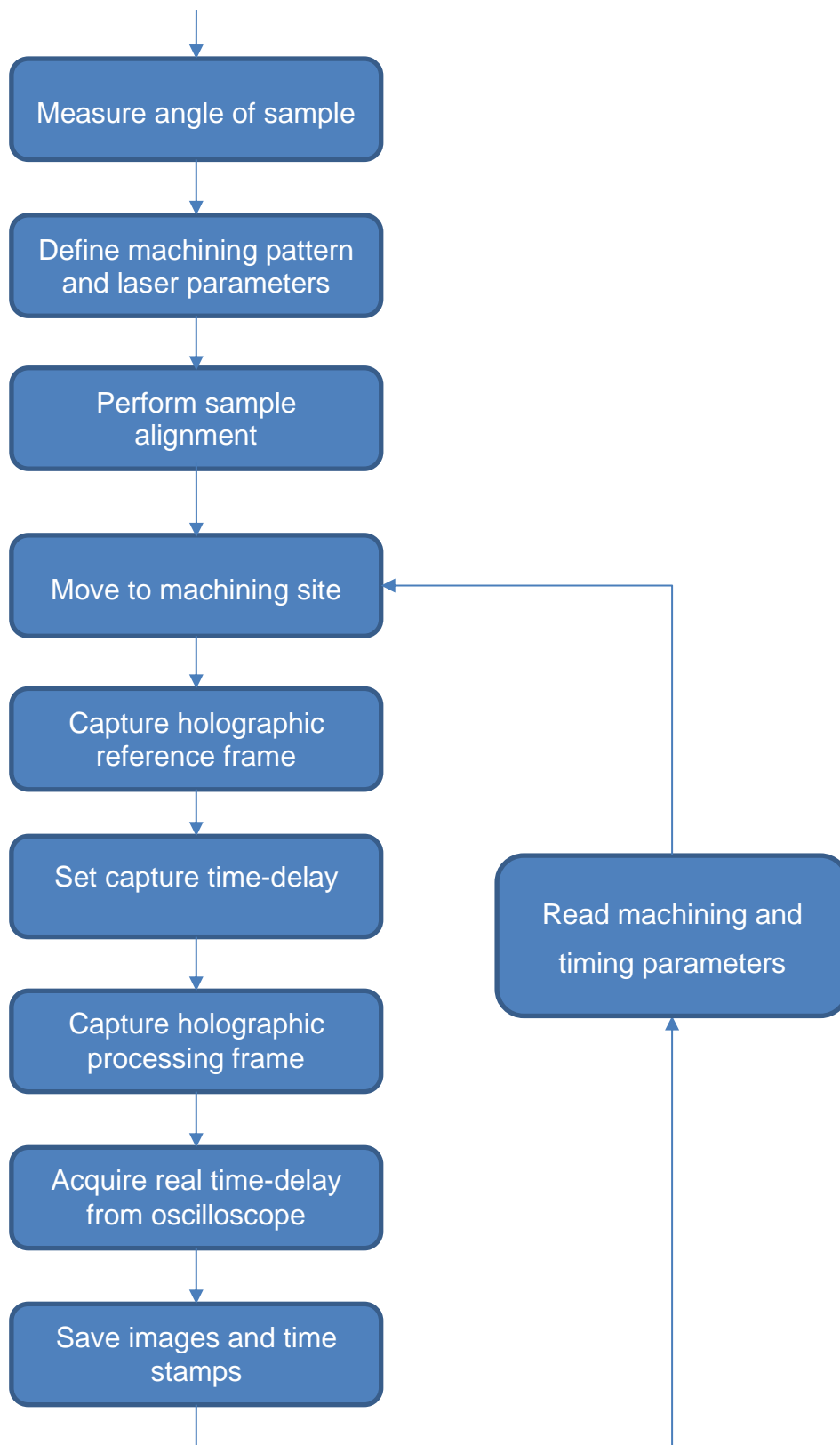


Figure 3-36 Method for automated holographic camera captures

3.3.1.1.4 System Integration

As part of the automation process many devices needed to be integrated into a singular system to shorten the time taken to capture an image and for the process to be unattended. Below is a table defining the devices used and the purpose of each device.

Table 3-20 Devices used for automated holographic camera capture.

Device	Purpose
MATLAB	Main controller – each device connects to MATLAB and saves data Calculating Sample Angle
Excel	Defines laser parameters, sample site coordinates and capture offset
Aerotech Stage	Moves sample relative to laser focal point
Xbox Controller	Aid for sample and laser positioning
Talisker Laser	Laser Source – Gross power and repetition rate can be controlled Internal shutter and AOM is used to control exposure
Watt Pilot Attenuator	Fine power control.
In-line Camera	Determining whether sample is at Ultrafast laser focus
Holographic camera	Captures plume event.
Tektronix Oscilloscope	Measure's time offset from photodiodes.
Photodiodes	Feed oscilloscope responding to laser exposure

3.3.1.1.5 Results Format

The automation program returns two images and a time-stamp. These can be processed using the Stetson formulation to extract the relative phase-difference between the reference and in-process capture. The unwrapped phase images can be stacked to form a film reel of the evolution of the event.

Figure 3-37 shows an example of the final processed output from the holographic camera. This shows the evolution of the plume generated by ultrafast ablation of a silicon target with the Talisker laser system. The field of view for the images is 878 μm wide by 660 μm high.

Further analysis techniques will be shown in section 5.3.

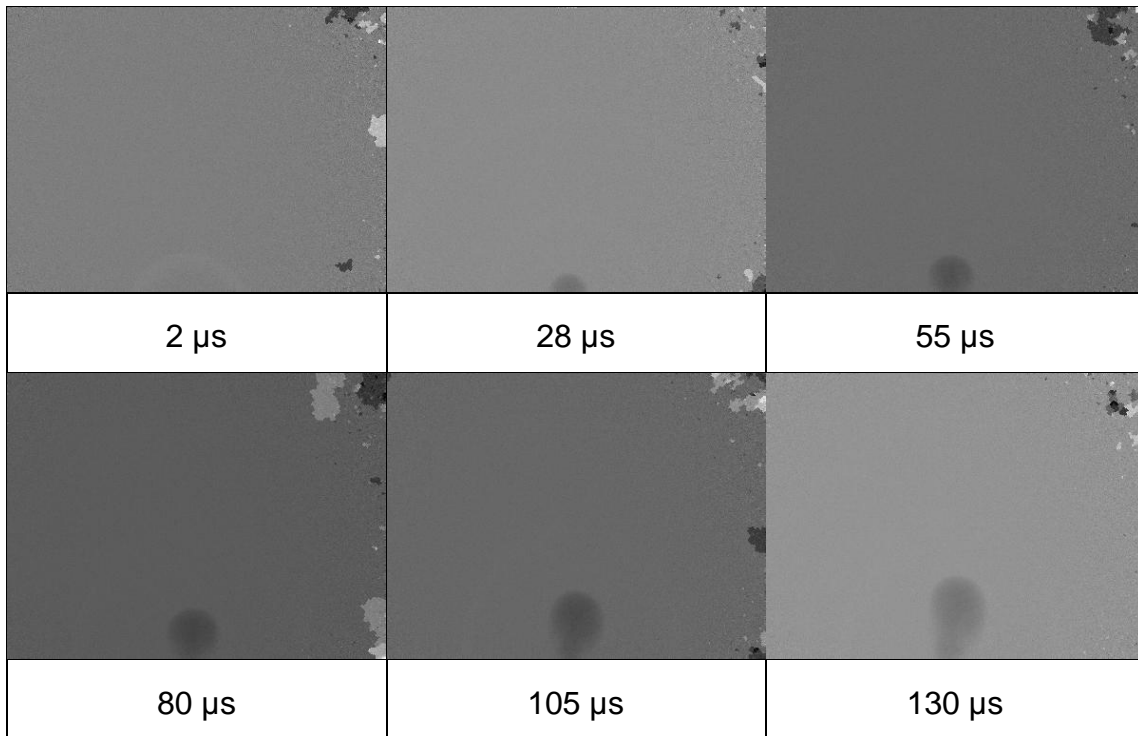


Figure 3-37 Sample of processed images produced by holographic camera for ultrafast ablation of target. Time is the difference from processing beginning and frame captured.

3.3.2 Post Processing Analysis

3.3.2.1 Optical Microscope

The Olympus BX51 optical microscope is a very simple piece of equipment that allows quick analysis of samples. A variety of magnifications are available along with the use of bright-field and dark-field illumination. The microscope can be used to gather a coarse estimation of the height of features on the sample by scanning the microscope vertically and viewing when features come into focus.

3.3.2.2 Scanning Electron Microscope and Energy Dispersive X-ray spectra

The Zeiss CrossBeam is a versatile ion microscopy solution. The CrossBeam is capable of SEM, FIB and EDX on the same platform without significant reconfiguring. SEM allows for high magnification images at a higher resolution than an optical microscope. FIB can be used to mill specific sample sites for cross-sectional views. The EDX gives accurate elemental analysis of the sample and can be used to determine relative concentrations.

3.3.2.3 White Light Interferometer

A Veeco Wyko NT3300 white light interferometer was used to determine the surface morphology of samples. This tool vertically scans a broad-spectrum light source over the site of interest to produce interference fringes which can then be interpreted by the computer to provide height information on the scanned sample. The data is returned as a three-dimensional plot.

Depending on the sample and the data required there are two different methods of scanning on the NT3300. Phase-shifting interferometry (PSI) is used for near-smooth surfaces with minor defects and is capable of a vertical resolution of 0.3 nm and a measurement range up to 160 nm. Vertical scanning interferometry (VSI) is more versatile and is used for rough surfaces. VSI has a vertical resolution of 3 nm and a scan range up to 2 mm.

When using the NT3300 the user must be aware of the implications of illumination level, thresholding, and 'batwing' error. These can affect the ability of the NT3300 to return real and accurate data.

3.4 Summary

A significant portion of time has been spent on the development of the ultra-precision platform to lay down the groundwork for future experiments and research. This has included the design and sourcing of the optical train and components with scope for the future integration of optical-based metrology technologies such as Raman and OCT. Equipment has been identified and installed to perform beam diagnostics and monitoring to determine beam stability and characteristics.

A unified software interface has been created to control the platform for processing and in-process data logging. Within the software development methodologies have been established for sample tilt correction and machining on an angled plane. Machining on an angled plane is a unique feature of this platform compared to competitors and opens a new approach to laser machining. Processes have been automated to achieve greater accuracy and repeatability than achievable manually such as microscope focusing, laser-microscope alignment, laser focusing and the determination of the rotary axis of the platform for a sample.

The integration of digital holographic microscopy allows the investigation of machining on an angled plane and the effect on the plume characteristics. Through the automation data capture, data acquisition rates have been significantly increased with a significant reduction in user error.

Equipment and techniques which allow the evaluation of samples after machining have been identified and include an optical microscope, SEM with electron dispersive spectra and white light interferometry.

Overall this provides a platform which provides a significant number of tools and different approaches that can be used for research within this body of work and beyond.

4 Effect of Laser Stability on ultra-precision laser machining

As determined from the literature review the stability of the beam influences the accuracy of the machining that can be performed.

In an ideal case a laser has fixed beam diameter, pointing position and pulse energy and this would remain constant for the lifetime of the laser. A laser which had these criteria would be considered stable. However, it is known that lasers are inherently fluctuate in these properties and is thus unstable. Therefore, before undertaking any further work on the platform, an initial baseline of performance measurements needs to be taken so that the implications on process stability can be considered.

The assessment will measure the power, position, and beam diameter stability for the 355, 532 and 1064 nm wavelength lasers for the Talisker Ultra laser system. The Talisker laser has the following specifications:

Table 4-1 Talisker Ultra specifications

Property	Value		
Output Wavelength (nm)	1064	532	355
Average power output (W)	>16	>8	>4
Repetition Rate Range (kHz)	Single pulse to 200		
Pulse width (ps)	<15		
Pulse to Pulse Stability (%)	<2	<2	<5
Average Power Stability (%)	<2		
1/e ² Beam Diameter (mm)	2.0±0.5	1.4±0.3	1.3±0.3
Beam Circularity (%)	>85		

The Talisker Ultra is a Nd:YAG laser which is optically pumped using laser diodes operating in Q-switching mode. Frequency doubling is used to achieve the 532 nm and 355 nm harmonics.

4.1 Equipment selection

A camera beam profiler and thermopile power meter have been selected for the initial beam diagnostic trials for the following reasons:

- Capable of recording all beam diagnostics synchronously.
- API interface available.
- Power meter has large range (20mW – 30W), removing the need to alter the set-up.

The Ophir SP300 Spiricon camera has the following specifications:

Table 4-2 Ophir Sp300 Spiricon camera specifications

Property	Value
Active Area	7.1mm x 5.3mm
Pixel Spacing	3.69 μ m x 3.69 μ m
Number of Effective Pixels	1928 x 1448
Frame Rate	26 FPS at full resolution

The power meter is an Ophir 30A-BB-18 with the following specifications:

Table 4-3 Ophir 30A-BB-18 specifications

Property	Value
Aperture (mm)	Φ 17.5
Power Range	20mW – 30W
Power Noise Level	1mW
Power Accuracy \pm %	3
Linearity with Power \pm %	1

The camera measures the intensity on each pixel to plot the beam profile in 2D and 3D. The software uses this data to calculate the centroid and diameter of the beam for each captured frame.

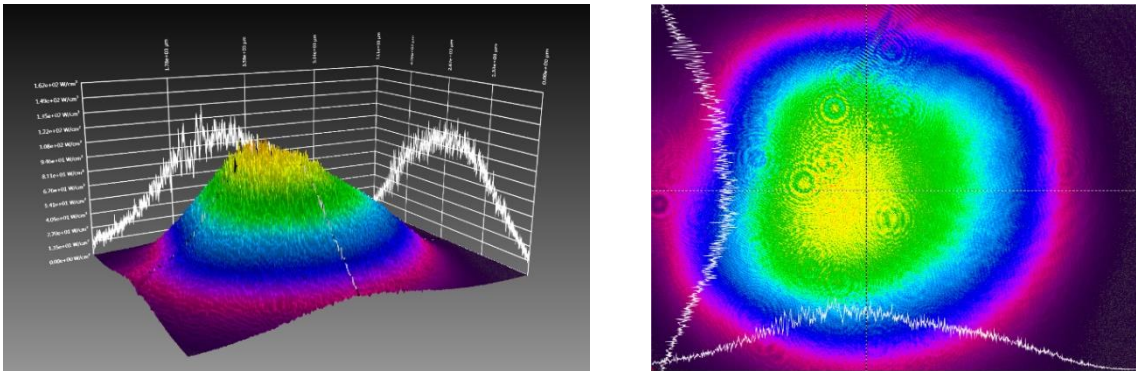


Figure 4-1 Examples of beam profile at maximum power

4.2 Experimental Setup

To perform the experiments, the Spiricon camera and power meter needed to be installed on the ultrafast platform to perform beam diagnostics. Ideally these would be placed in the positions shown in Figure 4-2 as this would give the same distance from the dichroic mirror to the focusing objective and the camera sensor, respectively.

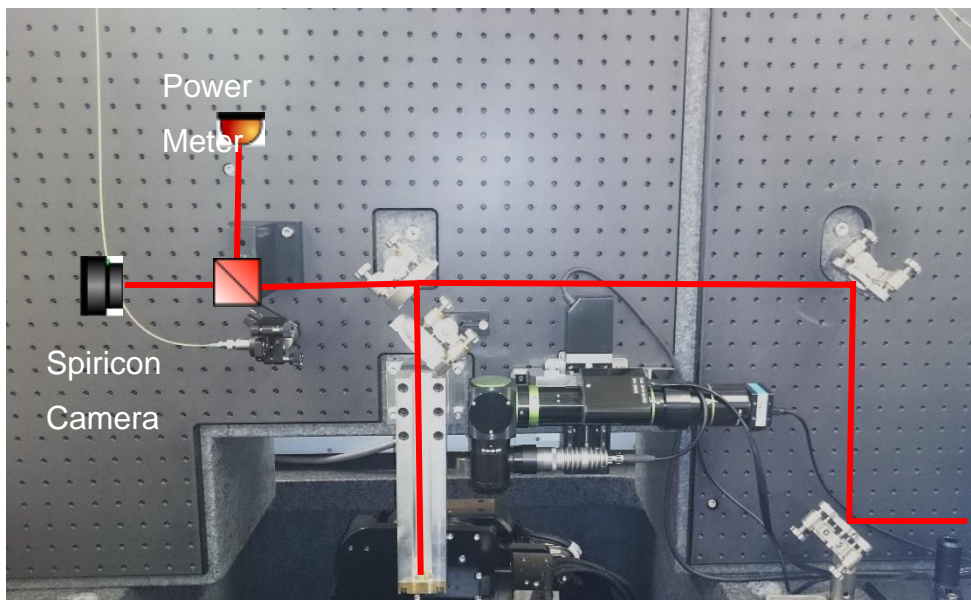


Figure 4-2 Ideal beam diagnostic layout

The issue with this arrangement is that the mount for the dichroic mirror, Figure 4-3, blocks the transmission beam. Therefore, a new mount was designed, machined and installed.

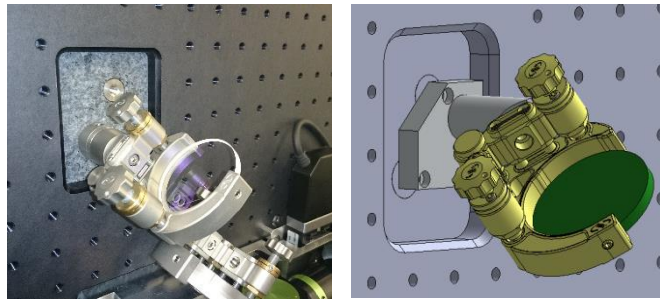


Figure 4-3 Left: Dichroic mirror mount Right: Redesigned mount

For the interim the equipment was assembled on the base of the table with approximately the same path length as the desired arrangement.

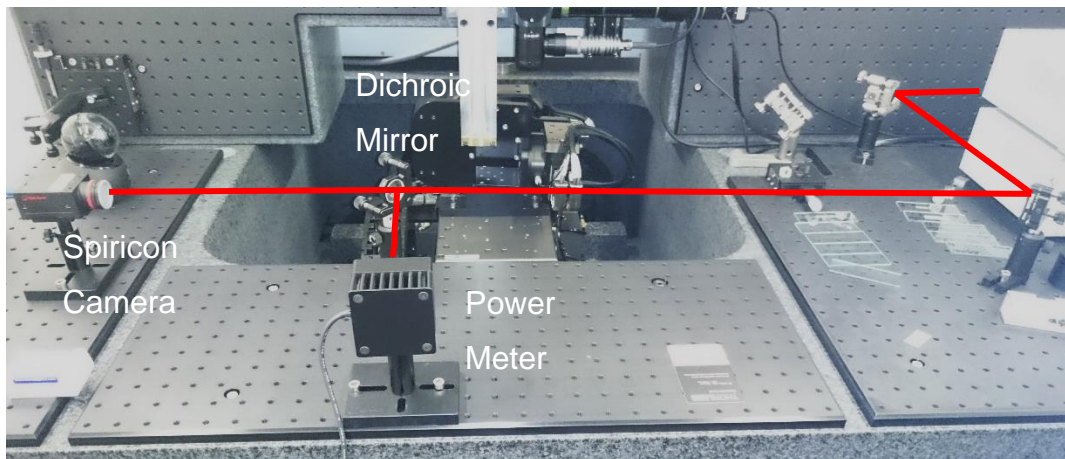


Figure 4-4 Interim beam diagnostics layout

The disadvantage of this method is that the angular and positional stability are coupled so cannot be measured separately. This would require a second position detector with an f-theta focusing lens to decouple the angular stability from positional stability. An f-theta lens has a linear relationship between the entry angle and focal spot position. The second position sensors would need to be compatible with measuring the beam at focus.

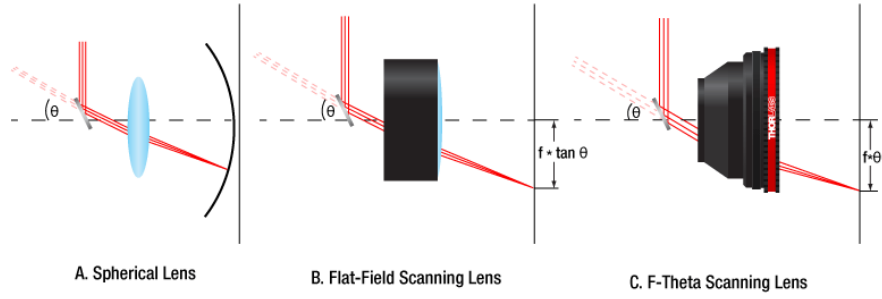


Figure 4-5 Effect of entry angle on focal spot position for different types of lenses [124]

By comparing the centroid position measured by the first camera normal to the beam and centroid position measured by the second detector at the focus of the lens, the angular stability and positional stability can be calculated.

$$(x, y)_{sensor1} = (x, y)_{linear\ offset} + (x, y)_{sensor2}$$

$$(x, y)_{sensor2} = f \times (\theta_x, \theta_y)$$

$$(x, y)_{linear\ offset} = (x, y)_{sensor1} - f \times (\theta_x, \theta_y)$$

$$f = \text{focal length of lens}$$

4.3 Measurement procedure

ISO standards 11670, 11146, 11145, 13694 define the experimental setup and procedure for performing beam diagnostics.

These define that three test durations should be performed:

- 1-second interval.
- 1-minute interval.
- 1-hour interval.

The ISO 11670 states that the beam should be sampled 1000 times in a measuring period. Unfortunately, the camera is limited to 26 FPS at full resolution such that it was not possible to achieve the 1000 samples for the 1 second interval tests.

The beam centroid and beam diameter were calculated using the ISO standard $d_{4\sigma}$ method which is defined as 4 times the standard deviation of the energy distribution. This is described by:

$$D_{4\sigma}: d_{\sigma} = 4 \times \sigma$$

The variance is defined as:

$$\sigma_{\sigma}^2 = \frac{\sum_x \sum_y (x - \bar{x})^2 \cdot Z(x, y)}{\sum_x \sum_y Z(x, y)}$$

Z = Intensity at pixel at x, y \bar{x} and \bar{y} are coordinates of centroid

Carrying out the trials at all three wavelengths (355, 532, 1064 nm) of the Talisker laser required changing the dichroic and reflective mirrors between wavelengths due to the different absorption and reflection properties.

A 1-hour stability test was performed for each wavelength at zero attenuation and 200 kHz repetition rate which showed the long-term properties of the laser at full power.

Instead of performing 1-minute duty cycle measurements, a simulated workload closer to the true duty cycle of the machine was used and is covered later in this section.

A programme was created to automate the stability tests. This ensured that the calibration of the Spiricon was carried out correctly and the warm up and warm down cycles were identical for every test.

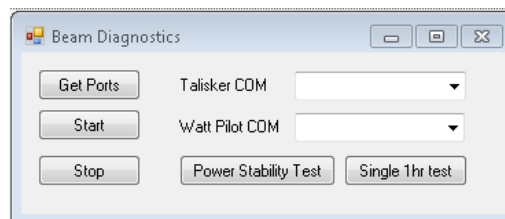


Figure 4-6 Beam stability testing interface

4.4 Talisker Laser 1 Hour Stability

4.4.1 1064 nm 1 hour Stability Results

4.4.1.1 Pointing stability

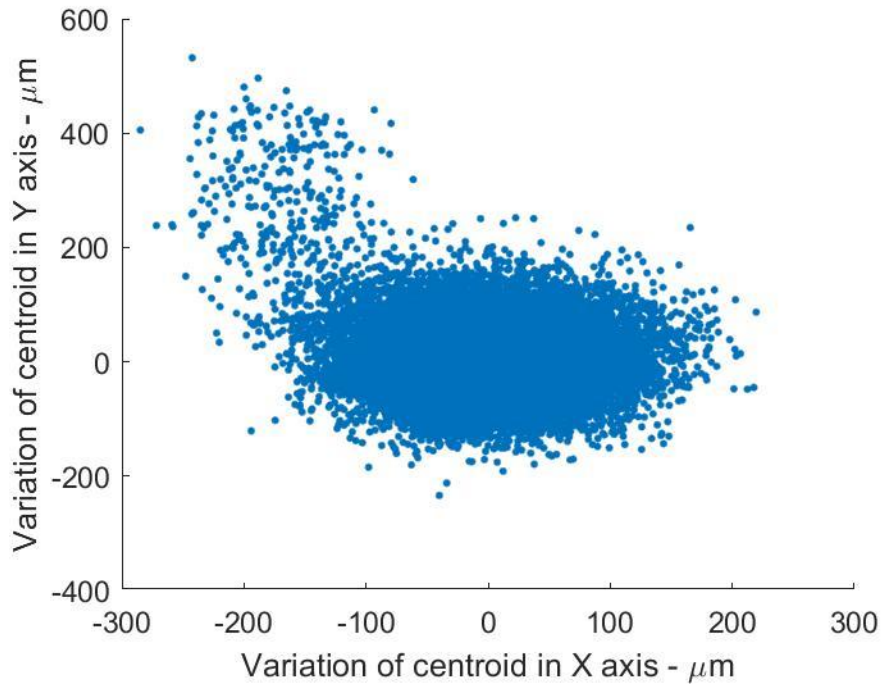


Figure 4-7 Variation in centroid position for 100% power at 1064 nm

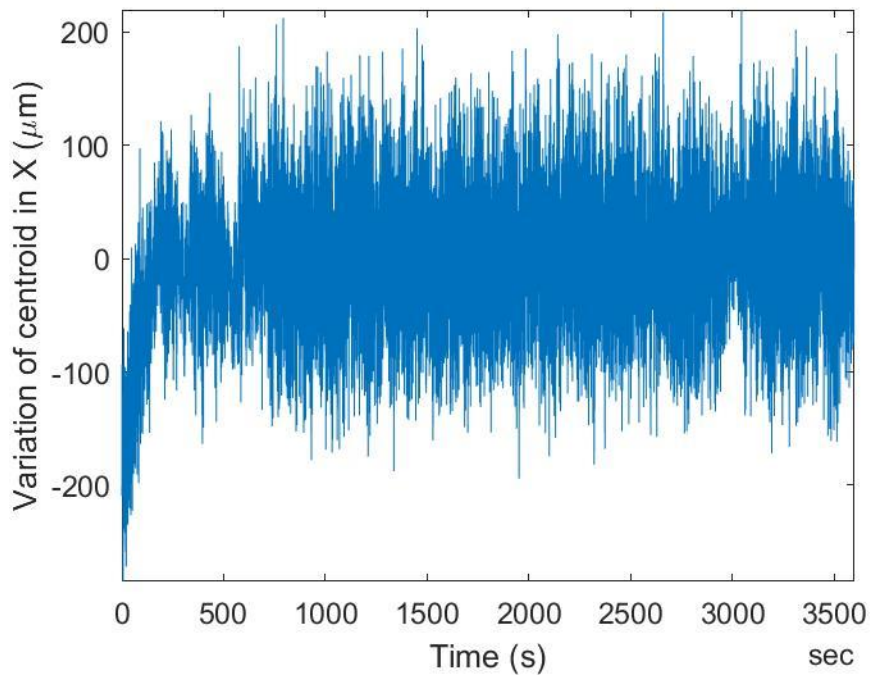


Figure 4-8 Variation of centroid position in X for 1 hour

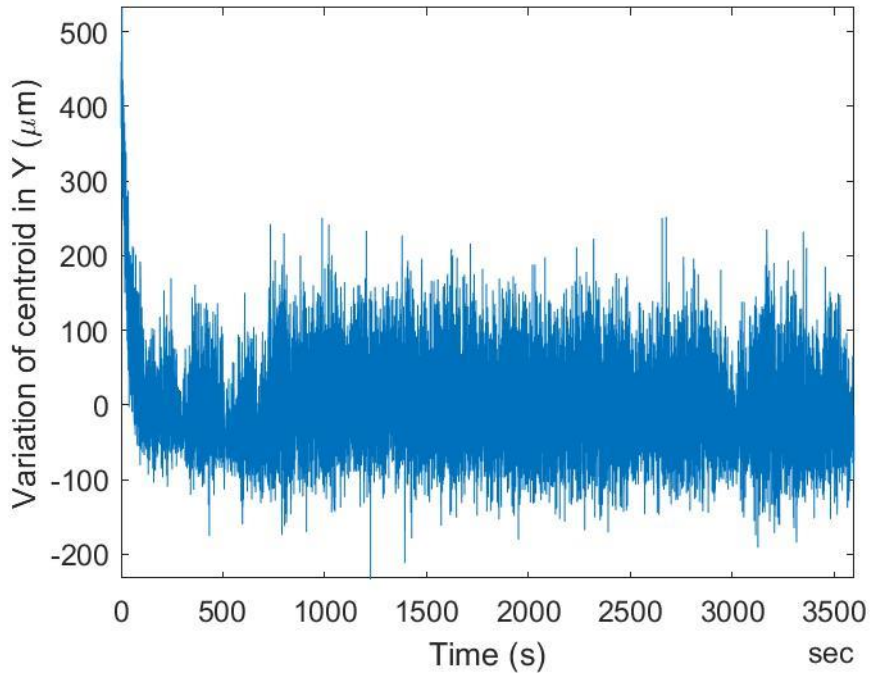


Figure 4-9 Variation of centroid position in Y for 1 hour

Table 4-4 Results from pointing stability test (1064 nm)

	Centroid variation in X (μm)	Centroid variation in Y (μm)
Minimum	-284.8	-233.9
Maximum	219.6	531.8
Standard Deviation	53.2	60.3

4.4.1.2 Beam diameter stability

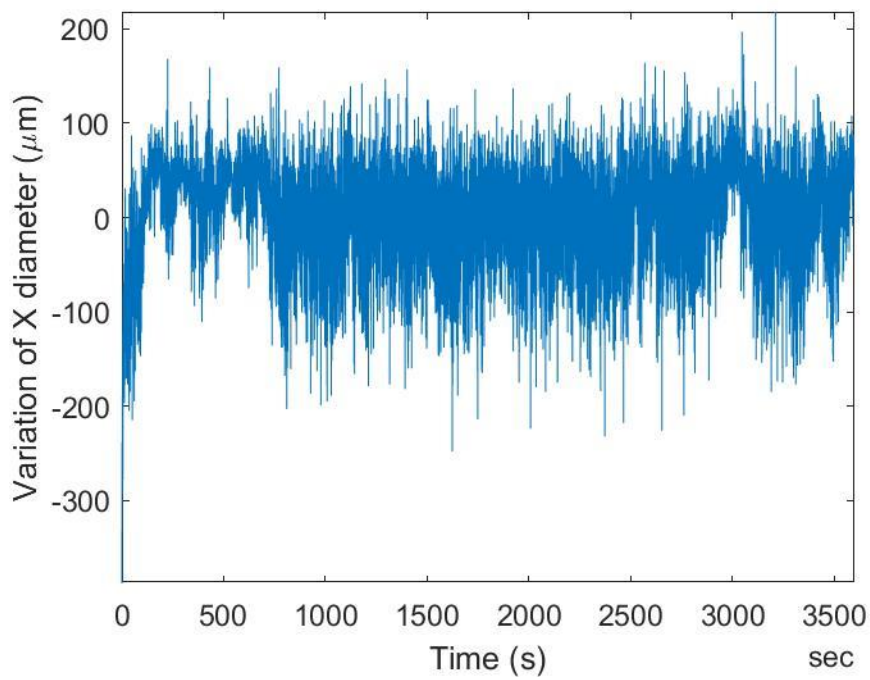


Figure 4-10 Variation of diameter in X (1064 nm)

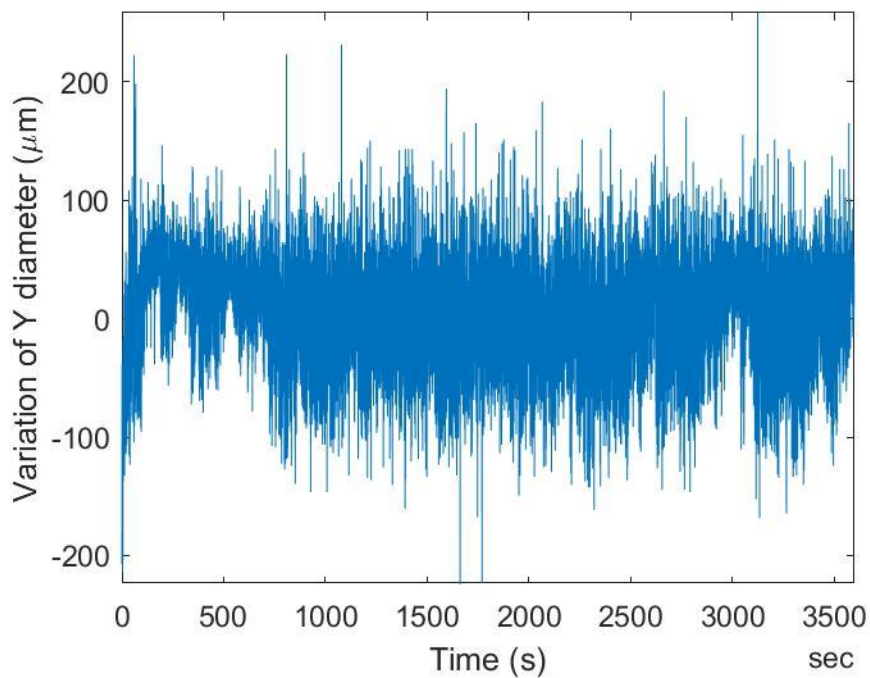


Figure 4-11 Variation of diameter in Y (1064 nm)

Table 4-5 Variation of beam diameter (1064 nm)

	Diameter variation in X (μm)	Diameter variation in Y (μm)
Mean value	5.3488×10^3	4.7745×10^3
Standard Deviation	46.8	40.6

4.4.1.3 Power stability

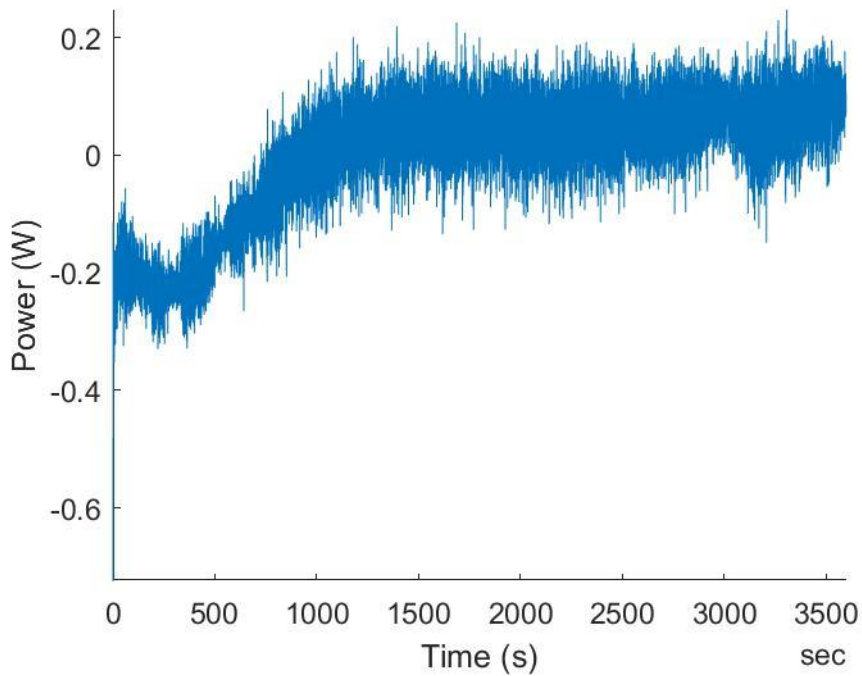


Figure 4-12 Power variation for test period normalised to mean value (1064 nm)

Table 4-6 Average power output (1064 nm)

Average power (W)	13.2376
Standard Deviation (W)	0.1058

4.4.2 532 nm 1 hour Stability Results

4.4.2.1 Pointing stability

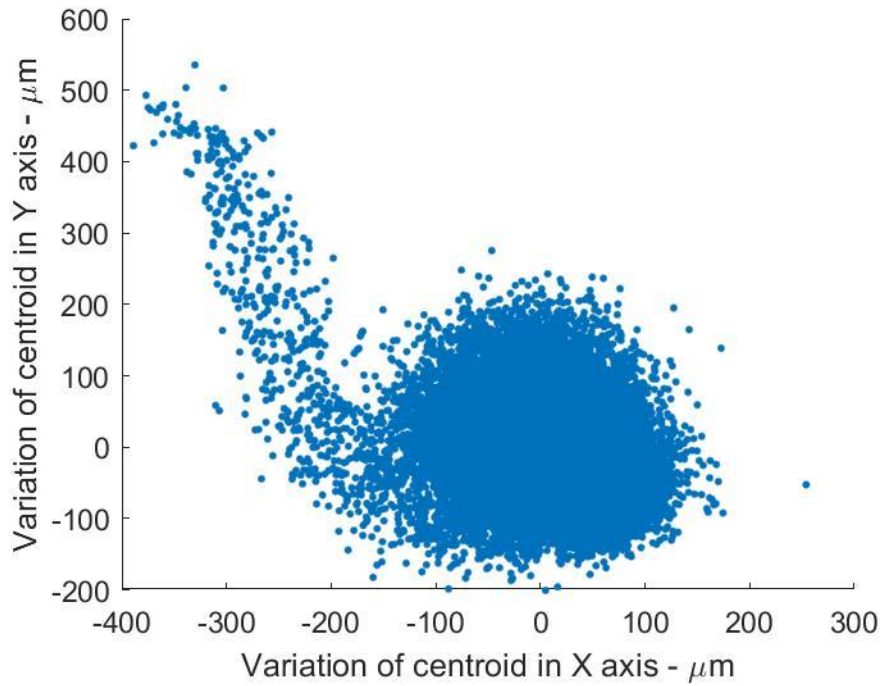


Figure 4-13 Variation in centroid position at max power (532 nm)

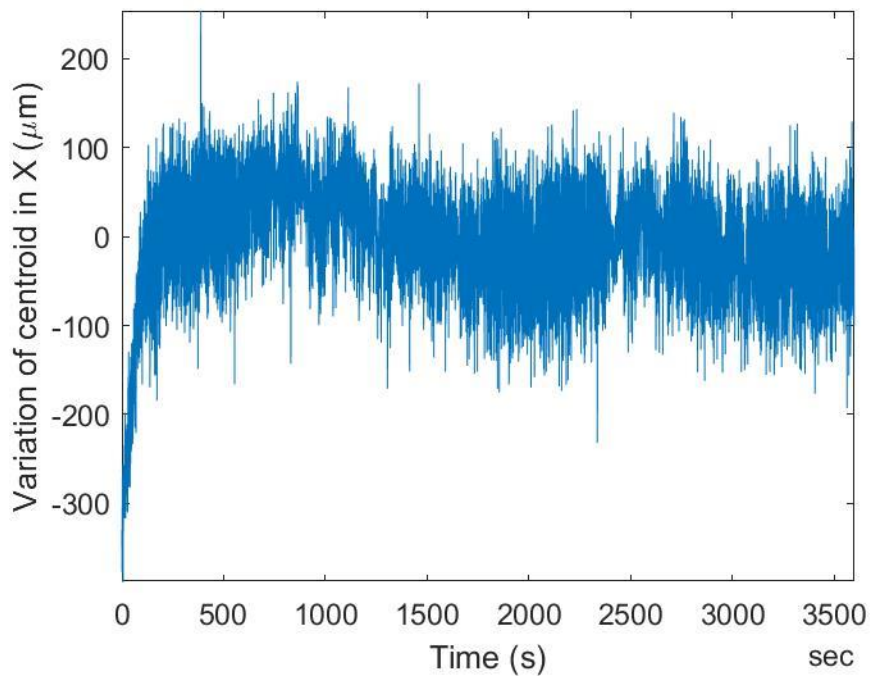


Figure 4-14 Variation of centroid position in X (532 nm)

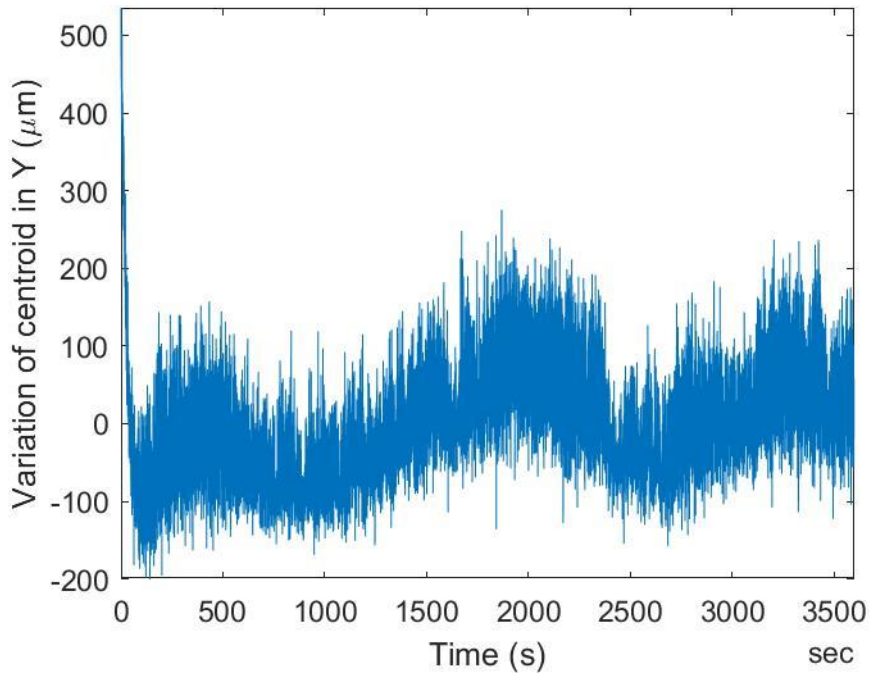


Figure 4-15 Variation of centroid position in Y (532 nm)

Table 4-7 Results from pointing stability test (532 nm)

	Centroid variation in X (μm)	Centroid variation in Y (μm)
Minimum	-389.0	-200.7
Maximum	254.0	535.9
Standard Deviation	55.4	69.3

4.4.2.2 Beam diameter stability

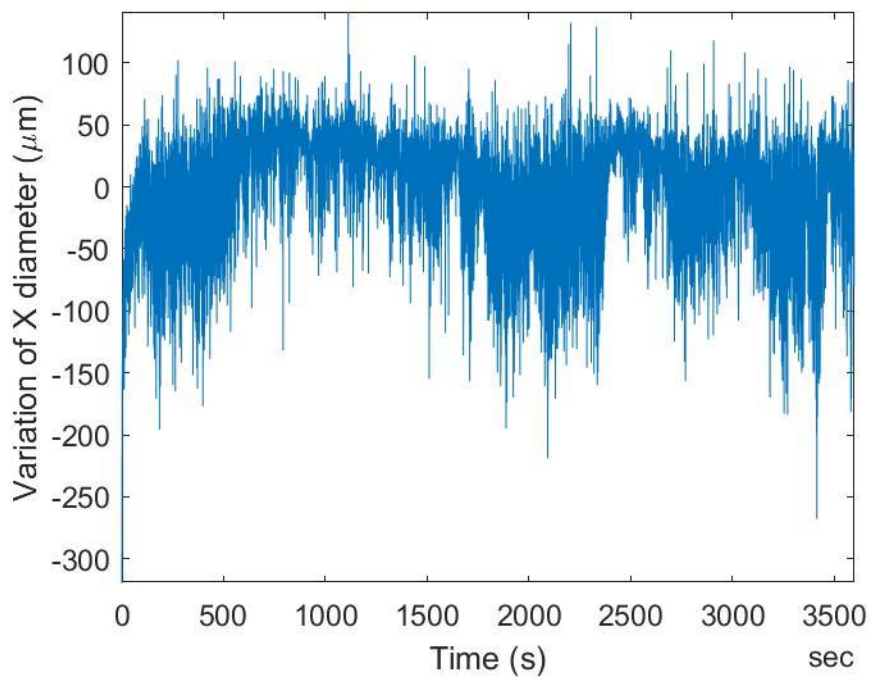


Figure 4-16 Variation of diameter in X (532 nm)

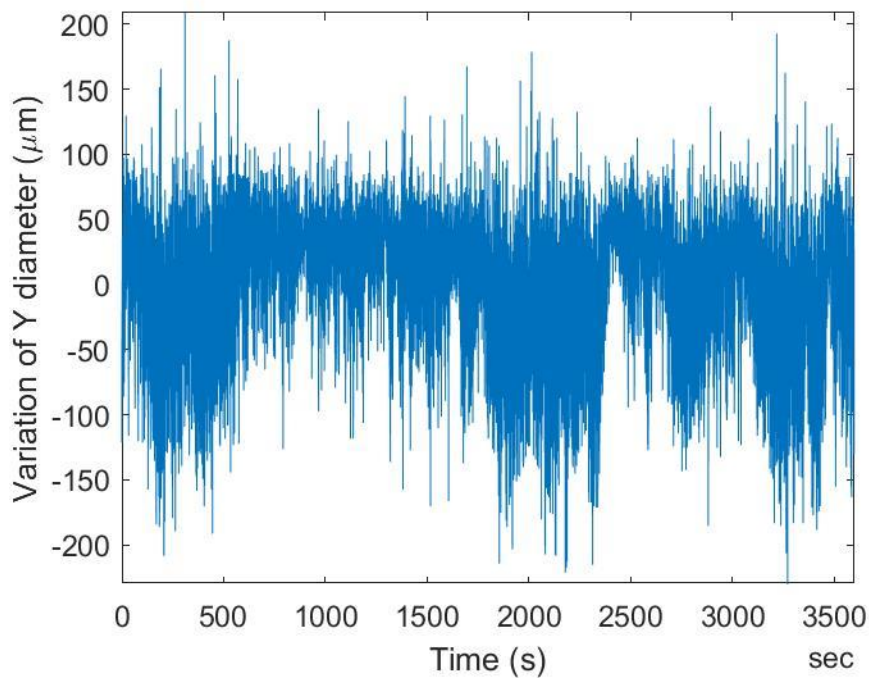


Figure 4-17 Variation of diameter in Y (532 nm)

Table 4-8 Variation of beam diameter (532 nm)

	Diameter variation in X (μm)	Diameter variation in Y (μm)
Mean value	4.1899×10^3	3.9074×10^3
Standard Deviation	37.0	44.1

4.4.2.3 Power stability

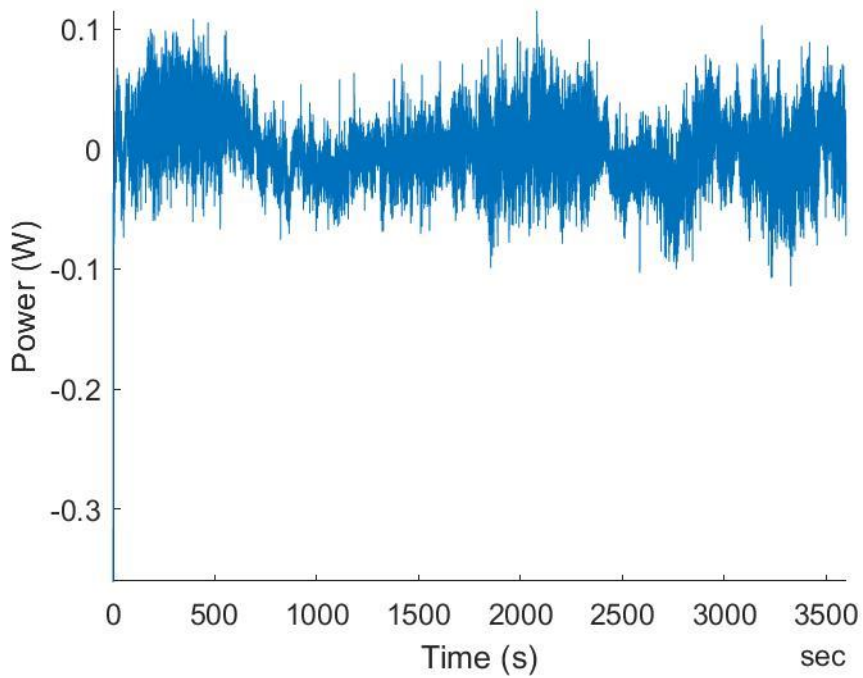


Figure 4-18 Power variation for test period normalised to mean value (532 nm)

Table 4-9 Average power output (532 nm)

Average power (W)	6.3793
Standard Deviation (W)	0.0262

4.4.3 355 nm 1 hour Stability Results

4.4.3.1 Pointing stability

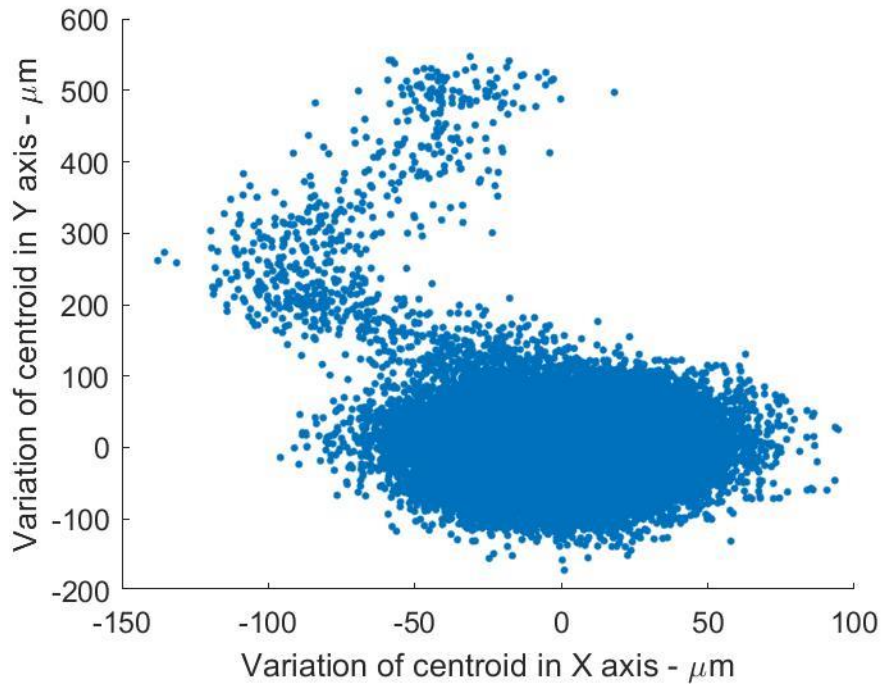


Figure 4-19 Variation in centroid position at max power (355 nm)

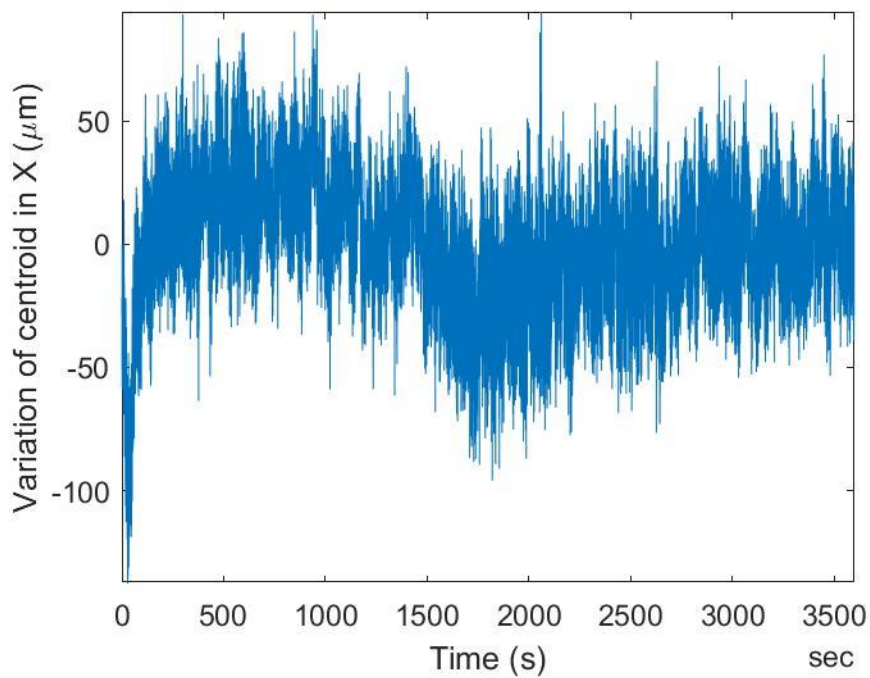


Figure 4-20 Variation of centroid position in X (355 nm)

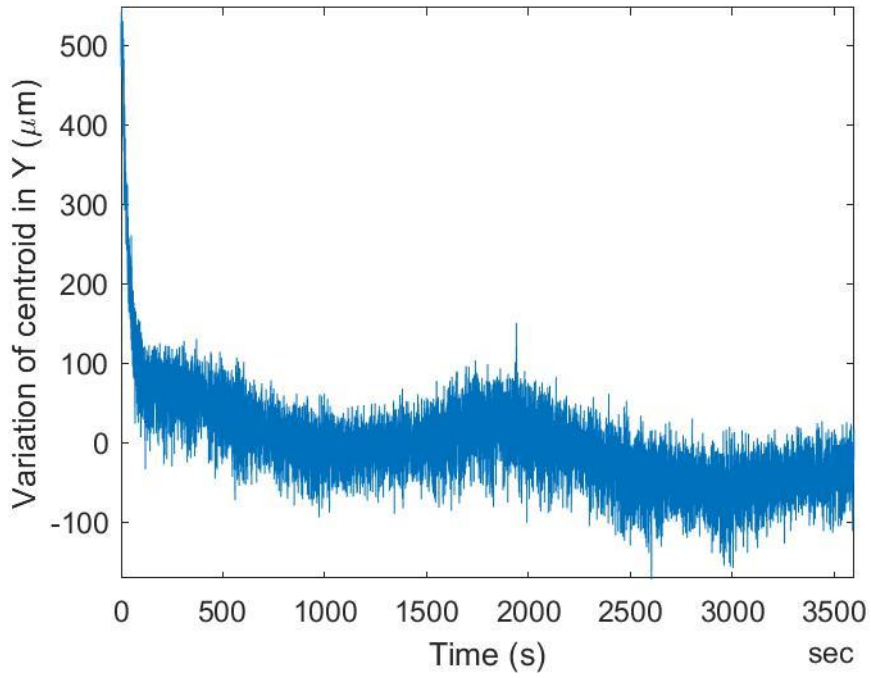


Figure 4-21 Variation of centroid position in Y (355 nm)

Table 4-10 Results from pointing stability test (355 nm)

	Centroid variation in X (μm)	Centroid variation in Y (μm)
Minimum	-137.7	-171.7
Maximum	94.5	547.0
Standard Deviation	25.0	60.0

4.4.3.2 Beam diameter stability

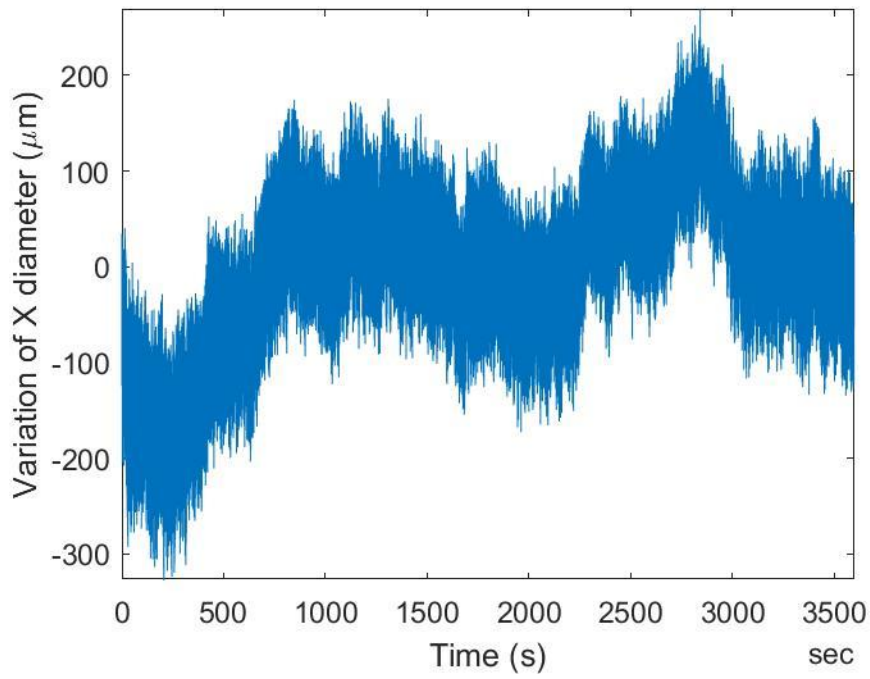


Figure 4-22 Variation of diameter in X (355 nm)

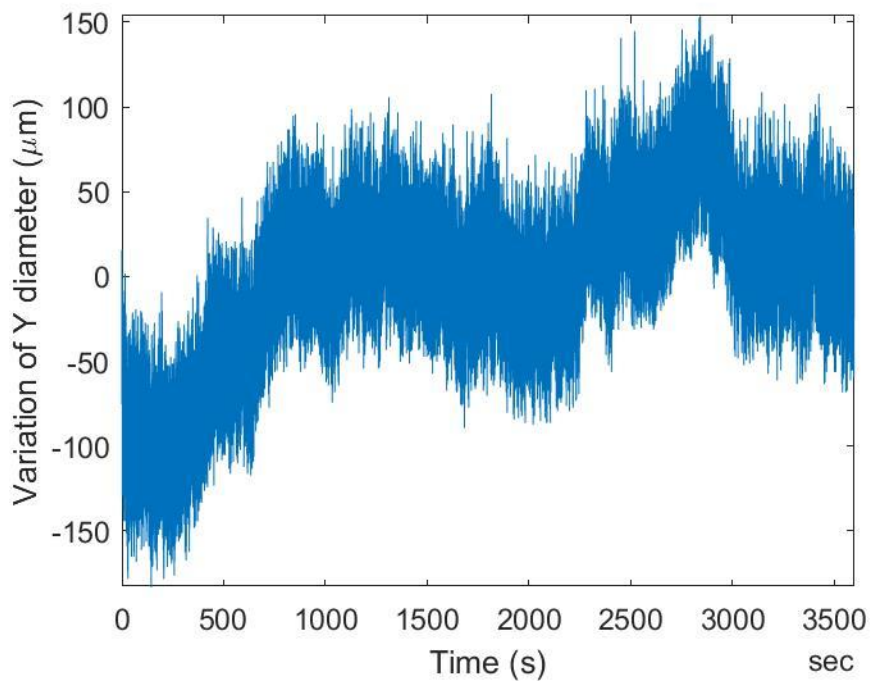


Figure 4-23 Variation of diameter in Y (355 nm)

Table 4-11 Variation of beam diameter (355 nm)

	Diameter variation in X (μm)	Diameter variation in Y (μm)
Mean value	2.4435×10^3	2.4743×10^3
Standard Deviation	90.3	5.3

4.4.3.3 Power stability

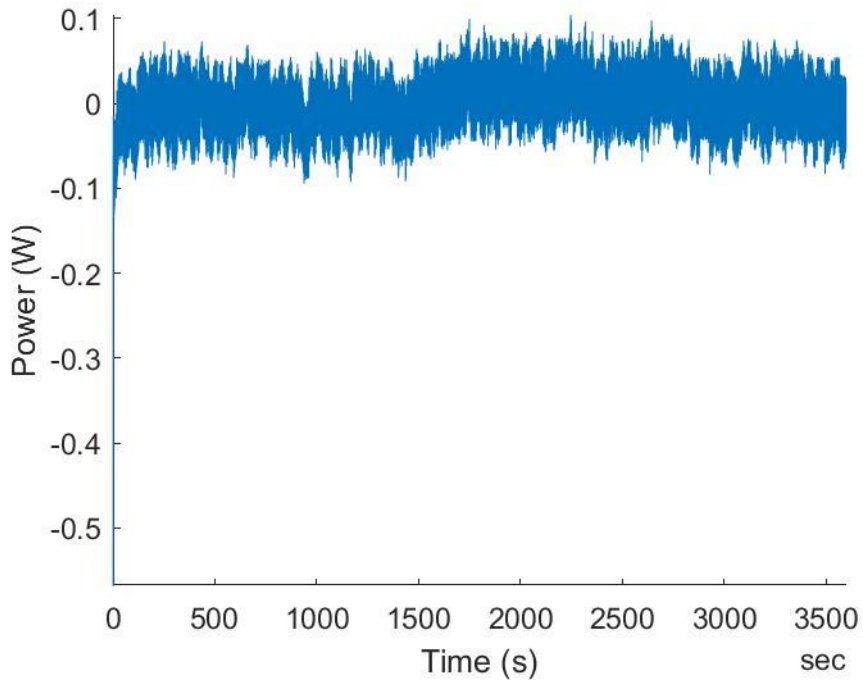


Figure 4-24 Power variation for test period normalised to mean value (355 nm)

Table 4-12 Average power output (355 nm)

Average power (W)	3.8749
Standard Deviation (W)	0.0398

4.4.4 Analysis and Discussion

4.4.4.1 Pointing stability

From these stability tests it is apparent that, during the first 600 seconds of opening the acoustic-optic modulator gate, there is a drastic change in the position of the centroid. After this period the centroid varies around the mean position within a consistent envelope. The stabilisation to a consistent mean value could be due to thermal stabilisation of laser and mirrors with the environment due to a consistent load. This 'soak in' time is roughly 600 seconds after activating the laser. The 532 nm and 355 nm show a periodicity of roughly 1500-2000 seconds in the recorded stability data, a possible reason for this could be the laser cooling system activating. High frequency noise is usually a symptom of operating at the resolution of the sensor, for this data it is not the case as the camera resolution is 3.69 μm and the measured deviation is significantly greater. The high frequency instability could be due to the type of laser used. The Talisker laser is a diode-pumped solid state type (DPSS). The high frequency instability could be a symptom of the heating and cooling of the gain medium whilst it is being pumped by the laser diodes.

4.4.4.1.1 Further assessment of 1064 nm

The 1064 nm measurement was chosen for further investigation due to the consistent envelope of the data. Inspecting a section of the variation of the centroid in X for a period of 20 to 40 minutes where the measured centroid position has steadied it is difficult to determine whether there are any underlying frequencies in the recorded data due to the low data acquisition rate of the Spiricon camera and the irregular time steps of the data. The low data acquisition rate results in a significant disparity with the pulse frequency of the laser, movement of the centroid could be a smoother transition than that measured. The irregular time steps of the data rule out the use of Fourier analysis.

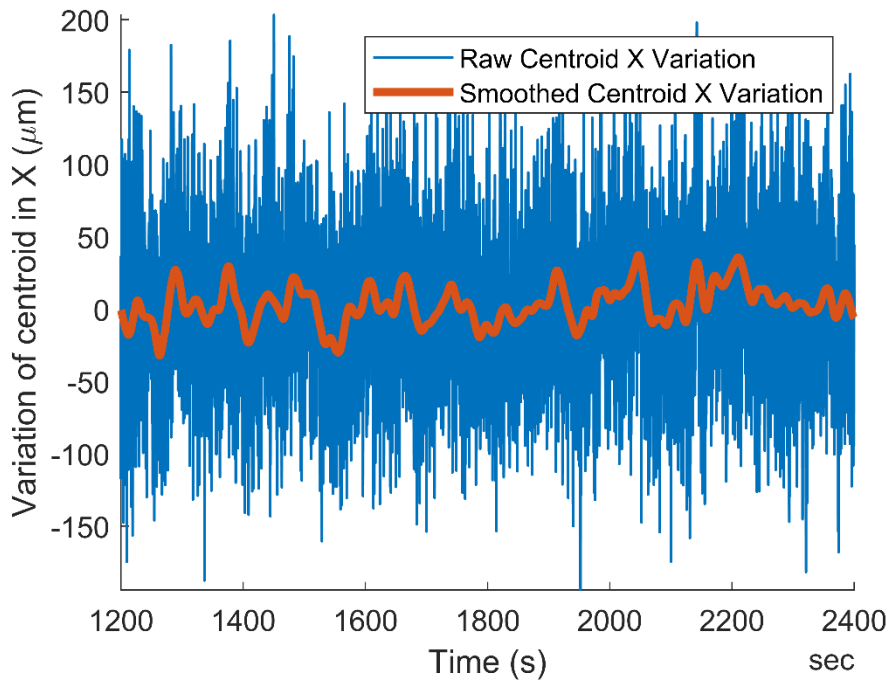


Figure 4-25 20-40 minutes section of variation of centroid position in X with polynomial regression

A second order polynomial regression was fitted to the subsection of data to aid in determining whether there was a periodicity to the variation in the centroid position. This method is susceptible to the sampling criteria defined by the user, as increasing the number of sampling points can excessively smooth the data which can reveal a false trend in the data. A broad range of sampling sizes was applied but no substantial trend was revealed.

4.4.4.1.2 Determining source of instability

There are two components to the pointing stability, angular stability and positional stability. When measuring the stability over long beam paths, the angular stability can be the most significant contribution. The contribution of the angular stability to the overall positional instability can be found by taking a second measurement of the beam with a different length of beam path. Using trigonometry, the change in beam angle leaving the laser can be calculated. The distance for laser aperture to camera for the initial test can be estimated to be approximately 3.2 m. A second 1 hour test was performed using the 1064 nm wavelength with a distance of 1.05 m from the laser aperture to the camera.

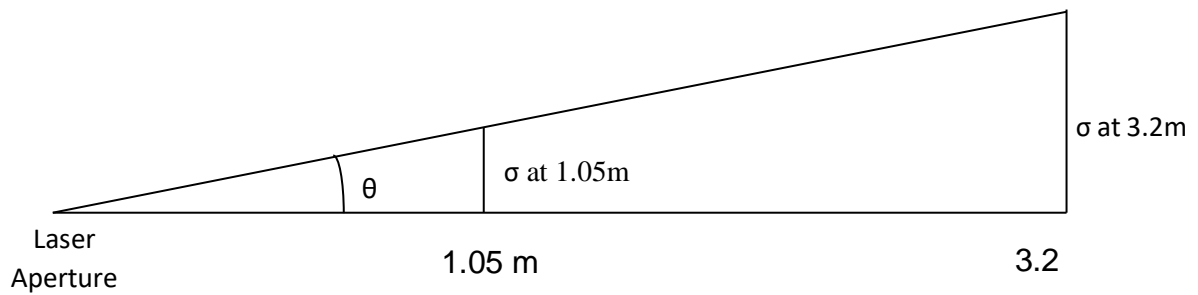


Figure 4-26 Diagram showing relationship between position of camera, measured deviation and angle deviation. Diagram not to scale.

Table 4-13 Comparison of angular stability between two camera positions for 1064 nm

Variable	3.2 m beam path	1.05 m beam path
Centroid X standard deviation (μm)	53.2	17.273
Standard deviation of angular variation in Y Plane (μrads)	16.625	16.450
Centroid Y standard deviation (μm)	60.3	17.034
Standard deviation of angular variation in X Plane (μrads)	18.844	16.228

This method is a rough estimation however it can be suggested that the angular stability is the greatest contribution to the positional stability measured at the equivalent focal lens position. If there was a greater disparity in the standard deviation of the two sets of measurements.

4.4.4.2 Beam diameter stability

From the Talisker laser specifications the minimum beam waist is 2 +/- 0.5 mm. At the objective position the measured beam diameter has diverged to approximately twice this. The variation in beam diameter appears to follow a similar pattern to that shown in the variation in the centroid position. An increase in the beam diameter entering the objective causes a smaller focal spot. The variation in diameter has the greatest effect on focal spot fluence due to the quadratic relationship; to ensure the correct focal spot fluence is maintained this parameter requires high resolution control.

The variation in beam diameter demonstrates a similar profile to the centroid stability, the level of variation appears to stabilise approximately 15 minutes into the test.

4.4.4.3 Power stability

For the power meter used the accuracy is +/- 3% of the measured value, indicating that the accuracy decreases as the laser power increases. Therefore, for the 1064 nm with an average power of 13.2376 W, the accuracy is limited to +/- 0.3971 W. Thus, the noise shown in Figure 4-12 cannot be attributed to variation in the power of the laser. This accuracy limitation is common across all of the power stability tests.

An increase in the accuracy could be achieved by reducing the measured power using a dichroic mirror which has a known transmission and reflection ratio, measuring the low power beam and then calculating the true laser power from this measured value.

4.5 Repeatability of Talisker Laser Power

Using the target fluence per pulse of $>0.6 \text{ J/cm}^2$ which, using the laser at 200 kHz translates to an output power of approximately 10 mW. Therefore, fine power control is required.

This led to several questions:

- What is the repeatability of the power when fired for a series of bursts?
- Which power levels are achievable with the current equipment?
- Are the attenuators repeatable?

Several issues were identified in trying to answer these questions:

First issue:

The power directly from the Talisker depends on the order the attenuator was set. Going from 0% to 50% attenuation gives a different output power than 100% to 50% attenuation. This was solved by building into the attenuator procedure and instruction that, whenever the attenuator changes position it first returns to 100% attenuation before moving to the required value.

Second issue:

The aim was to have a 'lookup' table for power to then set the Talisker attenuator and Watt Pilot attenuator for processing. This is not possible because, as the attenuator in the Talisker changes, this appears to affect the polarisation of the beam. This is an issue because the Watt Pilot attenuator is a polarising attenuator which requires being calibrated to the polarisation of the input beam. Therefore, as the orientation of the polarisation changes, this means the calibration is no longer correct and the linearity of the 0-100% attenuation scale no longer exists. An attempt to negate this has been made by setting the Talisker attenuation, calibrating the Watt Pilot attenuator to that setting and using only the Watt Pilot for power control.

Third issue:

Repeatability of the power output for a series of bursts has been a concern and has yet to be investigated. The difficulty of this is to correctly synchronise the measurement of the bursts when firing occurs. The ability to trigger recording of the beam power when firing has now been integrated giving the ability to carry out these trials.

4.5.1 Interval Exposure Measurements

The first trial was to perform the measurement of 100 10-second bursts with 10 seconds of rest which would be similar to the typical workload for the platform. This was repeated three times with different wait intervals to see whether duty cycle has an effect on the output.

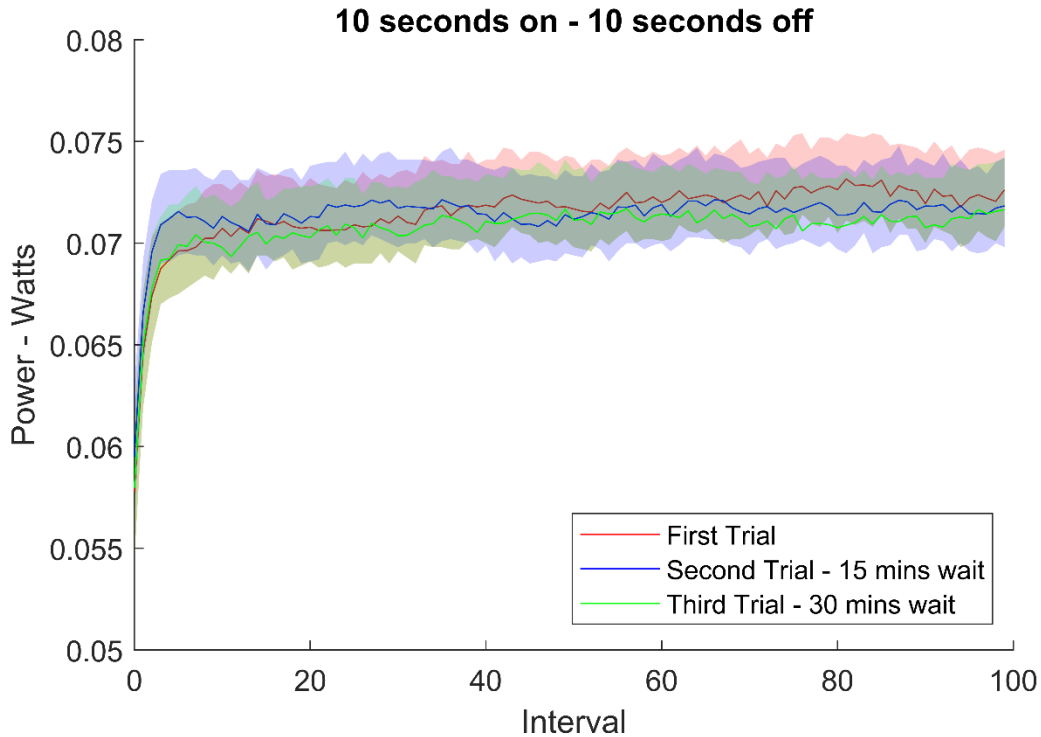


**Figure 4-27 Trial of 10 seconds burst with 10 seconds rest. Red: First trial.
Blue: Second trial with 15 minutes wait from previous trial.
Green: Third trial with 30 mins wait from previous trial**

This test demonstrates a significant rise in the output power in the first 10 intervals before reaching a steadier value. This could be suggestive of thermal effects and an equilibrium being achieved which correlates to the output power.

This led to the investigation of whether the type of workload affected the characteristics of the power output. The following combinations were measured:

Table 4-14 Different duty cycles tested.

Burst Duration (secs)	Rest Duration (secs)	Plot Colour
10	30	Pink
30	10	Blue
10	Random (5-30)	Green
Random (5-30)	10	Turquoise
Random (5-30)	Random (5-30)	Red

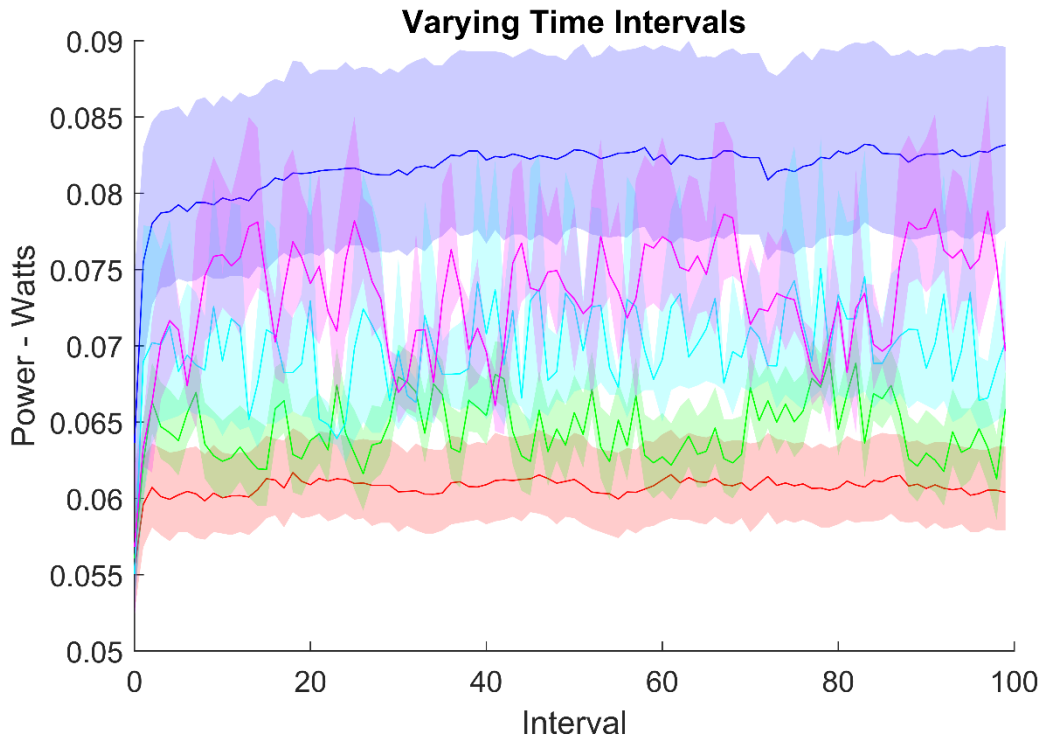


Figure 4-28 Plot of variation in power output for different duty cycles.

The graph above demonstrates that the workload can greatly affect the beam power that reaches the focusing objective. Due to the observed instability, the characteristics of the acoustic optical modulator (AOM) were investigated to determine whether this was a source of error and the impact could be reduced. The next test involved leaving the laser with the AOM set to not fire the laser for roughly 15-20 minutes, opening the shutter without the laser being fired and then setting the AOM to fire and recording the output.

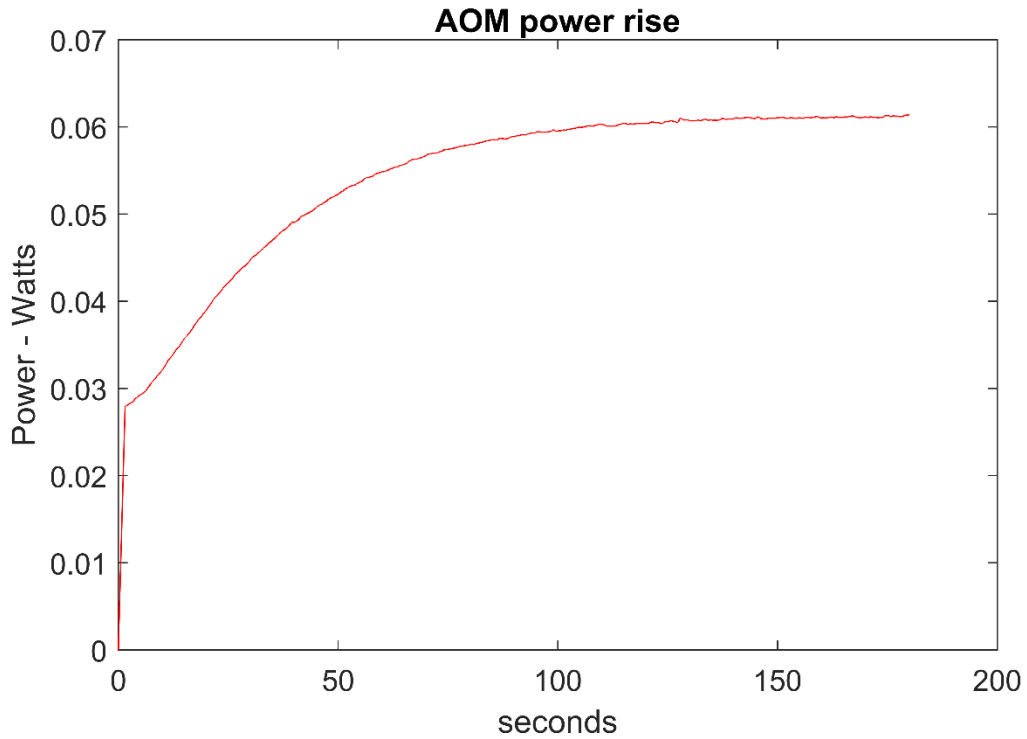


Figure 4-29 Plot showing variation in power rise from source after triggering.

It is apparent that the frequency of use of the AOM can affect the output power of the laser which is not desirable for a precision machining tool. Initially this result felt to be false and it was thought that there was an issue with the recording method or the equipment. However, following a check using a second power meter, this was found to be a true reading.

To see whether this can be negated a test was performed using a 'warm up' period of three minutes where the laser is fired but the shutter remains closed. This gives the following result:

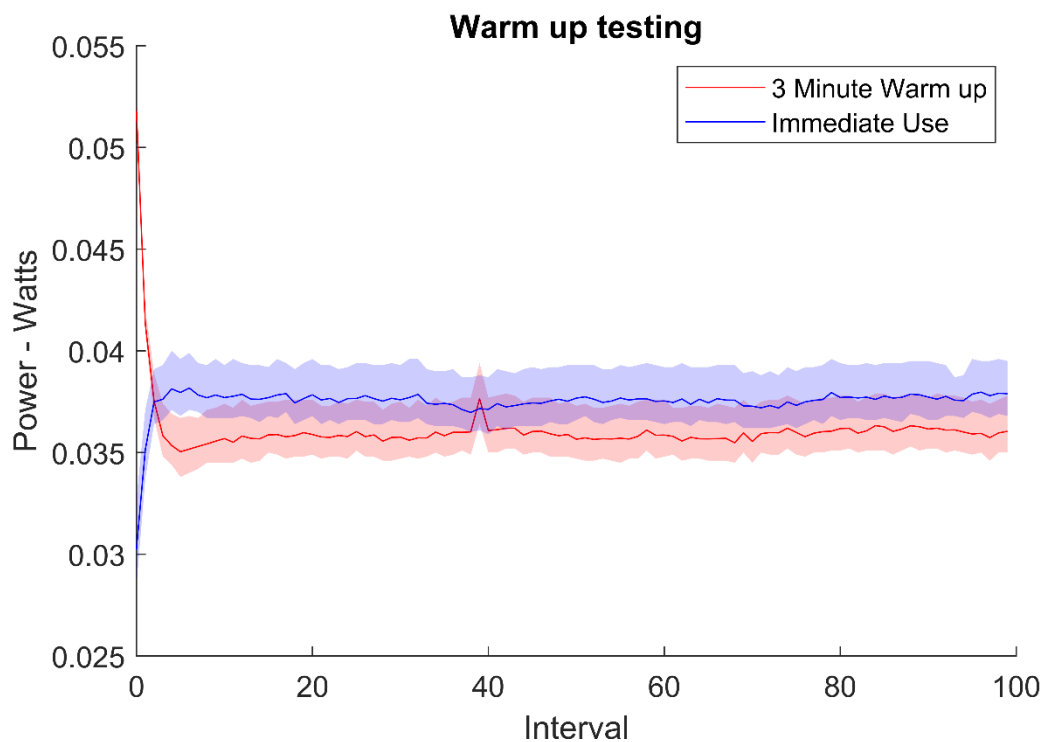


Figure 4-30 Plot showing different warm up strategies and the effect on power output. Red: Three minute warm up. Blue: Immediate use.

This suggests that the 'warm up' period may need to be tailored to the required output power. So, rather than a 3 minute period, 1-minute maybe more suitable as the final burst power doesn't settle at the fully 'warm' state. This would need further testing or the integration of active power control.

Fortunately, through the investigation of this part of the system, the ability to log power whilst processing is now possible, improving accuracy for the calculation of the ablation threshold for silicon.

4.6 Modelling of Stability Effects on Track Machining

To achieve high-quality laser machining, suitable operating parameters should be selected to achieve the accuracy required. This is determined by the fluence at the focal spot. The laser fluence of the energy density of the beam is determined by:

$$F_{Abs} = \frac{P/r}{\pi * w_0^2} \quad (4-1)$$

$P = Power$, $r = repetition\ rate$, $w_0 = focal\ spot\ radius$

The focal spot diameter is determined by the following equation:

$$2w_0 = \left(\frac{4\lambda}{\pi}\right) \left(\frac{f}{D}\right) \quad (4-2)$$

$\lambda = wavelength$, $f = Focal\ Length$, $D = Raw\ Beam\ Diameter$

A critical property affecting the fluence at the focal spot is the variation in beam diameter. The fluence at the focal spot is related to all of the measured properties by the following equation:

$$F_{Abs} = \frac{E}{\pi * w_0^2} = \frac{P/r}{\pi \left[\left(\frac{2\lambda}{\pi}\right) \left(\frac{f}{D}\right)\right]^2} \quad (4-3)$$

By taking the raw data from the laser stability tests, a simulation can be created to assess the implications of the variation of beam diameter, centroid position and power on machining a simple straight trench.

The simulation uses some parameters common to the experimental setups following later. The simulation uses the ThorLabs LMH-5X-1064 for the focusing objective, and the recorded beam stability data for 1064 nm. However, several assumptions were made to make the simulation computationally possible. Further issues with these assumptions will be outlined later.

For this simulation, the following parameters were used:

- Maximum milled depth per pulse = 50 nm
- Linear relationship for milled depth between threshold fluence and maximum fluence
- Sample is moving at 1 mm/s
- Focal length of lens = 40 mm
- Threshold fluence = mean of calculated focal spot fluence

The data used for the model was recorded with the following parameters:

- Wavelength = 1064 nm
- Repetition rate = 200 kHz
- Power = Maximum – As recorded in stability test

4.6.1 Simulation Results

4.6.1.1 Overall view of simulated trench

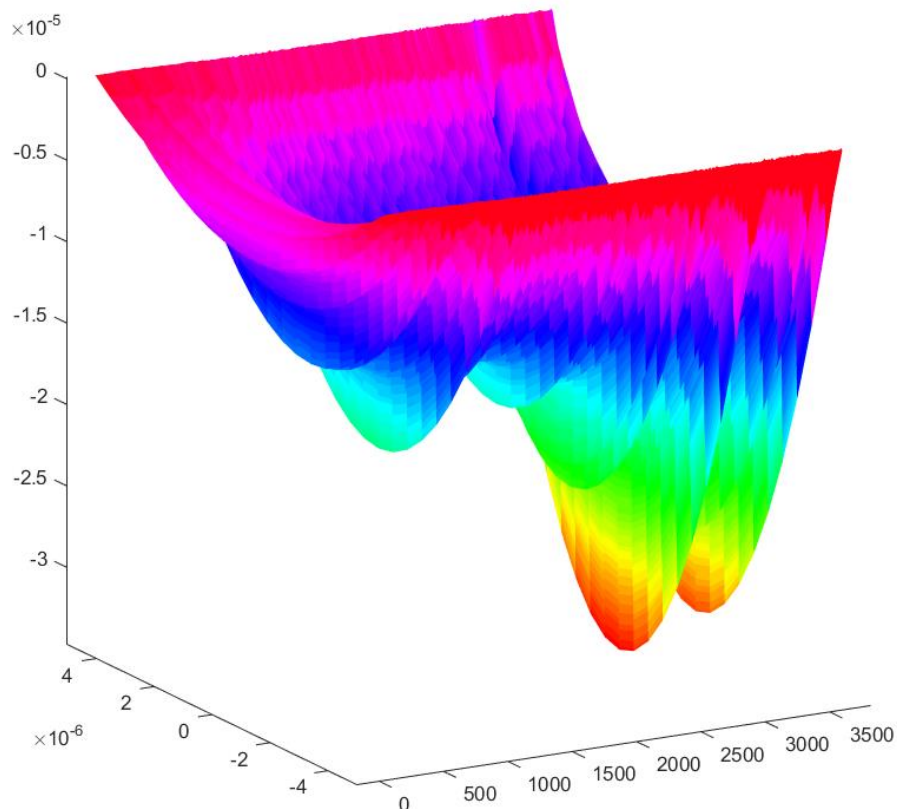


Figure 4-31 3D representation of simulated machining.

This three-dimensional representation of a trench shows that there is significant variation in the depth milled over the length of the track. A two-dimensional cross-sectional plot shows the following:

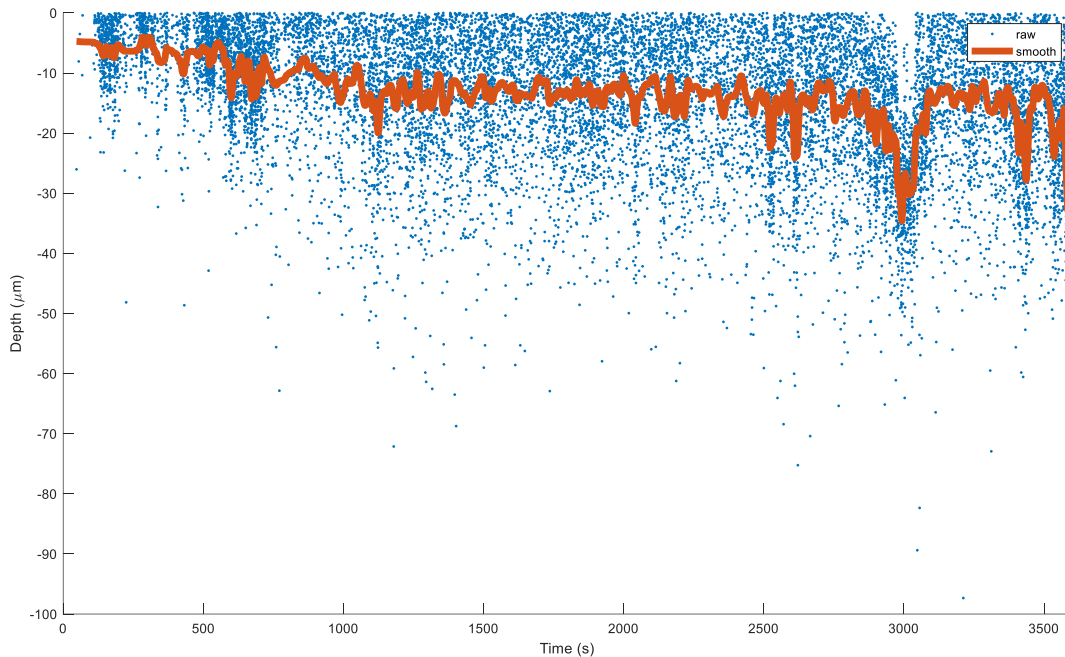


Figure 4-32 Variation in track depth of simulated machining.
Red line: Smoothed average of raw data.

The points in blue indicate when the fluence of the focal spot is greater than the threshold fluence of the material and has therefore ablated material. A smoothing curve was fitted to give a representation of the true trench profile.

At approximately the 3000 second mark the depth milled significantly increases and this can be correlated with changes in beam parameters shown in the raw data.

Two other areas to be assessed are the overall trench width and trench edge quality. The following figure shows an overall view of the milled trench. Blue indicates points where the fluence of the focal spot is greater than the threshold fluence of the material, red indicates when fluence is less than threshold fluence and green is a smoothed average of the above threshold points.

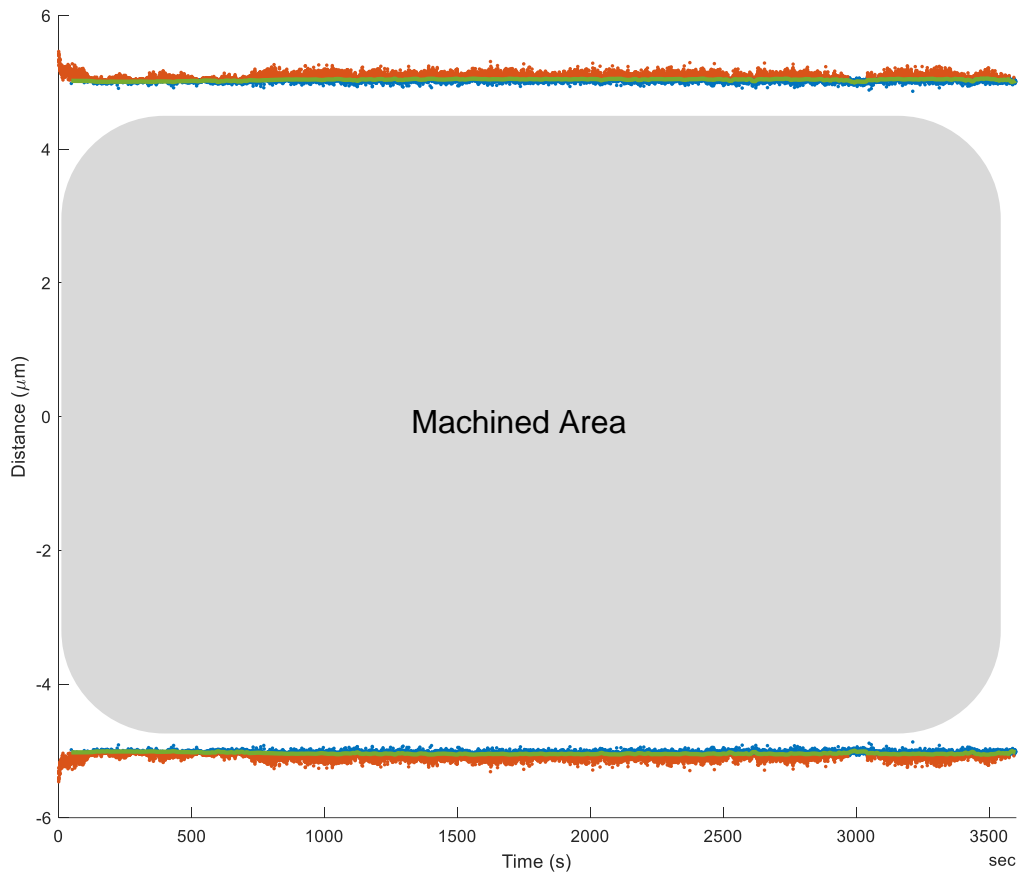


Figure 4-33 Top down view of simulated trench.

Blue: Data points above ablation threshold.

Red: Data points below ablation threshold.

Green: smoothed average of the above threshold points.

From this the simulated trench has an approximate track width of 11 μm . The track edges have significant variation by inspecting a micro section of the plot showing the spread of data points above and below the ablation threshold. Of the points greater than the ablation threshold the deviation is 0.227 μm .

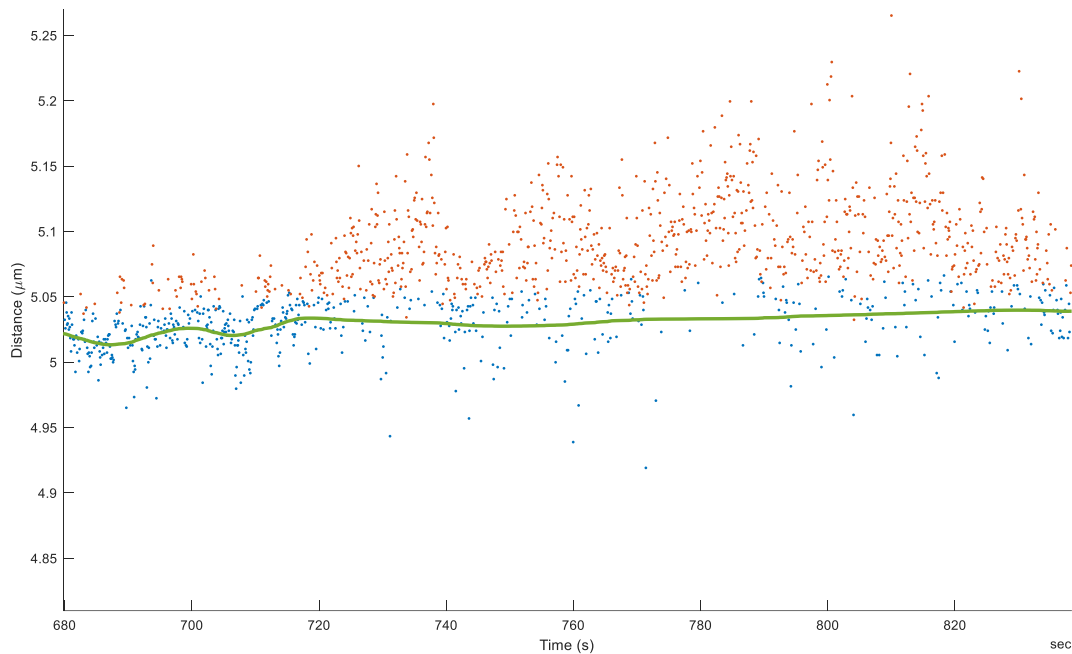


Figure 4-34 Macro view of the edge of simulated trench.

This model assumes that the beam profile is uniform whereas in real experimental trials a Gaussian profile is used which means that there may still be a region within the focal spot which has a fluence greater than the threshold fluence. The model doesn't consider incubation effects and other factors which have been identified in section 2.4. Another simplification that was applied was to only consider the variance of the centroid position of the beam perpendicular to the track direction. Furthermore, due to acquisition rate of the data being lower than the repetition rate of the laser, a scaling has had to be applied.

This model demonstrates how the variation in the measured beam parameters can affect the milled geometry. This model could be improved through higher data acquisition rates which could be recorded performing a milling operation so the simulated results can be compared to the real three-dimensional geometry. This could be developed into a feedforward control when closed-loop processing is carried out.

4.7 Summary

The critical property affecting the fluence of the focal spot is the variation in beam diameter. The fluence at the focal spot is related to all of the measured properties by the following equation:

$$F_{Abs} = \frac{E}{\pi * w_0^2} = \frac{P/r}{\pi \left[\left(\frac{2\lambda}{\pi} \right) \left(\frac{f}{D} \right) \right]^2} \quad (4-4)$$

It has been shown that the current experimental setup is susceptible to instability for both beam diameter and power delivery. This has been tested over both long one-hour durations and short intervals. Depending on the duty cycle undertaken this can affect the level of instability in the power output of the laser. There are suggestions that this is due to thermal effects, but this could not be monitored without modification to the laser. Comparisons have been made between the three available wavelengths to determine which is more stable. It is apparent that, for the shorter wavelength, the effect of frequency doubling of the source 1064 nm laser causes greater instability, possibly due to more optics being introduced to frequency double the laser to the achieve the shorter wavelength.

An important consideration is the fact that the platform has a wide range of applications which, in turn, means the length of the duty cycle can vary significantly. Some applications will require single pulse control and others will perform long continuous operations. This makes it difficult to determine the overall effect on machining without further engineering and experimentation.

Through simulation it has been demonstrated how laser instability can affect machining accuracy in terms of machined depth and edge fidelity. The implication of this instability is a reduction in the ability of the platform to carry out precise machining. A solution would be the use of closed-loop control to produce a more stable focal spot position and fluence at the focal spot.

It should be noted that on a laser platform the level of magnification by the focusing objective can be configured. This can increase or decrease the effects of the laser stability on the focal spot stability and intern the process stability. Therefore, through this investigation it has been identified that a factor which needs to be considered is what is the acceptable level of stability for the application. This could be whether the process is more sensitive to the geometric stability of the laser or the power variation which

could then be used to determine the type and magnitude of the focusing objective selected.

5 Laser ablation of silicon at varying incident angles

With lasers being used in manufacturing becoming commonplace, any techniques that could improve accuracy, repeatability and throughput deserve investigation. Micro-machining using ultrafast laser pulses is a significant area of development due to their reduced cost and simplicity in recent years. Ultrafast lasers have been of significant interest due to the potential for precise machining in a wide variety of materials. Silicon is widely used in the semi-conductor industry and is a material that has been studied in detail. Trials for silicon ablation are typically performed with the laser normal to the silicon target. In this arrangement laser pulses must pass through the plume generated by ablation which could affect the laser pulse due to the change in density and refractive index. It is unknown whether changing of the incident angle on the substrate changes the plume formation and the implications for precise machining deserve further study.

There are several factors which contribute to the variance in the ablation threshold:

- Defects
- Thermal effects
- Changes in stoichiometry
- Non-equilibrium effects
- Plasma shielding

An investigative point of this work is to determine whether an angular approach to machining using an ultrafast laser can reduce the variance of these effects. The factor that changing to an angular approach is believed to tackle most significantly is plasma shielding, as the laser pulse is assumed to be less likely to interact with the generated plume as the pulse is no longer required to travel through the plasma/plume to reach the substrate.

In this section the effect of incident angle on silicon ablation is investigated. The laser source is a 10 ps pulse duration near infra-red (1064 nm) 200 kHz laser with the incident angle varied between normal and 45 degrees. Trials are performed to correlate the change in incident angle with ablation threshold of the material. The relationship between angle, pulse energy and plume formation is then analysed through the use of a high-speed holographic camera.

5.1 Effect of angle on ablation threshold

The ablation threshold is defined as the minimum laser pulse fluence required to remove material. It is advantageous to machine close to the ablation threshold of the material because this reduces recast and the size of the heat-affected zone where undesirable form and surface roughness may occur.

Typically, the ablation threshold of the material is found by drilling a hole and measuring the ablated radius. This method is suitable to give a rough estimate of the threshold however, with the machining target in mind, it is best to look at the 'in process' ablation threshold rather than the 'steady state' threshold.

As identified in section 2.3.2 there are three 'in process' parameters which contribute to the final machining: pulse energy, repetition rate and feed rate. In typical ablation threshold literature where the hole radius method is used, little justification is given for the repetition rate chosen and the number of pulses used. Consequently, although the ablation thresholds presented in papers are advertised as the general ablation threshold, the ablation threshold found is only for that specific setup, making it difficult to transfer parameter combinations between experimental setups.

5.1.1 Material Used

Silicon, N<100> p-doped, was selected for investigation due to its wide application in the production of 2.5D or 3D MEMS devices. This crystal orientation reduces the effect of machining direction on the process as the absorption of the beam is not affected by laser polarisation.

5.1.2 Experimental Method

The silicon substrate was machined with a pulse duration of 10 ps, a repetition rate of 200 kHz at 1064 nm. The feed rate was set at 1 mm/s and is common to all experiments performed.

The beam was configured to be circularly polarised to remove any effects from the orientation of the polarisation on the machining process, hopefully removing, any signs of laser-induced periodic surface structures. Secondly, the laser can couple with the material differently depending on the crystal orientation and polarisation of the light. Therefore, silicon with an orientation of <100> p doped was used as this should mean the results are consistent for any machining direction.

The raw beam diameter was measured using a Spiricon beam profiling camera and was measured to be 5.34 mm in diameter. A 5X focusing objective was used with an effective focal length of 40mm, giving a focal spot diameter of approximately 10 μm .

Table 5-1 Specifications of LMH-5X-1064 Objective

Item	M ^b	WD	EFL	PFL	NA	EA	OFN	Spot Size
LMH-5X-1064	5X	35 mm	40 mm	58.9 mm	0.13	9.9 mm	12	7.8 μm

M = Magnification, WD = Working Distance, EFL = Effective Focal Length, PFL = Parfocal Length, NA = Numerical Aperture, EA = Entrance Aperture, OFN = Optical Field Number, Spot Size = Diffraction Limited, Measured at 1064 nm.

The method was adjusted to measure the width of ablated tracks rather than the radius of a hole because in real applications the ablation threshold of a track is more applicable when machining MEMS or similar devices.

The ablation threshold will be found for the following angles: normal, 15, 30 and 45 degrees. A 1 mm track will be machined with the track width recorded at the midpoint of the track to reduce any effects from the stage accelerating and decelerating.

5.1.3 Experimental Results

The maximum laser fluence must exceed a threshold value to initiate modification to the substrate surface and ablation. The tracks are measured using a calibrated Olympus BX51 optical microscope and recorded with the correlating beam power.

Below are examples of tracks machined at different beam powers and incident angles.

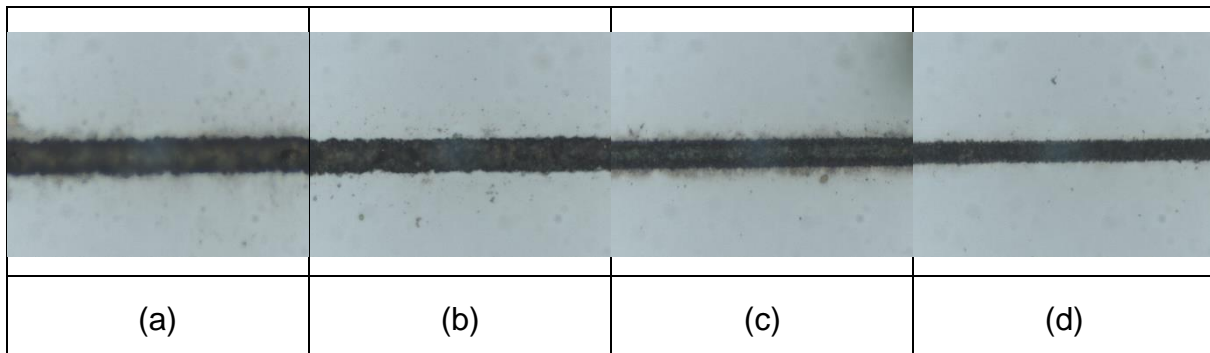
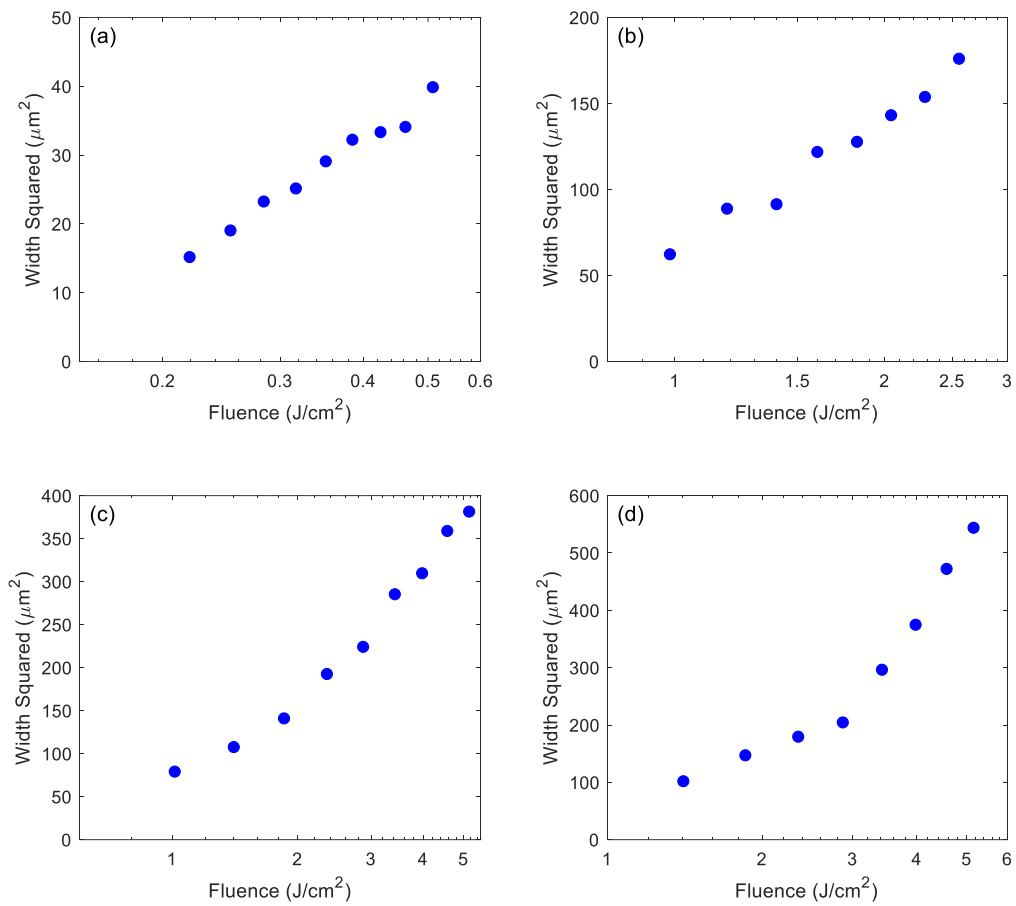


Figure 5-1 Examples of machined tracks captured with BX51 microscope. All tracks are at normal incidence – 0 degrees. Incident powers for tracks are a) 84.1 mW b) 70.2 mW c) 52.4 mW d) 36.3 mW

At larger incident powers some areas are cloudy and thermal effects can be seen on the edges of the ablated tracks. This is examined further in section 5.2.

Figure 5-2 shows the calculated focal spot fluence against measured machined track width squared for different incident angles.



**Figure 5-2 Plots of measured track width squared versus focal spot fluence.
a) 0 degrees b) 15 degrees c) 30 degrees d) 45 degrees**

5.1.4 Analysis

A common approach for calculating the ablation threshold is that given by Lui [125] where the relation between ablated radius is measured over a range of pulse energies. This relationship is governed by the following equation,

$$r_{abl}^2 = \frac{c^2}{2} \ln\left(\frac{F_0}{F_{th}}\right) = \frac{c^2}{2} \left[\ln\left(\frac{2E}{\pi c^2}\right) - \ln(F_{th}) \right] \quad (5-1)$$

where r_{abl} is the ablated radius, c is the focal spot diameter, F_0 and F_{th} are the peak fluence of the laser pulse and the ablation threshold fluence, respectively by measuring the pulse energy, E , and the ablated radius the equation can be rearranged to solve for the ablation threshold.

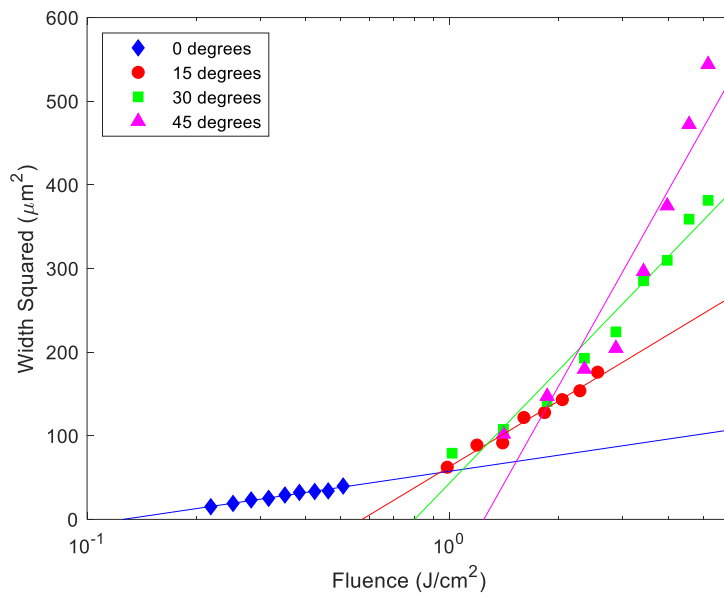


Figure 5-3 Plot of track width against laser fluence at different angles

Table 5-2 Ablation threshold at different incident angles.

Angle / deg	Ablation Threshold / J/cm ²
0	0.1257
15	0.5730
30	0.7995
45	1.2415

There is a clear correlation that an increase in incident angle leads to an increase in the ablation threshold. There are two obvious factors which influence this correlation which are the change in the effective focal spot size and losses due to increased reflection. It is of interest to know whether when applying corrections for these losses the ablation threshold is constant at all incident angles.

5.1.4.1 Focal Spot Area Correction

In Figure 5-3 it has been assumed that the focal spot on the material is the same for every angle of incidence. In reality, this is not the case, therefore a correction should be made for the projected ellipse. The relationship for beam profile against angle is given by:

$$\text{corrected diameter} = \frac{\text{normal diameter}}{\cos \theta} \quad (5-2)$$

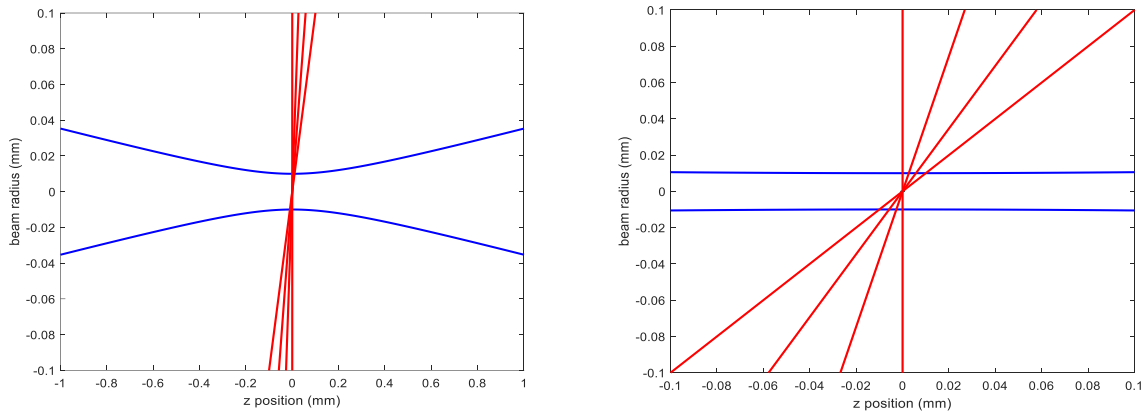


Figure 5-4 Visualization of the effect of sample angle on focal spot cross section. Blue Line shows focusing beam profile. Red Line indicates intersection with sample. Left: Overall view. Right: Zoom view.

Below is a plot of the change in energy distribution against angle for the Gaussian beam and the change in focal spot radius with angle.

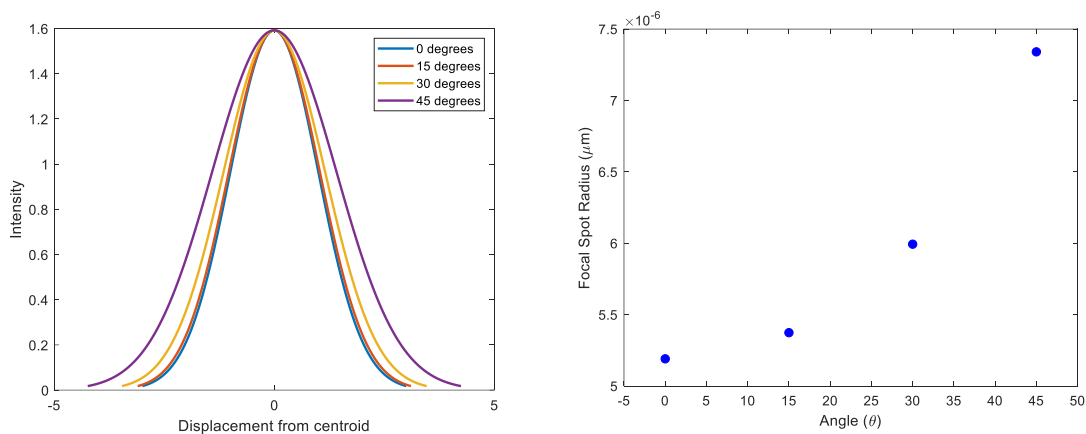


Figure 5-5 Left: Simulation of the effect of angle on Gaussian intensity profile. Right: Plot of focal spot radius versus incidence angle.

5.1.4.2 Losses due to Reflection

A second factor to be accounted for is the variance in reflectance at different incident angles. Using Snell's Law and Fresnel's equations, a plot for absorption of the different polarisations of light at different angles of incidence for Silicon can be obtained. Absorption, A, is the difference between the incident flux and the reflected flux. The refractive index for Silicon, n_2 is 3.56223 and the refractive index for air, n_1 , is 1.

$$\frac{\sin \theta_i}{\sin \theta_t} = \frac{n_2}{n_1} \quad R_s = \left| \frac{n_1 \cos \theta_i - n_2 \cos \theta_t}{n_1 \cos \theta_i + n_2 \cos \theta_t} \right|^2 \quad R_p = \left| \frac{n_1 \cos \theta_t - n_2 \cos \theta_i}{n_1 \cos \theta_t + n_2 \cos \theta_i} \right|^2 \quad (5-3)$$

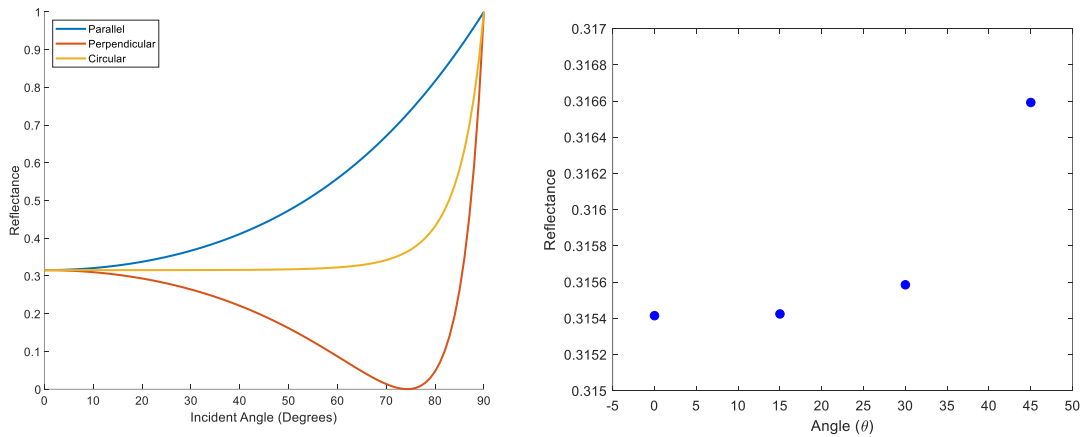


Figure 5-6 Left: Overview of Reflectance versus incident angle for 0 to 90 Degrees
Right: Zoomed in to show change in reflectance for 0 to 45 Degrees

To account for the losses due to reflection the following equation has been applied,

$$F_\theta = F_0 \cos \theta * \frac{(1 - R_\theta)}{(1 - R_0)} * \cos \theta \quad (5-4)$$

where F_θ is the fluence at the focal spot when accounting for losses due to increased area and increased reflection. F_0 is the calculated fluence normal to the sample. θ is the incident angle. R_0 and R_θ are the reflection coefficients for the material at normal and the incident angle.

Applying this correction to the experimental data gives the following plot for focal spot fluence versus track width squared and plotting incident angle versus ablation threshold is as follows:

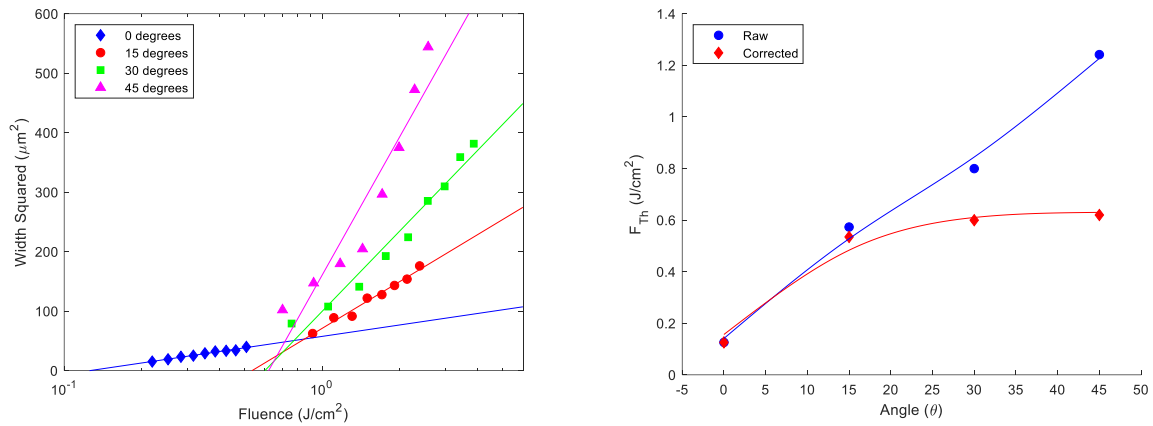


Figure 5-7 Left: Plot of track width squared corrected versus fluence.

Right: Plot of adjusted threshold fluence versus angle.

Table 5-3 Focal spot area, reflectance, ablation threshold and adjusted ablation threshold for different incident angles

Angle / deg	Focal Spot Area / cm ²	R_{θ}	Threshold Fluence F_{Th} / J/cm ²	Adjusted Threshold Fluence $F_{\theta Th}$ / J/cm ²
0	8.2737x10 ⁻⁷	0.31541	0.1257	0.1257
15	8.5656x10 ⁻⁷	0.31542	0.5730	0.5346
30	9.5537x10 ⁻⁷	0.31559	0.7995	0.5995
45	1.1701 x10 ⁻⁶	0.31659	1.2415	0.6197

5.1.5 Discussion

It can be seen from Figure 5-7 that applying the correction to the ablation threshold gives an ablation threshold of approximately 0.6 J/cm^2 when the laser isn't normal to the surface of the material. It is of interest that the correction does not have an effect on the ablation threshold when normal to the surface and there are a couple of possible reasons for this:

1. The absorption coefficient of the material varies with incident angle. From the data it could be suggested that the absorption coefficient reduces with an increase in incident angle.
2. It is well-documented that the absorption coefficient changes significantly with temperature and as shown by Figure 5-6 the closer to normal the tighter the Gaussian intensity profile which means a higher fluence for the same pulse energy. Consequently, there is increased localised heating which increases the absorption coefficient and thus reduces the required energy from the laser to cause ablation.
3. At normal the laser must travel through the plasma generated by the previous pulse. This could lead to a sustained plasma which aids ablation and reduces the pulse energy required. This effect would be reduced as the laser departs from the normal and interaction with the plume diminishes or even disappears.

To surmise Figure 5-7 indicates that there is a pulse-plume interaction which occurs and attenuates the energy of the pulse at normal incidence and cannot be accounted for using geometric and optical corrections. Evidence for this attenuation should be looked for on the effect of the tracks machined by the process.

5.2 Effect of Angle on Track Fidelity

One area of interest is the effect of changing incident angle on track fidelity.

Due to using the same focusing objective for every trial the minimum effective focal spot size is affected by the incident angle. At higher incident angles the minimum spot size will be larger.

Therefore, tracks of similar widths machined at different angles will be compared to investigate how the edge of the track is affected.

5.2.1 Experimental Results

From the ablation trials the widest zero-degree track was at 12.6 μm and larger tracks were not measured as from the researcher's experience the heat-affected zone and recast become a problem when moving to the higher fluences which would be needed to increase the ablated track above this width.

The 15-, 30- and 45-degree samples exhibit comparable track widths at approximately 20, 24 and 27 μm . The following analysis technique was applied:

1. Capture image of track using BX51 microscope.
2. Apply binary threshold to image to simplify identifying ablated track.
3. Sum pixels along the horizontal axis of the image.
4. Plot sum of pixels and identify the minimum and maximum track width. The minimum track width is defined as the region where the track is consistent. The maximum track width is defined as the largest distance in the vertical axis between machined edges.
5. Calculate the minimum-maximum ratio for the track. An ideal track will have a minimum-maximum ratio equal to 1.

Minimum-maximum ratio (MMR):

$$MMR = \frac{\textit{Minimum Track Width}}{\textit{Maximum Track Width}} \quad (5-5)$$

Figure 5-8 shows the analysis outline above:



Figure 5-8 Nominal 27 μm Track at 45 degrees. Left: Microscope Image

Centre: Threshold Image

Right: Plot of horizontal sum of pixels. Red lines indicate maximum width. Green lines indicate minimum width.

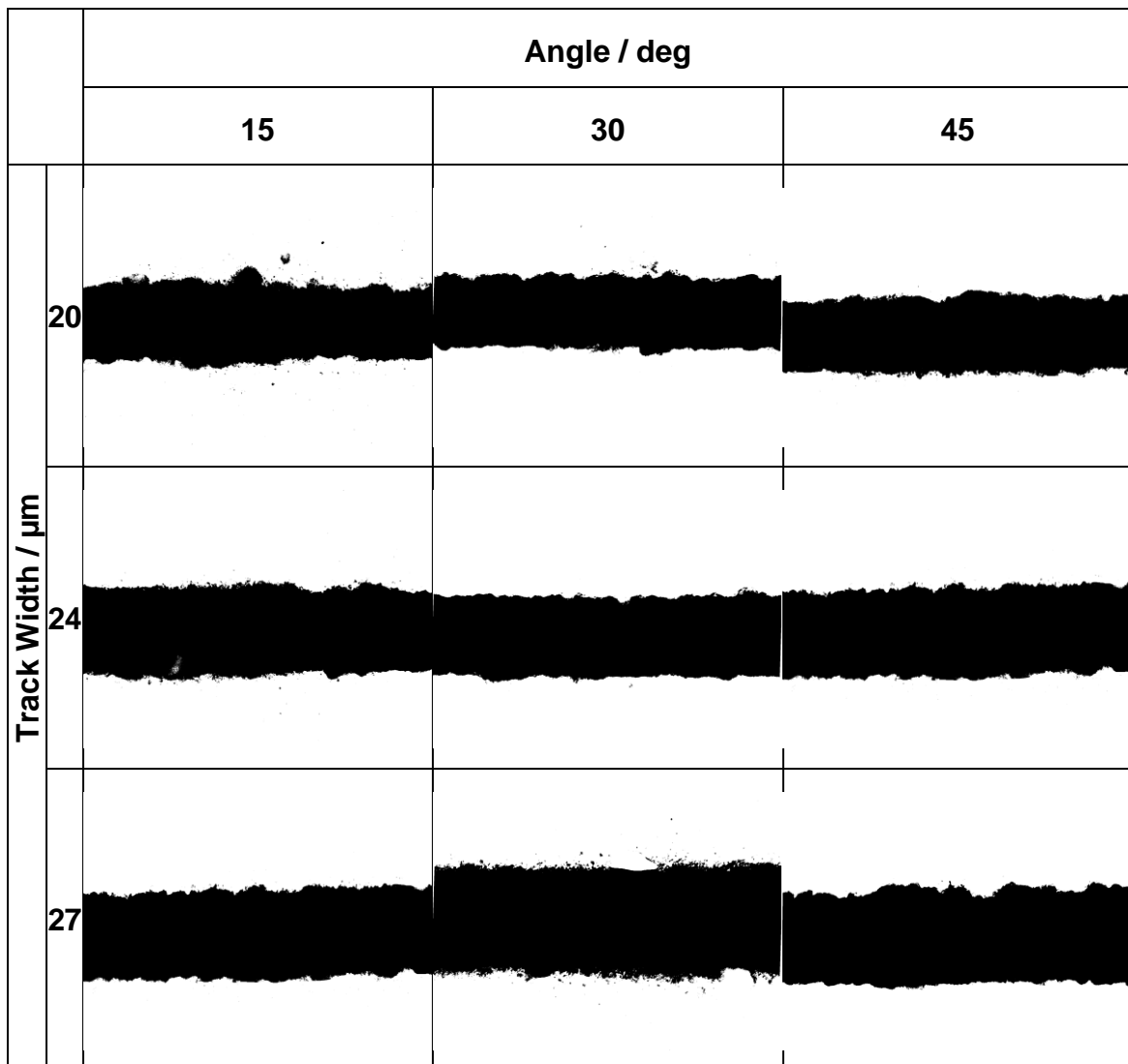


Figure 5-9 Threshold Images for ablated tracks

5.2.2 Analysis

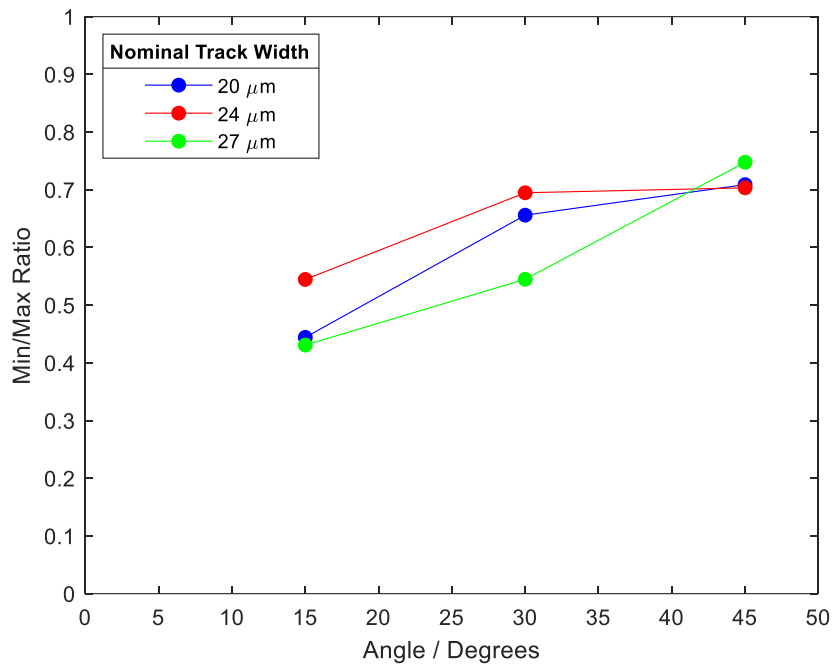


Figure 5-10 Plot of minimum-maximum track width ratio versus angle

Table 5-4 Values for calculated minimum-maximum track width ratio

		Angle / deg		
		15	30	45
Track Width / μm	20	0.4442	0.6559	0.7089
	24	0.5446	0.6948	0.7033
	27	0.4308	0.5448	0.7477

It is clear to see that when increasing the incident angle to achieve the same track width the minimum-maximum ratio (MMR) increases. Surprisingly, the greatest improvement is from 15 to 30 degrees with only a marginal improvement when machining at 45 degrees.

One factor to consider as a possible cause of the improved MMR is that the effective fluence is lower at a higher angle and therefore closer to the ablation threshold meaning a reduced heat-affected zone, melt regions, and recast.

5.2.3 Discussion

Figure 5-10 correlates with the suggestion in section 5.1.5 that there is a pulse-plume interaction occurring which causes the ablation process to be more unstable at incident angles closer to normal. Thus, how the plume forms at different fluences and incident angles should be inspected to corroborate this theory.

5.3 Plume Formation for Varying Incident Angles and Laser Parameters

As it has been established that the material ablation threshold correlates with incident angle, it is of interest to see how this affects plume generation during machining. The state of the plume can be used to learn about the ablative process that the material is undergoing. Another point to investigate is whether a plume appears to form directly after the first pulse, or whether a sequence of pulses is required. By taking regular snapshots of the plume using the holographic camera the evolution of the plume over a number of pulses can be recorded.

5.3.1 Experimental Setup

The setup for holographic imaging is explained in section 3.3.1.1.

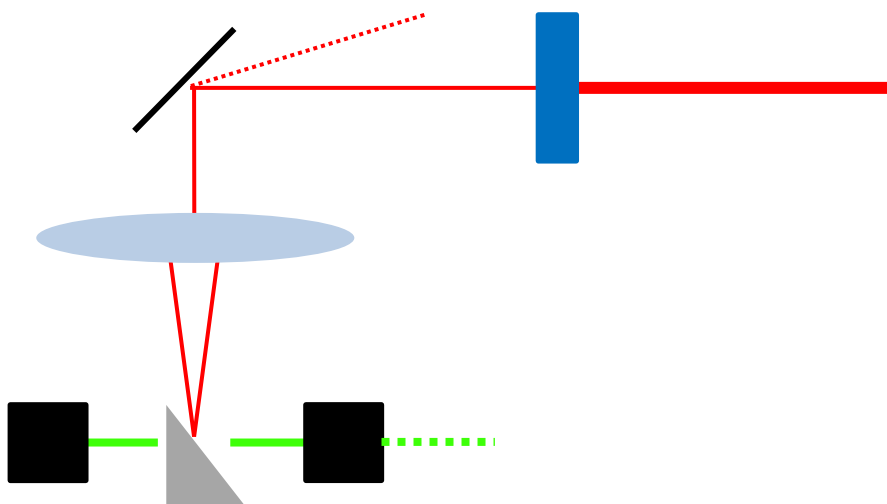


Figure 5-11 Schematic of arrangement for holographic camera trials.

The following equipment was used:

- LMH-5X-1064 Focusing Objective
- Talisker Ultra laser system – 1064 nm
- Holographic camera
- Inline camera

The arrangement for each angle used in the holographic camera trials is shown in Figure 5-12. The red arrow indicates the position of the incident ultrafast laser. The blue arrow indicates the assumed direction of the plume generated from ablation. The dashed green rectangle resembles the FOV of the holographic camera.

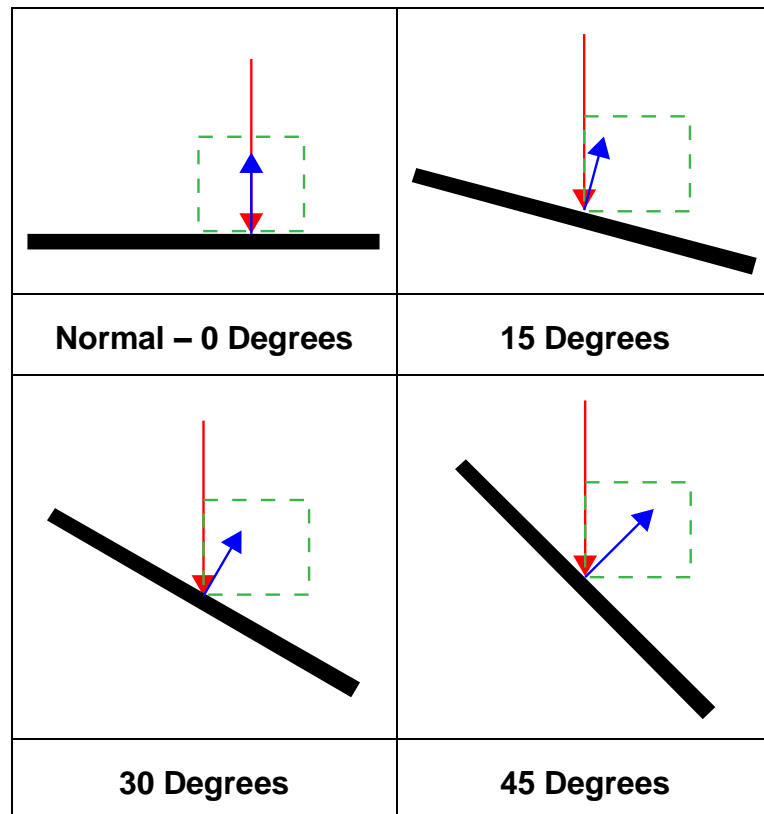


Figure 5-12 Schematic of laser and FOV orientation for holographic camera trails

5.3.2 Methodology

The parameter space identified five key variables that could be investigated which were:

- Number of Pulses
- Capture Frequency
- Overall Capture Duration
- Angle
- Pulse Energy / Beam Power

Previous sequential holographic captures have been carried out in the nanosecond domain and have been interested in the interaction of a single pulse with the substrate. However, in the present investigation the longer-term plume dynamics are of more interest, which led to the choice of capturing the first millisecond of ablation. This duration was chosen because, although the machining point is static in this case, it

could offer a close approximation in the event that a significantly slow feed-rate was being used in a real machining application. In previous ablation threshold trials a repetition rate of 200 kHz was used therefore it is logical to continue further investigation with this. From this it was determined that the camera sampling frequency should match the frequency of the laser so the evolution per pulse could be monitored.

The first angles selected for investigation were normal and at 45 degrees as these were the most critical cases for determining the effect of angle on the plume dynamics. Experiments were then performed at 15 & 30 degrees to try to determine whether there was any mathematical relationship and to obtain a clearer picture.

Initially attempts were made to capture sequences close to the ablation threshold of the material as it is presumed this is the regime in which the most ultra-precise machining would be performed. Unfortunately, the camera lacked the ability to resolve the plumes forming in this regime both in terms of pixel resolution and contrast. Limitations were also found from laser power being too high and overexposing the image. Also, when trying to adjust relative fluence at the focal spot with angle, the ceiling of maximum output from the laser was reached. This led to a slightly erratic parameter sweep of power in order to view plume evolution at different power and angle.

To summarize the above:

- Laser repetition rate = 200 kHz
- Capture Frequency = 200 kHz
- Overall capture duration = 1 ms
- Angles and average power combinations are shown in Table 5-5

Table 5-5 Different angle and power combinations captured.

		Average Power (W)					
Angle (Degrees)	0	0.539	1.324	2.655	3.983	5.770	
	15	0.326	1.628	4.070	8.140	11.600	
	30	0.334	1.67	4.175	8.350	11.600	
	45	0.312	1.558	3.895	5.770	7.790	11.685

As noted in section 3.3.1.1.5, the field of view for the images is 878 μm wide by 660 μm high.

5.3.3 Limitations

There are two significant limitations on the method used to capture this data set.

- Ideally the camera would have been able to capture the holographic image whilst moving the sample to get a true representation of the plume when undergoing line machining. However, due to the technique requiring the use of a reference frame that is captured before processing, the field of view for the camera must remain constant. If the sample were to move this would mean the reference frame does not match with the acquisition frame and this would lead to resolving an incorrect phase image.
- There is a significant challenge in aligning the field of view for the camera. For the camera to function correctly there must not be any static objects in the field of view such as the fixturing or the substrate. This has the consequence that, for the experiments with a significant incident angle, the actual ablation point may be slightly out of the field of view. Secondly, having static objects in the field of view can lead to noise or interference which can affect the internal scaling (ratio of black to white) of the images and could lead to detail being lost.

5.3.4 Holographic Images of Plume Development

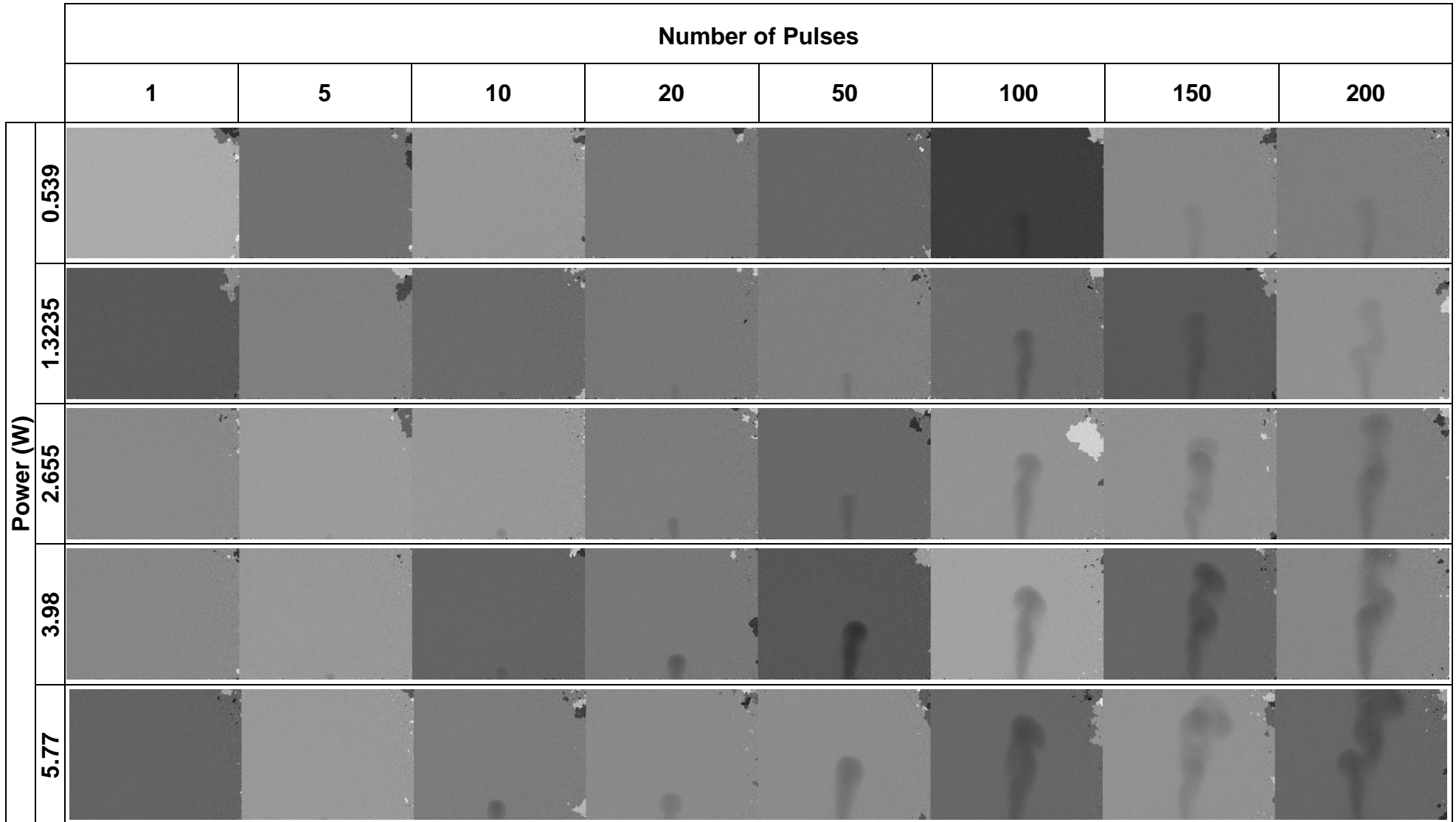


Figure 5-13 Incident angle from normal = 0 Degrees

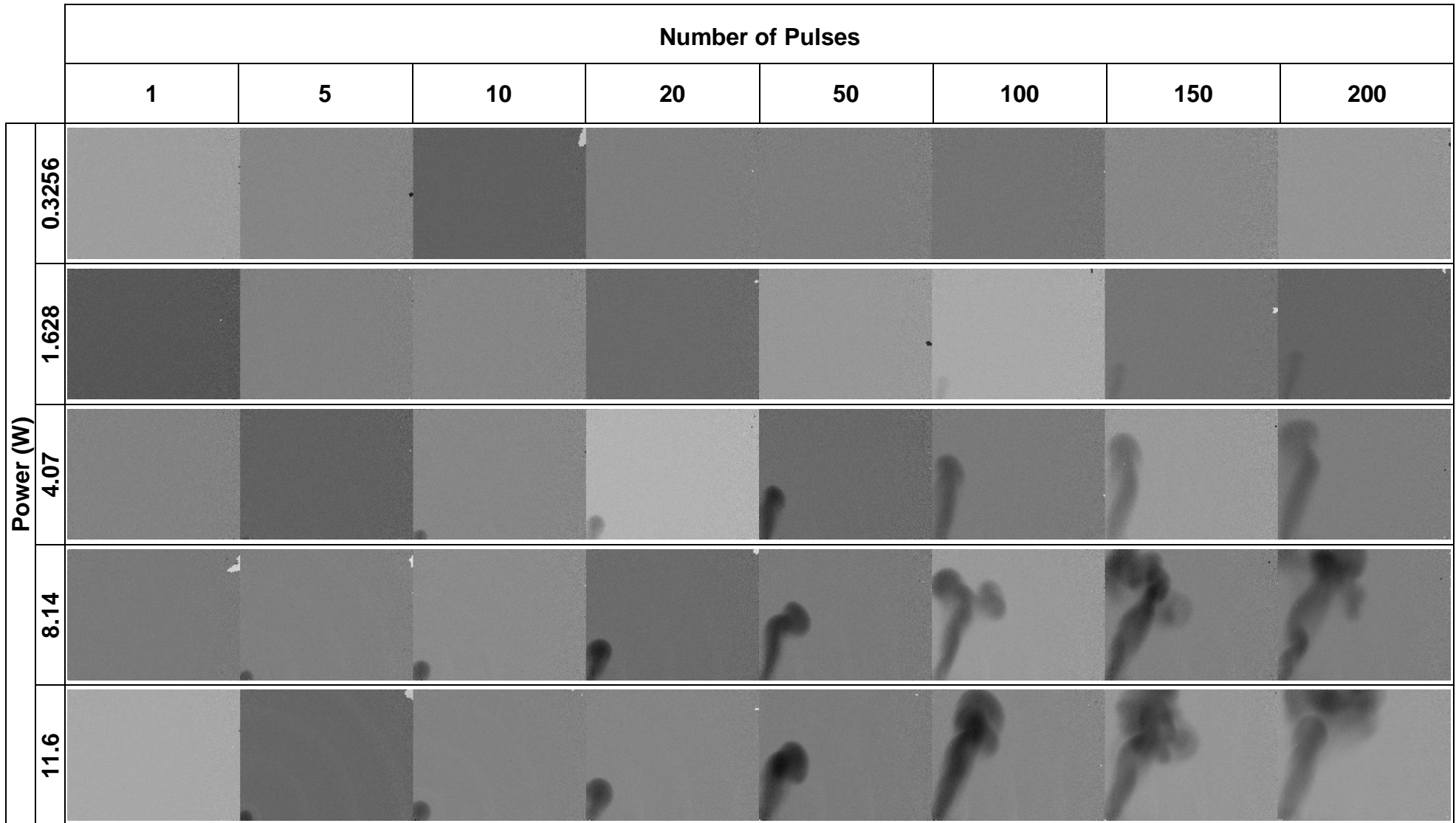


Figure 5-14 Incident angle from normal = 15 Degrees

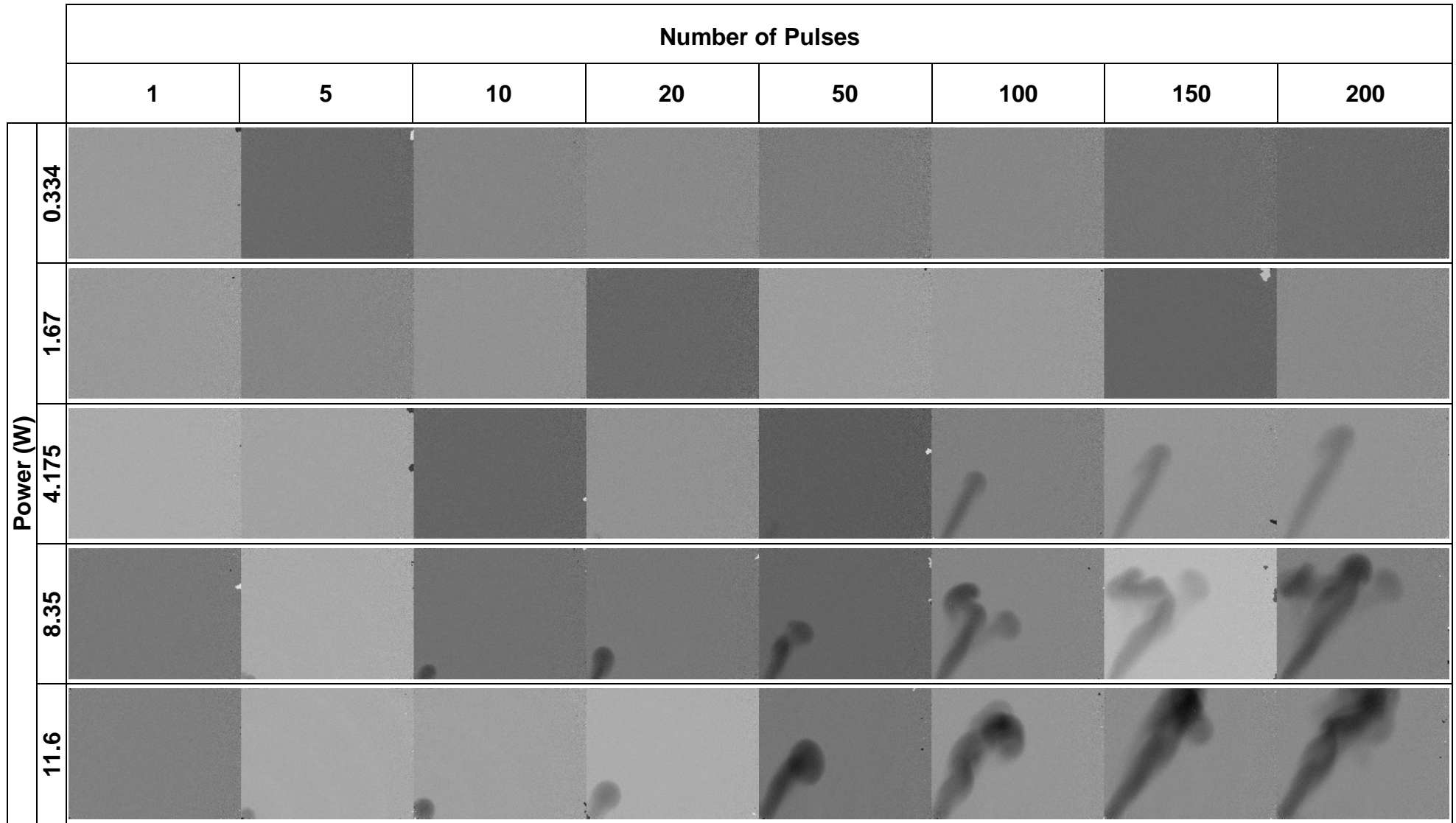


Figure 5-15 Incident angle from normal = 30 Degrees

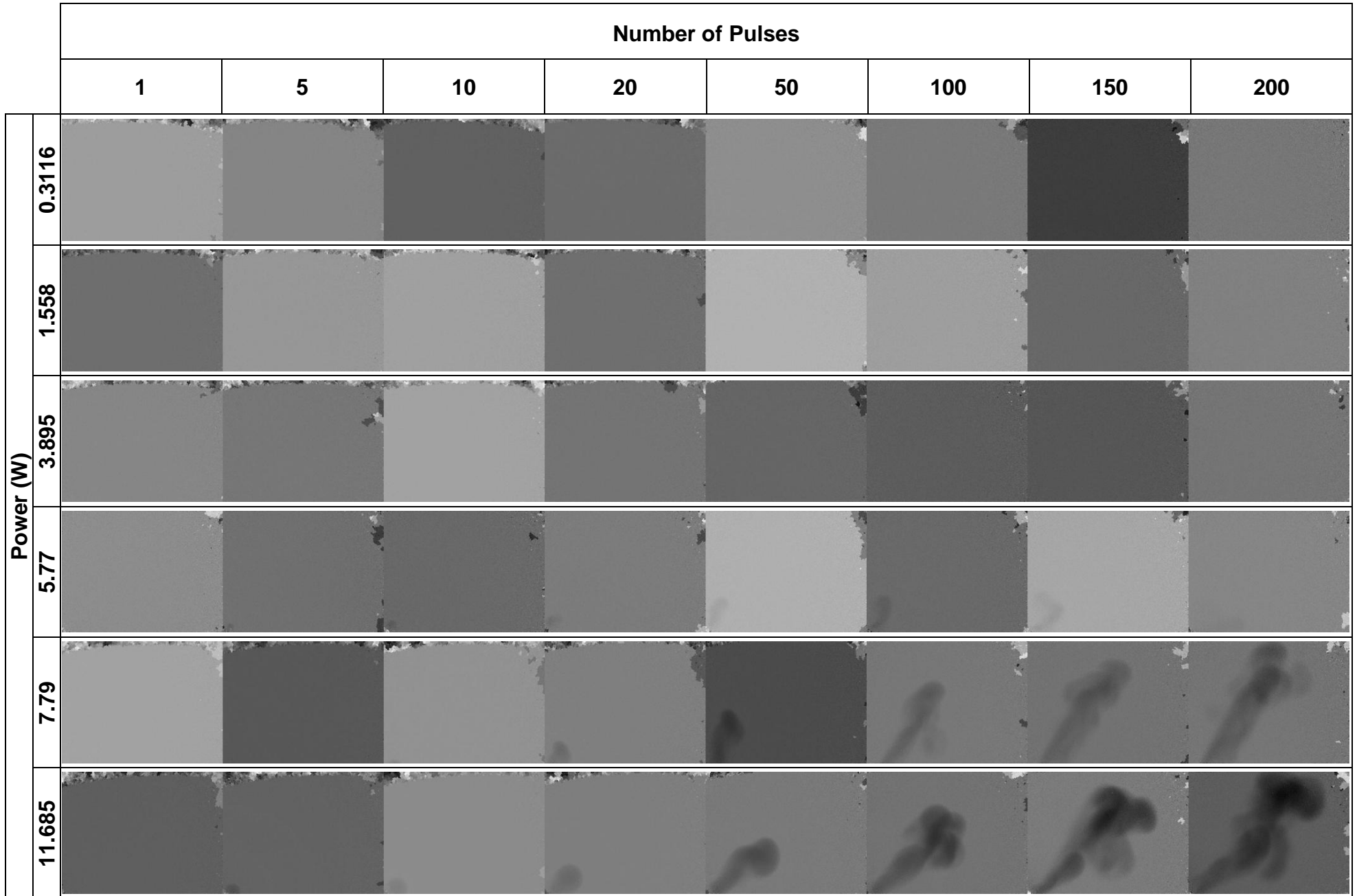


Figure 5-16 Incident angle from normal = 45 Degrees

5.3.5 Comparison of Plume Development at Same Power and Varying Angle

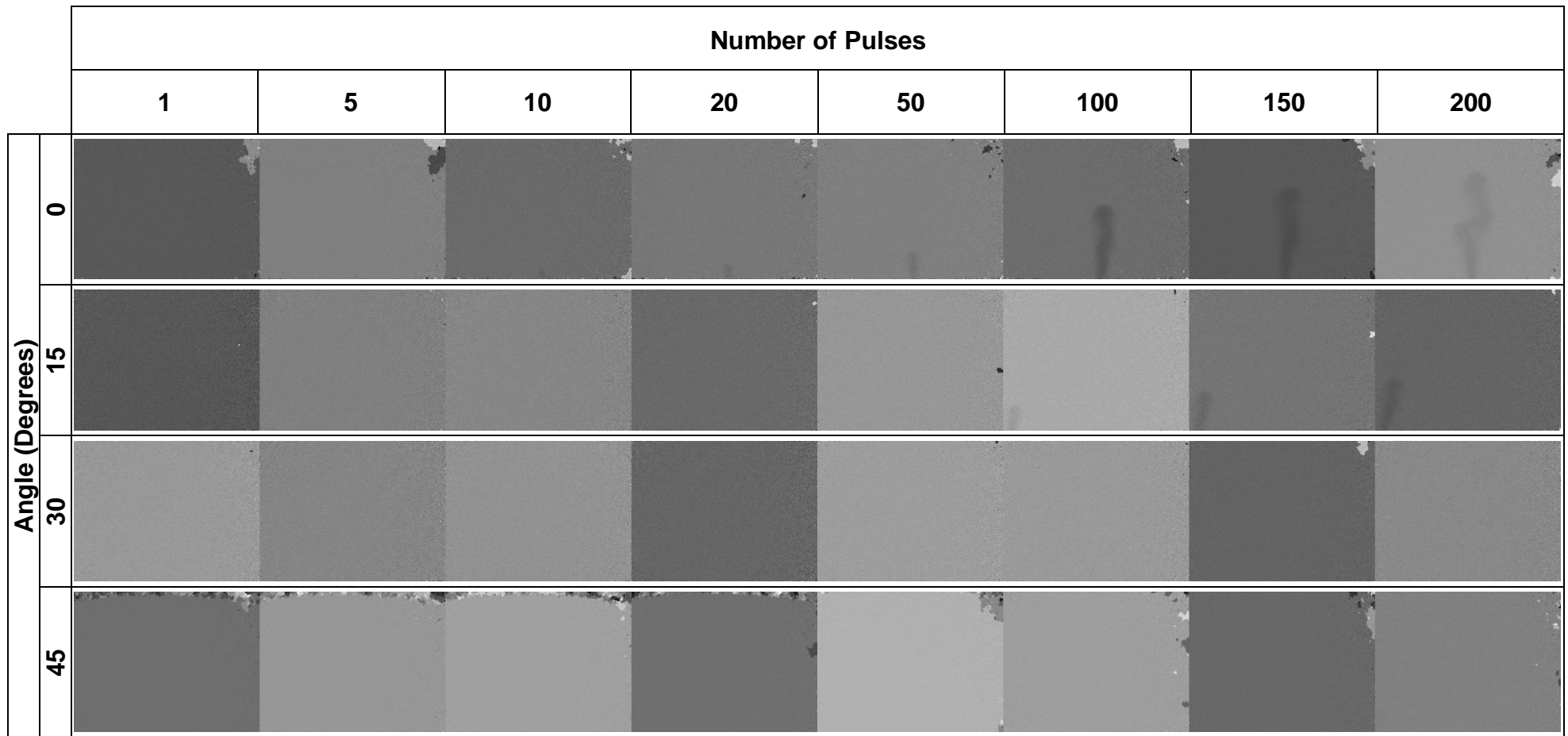


Figure 5-17 Power Values – a) 0 Degrees = 1.3275 W b) 15 Degrees = 1.628 W c) 30 Degrees = 1.67 W d) 45 Degrees = 1.558 W

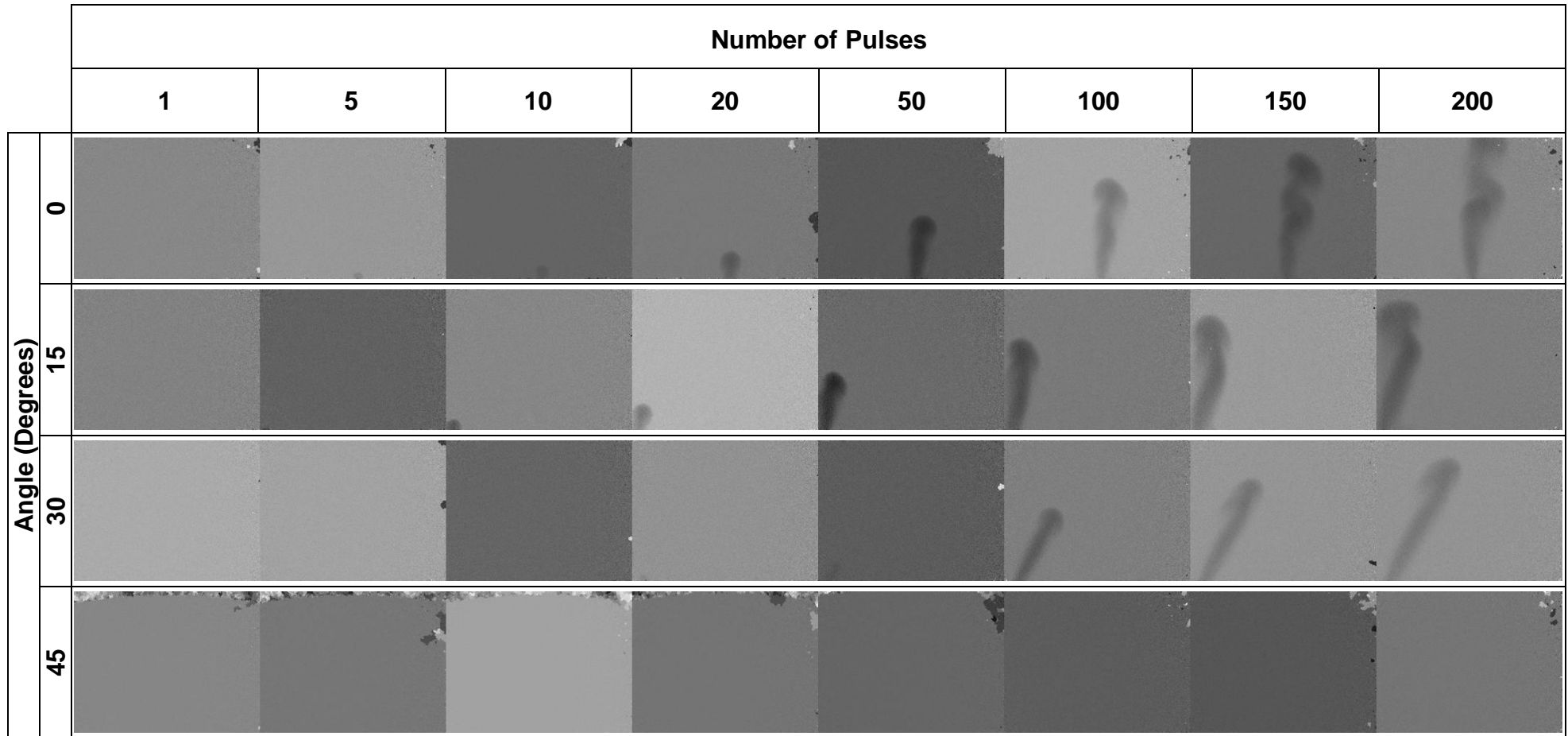


Figure 5-18 Power Values – a) 0 Degrees = 3.98 W b) 15 Degrees = 4.07 W c) 30 Degrees = 4.125 W d) 45 Degrees = 3.895 W

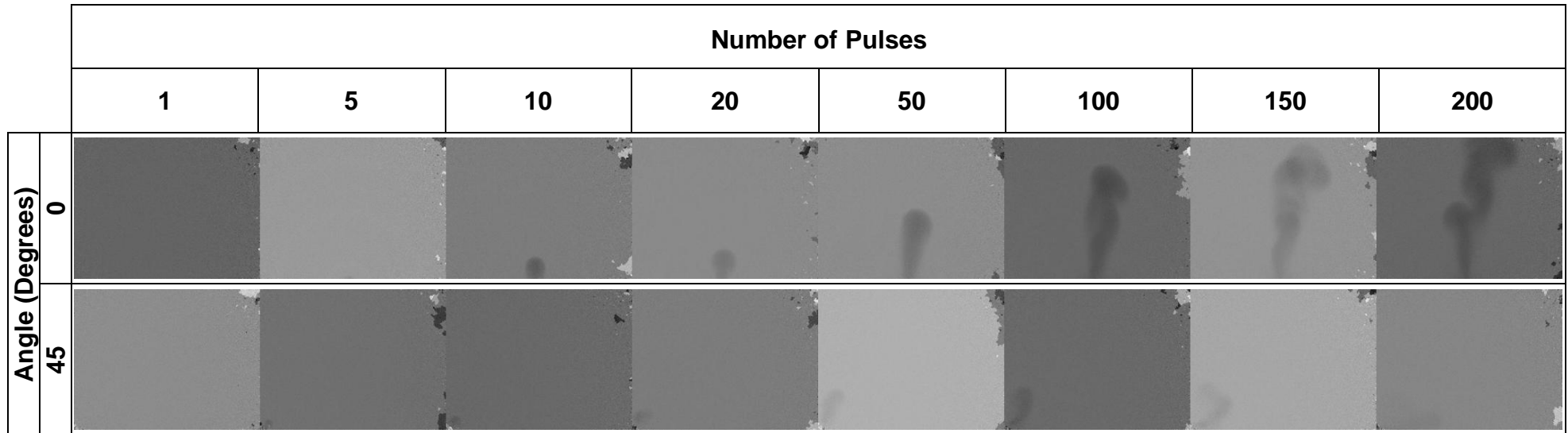


Figure 5-19 Power Values – a) 0 Degrees = 5.77 W b) 45 Degrees = 5.77 W

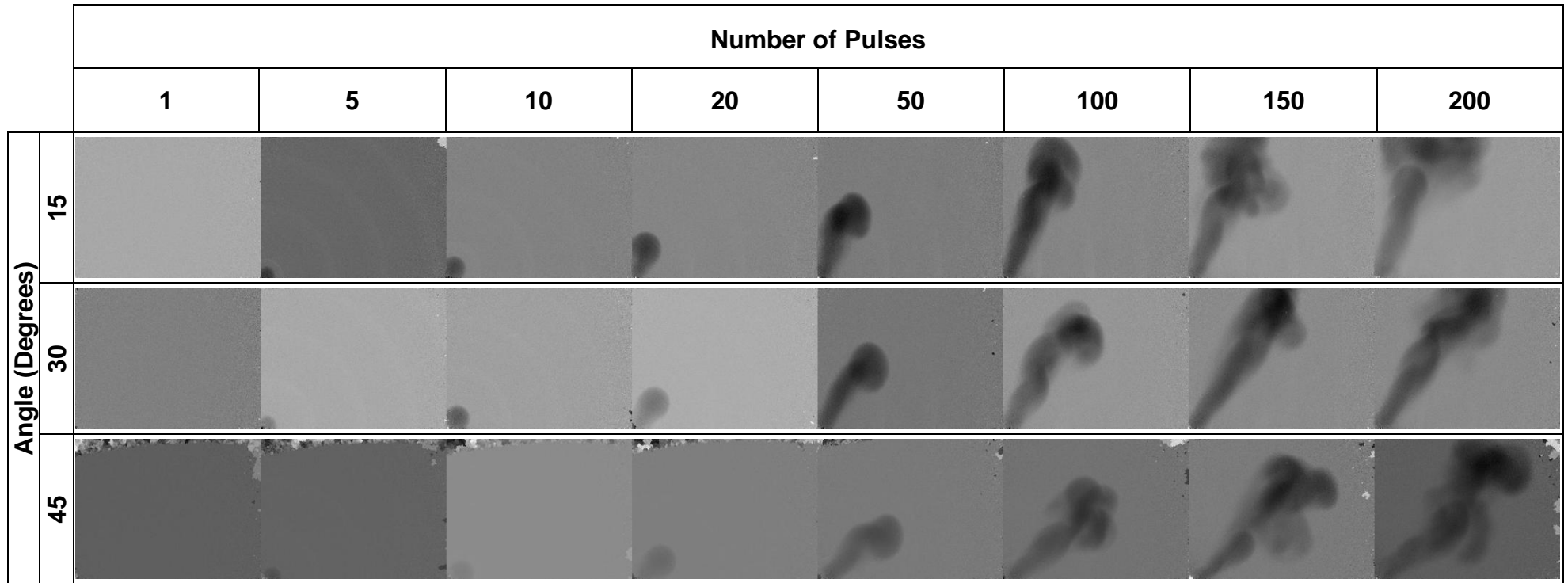


Figure 5-20 Power Values –a) 15 Degrees = 11.6 W b) 30 Degrees = 11.6 W c) 45 Degrees = 11.6 W

5.3.6 Plume Angle at Varying Incident Angles

From the images below it is clear to see that the plume is always normal to the surface of the substrate and is independent of the incident angle of the laser. This has been hypothesised but has not been demonstrated in literature.

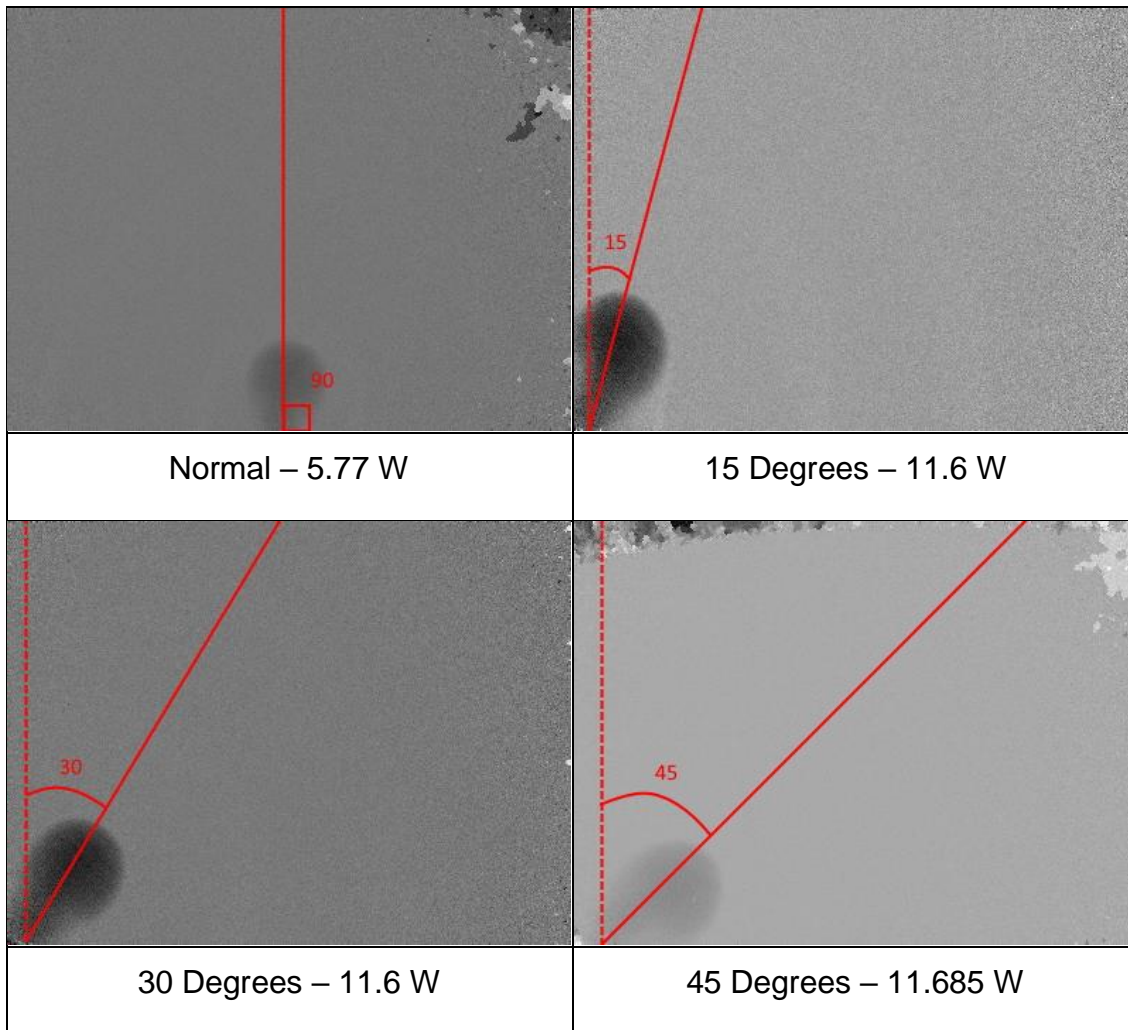


Figure 5-21 Measurement of plume angle from normal after 20 pulses.

5.3.7 Analysis Method

For each hologram captured the following process was carried out to measure and calculate the following:

- Plume Height
- Plume Width
- Refractive Index

The refractive index is calculated from the width of the plume and a reference for the ambient refractive index is taken from the background area of the hologram. These measurements are shown on Figure 5-22.

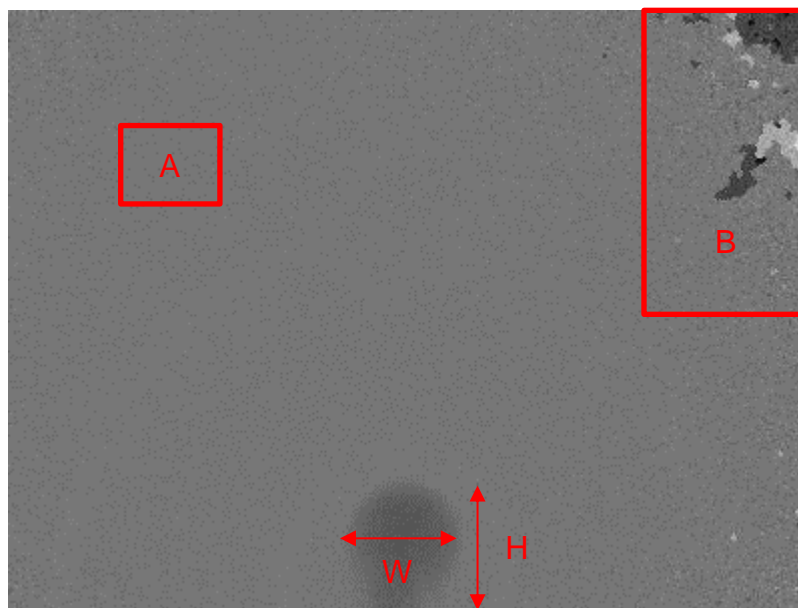


Figure 5-22 Holographic camera measurements and regions of interest.

The area A is an example of the region used as a background reference for the ambient refractive index. The average pixel intensity of the area is taken and then used to normalise the final plot of refractive index.

W and H indicate the measured plume width and height respectively.

The area B shows an example of the phase wrapping artefacts that can occur. Attempts were made to remove these from the images, but a decision was made to simply negate them from measurements through thresholding rather than applying image filtering techniques, as this could cause degradation of the data.

5.3.8 Plume Evolution Analysis

It is of interest to measure the evolution characteristics of the plumes over the first microsecond of processing. The first microsecond was chosen because, over all of the regimes, a steady state appears to be reached in terms of overall visible plume height. The first microsecond is equal to the first 20 pulses when a repetition rate of 200 kHz is used.

5.3.8.1 Plume Evolution at Normal

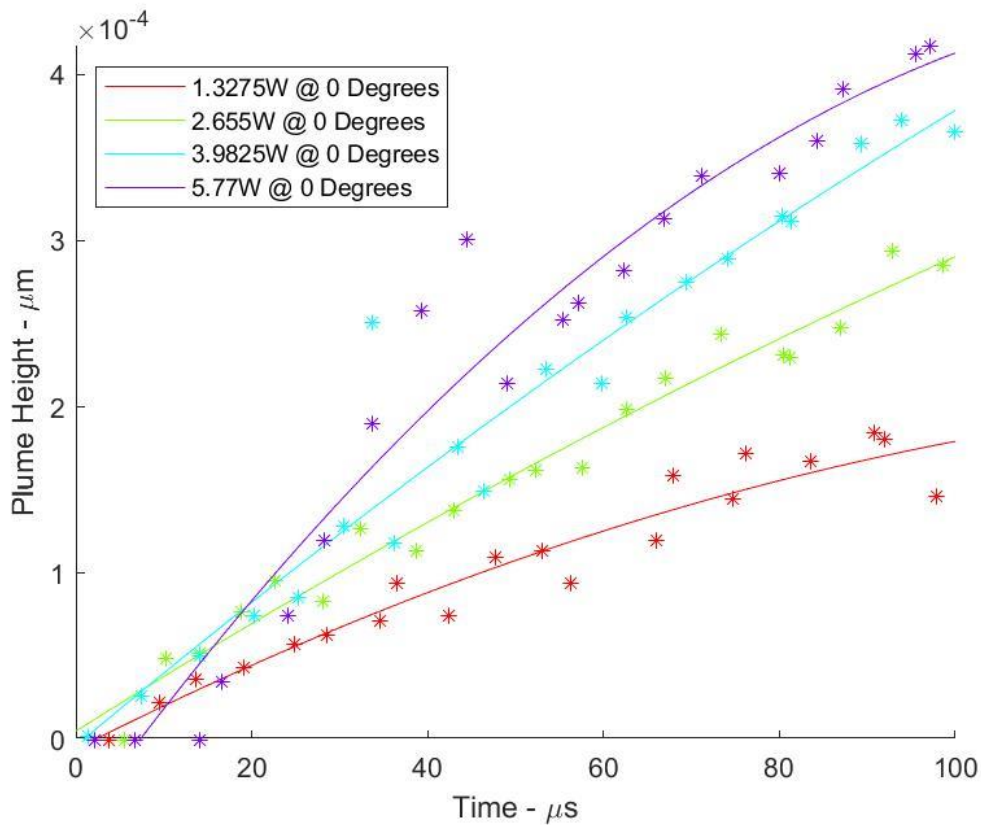


Figure 5-23 Plot of plume height versus time at 0 degrees incident angle.

There appears to be a direct correlation between power and plume height. For each dataset, a quadratic fit has been applied which has an R^2 greater than 0.9. The application of a quadratic fit indicates that the velocity of the leading edge of the plume correlates linearly with time and plume acceleration remains constant throughout the first microsecond.

5.3.8.1.1 Refractive Index of Plume

Figure 5-24 shows the evolution of the plume at the centroid. The ambient refractive index of the air has been set to 1.000277. These plots clearly show that regions in which the plumes are formed have a lower refractive index which, in turn, means that the area is less dense and therefore expanding.

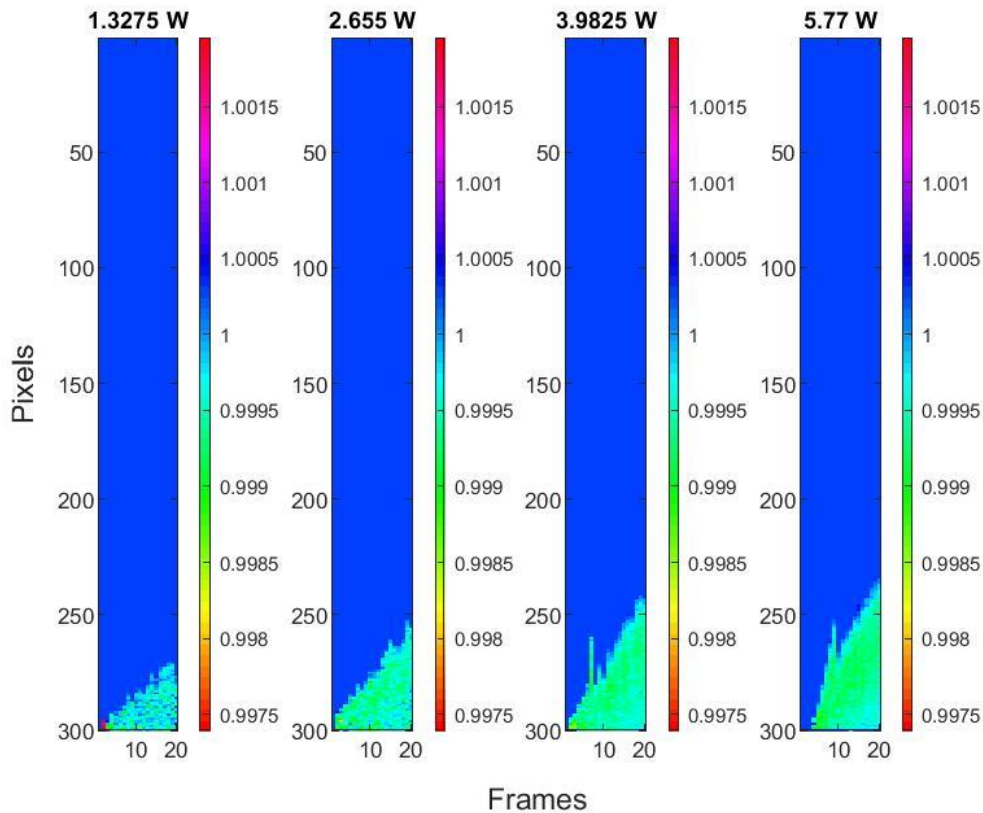


Figure 5-24 Composition of plume changes in refractive index along centroid at different incident angles. Scale indicates refractive index.

This shows that the plume is a continuous event and each pulse contributes to its expansion. The change in refractive index of the plume in contrast to the ambient refractive index could cause a dispersive effect to the incoming pulse although the difference in magnitudes is less than 0.2%. A factor that these results do not show is whether there is any solid material present from the ablated substrate which could cause a dispersive effect.

5.3.8.1.2 Holograms of Significance

In the early stages of plume formation it is possible to see shockwaves generated from the initial ablation of the substrate. These are visible at the highest laser power of 5.77 W. Due to the relatively low sampling-rate compared to other plume imaging research the probability of capturing these is significantly lower as they are very transient. The shockwaves form due to the high energy intensity and short pulse duration which causes the air to expand faster than the speed of sound. These are presented in Figure 5-25.

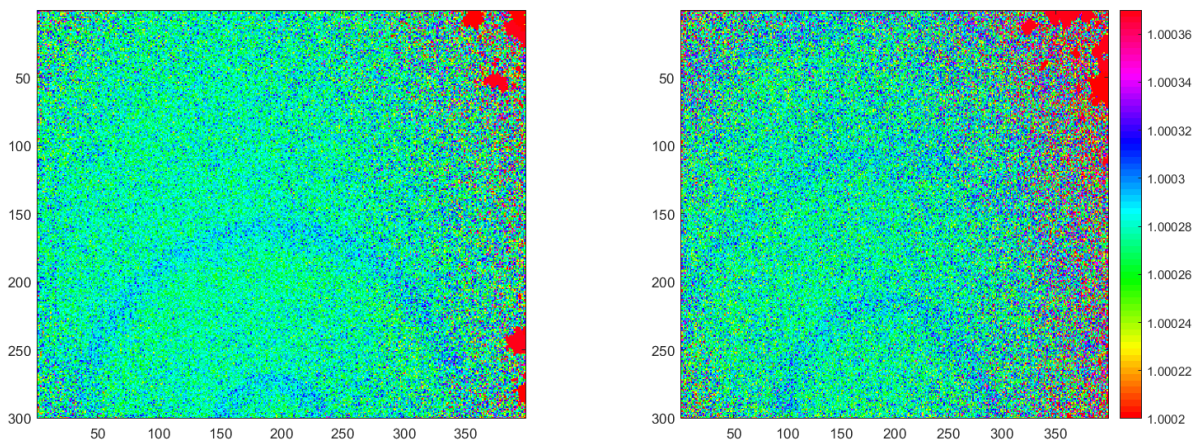


Figure 5-25 Holograms showing examples of shockwaves. Left 5.77 W at 6.74 μ s. Right: 5.77 W at 14.16 μ s. Scale indicates refractive index

5.3.8.2 Plume Evolution at 15 Degrees

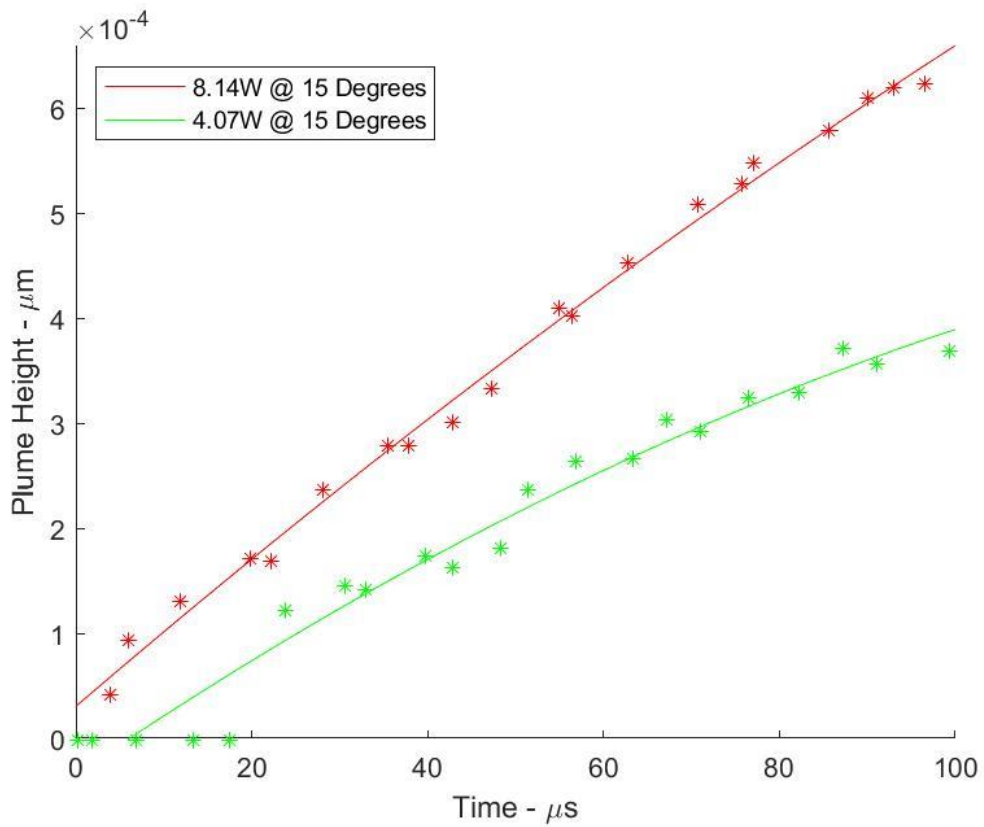


Figure 5-26 Plot of plume height versus time at 15 degrees incident angle.

Unfortunately, there might be an error in 11.6 W capture sequence as the measured plume heights appear to be inconsistent with the other data available. This could have been caused by user error or the automation script used to generate the holographic images may have had a fault. Due to limited access to equipment this trial could not be rerun and therefore has been omitted from the figure above.

5.3.8.3 Plume Evolution at 30 Degrees

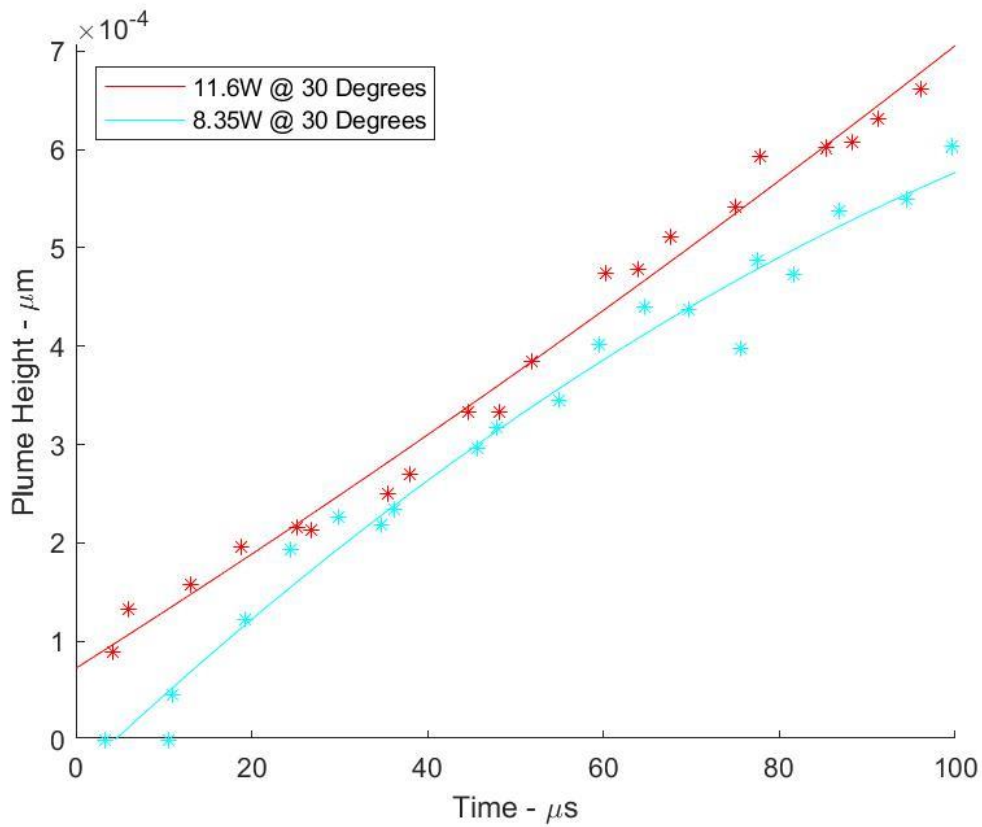


Figure 5-27 Plot of plume height versus time at 30 degrees incident angle.

It was not possible to achieve an accurate measurement for the data set performed at 4.175 W. Unfortunately, the field of view had drifted by less than 1 mm and, as the plume was smaller due to the lower laser power, part of the plume was out of the field of view. This result was therefore omitted.

5.3.8.4 Plume Evolution at 45 Degrees

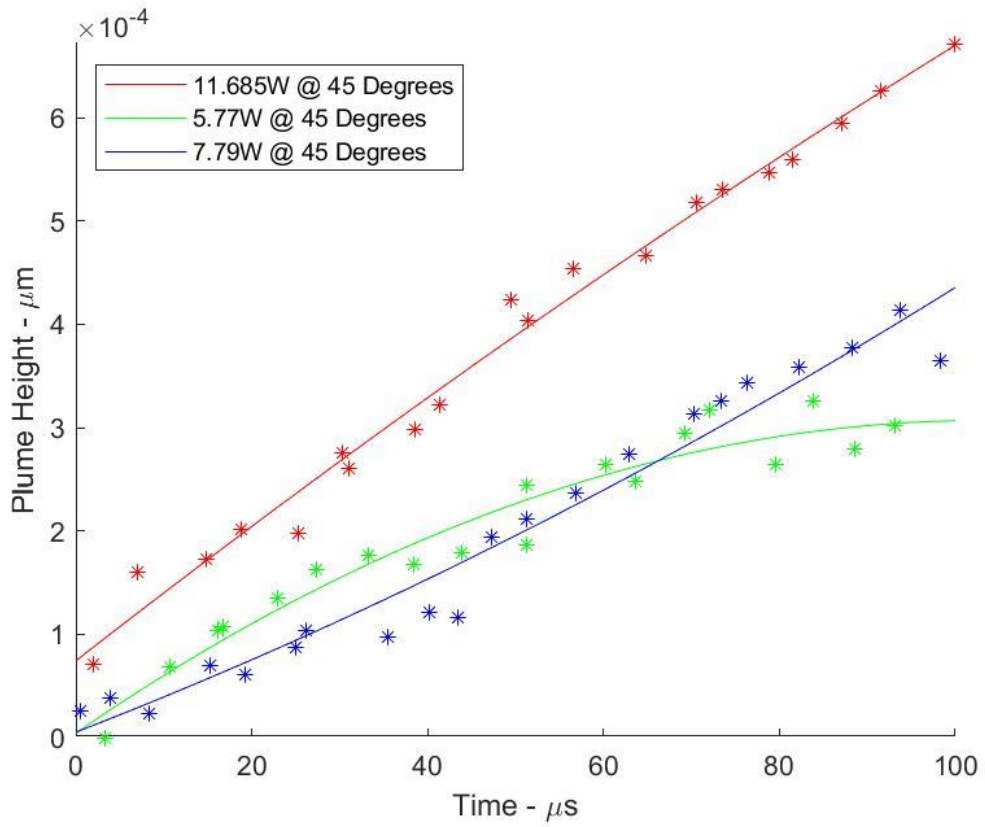


Figure 5-28 Plot of plume height versus time at 45 degrees incident angle.

It should be noted that for the 7.79 W the frame alignment was not perfect and there was a slight drift in the field of view. This issue was corrected and later measurements have an improved accuracy.

5.3.9 Plume Evolution Discussion

From the results obtained, several observations can be made for the effect of changing pulse energy and incident angle on plume evolution:

- The trials performed at normal show that an increase in pulse energy leads to an increase in the maximum height of the plume.
- For all trials, the maximum plume height appears to level off and reach a steady-state when approaching 1 ms of ablation.
- From comparing trials of similar pulse energies at different angles the maximum plume height appears to reduce with increased incident angle. This would correlate with the effect of angle on effective fluence and an increased ablation threshold when moving away from normal incidence as identified in section 5.1.4.

5.3.10 Improvements to Experimental Method

One of the greatest issues with this method is the inability of the equipment to handle static objects in the field of view. This required a compromise when trying to capture images for trials performed at an angle, which involved placing the event in the corner of the field of view of the camera. As evidenced in the results gathered, this led to issues with consistent alignment and clipping of the plumes. Although initial trials were performed, and this method appeared acceptable, not all the parameter space was covered nor the effect of repeated movements of the axis and possible drift of the field of view accounted for.

Clipping of the images did not have a significant effect on the measurement of the plume height. However, for finding the change in refractive index the plume width needed to be measured. Sometimes it was difficult to ensure that the edge of the plume was measured correctly. In Figure 5-29 an exaggerated example of this is shown where the blue line is the edge of the plume and the dotted red line is the field of view of the camera. It is apparent that, depending on the shape of the plume, there is the potential for the plume to expand out of the FOV.

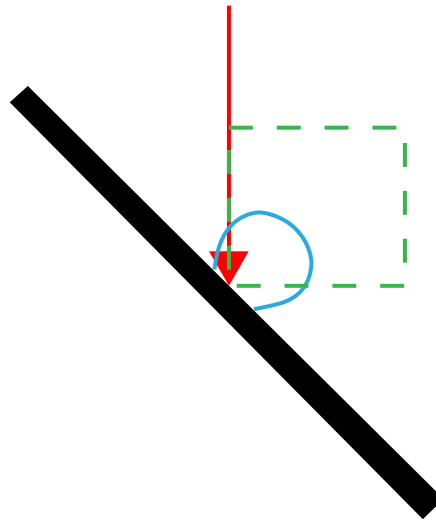


**Figure 5-29 Green dotted line shows the field of view of the holographic camera.
Blue line shows the edge of the plume. Red arrow indicates incident laser.**

The results show that the best quality data occurred when the sample was machined at normal and the event was captured in the centre of the field of view. This approach should therefore be implemented in future when investigating plumes at incident angles. In Figure 5-30 a new design for the holographic camera and fixturing for holding the sample is proposed. This design takes advantage of the fibre-based platform of the holographic camera to implement an improved and more flexible solution.

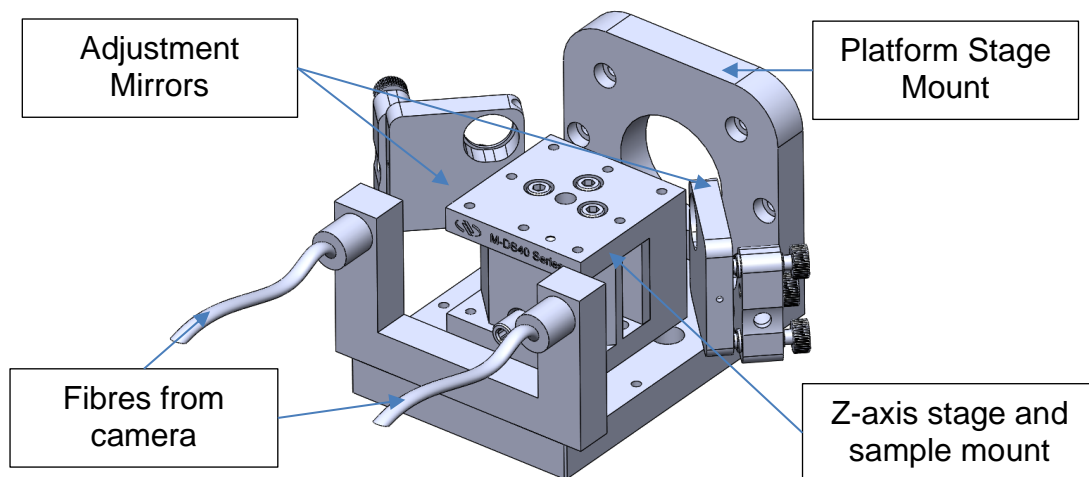


Figure 5-30 Design of fixturing for holographic camera on the ultra-precision platform

In this solution optical fibres are mounted to the 5-axis stage of the platform. This means that algorithms developed for this platform can be used to capture holographic images of ablation at any angle. Fine adjustment has been built into the design to allow adjustment of the holographic camera beam path and z-axis adjustment to allow

samples of different heights. This would ensure that the plume is always in full view of the camera and there are no static objects in the field of view.

5.4 Summary

It is evident that, even with corrections for focal spot fluence, there are other contributing factors which affect the ablation threshold at an angle and a simple trigonometric correction cannot be applied to thresholds found at normal to the surface.

One assumption in the literature postulates that laser plumes form normal to the surface and along the incident access of the laser. The holographic images captured here confirm that the plume consistently forms normal to the surface.

There is a clear correlation between plume expansion and input beam power. For the results measured at normal, a plume height steady state appears to be reached. As expected, as the angle of incidence increases, plume height reduces for the same power level.

A redesign of the equipment is proposed to improve acquisition consistency of the camera and to improve the accuracy of measurements recorded from images by ensuring the whole plume is in the field of view of the camera for any angle at any power level.

Overall, there is significant evidence from sections 5.1, 5.2, and 5.3 that indicates that the pulse-plume interaction which occurs when the incident angle is normal is reduced which affects the ablation threshold, track fidelity and plume evolution. These results give scope for more detailed investigation into the dynamics of the pulse-plume interaction at normal.

6 Conclusions and Future Work

The scope of this body of work was to develop an ultra-precision manufacturing route which was based upon ultrafast lasers. All previous developments in this domain were either open-loop, low precision, or a prototyping process which were lacking in the repeatability and accuracy required to challenge established technologies for the manufacture of MEMS devices. Although this work does not provide a finalised pathway for MEMS manufacture using ultrafast lasers a significant amount of groundwork has been carried out to increase the accuracy and repeatability to future users of the ultra-precision platform along with new machining strategies to be further developed and investigated.

6.1 Platform Development

Objective: Identify, design, and implement equipment and methodologies to improve the accuracy and repeatability of the ultra-precision platform.

- The system should be designed to allow the development of other closed-loop metrology methods.
- Procedures should be developed to improve on current methods for sample alignment and machining.
- The platform should have the ability to monitor laser characteristics whilst performing machining.

6.1.1 Designs and Methods Implemented

- Optical layout for integration and further development of closed loop machining.
- Integration of beam control equipment and laser source control.
- In-process power logging for machining trials.
- Bespoke autofocus method for in-situ measurement of machining.
- A platform tailored method to ensure highest possible accuracy of beam alignment.
- An automated process for laser focus and microscope field of view alignment.
- Tilt correction methodology to ensure substrate is normal to the laser across the whole machining area.
- Automated routine for finding laser focus on substrate.
- Routine for finding relative rotary axis for samples of any thickness.

- Created a method which allows for the machining at any angle (0 - 45 degrees) on a planar material.
- Unified all the above techniques and methodologies into a singular GUI application which provides a steppingstone for further development of the ultra-precision platform.
- Implemented the first ever automated holographic camera capture routine to markedly reduce data acquisition times.

6.1.2 Summary

The development of the ultrafast platform was a significant portion of this body of work. This required a range of technical skills covering mechanical, electrical, optical and software design. These developments could only be performed through many iterations, testing improvements and changes to the setup. Throughout the development of the platform a consideration was always made to ensure that the work performed can lead into further research and advancement of the ultra-precision platform. From this, future researchers have access to in-process monitoring, improved repeatability in setup, and a new approach to laser machining.

6.2 Beam Stability Investigation

Objective: Investigate the characteristics of the picosecond laser installed on the ultra-precision platform and the effect this can have on machining.

- Measure the point stability, beam diameter and power stability of the laser system.
- Identify the effects of duty cycle on beam stability.
- Simulate the effect of beam stability on machining accuracy.

An initial investigation of the three available wavelengths (355 nm, 532 nm, and 1064 nm) in terms of beam diameter, pointing stability and power on the platform was performed. There is evidence that there is a settling time which occurs in the initial period of laser use. For the 1064 nm wavelength the standard deviation for the centroid position was approximately 55 μm . For 1064 nm the standard deviation for the average power reading was 0.11 W with a mean reading of 13.24 W. This showed that the laser was unstable and would have an effect on machining operations.

It was found that, depending on how the attenuation level of the Talisker laser system was set, the measured laser output power would vary even though the value in the

software was the same. Therefore, a solution which rehomed the attenuator after every request was implemented to improve the repeatability when requesting a power output.

When trying to achieve low beam powers it was identified that using two polarisation based optical attenuators in series would limit the minimum power output. This is due to the laser source not being perfectly linear and, as the p-polarisation is reduced by the attenuators, the s-polarisation becomes more significant. The polarisation-based attenuators were retained as they allowed digital control of the laser power which was advantageous over traditional manually adjusted attenuators. In the cases where very lower power levels were required a diffractive attenuator could be used.

Another area of interest with regards to laser stability was the effect of different duty cycles on the repeatability of the power output. A number of different duty cycles were used which included a randomised workload with varying on off durations and a repeated workload of either 10 seconds off, 30 seconds on. This showed that duty cycle had a significant effect on the measured output power.

Finally, using the hour-long stability test data, a model for the effects of the laser instability on a machined track was created. This demonstrated how the stability of the centroid position of the laser and the variance of fluence at the focal spot had an effect on both track width and track depth.

6.3 Ablation at Varying Incident Angles

Objective: Investigate how changing incident angle affects laser ablation at an angle.

- Determine the result of changing the incident angle on the ablation threshold for silicon.
- Measure the effect of incident angle on plume dynamics.

The first stage in this area of research was to investigate the effect of incident angle on ablation threshold and performed analysis to offer an explanation as to why the ablation threshold at angles is not related by a trigonometric function. It was found that the introduction of an incident angle causes the ablation threshold to be greater than what can be explained by the effect on the area at the focal spot and Snell's Law.

Using the automated holographic camera capture method, the effect of different incident powers and angles on plume evolution was acquired. The first 100

microseconds, roughly 20 pulses, of ablation were evaluated with respect to the change in plume evolution.

It was evident in the final analysis that the quality of the data could be improved. A redesign of equipment to improve data accuracy was proposed which would also aid in looking into more advanced cases such as a moving focal spot.

Through the experiments carried out there is significant evidence that by changing the incidence angle of the laser to the surface this affects the pulse-plume interaction which leads to changes in ablation threshold, track fidelity and plume evolution. This change in interaction between the pulse and plume opens an avenue for exploitation for improved machining process but also to further increase the understanding of the ablation process.

6.4 Future Work

There is a large scope of areas in which the ultra-precision platform can be used and developed for future research. These have been identified and broken down into two categories. Those that are specific to the development of the ultra-precision platform as a machine tool, and those that relate to the development of an ultra-precise laser-based machining technique.

6.4.1 Ultra-Precision Platform Development

Although a great deal of progress has been made with regards to understanding the current performance of the platform and a large number of developments and methods implemented the original concept for the platform should be revisited. This is a schematic with different options of systems which can be implemented on the platform. This shows that there is still a significant scope for development for this platform.

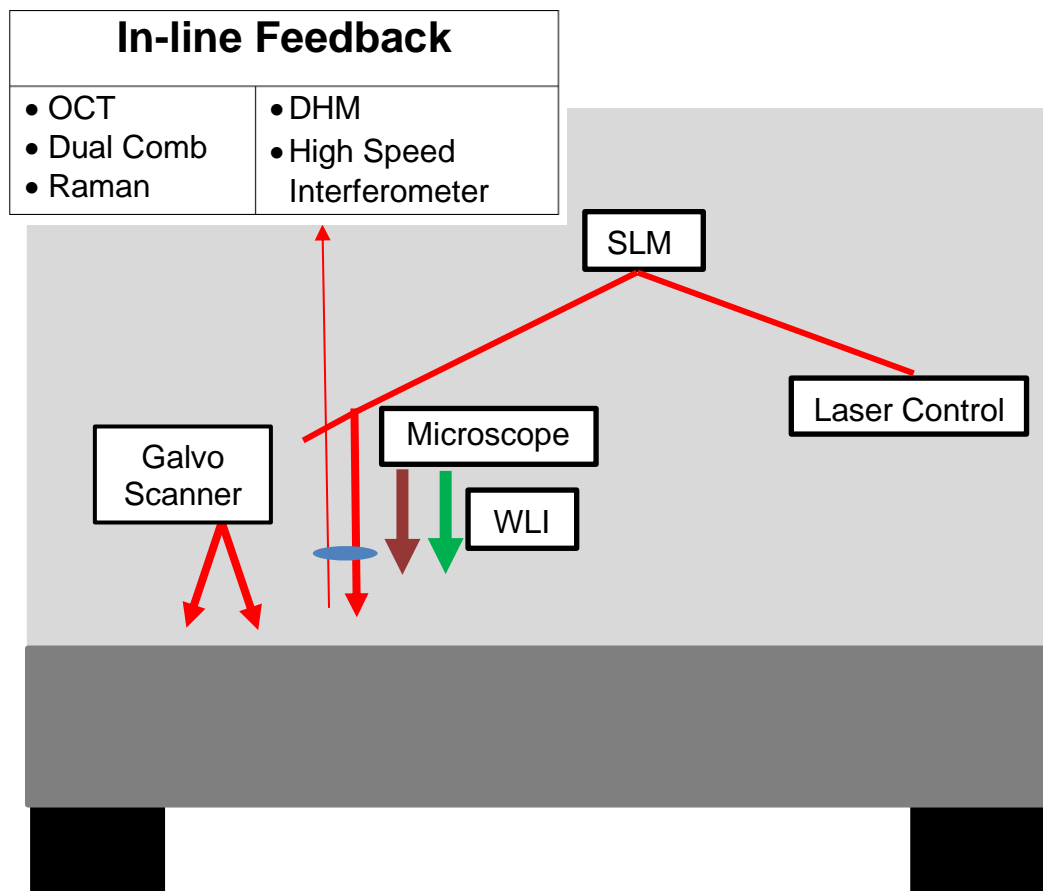


Figure 6-1 Schematic of future developments on the ultra-precision platform

- Improve laser source and beam stability possibly through the implementation of beam steering.

The CCD used to log the stability of the laser is limited to 26 Hz whereas quadrant sensors have 10 nanoseconds rise time which gives a <200 kHz response rate. This means quadrant sensors could be used to perform feedback. The position of the centroid can be adjusted using piezo-actuated mirror mounts. The piezo mirror mounts have a response in the kHz range. Some preliminary trials were performed to measure the stability of the laser using quadrant sensors but a suitable data logger and controller for the piezo mirrors needs to be installed to provide a stable solution.

- Power control feedback and improved interrogation rate

Currently, the performance of the power stability is limited by the response of the motorised attenuators. The response is limited by the drive motor acceleration, motor resolution and time delay when using serial control. This means that only low frequency changes in power can be controlled. An investigation should be carried out into the use of power control devices with a significantly faster response rate or whether other laser sources such as fibre-based lasers are more stable.

- Geometry correction feedback through – OCT, DHM, WLI and dual-comb interferometer.

While the basic OCT system has been implemented it is yet to be used to carry out in-process depth measurement and provide feedback for optimised 2D and 3D processing. OCT would provide a proof of concept for in-process closed-loop 3D ultrafast machining, however the system is limited by the axial resolution. When the laser is capable of machining axial in the <100 nanometre range it seems counterintuitive to use a metrology method which limits the machining accuracy.

There has been little process development of a DHM solution, and this has yet to be operated in-line with a laser. DHM could be developed to measure the sample in-line and provide feedback to optimise 2D and 3D processing. DHM provides a solution for in-line metrology which can be used to carryout closed-loop corrective feedback for 2D and 3D structures. However, the reduced field of view and the low data acquisition rate mean that when performing corrections at the 10-100 nanometre scale the machining time will be lengthy.

The use of a dual frequency combs is an emerging metrology technique. Currently dual-comb metrology has been considered for high axial accuracy (< 100 nm) measurements over large distances (> 100 m). These systems do not take advantage of the high data-acquisition rate of the technique. Dual comb metrology could be developed into an in-line technique which could then be used to measure the sample and provide feedback to optimise 2D and 3D processing. Dual comb metrology could provide a solution which is capable of high frequency and high accuracy measurements. However, this technology is far from established and will require significant development. A concern is the level of computation which would be required to reach nanometre resolution at hundreds of hertz let alone the megahertz level. A solution which may be more suitable could be to use two single-mode frequency stable femtosecond lasers which could possibly reach sub-micrometre accuracy at a lower capital cost. The difference between a frequency comb-based system and a single mode based system is the difference in the pulse used. The frequency-based comb uses a mode-locked laser pulse; the advantage of using a comb is that the phase difference between the combs can be used to attain sub-wavelength accuracy.

Installation of off-axis white light interferometer (WLI) to carry out measurement of milled features and allow for intermittent inspection which could be used as a method of geometrical feedback. An ultrafast platform with integrated WLI would provide geometrical feedback however this represents a time-consuming solution. An improved solution could be to use alignment markers and a commercial WLI system would give traceable topology.

Comparing the different options for development based on performance a dual comb system would provide the best in-process solution. However, the system is most probably prohibitively expensive for the funded research in progress. The next best option is the development of a dual single mode laser metrology solution although this needs further investigation. Of the established technologies DHM, high speed interferometer and OCT should be examined. The deciding factor will be whether the low resolution, but high acquisition rate of OCT is advantageous over the high resolution, low acquisition rate of DHM.

- Integration of Raman for sample property analysis such as processing and diagnostics of graphene and CNT.

A Raman system gives the potential to inspect the structure of the graphene on the sample then machine an area with the required qualities such as single or multi-layer regions. With an implemented metrology system and Raman spectroscopy all processing and measurement for a graphene- or CNT-based device could be completed on a single platform.

- Effect of beam shaping on process stability and accuracy

Spatial Light Modulators (SLM) have been used to demonstrate high speed parallel and selective patterning and beam shaping when combined with an ultrafast laser [126]. The combination of SLM, galvo scanner and in-line metrology could be used to increase the throughput of the platform.

- Improved image recognition for fiducial markers and machined features.

Fiducial markers are useful for realignment and cross-alignment of systems. Fiducial markers in the form of crosses were used in the alignment procedure to gain accurate laser-microscope alignment. However, these were not used for realignment of samples. In practice, this would not be difficult to implement with the existing code and the only addition required would be the databasing of coordinates when placing the initial markers. An interpreter would be required to adjust for the misalignment when the sample is remounted on the platform.

The more interesting use case for fiducial markers is for cross-alignment between the ultra-precision platform and the FIB platform. The FIB platform has an API and is capable of machine vision techniques, however the integration of the two platforms would require a high level of software and process engineering.

- Installation of in-line camera.

Although methods which achieve a high level of accuracy for finding laser focus on a sample have been implemented, a tool which would help in finding a rough focus for new samples would be the installation of an in-line camera. A zoom lens which will focus at infinity has been purchased and fixturing created and would only take a short time to commission on the platform.

- Further fixturing designs

As mentioned in section 5.3.9, a redesign of the setup for the holographic camera would greatly improve the quality of the results captured. Secondly, the investigation of the effect of different atmospheres on processing is of significant interest. This would require the design of a vacuum chamber that could be fixed to the 5-axis stage. Ray-tracing assessments would need to be carried out to see the effect of the laser entering the window of the chamber at an angle.

- Improved GUI for other users.

One disadvantage of the current software implementation is that a moderate level of programming knowledge is required to be able to implement customised routines. This would require the software being broken down into more accessible functions but, as the hard work involved in the development of the methods has been, done this should be a simple task to perform.

6.4.2 Experimental work

There is a wide range of areas in which the ultra-precision platform could be used to investigate laser-based machining processes. Below are those that are closest to the scope carried out in this body of research.

- Effect of angle on surface roughness

The next stage of development of using an angular approach to laser machining is to assess the correlation of incident angle with surface roughness. During this research a set of trials was performed changing angle, power and laser path overlap. Unfortunately, there was an issue with silicon dioxide build up on the area machined which would require post processing. This is shown in Figure 6-3 where the EDX of the sample shows an increase in the presence of oxygen in the machined region.

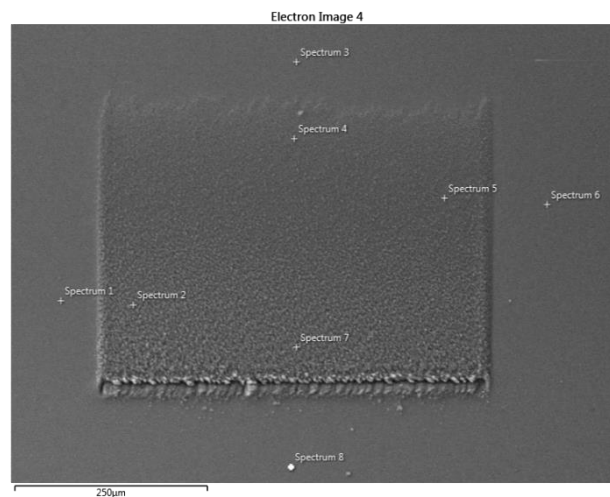


Figure 6-2 SEM of ablated region

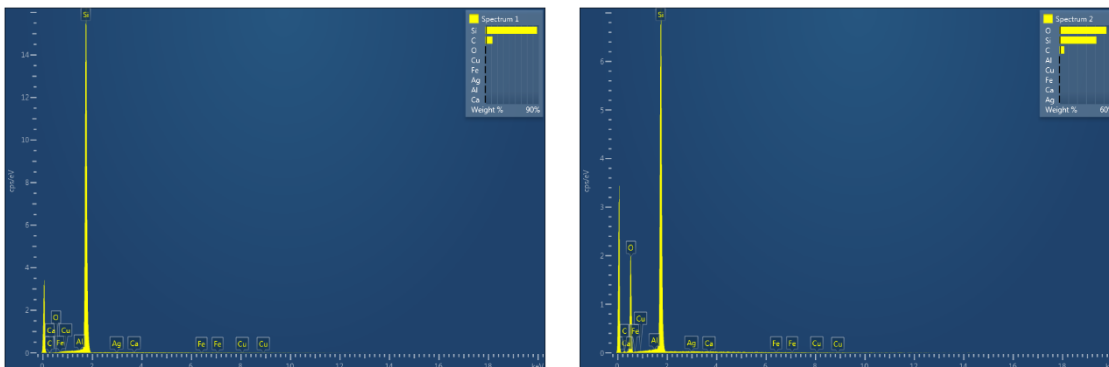


Figure 6-3 Left: EDX of region outside ablated region. Right: EDX of ablated region.

The use of a vacuum chamber or improved gas shielding would be the first stage of development for an improvement in process quality.

- Cover a greater parameter space.

Depending on the findings with regards to taking an angular approach the parameter space covered by performing trials should now be repeated with different materials such as metals and plastics to see whether this method has a similar effect to those found in silicon. Shorter focal-length lenses should be used to achieve a smaller focal spot to target smaller feature resolution. Additional laser wavelengths should be trialled to take advantage of materials that have higher absorption at different wavelengths. Using wavelengths which correspond with a higher absorption should mean that less incident power is required, which should minimise effects such as the heat affected zone.

- Machine a TEM lamella.

A target for ultra-precision manufacturing using a laser-based process could be to demonstrate a process for the production of a TEM lamella. TEM lamellas require a high level of accuracy and repeatability with well understood laser-material interactions which, if successful, could open up this production route to wide application in the field of MEMs device creation.

6.5 Conclusion

The ultra-precision platform is a piece of equipment that provides many avenues to investigate within the realm of ultrafast laser processing, and the work conducted here provides the footing for these to be investigated. The development of ultra-precision laser manufacturing is defined by how accurately and repeatable the process is and this work has hopefully contributed to this area of manufacturing moving forward.

REFERENCES

- [1] P. Shore and P. Morantz, 'Ultra-precision: enabling our future', *Philos. Trans. R. Soc. Lond. Math. Phys. Eng. Sci.*, vol. 370, no. 1973, pp. 3993–4014, Aug. 2012, doi: 10.1098/rsta.2011.0638.
- [2] A. Pimpin and W. Srituravanich, 'Review on Micro- and Nanolithography Techniques and their Applications', *Eng. J.*, vol. 16, no. 1, pp. 37–56, Jan. 2012, doi: 10.4186/ej.2012.16.1.37.
- [3] W.-S. Chu *et al.*, 'Hybrid manufacturing in micro/nano scale: A Review', *Int. J. Precis. Eng. Manuf.-Green Technol.*, vol. 1, no. 1, pp. 75–92, Jan. 2014, doi: 10.1007/s40684-014-0012-5.
- [4] P. Kwee, B. Willke, and K. Danzmann, 'New concepts and results in laser power stabilization', *Appl. Phys. B*, vol. 102, no. 3, pp. 515–522, Feb. 2011, doi: 10.1007/s00340-011-4399-1.
- [5] Eric Mounier, 'Future of MEMS. A Market and Technologies Perspective', Oct. 2014, Accessed: Aug. 22, 2015. [Online].
- [6] M. Tanaka, 'An industrial and applied review of new MEMS devices features', *Microelectron. Eng.*, vol. 84, no. 5–8, pp. 1341–1344, May 2007, doi: 10.1016/j.mee.2007.01.232.
- [7] H. C. Nathanson, W. E. Newell, R. A. Wickstrom, and Jr. J.R. Davis, 'The resonant gate transistor', *IEEE Trans. Electron Devices*, vol. 14, no. 3, pp. 117–133, Mar. 1967, doi: 10.1109/T-ED.1967.15912.
- [8] V. Choudhary and K. Iniewski, *MEMS: Fundamental Technology and Applications*. CRC Press, 2013.
- [9] Marc J. Madou, *From MEMS to Bio-MEMS and Bio-NEMS: Manufacturing Techniques and Applications*, 3 edition. Boca Raton, FL: CRC Press, 2011.
- [10] H. Weinberg, 'Dual axis, low g, fully integrated accelerometers', *Analog Dialogue*, vol. 33, no. 1, pp. 23–24, 1999.
- [11] G. M. Whitesides, 'The origins and the future of microfluidics', *Nature*, vol. 442, no. 7101, pp. 368–373, Jul. 2006, doi: 10.1038/nature05058.
- [12] P. Tabeling, *Introduction to Microfluidics*. OUP Oxford, 2010.
- [13] E. Verpoorte and N. F. De Rooij, 'Microfluidics meets MEMS', *Proc. IEEE*, vol. 91, no. 6, pp. 930–953, Jun. 2003, doi: 10.1109/JPROC.2003.813570.
- [14] V. Shilpiekandula *et al.*, 'Metrology of Microfluidic Devices: A Review', 2006, Accessed: Aug. 22, 2015. [Online]. Available: http://web.mit.edu/cpmweb/library/300000_Metrology_of_Microfluidic_Devices_A_Review_2006_Shilpieka.pdf.
- [15] K. J. Vahala, 'Optical microcavities', *Nature*, vol. 424, no. 6950, pp. 839–846, Aug. 2003, doi: 10.1038/nature01939.
- [16] A. A. Savchenkov, V. S. Ilchenko, A. B. Matsko, and L. Maleki, 'Kilohertz optical resonances in dielectric crystal cavities', *Phys. Rev. A*, vol. 70, no. 5, p. 051804, Nov. 2004, doi: 10.1103/PhysRevA.70.051804.

- [17] G. A. Cohoon, R. Norwood, K. Tada, K. Kieu, and M. Mansuripur, 'Fabrication of High-Q Microresonators using Femtosecond Laser Micromachining', in *CLEO: Science and Innovations*, 2012, pp. CM1M–6, Accessed: Aug. 22, 2015. [Online]. Available: http://www.osapublishing.org/abstract.cfm?uri=CLEO_SI-2012-CM1M.6.
- [18] L. a. M. Barea, F. Vallini, A. R. Vaz, J. R. Mialichi, and N. C. Frateschi, 'Low-roughness active microdisk resonators fabricated by focused ion beam', *J. Vac. Sci. Technol. B*, vol. 27, no. 6, pp. 2979–2981, Nov. 2009, doi: 10.1116/1.3264481.
- [19] J. Lin, J. Song, J. Tang, W. Fang, K. Sugioka, and Y. Cheng, 'Fabrication of optical cavities with femtosecond laser pulses', 2014, vol. 8960, pp. 89601A–89601A–6, doi: 10.1117/12.2041353.
- [20] V. Georgakilas *et al.*, 'Functionalization of Graphene: Covalent and Non-Covalent Approaches, Derivatives and Applications', *Chem. Rev.*, vol. 112, no. 11, pp. 6156–6214, Nov. 2012, doi: 10.1021/cr3000412.
- [21] A. K. Geim and K. S. Novoselov, 'The rise of graphene', *Nat. Mater.*, vol. 6, no. 3, pp. 183–191, Mar. 2007, doi: 10.1038/nmat1849.
- [22] M. Chang, 'Annual Report 2014', Taiwan Semiconductor Manufacturing Company, Ltd, Annual Report, 2014.
- [23] G. Denes, 'Design for Semiconductor Reliability', 2009. [http://www.ewh.ieee.org/r6/scv/rl/articles/Design%20for%20Semiconductor%20Reliability%20\(01.12.09\).ppt](http://www.ewh.ieee.org/r6/scv/rl/articles/Design%20for%20Semiconductor%20Reliability%20(01.12.09).ppt).
- [24] J. Handy, 'Why Are Computer Chips So Expensive?', *Forbes*, 2014. <http://www.forbes.com/sites/jimhandy/2014/04/30/why-are-chips-so-expensive/> (accessed Aug. 12, 2015).
- [25] M. J. Madou, *Fundamentals of Microfabrication: The Science of Miniaturization, Second Edition*. CRC Press, 2002.
- [26] B. A. Fuchs, C. Syn, and S. P. Velsko, 'Diamond turning of lithium niobate for optical applications', *Appl. Opt.*, vol. 31, no. 27, pp. 5788–5793, Sep. 1992.
- [27] 'Kern Evo Machining Center'. <http://swissinstruments.com/kern-evo.html>.
- [28] 'Nanoform 250 ultra'. http://www.precitech.com/products/nanoform250ultra/nanoform_250_ultra.html.
- [29] B. W. Ward, J. A. Notte, and N. P. Economou, 'Helium ion microscope: A new tool for nanoscale microscopy and metrology', *J. Vac. Sci. Technol. B*, vol. 24, no. 6, pp. 2871–2874, Nov. 2006, doi: 10.1116/1.2357967.
- [30] John Melngailis, 'Focused Ion Beam Applications: Milling and Implantation'. .
- [31] Richard Langford, 'Focused Ion Beam Milling - Lecture Notes'. .
- [32] N.S. Smith, 'Metrology for 3D Devices: Plasma-FIB for High Throughput Sectioning of Large Dimensions'. Oregon Physics, 2011.
- [33] 'Helios NanoLab G3 Datasheet'. .
- [34] 'Zeiss Crossbeam Data Sheet'. .

- [35] 'AURIGA Laser: Innovative Combination of FIB/SEM Technology with Laser Ablation for Fast Sample Preparation'. <http://www.businesswire.com/news/home/20120308005232/en/AURIGA-Laser-Innovative-Combination-FIBSEM-Technology-Laser#.VWjw2M9VhBc>.
- [36] M. P. Echlin, M. Straw, S. Randolph, J. Filevich, and T. M. Pollock, 'The TriBeam system: Femtosecond laser ablation in situ SEM', *Mater. Charact.*, vol. 100, pp. 1–12, Feb. 2015, doi: 10.1016/j.matchar.2014.10.023.
- [37] W. M. Steen and J. Mazumder, *Laser Material Processing*. London: Springer London, 2010.
- [38] K. Sugioka, M. Meunier, and A. Piqué, Eds., *Laser precision microfabrication*. Berlin: Springer, 2010.
- [39] R. L. McCally, 'Measurement of Gaussian beam parameters', *Appl. Opt.*, vol. 23, no. 14, pp. 2227–2227, 1984.
- [40] IDEX Optics & Photonics, 'Guassian Beam Propagation'. [Online]. Available: http://marketplace.idexop.com/store/SupportDocuments/Gaussian_Beam_PropagationWEB.pdf.
- [41] R. Paschotta, 'Flat-top Beams', *Flat-top Beams*, 2010. http://www.rp-photonics.com/flat_top_beams.html.
- [42] ISO, 'ISO 11670', *BS EN*, 2003.
- [43] J. M. Khosrofian and B. A. Garetz, 'Measurement of a Gaussian laser beam diameter through the direct inversion of knife-edge data', *Appl. Opt.*, vol. 22, no. 21, p. 3406, Nov. 1983, doi: 10.1364/AO.22.003406.
- [44] P. J. Shayler, 'Laser beam distribution in the focal region', *Appl. Opt.*, vol. 17, no. 17, p. 2673, Sep. 1978, doi: 10/ft4kz5.
- [45] P. B. Chapple, 'Beam waist and M2 measurement using a finite slit', *Opt. Eng.*, vol. 33, no. 7, pp. 2461–2466, 1994.
- [46] J. G. Webster and H. Eren, *Measurement, Instrumentation, and Sensors Handbook, Second Edition: Electromagnetic, Optical, Radiation, Chemical, and Biomedical Measurement*. CRC Press, 2014.
- [47] Photon Inc., 'Measuring Laser Position & Pointing Stability'. 2016, [Online]. Available: http://www.ophiropt.com/user_files/laser/beamprofilers/LaserPointingStability.pdf.
- [48] C. R. Phipps and B. S. Luk'ianchuk, Eds., *Laser ablation and its applications*. New York, N.Y: Springer, 2007.
- [49] B. Rethfeld, D. S. Ivanov, M. E. Garcia, and S. I. Anisimov, 'Modelling ultrafast laser ablation', *J. Phys. Appl. Phys.*, vol. 50, no. 19, p. 193001, May 2017, doi: 10/gf7mvg.
- [50] B. Rethfeld, K. Sokolowski-Tinten, D. von der Linde, and S. I. Anisimov, 'Timescales in the response of materials to femtosecond laser excitation', *Appl. Phys. A*, vol. 79, no. 4–6, pp. 767–769, Sep. 2004, doi: 10/br9jxs.

- [51] 'Transverse mode', *Wikipedia*. May 04, 2019, Accessed: Jun. 02, 2020. [Online]. Available: https://en.wikipedia.org/w/index.php?title=Transverse_mode&oldid=895527773.
- [52] 'πShaper Series'. <http://pishaper.com/shaper.html> (accessed Jun. 02, 2020).
- [53] D. J. Hwang, C. P. Grigoropoulos, and T. Y. Choi, 'Efficiency of silicon micromachining by femtosecond laser pulses in ambient air', *J. Appl. Phys.*, vol. 99, no. 8, p. 083101, Apr. 2006, doi: 10/d6bg93.
- [54] X. Zeng, X. L. Mao, R. Greif, and R. E. Russo, 'Experimental investigation of ablation efficiency and plasma expansion during femtosecond and nanosecond laser ablation of silicon', *Appl. Phys. A*, vol. 80, no. 2, pp. 237–241, Feb. 2005, doi: 10/bvvxrs.
- [55] M. Amer, M. El Ashry, L. Dosser, K. Hix, J. Maguire, and B. Irwin, 'Femtosecond versus nanosecond laser machining: Comparison of induced stresses and structural changes in silicon wafers', *Appl. Surf. Sci.*, vol. 242, pp. 162–167, Mar. 2005, doi: 10/bf3msn.
- [56] A. Semerok, B. SALLÉ, J.-F. WAGNER, and G. Petite, 'Femtosecond, picosecond, and nanosecond laser microablation: Laser plasma and crater investigation', *Laser Part. Beams*, vol. 20, Mar. 2002, doi: 10/c8wg4k.
- [57] 'Classification of Polarization'. <http://hyperphysics.phy-astr.gsu.edu/hbase/phyopt/polclas.html> (accessed Jun. 02, 2020).
- [58] O. Varlamova, F. Costache, M. Ratzke, and J. Reif, 'Control parameters in pattern formation upon femtosecond laser ablation', *Appl. Surf. Sci.*, vol. 253, pp. 7932–7936, Jul. 2007, doi: 10/d5f45g.
- [59] J. Reif, O. Varlamova, and F. Costache, 'Femtosecond laser induced nanostructure formation: self-organization control parameters', *Appl. Phys. A*, vol. 92, no. 4, pp. 1019–1024, Sep. 2008, doi: 10/bshkj8.
- [60] T. Sarnet *et al.*, 'Femtosecond laser for black silicon and photovoltaic cells', San Jose, CA, Feb. 2008, p. 688119, doi: 10/d3sfz4.
- [61] 4000 Central Florida Blvd Orl, o, Florida, 32816 | 407 823 2000 Comments, and F. | © U. of C. Florida, 'UCF Researchers Record World Record Laser Pulse', *UCF News - University of Central Florida Articles - Orlando, FL News*. <http://today.ucf.edu/ucf-researchers-record-world-record-laser-pulse/> (accessed Feb. 26, 2016).
- [62] K. Sugioka and Y. Cheng, 'Ultrafast lasers—reliable tools for advanced materials processing', *Light Sci. Appl.*, vol. 3, no. 4, p. e149, Apr. 2014, doi: 10.1038/lssa.2014.30.
- [63] B. N. Chichkov, C. Momma, S. Nolte, F. von Alvensleben, and A. Tünnermann, 'Femtosecond, picosecond and nanosecond laser ablation of solids', *Appl. Phys. A*, vol. 63, no. 2, pp. 109–115, Aug. 1996, doi: 10.1007/BF01567637.
- [64] S. Nolte *et al.*, 'Ablation of metals by ultrashort laser pulses', *J. Opt. Soc. Am. B*, vol. 14, no. 10, p. 2716, Oct. 1997, doi: 10.1364/JOSAB.14.002716.

- [65] J. Bonse, S. Baudach, J. Krüger, W. Kautek, and M. Lenzner, 'Femtosecond laser ablation of silicon—modification thresholds and morphology', *Appl. Phys. A*, vol. 74, no. 1, pp. 19–25, Jan. 2002, doi: 10/ff28f8.
- [66] 'Machining with Ultrafast Laser Pulses'. <http://www.cmxr.com/Education/Short.html>.
- [67] W. O'Neill, 'Fundamentals of laser induced processes'. EPSRC Doctoral Training Centre in Ultra Precision, 2014.
- [68] I. F. Almog, M. S. Bradley, and V. Bulovic, 'The Lorentz Oscillator and its Applications'. MIT.
- [69] A. M. Fox and D. of P. and A. M. Fox, *Optical Properties of Solids*. Oxford University Press, 2001.
- [70] W. Kautek and J. Krueger, 'Femtosecond pulse laser ablation of metallic, semiconducting, ceramic, and biological materials', Vienna, Austria, Sep. 1994, p. 600, doi: 10/bzgr2m.
- [71] L. Torrisi, A. Borrielli, and D. Margarone, 'Study on the ablation threshold induced by pulsed lasers at different wavelengths', *Nucl. Instrum. Methods Phys. Res. Sect. B Beam Interact. Mater. At.*, vol. 255, no. 2, pp. 373–379, Feb. 2007, doi: 10/cnzs9p.
- [72] E. D. Palik, *Handbook of Optical Constants of Solids*. Academic Press, 1998.
- [73] M. S. Brown and C. B. Arnold, 'Fundamentals of Laser-Material Interaction and Application to Multiscale Surface Modification', in *Laser Precision Microfabrication*, K. Sugioka, M. Meunier, and A. Piqué, Eds. Berlin, Heidelberg: Springer, 2010, pp. 91–120.
- [74] J. Thorstensen and S. Erik Foss, 'Temperature dependent ablation threshold in silicon using ultrashort laser pulses', *J. Appl. Phys.*, vol. 112, no. 10, p. 103514, Nov. 2012, doi: 10/gg7r4m.
- [75] F. Giessibl, 'Advances in atomic force microscopy', *Rev. Mod. Phys.*, vol. 75, no. 3, pp. 949–983, Jul. 2003, doi: 10.1103/RevModPhys.75.949.
- [76] Y. Seo and W. Jhe, 'Atomic force microscopy and spectroscopy', *Rep. Prog. Phys.*, vol. 71, no. 1, p. 016101, Jan. 2008, doi: 10.1088/0034-4885/71/1/016101.
- [77] N. Jalili and K. Laxminarayana, 'A review of atomic force microscopy imaging systems: application to molecular metrology and biological sciences', *Mechatronics*, vol. 14, no. 8, pp. 907–945, Oct. 2004, doi: 10.1016/j.mechatronics.2004.04.005.
- [78] K. D. Vernon-Parry, 'Scanning electron microscopy: an introduction', *III-Vs Rev.*, vol. 13, no. 4, pp. 40–44, Jul. 2000, doi: 10.1016/S0961-1290(00)80006-X.
- [79] J.-L. Pouchou, D. Boivin, P. Beauchêne, G. L. Besnerais, and F. Vignon, '3D Reconstruction of Rough Surfaces by SEM Stereo Imaging', *Microchim. Acta*, vol. 139, no. 1–4, pp. 135–144, May 2002, doi: 10.1007/s006040200052.
- [80] R. Szeliski, *Computer vision: algorithms and applications*. Springer Science & Business Media, 2010.

- [81] A. D. H. Thomas, M. G. Rodd, J. D. Holt, and C. J. Neill, 'Real-time Industrial Visual Inspection: A Review', *Real-Time Imaging*, vol. 1, no. 2, pp. 139–158, Jun. 1995, doi: 10.1006/rtim.1995.1014.
- [82] M. Short, M. Madden, and H. Stefanova, 'Machine Vision: The key considerations for successful visual inspection'. Optima.
- [83] G. R. Bradski and A. Kaehler, *Learning OpenCV: [computer vision with the OpenCV library]*, 1. ed., [Nachdr.]. Beijing: O'Reilly, 2011.
- [84] A. Fercher, W. Drexler, C. Hitzenberger, and T. Lasser, 'Optical coherence tomography - principles and applications', *Rep. Prog. Phys.*, vol. 66, no. 2, pp. 239–303, Feb. 2003, doi: 10.1088/0034-4885/66/2/204.
- [85] 'Thor Labs GANYMEDE-II-HR-Manual'. .
- [86] J. X. Z. Yu, P. J. L. Webster, B. Y. C. Leung, and J. M. Fraser, 'High-quality percussion drilling of silicon with a CW fiber laser', in *Laser Applications in Microelectronic and Optoelectronic Manufacturing XV*, 2010, vol. 7584, doi: 10.1117/12.842616.
- [87] P. J. Webster, J. X. Yu, B. Y. Leung, M. D. Anderson, V. X. Yang, and J. M. Fraser, 'In situ 24 kHz coherent imaging of morphology change in laser percussion drilling', *Opt. Lett.*, vol. 35, no. 5, pp. 646–648, 2010.
- [88] Y. Ji, C. V. Vlack, P. J. L. Webster, and J. M. Fraser, 'Real-time depth monitoring of galvo-telecentric laser machining by inline coherent imaging', in *2013 Conference on Lasers and Electro-Optics (CLEO)*, Jun. 2013, pp. 1–2, doi: 10.1364/CLEO_QELS.2013.JTh2A.05.
- [89] M. K. Kim, 'Principles and techniques of digital holographic microscopy', *J. Photonics Energy*, pp. 018005-018005–50, 2010, doi: 10.1117/6.0000006.
- [90] 'Digital Holographic Microscope Overview - Lyncée Tec', *Lyncee Tec*. <http://www.lynceetec.com/dhm-digital-holographic-microscopy/> (accessed Aug. 25, 2015).
- [91] Princeton Instruments, 'Raman Spectroscopy Basics'. Princeton Instruments, 2011, Accessed: Feb. 23, 2016. [Online]. Available: http://web.pdx.edu/~larosaa/Applied_Optics_464-564/Projects_Optics/Raman_Spectroscopy/Raman_Spectroscopy_Basics_PRIN_CETON-INSTRUMENTS.pdf.
- [92] E. V. Efremov, F. Ariese, and C. Gooijer, 'Achievements in resonance Raman spectroscopy: Review of a technique with a distinct analytical chemistry potential', *Anal. Chim. Acta*, vol. 606, no. 2, pp. 119–134, Jan. 2008, doi: 10.1016/j.aca.2007.11.006.
- [93] A. C. Ferrari *et al.*, 'Raman Spectrum of Graphene and Graphene Layers', *Phys. Rev. Lett.*, vol. 97, no. 18, p. 187401, Oct. 2006, doi: 10.1103/PhysRevLett.97.187401.
- [94] M. S. Dresselhaus, G. Dresselhaus, A. Jorio, A. G. Souza Filho, and R. Saito, 'Raman spectroscopy on isolated single wall carbon nanotubes', *Carbon*, vol. 40, no. 12, pp. 2043–2061, 2002, doi: 10.1016/S0008-6223(02)00066-0.

- [95] N. Bobroff, 'Recent advances in displacement measuring interferometry', *Meas. Sci. Technol.*, vol. 4, no. 9, p. 907, 1993, doi: 10.1088/0957-0233/4/9/001.
- [96] Menlo Systems, 'MENLO-FC8004 Data Sheet'. 2014, [Online]. Available: <http://www.menlosystems.com/assets/datasheets/MENLO-FC8004-D-EN-2014-07-3w.pdf>.
- [97] D. Reid, 'Frequency-comb metrology for manufacturing', 2016.
- [98] R. Eason, Ed., *Pulsed laser deposition of thin films: applications-led growth of functional materials*. Hoboken, N.J: Wiley-Interscience, 2007.
- [99] M. Han *et al.*, 'Plume dynamics during film and nanoparticles deposition by pulsed laser ablation', *Phys. Lett. A*, vol. 302, no. 4, pp. 182–189, Sep. 2002, doi: 10/c8v6h3.
- [100] D. B. Geohegan, 'Fast intensified-CCD photography of YBa₂Cu₃O_{7-x} laser ablation in vacuum and ambient oxygen', *Appl. Phys. Lett.*, vol. 60, no. 22, pp. 2732–2734, Jun. 1992, doi: 10/dkwcw3.
- [101] J. C. S. Kools, T. S. Baller, S. T. De Zwart, and J. Dieleman, 'Gas flow dynamics in laser ablation deposition', *J. Appl. Phys.*, vol. 71, no. 9, pp. 4547–4556, May 1992, doi: 10/cb84n6.
- [102] T. E. Itina, J. Hermann, Ph. Delaporte, and M. Sentis, 'Combined continuous–microscopic modeling of laser plume expansion', *Appl. Surf. Sci.*, vol. 208–209, pp. 27–32, Mar. 2003, doi: 10/d34qvs.
- [103] J. L. Bobin, Y. A. Durand, Ph. P. Langer, and G. Tonon, 'Shock-Wave Generation in Rarefied Gases by Laser Impact on Beryllium Targets', *J. Appl. Phys.*, vol. 39, no. 9, pp. 4184–4189, Aug. 1968, doi: 10/bcwwsh.
- [104] R. F. Wood, K. R. Chen, J. N. Leboeuf, A. A. Puretzky, and D. B. Geohegan, 'Dynamics of Plume Propagation and Splitting during Pulsed-Laser Ablation', *Phys. Rev. Lett.*, vol. 79, no. 8, pp. 1571–1574, Aug. 1997, doi: 10/djrrhs.
- [105] K. Schildbach, 'Simple analytic model including shielding by the plume during excimer laser ablation of polyimide', The Hague, Netherlands, Aug. 1990, pp. 60–65, doi: 10/b7mw72.
- [106] B. S. Haq, H. U. Khan, K. Alam, M. Mateenullah, S. Attaullah, and I. Zari, 'Femtosecond pulsed laser ablation of polyimide at oblique angles for medical applications', *Appl. Opt.*, vol. 54, no. 24, p. 7413, Aug. 2015, doi: 10/gg7r4v.
- [107] D. S. George, A. Onischenko, and A. S. Holmes, 'On the angular dependence of focused laser ablation by nanosecond pulses in solgel and polymer materials', *Appl. Phys. Lett.*, vol. 84, no. 10, pp. 1680–1682, Mar. 2004, doi: 10/fqk3kx.
- [108] J. Pedder and A. Holmes, 'A study of angular dependence in the ablation rate of polymers by nanosecond pulses - art. no. 61061B', *Proc. SPIE - Int. Soc. Opt. Eng.*, vol. 6106, Jan. 2005, doi: 10/cf24f8.
- [109] J. Pedder, A. Holmes, and P. Dyer, 'Improved model for the angular dependence of excimer laser ablation rates in polymer materials', *Appl. Phys. Lett.*, vol. 95, pp. 174105–174105, Nov. 2009, doi: 10/c4rcks.






- [110] S. Amoruso, R. Bruzzese, N. Spinelli, and R. Velotta, 'Characterization of laser-ablation plasmas', *J. Phys. B At. Mol. Opt. Phys.*, vol. 32, no. 14, pp. R131–R172, Jul. 1999, doi: 10/brr9cj.
- [111] H. R. Griem, *Principles of Plasma Spectroscopy*. Cambridge University Press, 2005.
- [112] R. E. Russo, X. L. Mao, H. C. Liu, J. H. Yoo, and S. S. Mao, 'Time-resolved plasma diagnostics and mass removal during single-pulse laser ablation', *Appl. Phys. A*, vol. 69, no. 1, pp. S887–S894, Dec. 1999, doi: 10/dfk3s5.
- [113] D. Breitling, H. Schittenhelm, P. Berger, F. Dausinger, and H. Hügel, 'Shadowgraphic and interferometric investigations on Nd:YAG laser-induced vapor/plasma plumes for different processing wavelengths', *Appl. Phys. A*, vol. 69, no. 1, pp. S505–S508, Dec. 1999, doi: 10/bh738t.
- [114] J. H. Yoo, S. H. Jeong, R. Greif, and R. E. Russo, 'Explosive change in crater properties during high power nanosecond laser ablation of silicon', *J. Appl. Phys.*, vol. 88, no. 3, pp. 1638–1649, Jul. 2000, doi: 10/c77t2d.
- [115] H. Schittenhelm, G. Callies, A. Straub, P. Berger, and H. Hügel, 'Measurements of wavelength-dependent transmission in excimer laser-induced plasma plumes and their interpretation', *J. Phys. Appl. Phys.*, vol. 31, no. 4, pp. 418–427, Feb. 1998, doi: 10/dw2wgz.
- [116] S.-B. Wen, X. Mao, R. Greif, and R. E. Russo, 'Laser ablation induced vapor plume expansion into a background gas. II. Experimental analysis', *J. Appl. Phys.*, vol. 101, no. 2, p. 023115, Jan. 2007, doi: 10/bv3tzt.
- [117] S. Tao, Y. Zhou, B. Wu, and Y. Gao, 'Infrared long nanosecond laser pulse ablation of silicon: Integrated two-dimensional modeling and time-resolved experimental study', *Appl. Surf. Sci.*, vol. 258, no. 19, pp. 7766–7773, Jul. 2012, doi: 10/f3zv8x.
- [118] E. Amer, P. Gren, and M. Sjö Dahl, 'Laser-ablation-induced refractive index fields studied using pulsed digital holographic interferometry', *Opt. Lasers Eng.*, vol. 47, no. 7, pp. 793–799, Jul. 2009, doi: 10/b58vzq.
- [119] M. Centurion, Y. Pu, Z. Liu, D. Psaltis, and T. W. Hänsch, 'Holographic recording of laser-induced plasma', *Opt. Lett.*, vol. 29, no. 7, p. 772, Apr. 2004, doi: 10/d36fwq.
- [120] J. W. Goodman and R. W. Lawrence, 'Digital image formation from electronically detected holograms', *Appl. Phys. Lett.*, vol. 11, no. 3, pp. 77–79, Aug. 1967, doi: 10/dcw6z8.
- [121] E. Amer, P. Gren, and M. Sjö Dahl, 'Shock wave generation in laser ablation studied using pulsed digital holographic interferometry', *J. Phys. Appl. Phys.*, vol. 41, no. 21, p. 215502, Nov. 2008, doi: 10/ckvd2w.
- [122] P. Gren, S. Schedin, and X. Li, 'Tomographic reconstruction of transient acoustic fields recorded by pulsed TV holography', *Appl. Opt.*, vol. 37, no. 5, pp. 834–840, Feb. 1998, doi: 10/bqc4bw.
- [123] 'Gaussian Beam Propagation | Edmund Optics'. <https://www.edmundoptics.eu/knowledge-center/application-notes/lasers/gaussian-beam-propagation/> (accessed Jun. 12, 2020).

- [124] Thor Labs, 'F-Theta Scan Lenses', 2015.
http://www.thorlabs.de/newgrouppage9.cfm?objectgroup_id=6430.
- [125] J. M. Liu, 'Simple technique for measurements of pulsed Gaussian-beam spot sizes', *Opt. Lett.*, vol. 7, no. 5, p. 196, May 1982, doi: 10.1364/OL.7.000196.
- [126] D. Liu *et al.*, 'Ultrafast parallel laser processing of materials for high throughput manufacturing', *Proc. LAMP*, pp. 09–021, 2009.

APPENDICES

Appendix A - Holographic Captures GIFS

Normal	15 Degrees	30 Degrees	45 Degrees
			
0.539 W	0.3256 W	0.334 W	0.3116 W
			
1.3235 W	1.628 W	1.67 W	1.558 W
			
2.655 W	4.07 W	4.175 W	3.895 W
			
3.98 W	8.14 W	8.35 W	5.77 W

			
5.77 W	11.6 W	11.6 W	7.79 W
			
			11.685 W

Appendix B - Code Segments

B.1 Autofocus for microscope

```
1. private void uScope_focus_check(Boolean zoom)
2. {
3.     icImagingControl1.OverlayBitmap.Enable = false;
4.
5.     ImageProcessing IPForm = new ImageProcessing();
6.
7.     IPForm.Show();
8.     IPForm.Activate();
9.
10.    double Focus_max_area = 0;
11.    double Laplace_max = 0;
12.    double scan_length = 0;
13.    double scan_length_2 = 0;
14.    double scan_length_3 = 0;
15.    double scan_steps;
16.    int iteration = 0;
17.    int cycle_count = 0;
18.    Boolean Completed_Gross_Pass = false;
19.
20.    if (zoom == false)
21.    {
22.        scan_length = 0.5;
23.        scan_length_2 = 0.1;
24.        scan_length_3 = 0.01;
25.        scan_steps = scan_length / 0.01;
26.    }
27.    else
28.    {
29.        scan_length = 0.3;
30.        scan_length_2 = 0.02;
31.        scan_length_3 = 0.005;
32.        scan_steps = scan_length / 0.001;
33.    }
34.
35.    double Daxis_intial = myController.Commands.Status.AxisStatus("D", AxisStatusSignal.ProgramPositionFeedback);
36.    double Daxis_max = 0;
37.
38.    while (AlignmentFocus_Container.Focused != true)
39.    {
40.        for (int i = 0; i < scan_steps; i++)
41.        {
42.            myController.Commands.Motion.Setup.Absolute();
43.            myController.Commands.Motion.Linear("D", Daxis_intial + scan_length / 2
- scan_length / scan_steps * i, 1);
44.
45.            icImagingControl1.MemorySnapImage(1000);
46.            Bitmap live_bmp = icImagingControl1.ImageActiveBuffer.Bitmap;
47.
48.            //string file_directory = "C:/Users/User/Desktop/Share/Chris/Laplace" +
scan_length.ToString();
49.            //System.IO.Directory.CreateDirectory(file_directory);
50.            //live_bmp.Save(file_directory + "/" + i + ".bmp");
51.
52.            IPForm.DetectHole(15, live_bmp, true);
53.
54.            if (AlignmentFocus_Container.Max_Area >= Focus_max_area)
55.            {
56.                Focus_max_area = AlignmentFocus_Container.Max_Area;
57.                Daxis_max = myController.Commands.Status.AxisStatus("D", AxisStatusSignal.ProgramPositionFeedback);
```

```

58.
59.         myController.Commands.Motion.Setup.Incremental();
60.         myController.Commands.Motion.Linear("X", -
AlignmentFocus_Container.X_Correction_MM, 1);
61.         myController.Commands.Motion.Linear("Y", -
AlignmentFocus_Container.Y_Correction_MM, 1);
62.         myController.Commands.Motion.Setup.Absolute(); ;
63.
64.         iteration = i;
65.     }
66.
67.         IPForm.StepValue((Daxis_intial + scan_length / 2 - scan_length / scan_st
eps * i).ToString());
68.         IPForm.IterationValue(i.ToString());
69.     }
70.
71.     Daxis_intial = Daxis_max;
72.     scan_length = scan_length_2;
73.     scan_steps = scan_length_2 / 0.0001;
74.
75.
76.     if (iteration >= (scan_steps / 2 - scan_steps / 10) && iteration <= (scan_st
eps / 2 + scan_steps / 10) && Completed_Gross_Pass == true)
77.     {
78.         AlignmentFocus_Container.Focused = true;
79.     }
80.
81.     if (cycle_count == 2)
82.     {
83.         AlignmentFocus_Container.Focused = true;
84.     }
85.
86.     Completed_Gross_Pass = true;
87.     cycle_count = cycle_count + 1;
88. }
89.
90. // Laplace Transform Scan
91.
92. Daxis_intial = Daxis_max;
93. scan_length = scan_length_3;
94. scan_steps = scan_length_3 / 0.0001;
95.
96. for (int i = 0; i < scan_steps; i++)
97. {
98.     myController.Commands.Motion.Setup.Absolute();
99.     myController.Commands.Motion.Linear("D", Daxis_intial + scan_length / 2 - sc
an_length / scan_steps * i, 1);
100.
101.     icImagingControl1.MemorySnapImage(1000);
102.     Bitmap live_bmp = icImagingControl1.ImageActiveBuffer.Bitmap;
103.
104.     IPForm.focus_determination(live_bmp);
105.
106.     if (AlignmentFocus_Container.Laplace_std >= Laplace_max)
107.     {
108.         Laplace_max = AlignmentFocus_Container.Laplace_std;
109.         Daxis_max = myController.Commands.Status.AxisStatus("D", AxisStat
usSignal.ProgramPositionFeedback);
110.         iteration = i;
111.     }
112.
113.     IPForm.StepValue((Daxis_intial + scan_length / 2 - scan_length / scan
_steps * i).ToString());
114.     IPForm.IterationValue(i.ToString());
115. }
116.
117. myController.Commands.Motion.Linear("D", Daxis_max, 1);
118.
119. icImagingControl1.OverlayBitmap.Enable = true;

```

```

120.         IPForm.Close();
121.         AlignmentFocus_Container.Focused = false;
122.         Completed_Gross_Pass = false;
123.         Focus_max_area = 0;
124.         Laplace_max = 0;
125.     }

```

B.2 Autofocus of laser

```

1. private void FindFocus_Xaxis(double Z_Scan_length, int Mark_Number, double Line_Spac
ing, double MarkLength)
2.     {
3.         int NumberOfLines = 0;
4.
5.         double LaserFocus_Xaxis_Total = 0;
6.         double LaserFocus_Yaxis_Total = 0;
7.         double LaserFocus_Zaxis_Total = 0;
8.
9.         double[] Machined_X_Pos = new double[Mark_Number];
10.        double[] Machined_Y_Pos = new double[Mark_Number];
11.        double[] Machined_Z_Pos = new double[Mark_Number];
12.
13.        int pos_count = 0; // Variable for recording position of minimum track w
idth - starts on zero for X
14.
15.        myController.Commands.Motion.Linear("D", 0, 1);
16.
17.        shutter_open();
18.        aommode_0();
19.        aomgate_high_trigger();
20.        talisker_attenuation(96); // 99 for 20x + Wheel ATT
21.        watt_pilot_attenuation(0);
22.
23.        for (int hold = 0; hold < 4; hold++)
24.        {
25.            if (hold == 0)
26.            {
27.                Movement_3D_ablation(Refined_Xaxis[hold] + MarkLength / 2, Refin
ed_Yaxis[hold] - 0.5, 0, 5);
28.            }
29.            else if (hold == 1)
30.            {
31.                Movement_3D_ablation(Refined_Xaxis[hold] + MarkLength / 2, Refin
ed_Yaxis[hold] + (Line_Spacing * Mark_Number) + 0.5, 0, 5);
32.            }
33.            else if (hold == 2)
34.            {
35.                Movement_3D_ablation(Refined_Xaxis[hold] + MarkLength / 2, Refin
ed_Yaxis[hold] + (Line_Spacing * Mark_Number) + 0.5, 0, 5);
36.            }
37.            else if (hold == 3)
38.            {
39.                Movement_3D_ablation(Refined_Xaxis[hold] + MarkLength / 2, Refin
ed_Yaxis[hold] - 0.5, 0, 5);
40.            }
41.        }
42.
43.        // Ensure Z axis is at rough focus minus half scan length
44.
45.        myController.Commands.Motion.Setup.Incremental();
46.        myController.Commands.Motion.Linear("Z", -(Z_Scan_length / 2), 1);
47.
48.        // X axis find focus
49.        for (int i = 0; i < Mark_Number; i++)
50.        {
51.            // Change Z height
52.            myController.Commands.Motion.Setup.Incremental();

```

```

53.         myController.Commands.Motion.Linear("Z", (Z_Scan_length / Mark_N
umber), 1);
54.         Machined_X_Pos[i] = myController.Commands.Status.AxisStatus("X",
AxisStatusSignal.ProgramPositionFeedback) - MarkLength / 2;
55.         Machined_Y_Pos[i] = myController.Commands.Status.AxisStatus("Y",
AxisStatusSignal.ProgramPositionFeedback);
56.         Machined_Z_Pos[i] = myController.Commands.Status.AxisStatus("Z",
AxisStatusSignal.ProgramPositionFeedback);
57.         myController.Commands.PSO.Control("X", Aerotech.A3200.Commands.P
soMode.On);
58.         myController.Commands.Motion.Linear("X", -MarkLength, 1);
59.         myController.Commands.PSO.Control("X", Aerotech.A3200.Commands.P
soMode.Off);
60.         myController.Commands.Motion.Linear("X", +MarkLength, 1);
61.         myController.Commands.Motion.Linear("Y", -(Line_Spacing), 1);
62.         myController.Commands.Motion.Setup.Absolute();
63.     }
64. }
65.
66. // Inspect Lines and record minimum line thickness
67.
68.
69.     ImageProcessing IPForm = new ImageProcessing();
70.
71.     IPForm.Show();
72.     IPForm.Activate();
73.
74.     for (int hold = 0; hold < 4; hold++)
75.     {
76.         if (hold == 0)
77.         {
78.             Movement_3D_uScope(Refined_Xaxis[hold], Refined_Yaxis[hold] - 0.
5, 0, false);
79.         }
80.         else if (hold == 1)
81.         {
82.             Movement_3D_uScope(Refined_Xaxis[hold], Refined_Yaxis[hold] + (L
ine_Spacing * Mark_Number) + 0.5, 0, false);
83.         }
84.         else if (hold == 2)
85.         {
86.             Movement_3D_uScope(Refined_Xaxis[hold], Refined_Yaxis[hold] + (L
ine_Spacing * Mark_Number) + 0.5, 0, false);
87.         }
88.         else if (hold == 3)
89.         {
90.             Movement_3D_uScope(Refined_Xaxis[hold], Refined_Yaxis[hold] - 0.
5, 0, false);
91.         }
92.
93.         #region Version 2
94.
95.         LaserFocus_Xaxis_Total = 0;
96.         LaserFocus_Yaxis_Total = 0;
97.         LaserFocus_Zaxis_Total = 0;
98.         NumberOfLines = 0;
99.
100.        for (int i = 0; i < Mark_Number; i++)
101.        {
102.            icImagingControl1.OverlayBitmap.Enable = false;
103.
104.            Thread.Sleep(1500);
105.
106.            icImagingControl1.MemorySnapImage(1000);
107.            Bitmap live_bmp = icImagingControl1.ImageActiveBuffer.Bit
map;
108.
109.            IPForm.Detect_Line(40, live_bmp);
110.

```

```

111.             if (AlignmentFocus_Container.Feature_Visible == true)
112.             {
113.                 LaserFocus_Xaxis_Total = LaserFocus_Xaxis_Total + Mac
hined_X_Pos[i];
114.                 LaserFocus_Yaxis_Total = LaserFocus_Yaxis_Total + Mac
hined_Y_Pos[i];
115.                 LaserFocus_Zaxis_Total = LaserFocus_Zaxis_Total + Mac
hined_Z_Pos[i];
116.                 NumberOfLines++;
117.
118.                 string save_dir = universal_path + "\\Focus Lines\\"
+ pos_count;
119.                 System.IO.Directory.CreateDirectory(save_dir);
120.
121.                 string save_image = save_dir + "\\" + Machined_Z_Pos[
i].ToString() + ".bmp";
122.
123.                 Thread.Sleep(500);
124.
125.                 icImagingControl1.MemorySnapImage();
126.                 icImagingControl1.MemorySaveImage(save_image);
127.
128.             }
129.
130.             icImagingControl1.OverlayBitmap.Enable = true;
131.             AlignmentFocus_Container.Feature_Visible = false;
132.
133.             myController.Commands.Motion.Setup.Incremental();
134.             myController.Commands.Motion.Linear("Y", -
(Line_Spacing), 1);
135.             myController.Commands.Motion.Setup.Absolute();
136.         }
137.
138.         LaserFocus_Xaxis[pos_count] = LaserFocus_Xaxis_Total / Number
OfLines;
139.         LaserFocus_Yaxis[pos_count] = LaserFocus_Yaxis_Total / Number
OfLines;
140.         LaserFocus_Zaxis[pos_count] = LaserFocus_Zaxis_Total / Number
OfLines;
141.
142.         pos_count = pos_count + 1;
143.
144.         #endregion
145.     }
146.     IPForm.Close();
147.     shutter_closed();
148.
149.     double [] Focus_A_coords = { LaserFocus_Xaxis[0], LaserFocus_Yaxi
s[0], LaserFocus_Zaxis[0] };
150.     double [] Focus_B_coords = { LaserFocus_Xaxis[1], LaserFocus_Yaxi
s[1], LaserFocus_Zaxis[1] };
151.     double [] Focus_C_coords = { LaserFocus_Xaxis[2], LaserFocus_Yaxi
s[2], LaserFocus_Zaxis[2] };
152.     double [] Focus_D_coords = { LaserFocus_Xaxis[3], LaserFocus_Yaxi
s[3], LaserFocus_Zaxis[3] };
153. }

```

B.3 Tilt Correction Methodology

```

1. private void PlaneFit(double [] A, double [] B, double [] C, double [] D)
2.
3.     {
4.         double[] x = { A[0], B[0], C[0], D[0] };
5.         double[] y = { A[1], B[1], C[1], D[1] };
6.         double[] z = { A[2], B[2], C[2], D[2] };
7.

```

```

8.      Vector<double> X = Vector<double>.Build.DenseOfArray(x);
9.      Vector<double> Y = Vector<double>.Build.DenseOfArray(y);
10.     Vector<double> Z = Vector<double>.Build.DenseOfArray(z);
11.
12.     // number of coords
13.     var n = x.Length;
14.     // sum of X
15.     var SX = X.Sum();
16.     // sum of Y
17.     var SY = Y.Sum();
18.     // sum of X squared
19.     var SX2 = X.PointwisePower(2).Sum();
20.     // sum of Y squared
21.     var SY2 = Y.PointwisePower(2).Sum();
22.     // sum of X * Y
23.     var SXY = X.PointwiseMultiply(Y).Sum();
24.     // sum of Z
25.     var SZ = Z.Sum();
26.     // sum of X * Z
27.     var SXZ = X.PointwiseMultiply(Z).Sum();
28.     // Sum of Y * Z
29.     var SYZ = Y.PointwiseMultiply(Z).Sum();
30.
31.     // Sum Matrix
32.
33.     //Matrix<double> SumMatrix = Matrix<double>.Build.Dense(3, 3);
34.
35.     var M = Matrix<double>.Build;
36.
37.     var SumMatrix = M.DenseOfArray(new[,] {{ n, SX, SY},
38.                                           {SX, SX2, SXY},
39.                                           { SY, SXY, SY2}});
40.
41.     // Sum Vector
42.
43.     var V = Vector<double>.Build;
44.
45.     var SumVector = V.DenseOfArray(new[] { SZ, SXZ, SYZ });
46.
47.     // Find coefficients Matrix \ Vector
48.
49.     var coefficients = SumMatrix.QR().Solve(SumVector);
50.
51.     //MessageBox.Show("calculated");
52.
53.     // Define Plane Vector
54.
55.     var A_Plane_Vector_1 = Vector<double>.Build.Dense(new[] { -
coefficients[1], -coefficients[2], 1 });
56.
57.     var theta = -
1 * (Math.Atan(A_Plane_Vector_1[0] / A_Plane_Vector_1[2]));
58.
59.     var theta_degrees = theta * (180 / Math.PI);
60.
61.     // Calculate rotation around Y
62.
63.     var rot_y_matrix = M.DenseOfArray(new[,] { { Math.Cos(theta), 0, Math.
Sin(theta) },
64.         { 0, 1,
0 },
65.         { -
Math.Sin(theta), 0, Math.Cos(theta) }});
66.
67.     var A_Plane_Vector_2 = rot_y_matrix * A_Plane_Vector_1;
68.
69.     // Calculate rotation around X
70.
71.     var phi = (Math.Atan(A_Plane_Vector_2[1] / A_Plane_Vector_2[2]));

```

```

72.         var phi_degrees = phi * (180 / Math.PI);
73.
74.         theta_hold = theta_hold + theta_degrees;
75.         phi_hold = phi_hold + phi_degrees;
76.
77.         // Apply rotation angles
78.
79.         myController.Commands.Motion.Setup.Absolute();
80.         //MessageBox.Show(theta_hold.ToString());
81.         myController.Commands.Motion.Linear("A", theta_hold, 1);
82.         //MessageBox.Show(phi_hold.ToString());
83.         myController.Commands.Motion.Linear("B", phi_hold, 1);
84.
85.     }

```

B.4 Determining relative centre of rotary axis position

```

1. private void btn_RotationalCentre_Click(object sender, EventArgs e)
2. {
3.     btn_PosJogD.Enabled = false;
4.     btn_NegJogD.Enabled = false;
5.
6.     double CentreTestRotation = 10;
7.
8.     // Move to rough marker position
9.
10.    myController.Commands.Motion.Setup.Absolute();
11.    //myController.Commands.Axes["X", "Y"].Motion.Linear(new double[] { Refined_Xaxis[1], Refined_Yaxis[1] }, 1);
12.    //myController.Commands.Motion.Linear("D", microscope_focus, 1);
13.
14.    Movement_3D_uScope(Refined_Xaxis[1], Refined_Yaxis[1], 0, false);
15.
16.    myController.Commands.Motion.Setup.Incremental();
17.    myController.Commands.Motion.Linear("Z", -5, 1);
18.    myController.Commands.Motion.Setup.Absolute();
19.
20.    // Apply +10 degree rotation
21.
22.    myController.Commands.Motion.Setup.Absolute();
23.    myController.Commands.Motion.Linear("B", CentreTestRotation + phi_hold, 1);
24.
25.    MessageBox.Show("When marker is aligned press Point 1 button");
26.
27.    btn_RotationalCentre.Enabled = false;
28.    btn_point1.Enabled = true;
29. }
30.
31. private void btn_point1_Click(object sender, EventArgs e)
32. {
33.     double CentreTestRotation = 10;
34.
35.     Point1_Xaxis = myController.Commands.Status.AxisStatus("X", AxisStatusSignal.ProgramPositionFeedback);
36.     Point1_Yaxis = myController.Commands.Status.AxisStatus("Y", AxisStatusSignal.ProgramPositionFeedback);
37.     Point1_Daxis = myController.Commands.Status.AxisStatus("D", AxisStatusSignal.ProgramPositionFeedback);
38.
39.     // Due to having to Lower Z to find the marker which is higher than the ablation focus this has to be adjusted
40.
41.     double Point1_Zaxis_Measured = myController.Commands.Status.AxisStatus("Z", AxisStatusSignal.ProgramPositionFeedback);
42.     Point1_Zaxis = (z_stage_position - Point1_Zaxis_Measured) + z_stage_position;
43.
44.     btn_point1.Enabled = false;

```

```

45.
46.     double theta_rad = CentreTestRotation * (Math.PI / 180); // Radians
47.
48.     // Calculate Z Offset
49.
50.     double p = -
1   * ((Point1_Yaxis - Refined_Yaxis[1]) * Math.Sin(theta_rad) / (1 - Math.Cos(theta_r
ad)));
51.
52.     double q = (Point1_Zaxis - z_stage_position);
53.
54.     Z_Offset = 0.5 * (p + q);
55.
56.     // Calculate Y Offset
57.
58.     double a = (Point1_Yaxis - Refined_Yaxis[1]);
59.
60.     double b = (Point1_Zaxis - z_stage_position) * (1 + Math.Cos(theta_rad)) / Math.
Sin(theta_rad);
61.
62.     Y_Offset = 0.5 * (a + b);
63.
64.     Rot_Z_Coords = z_stage_position + Z_Offset;
65.
66.     Rot_Y_Coords = Refined_Yaxis[1] + Y_Offset;
67.
68.     MessageBox.Show("Rot Y = " + Rot_Y_Coords.ToString());
69.     MessageBox.Show("Rot Z = " + Rot_Z_Coords.ToString());
70.
71.     // Delete previous reference file
72.
73.     //File.Delete("C:/Users/User/Documents/GitHub/PrecisionPlatformControl/Reference
Values/Rotpoints.txt");
74.
75.     // Write all variables to text file
76.
77.     using (StreamWriter writer = new StreamWriter(universal_path + "\\Setup\\Rotpoin
ts.txt", true))
78.     {
79.         writer.WriteLine("Rotation = " + CentreTestRotation.ToString());
80.
81.         writer.WriteLine("Reference Y = " + Refined_Yaxis[1].ToString());
82.         writer.WriteLine("Reference Z = " + z_stage_position.ToString());
83.         writer.WriteLine("Ablation Focus = " + ablation_focus.ToString());
84.         writer.WriteLine("Microscope at ablation focus = " + microscope_focus.ToStr
ing());
85.
86.         writer.WriteLine("Point 1 Y = " + Point1_Yaxis.ToString());
87.         writer.WriteLine("Point 1 Z Measured = " + Point1_Zaxis_Measured.ToString());
88.     };
89.     writer.WriteLine("Point 1 Z = " + Point1_Zaxis.ToString());
90.
91.     writer.WriteLine("Z Offset = " + Z_Offset.ToString());
92.     writer.WriteLine("Y Offset = " + Y_Offset.ToString());
93.
94.     writer.WriteLine("Z Rot Centre = " + Rot_Z_Coords.ToString());
95.     writer.WriteLine("Y Rot Centre = " + Rot_Y_Coords.ToString());
96.     }
97.     myController.Commands.Motion.Setup.Absolute();
98.     myController.Commands.Motion.Linear("B", phi_hold, 1);
99.     myController.Commands.Motion.Setup.Absolute();
100.
101.     Movement_3D_uScope(Refined_Xaxis[1], Refined_Yaxis[1], 0, false);
102.
103.     btn_point1.Enabled = false;
104.     btn_Move_Zoom.Enabled = true;
105.
106.     }

```



```

107.
108.     private void btn_RotationTest_Click(object sender, EventArgs e)
109.     {
110.         // Move to have marker in focus at accurate ablation focus and visible on
the microscope
111.
112.         btn_Move_Zoom.Enabled = true;
113.
114.         myController.Commands.Motion.Setup.Absolute();
115.         //myController.Commands.Axes["X", "Y", "Z", "D"].Motion.Linear(new double
[] { Refined_Xaxis[2], Refined_Yaxis[2], ablation_focus_accurate, microscope_focus},
5); *****
116.         //myController.Commands.Motion.Linear("B", phi_hold, 1); *****
117.
118.         Movement_3D_uScope(Refined_Xaxis[1], Refined_Yaxis[1], 0, false);
119.
120.         MessageBox.Show("Is marker in focus and visible?");
121.
122.         double Rotation = Convert.ToDouble(txtbx_rotangle.Text);
123.
124.         Movement_3D_uScope(Refined_Xaxis[1], Refined_Yaxis[1], Rotation, false);
125.
126.         //myController.Commands.Motion.Linear("D", microscope_focus, 2);
127.
128.         MessageBox.Show("Visible?");
129.
130.         Movement_3D_uScope(Refined_Xaxis[1], Refined_Yaxis[1], 0, false);
131.
132.     }
133.
134.     private void Movement_3D_uScope(double X, double Y, double B, Boolean zoom)
135.     {
136.         lbl_uscopemoving.Visible = true;
137.
138.         this.Update();
139.
140.         // X, Y, B are all the requested coordinates
141.
142.         double theta_rad = B * (Math.PI / 180); // Radians
143.
144.         //Refined_Yaxis[1] is the input used to calculate the correction for both
Y and Z
145.
146.         // Y distance from point of interest and rotational centre
147.
148.         double PointOffset_Y = Math.Abs(Y - Rot_Y_Coords);
149.
150.         double Point_calc_Y = Y + PointOffset_Y * (1 - Math.Cos(theta_rad)) - Z_0
ffset * Math.Sin(theta_rad);
151.
152.         double Point_calc_Z = z_stage_position + (Z_Offset * (1 - Math.Cos(theta_
rad))) + (PointOffset_Y * Math.Sin(theta_rad));
153.
154.         double Correction_Z = Point_calc_Z - z_stage_position;
155.
156.         double Movement_z = z_stage_position - Correction_Z;
157.
158.         // Perform compensated movement
159.
160.         myController.Commands.Motion.Setup.Absolute();
161.
162.         if (B_hold != B + phi_hold)
163.         {
164.             myController.Commands.Motion.Linear("Z", z_stage_position - 10, 5);
165.             myController.Commands.Motion.Linear("B", B + phi_hold, 1);
166.         }
167.
168.         B_hold = B + phi_hold;

```

```

169.
170.         //if (zoom == false)
171.         //{
172.         //    myController.Commands.Axes["X", "Y", "Z"].Motion.Linear(new double[
173.         //    ] { X, Point_calc_Y, Movement_z }, 5);
174.         //    myController.Commands.Axes["Z"].Motion.Linear(new double[] { Move
175.         //    ment_z }, 5);
176.         //    myController.Commands.Motion.Linear("D", microscope_focus, 2);
177.         //    uScope_zoom_SerialPortCommunicator.SerialPort.Write("XG00000\r");
178.
179.
180.         //    Thread.Sleep(7500);
181.
182.         //    //uScope_focus_check(zoom);
183.         //}
184.         //else if (zoom == true)
185.         //{
186.         //    myController.Commands.Axes["X", "Y", "Z"].Motion.Linear(new double[
187.         //    ] { X + microscope_zoom_x_correction, Point_calc_Y + microscope_zoom_y_correction, M
188.         //    ovement_z }, 5);
189.         //    myController.Commands.Motion.Linear("D", microscope_focus + zoom_of
190.         //    fset, 2);
191.         //    lbl_Moving_Zoom.Visible = true;
192.         //    this.Update();
193.         //    //uScope_zoom_SerialPortCommunicator.SerialPort.Write("XH\r");
194.
195.         //    //Thread.Sleep(7500);
196.
197.         //    uScope_zoom_SerialPortCommunicator.SerialPort.Write("XG006C48\r");
198.
199.         //    Thread.Sleep(7500);
200.
201.         //    //uScope_focus_check(zoom);
202.
203.         //    lbl_Moving_Zoom.Visible = false;
204.         //    this.Update();
205.         //}
206.
207.         myController.Commands.Axes["X", "Y", "Z"].Motion.Linear(new double[] { X,
208.         Y, z_stage_position }, 5);
209.         myController.Commands.Motion.Linear("D", microscope_focus, 2);
210.
211.         lbl_uscopemoving.Visible = false;
212.         this.Update();
213.
214.     }

```

B.5 Machining on an angled plane

```

1. private void Movement_3D_ablation(double X, double Y, double B, double Speed)
2.     {
3.         Offset_Xaxis = Convert.ToDouble(File.ReadAllText("C:/Users/User/Document
4.         s/GitHub/PrecisionPlatformControl/Reference Values/OFFSETX.txt", Encoding.UTF8));
5.         Offset_Yaxis = Convert.ToDouble(File.ReadAllText("C:/Users/User/Document
6.         s/GitHub/PrecisionPlatformControl/Reference Values/OFFSETY.txt", Encoding.UTF8));
7.
8.         lbl_uscopemoving.Visible = true;
9.
10.        this.Update();

```

```

9.
10.         // X, Y, B are all the requested coordinates
11.
12.         double theta_rad = B * (Math.PI / 180); // Radians
13.
14.         //Refined_Yaxis[1] is the input used to calculate the correction for bot
h Y and Z
15.
16.         // Y distance from point of interest and rotational centre
17.
18.         double PointOffset_Y = -
19.         1 * (Y - Rot_Y_Coords); // Math.Abs(Y - Rot_Y_Coords);
20.
21.         double Point_calc_Y = Y + PointOffset_Y * (1 - Math.Cos(theta_rad)) - Z_
22.         Offset * Math.Sin(theta_rad);
23.
24.         double Point_calc_Z = ablation_focus + (Z_Offset * (1 - Math.Cos(theta_r
25.         ad))) + (PointOffset_Y * Math.Sin(theta_rad));
26.
27.         double Correction_Z = Point_calc_Z - ablation_focus;
28.
29.         double Movement_z = ablation_focus - Correction_Z;
30.
31.         // Perform compensated movement
32.
33.         myController.Commands.Motion.Setup.Absolute();
34.
35.         myController.Commands.Motion.Linear("D", 0, 2);
36.
37.         if (B_hold != B + phi_hold)
38.         {
39.             myController.Commands.Motion.Linear("Z", 0, 5);
40.             myController.Commands.Motion.Linear("B", B + phi_hold, 1);
41.         }
42.
43.         B_hold = B + phi_hold;
44.
45.         myController.Commands.Axes["X", "Y", "Z", "A", "B"].Motion.Linear(new dou
46.         ble[] { X - Offset_Xaxis, Point_calc_Y - Offset_Yaxis, Movement_z, theta_hold, B_hold
47.         }, 5);
48.
49.         lbl_uscopemoving.Visible = false;
50.
51.         this.Update();
52.
53.     }

```

B.6 Automated Holographic Camera Method

```

1. % Automation of Holographic Camera
2.
3. clc
4. clear
5. close all
6.
7. if ~isempty(instrfind)
8.     fclose(instrfind);
9.     delete(instrfind);
10. end
11.
12. % Choose default command line output for FalconGHZ_manualAcquisition
13. %handles.output = hObject;
14.
15. % --- Initialise Watt Pilot
16.
17. WP = serial('COM5');
18. set(WP, 'BaudRate', 38400, 'Terminator', {'CR', 'CR'});

```

```

19.     fopen(WP);
20.     disp('Connected to Watt Pilot');
21.
22. % --- Initialise Talisker
23.
24.     T = serial('COM6');
25.     set(T,'BaudRate',115200, 'DataBits',8, 'Parity', 'none', 'StopBits', 1, 'Terminator', {'LF','CR/LF'});
26.     fopen(T);
27.     disp('Connected to Talisker');
28.
29. % --- Initialise Aerotech
30.
31.     AT = tcpip('129.169.49.59',8000,'Timeout',100);
32.     fopen(AT);
33.     fprintf(AT, 'ABSOLUTE');
34.     disp('Connected to Aerotech');
35.
36. % --- Initialise CCD -----
37. % The line below only needs to be run when building the iDS Mex library after changing camera settings
38.
39.     % mex uEyeMex.cpp '-IC:\Program Files\IDS\uEye\Develop\include' '-LC:\Program Files\IDS\uEye\Develop\Lib' -luEye_api_64
40.
41.     handles.Holocam_sensor_1 = uEyeMexObj;
42.     disp('Connected to Camera');
43.
44. % --- Initialise Oscilloscope
45.
46.     % Find a VISA-USB object.
47.     TekOsc = instrfind('Type', 'visa-usb', 'RsrcName', 'USB0::0x0699::0x0421::C021422::0::INSTR', 'Tag', '');
48.
49.     % Create the VISA-USB object if it does not exist
50.     % otherwise use the object that was found.
51.     if isempty(TekOsc)
52.         TekOsc = visa('TEK', 'USB0::0x0699::0x0421::C021422::0::INSTR');
53.     else
54.         fclose(TekOsc);
55.         TekOsc = TekOsc(1);
56.     end
57.
58.     % Connect to instrument object, obj1.
59.     fopen(TekOsc);
60.     disp('Connected to Oscilloscope');
61.
62.
63. % --- Open Red Pitaya for Global use
64.
65.     IP= '192.168.137.109';           % Input IP of your Red Pitaya...
66.     port = 5000;                   % If you are using WiFi then IP is:
67.     RedPitaya=tcpip(IP, port);     % 192.168.128.1
68.     % flushinput(tcpipObj)
69.     % flushoutput(tcpipObj)
70.
71.     RedPitaya.Terminator = 'CR/LF';
72.     RedPitaya.InputBufferSize = 16384*32;
73.     RedPitaya.OutputBufferSize = 16384*32;
74.
75.     fopen(RedPitaya);
76.     disp('Connected to Red Pitaya');
77.
78. % --- Initialise RedPitayas
79.
80.     fprintf(RedPitaya,'DIG:PIN:DIR OUT,DIO1_P'); % Set DIO1_P to be input
81.     fprintf(RedPitaya,'DIG:PIN DIO1_P,0'); % Suppresses output of RF Channels
82.     fprintf(RedPitaya,'DIG:PIN:DIR OUT,DIO2_P'); % Set DIO2_P to be input
83.     fprintf(RedPitaya,'DIG:PIN DIO2_P,0'); % Suppresses output of RF Channels

```

```

84.     fprintf(RedPitaya, 'GEN:RST');
85.     fprintf(RedPitaya, 'SOUR1:VOLT 1');
86.     fprintf(RedPitaya, 'SOUR2:VOLT 1');
87.     fprintf(RedPitaya, 'SOUR1:BURS:NCYC 1');
88.     fprintf(RedPitaya, 'SOUR2:BURS:NCYC 1');
89.     fprintf(RedPitaya, 'SOUR1:BURS:NOR 1');
90.     fprintf(RedPitaya, 'SOUR2:BURS:NOR 1');
91.     fprintf(RedPitaya, 'SOUR1:BURS:INT:PER 5000');
92.     fprintf(RedPitaya, 'SOUR2:BURS:INT:PER 5000');
93.     fprintf(RedPitaya, 'SOUR1:FUNC SQUARE');
94.     fprintf(RedPitaya, 'SOUR2:FUNC SQUARE');
95.     fprintf(RedPitaya, 'SOUR1:PHAS 1');           % Inverts signal
96.     fprintf(RedPitaya, 'SOUR2:PHAS 1.000');       % Inverts signal
97.     fprintf(RedPitaya, 'SOUR1:VOLT:OFFS 0');
98.     fprintf(RedPitaya, 'SOUR2:VOLT:OFFS 0');
99.     fprintf(RedPitaya, 'SOUR1:FREQ:FIX 12000');   % Set frequency of output signal

100.          fprintf(RedPitaya, 'SOUR2:FREQ:FIX 12000');   % Set frequency of output
signal
101.          fprintf(RedPitaya, 'OUTPUT1:STATE ON');       % Set Ch1 output to ON
102.          fprintf(RedPitaya, 'OUTPUT2:STATE ON');       % Set Ch2 output to ON
103.          fprintf(RedPitaya, 'SOUR1:TRIG:SOUR EXT_NE');   % Set Ch1 generator trigge
r to external
104.          fprintf(RedPitaya, 'SOUR2:TRIG:SOUR EXT_NE'); % Set Ch2 generator trigge
r to external
105.          %fclose(RedPitaya);
106.
107.          % --- Setup file variables
108.
109.          handles.o_padding = 0;                          % Padding i
n x-y of lobes
110.          handles.xFOV = 0.00255;                        % x-
dimension of acquire image hologram in m
111.          handles.yFOV = handles.xFOV*1.333;            % y-
dimension of acquire image hologram in m
112.          handles.CCD_pixel_size = 2.2e-
6;                                                         % Size of the CCD pixel
113.          handles.imaging_wavelength = 532e-
9;                                                         % Wavelength of imaging laser
114.          handles.background_refractive_index = double(1.4607); % Refractive
index of ambient background (air at STP = 1.000277)
115.          handles.gas_background_filtering_ROI = 25;    % Region of i
nterest for setting background n to ambient
116.          handles.time_delay_offset = 0;                % Time offset
between the measured and actual time in nanoseconds
117.          handles.area_y_ROI = 300;                     % Area of int
erest in Fourier domain
118.          handles.area_x_ROI = handles.area_y_ROI*1.3333; % Area of i
nterest in Fourier domain
119.          handles.virtual_pixel_size= handles.xFOV/handles.area_x_ROI;% in meters p
er pixel. Pixel size of MAIN image (after FFT function)
120.
121.          % --- Load tilt correction angles
122.
123.          load('angles.mat');
124.
125.          % --- Get initial starting position
126.
127.          fprintf(AT, '$global[4] = AXISSTATUS(X, DATAITEM_ProgramPositionFeedback
)');
128.          response = strrep(fscanf(AT), '%', '');
129.          fprintf(AT, '$global[4]');
130.          response = strrep(fscanf(AT), '%', '');
131.          X = str2double(response);
132.
133.          fprintf(AT, '$global[4] = AXISSTATUS(Y, DATAITEM_ProgramPositionFeedback
)');
134.          response = strrep(fscanf(AT), '%', '');
135.          fprintf(AT, '$global[4]');

```

```

136.         response = strrep(fscanf(AT,'%',''));
137.         Y = str2double(response);
138.
139.         fprintf(AT, '$global[4] = AXISSTATUS(Z, DATAITEM_ProgramPositionFeedback
)');
140.         response = strrep(fscanf(AT,'%',''));
141.         fprintf(AT, '$global[4]');
142.         response = strrep(fscanf(AT,'%',''));
143.         Z = str2double(response);
144.
145.         initial_pos = [X, Y, Z];
146.
147.         Y = initial_pos(2);
148.
149.         TaliskerAttenuatorPos = [ 0 37 68 86 96];
150.         WattPilotAttenuatorPos = [ 98 100 100 98 67];
151.
152.         for j = 1:1:5
153.
154.             % --- Set laser parameters
155.
156.                 Talisker_current_rep_rate = talisker_rep_rate(T,200);
157.                 talisker_gate(T,'high');
158.                 WP_Current = WP_att(WP,WattPilotAttenuatorPos(j));
159.                 talisker_att(T,TaliskerAttenuatorPos(j));
160.                 disp('Laser Conditions Set');
161.
162.                 Order_Settings = xlsread([pwd, '\Machining_Settings.xlsx'],'Order');
163.
164.                 [a , b] = size(Order_Settings);
165.
166.                 % Determine machinig order
167.
168.                 [val,ind] = sort(Order_Settings(:));
169.                 for n = 1:1:length(ind)
170.
171.                     [orderind(1,n),orderind(2,n)]=ind2sub(size(Order_Settings),ind(n)
);
172.
173.                 end
174.
175.
176.
177.                 time_step_increment = 0.000005:0.000005:0.001;
178.                 spacing = 0.05;
179.                 initial_pos(2) = Y - ((b + 1) * spacing) * (j-1);
180.
181.                 for i = 1:1: numel(Order_Settings)
182.                     disp(['Iteration = ' num2str(i)]);
183.
184.                     % --- Set Trigger 1 Delay
185.
186.                         time_period = (time_step_increment(i) + 5e-6)/0.159;
187.                         Ch1_delay = 1/time_period; %% CHANGE
188.
189.                         fprintf(RedPitaya,'DIG:PIN:DIR OUT,DI01_P'); % Set DI01_P to be
input
190.                         fprintf(RedPitaya,'DIG:PIN DI01_P,0'); % Supresses output of RF C
hannels
191.                         fprintf(RedPitaya,'DIG:PIN:DIR OUT,DI02_P'); % Set DI02_P to be
input
192.                         fprintf(RedPitaya,'DIG:PIN DI02_P,0'); % Supresses output of RF C
hannels
193.
194.                         % This code sets the duration and phase of two trigger signals
195.
196.                         fprintf(RedPitaya,'SOUR1:VOLT 1');
197.                         fprintf(RedPitaya,'SOUR1:BURS:NCYC 1');

```

```

198.         fprintf(RedPitaya, 'SOUR1:BURS:NOR 1');
199.         fprintf(RedPitaya, 'SOUR1:BURS:INT:PER 5000');
200.         fprintf(RedPitaya, 'SOUR1:FUNC SQUARE');
201.         fprintf(RedPitaya, 'SOUR1:PHAS 1');           % Inverts signal
202.         fprintf(RedPitaya, 'SOUR1:VOLT:OFFS 0');
203.
204.         ch1_delayRequest = ['SOUR1:FREQ:FIX ' num2str(Ch1_delay)];
205.
206.         fprintf(RedPitaya, ch1_delayRequest);       % Set frequency of output signal
207.         fprintf(RedPitaya, 'OUTPUT1:STATE ON');     % Set Ch1 output to ON
208.         fprintf(RedPitaya, 'SOUR1:TRIG:SOUR EXT_NE'); % Set Ch1 generator trigger to external
209.
210.         fprintf(RedPitaya, 'DIG:PIN:DIR OUT,DI01_P'); % Set DI01_P to be input
211.         fprintf(RedPitaya, 'DIG:PIN DI01_P,1'); % Releases output of RF Channels
212.         fprintf(RedPitaya, 'DIG:PIN:DIR OUT,DI02_P'); % Set DI02_P to be input
213.         fprintf(RedPitaya, 'DIG:PIN DI02_P,1'); % Releases output of RF Channels
214.         %fclose(RedPitaya);
215.
216.         % --- Set Trigger 2 Delay
217.
218.         Ch2_delay = 1/(time_period + 0.0005); %% CHANGE
219.
220.         fprintf(RedPitaya, 'DIG:PIN:DIR OUT,DI01_P'); % Set DI01_P to be input
221.         fprintf(RedPitaya, 'DIG:PIN DI01_P,0'); % Suppresses output of RF Channels
222.         fprintf(RedPitaya, 'DIG:PIN:DIR OUT,DI02_P'); % Set DI02_P to be input
223.         fprintf(RedPitaya, 'DIG:PIN DI02_P,0'); % Suppresses output of RF Channels
224.
225.         % This code sets the duration and phase of two trigger signals
226.
227.         fprintf(RedPitaya, 'SOUR2:VOLT 1');
228.         fprintf(RedPitaya, 'SOUR2:BURS:NCYC 1');
229.         fprintf(RedPitaya, 'SOUR2:BURS:NOR 1');
230.         fprintf(RedPitaya, 'SOUR2:BURS:INT:PER 5000');
231.         fprintf(RedPitaya, 'SOUR2:FUNC SQUARE');
232.         fprintf(RedPitaya, 'SOUR2:PHAS 1');           % Inverts signal
233.         fprintf(RedPitaya, 'SOUR2:VOLT:OFFS 0');
234.
235.         ch1_delayRequest = ['SOUR2:FREQ:FIX ' num2str((Ch2_delay))];
236.
237.         fprintf(RedPitaya, ch1_delayRequest);       % Set frequency of output signal
238.         fprintf(RedPitaya, 'OUTPUT2:STATE ON');     % Set Ch1 output to ON
239.         fprintf(RedPitaya, 'SOUR2:TRIG:SOUR EXT_NE'); % Set Ch1 generator trigger to external
240.
241.         fprintf(RedPitaya, 'DIG:PIN:DIR OUT,DI01_P'); % Set DI01_P to be input
242.         fprintf(RedPitaya, 'DIG:PIN DI01_P,1'); % Releases output of RF Channels
243.         fprintf(RedPitaya, 'DIG:PIN:DIR OUT,DI02_P'); % Set DI02_P to be input
244.         fprintf(RedPitaya, 'DIG:PIN DI02_P,1'); % Releases output of RF Channels
245.         %fclose(RedPitaya);
246.
247.         % --- Move to correct machining spot

```

```

248.
249.         % Line start_x
250.
251.         start_x = initial_pos(1) + (spacing)*(b - orderind(2,i)) + spacin
g;
252.
253.         % Line start_y - remove line length for lines add for boxes
254.
255.         start_y = initial_pos(2) - spacing -(spacing)*(orderind(1,i)-
1) ;
256.
257.         % Line start_z
258.
259.         start_z = initial_pos(3) + (start_x - initial_pos(1))*tan(theta)
- (start_y - initial_pos(2))*tan(phi);
260.
261.         aerotech_movement(start_x, start_y, start_z, 0, 0, theta, phi, -
1, 'on',AT);
262.         disp('Moved to Machining Point');
263.
264.         % --- Fire PSO with shutter closed to trigger reference capture
265.
266.         disp('Waiting for Trigger for Reference')
267.         fprintf(TekOsc, 'FPAnel:PRESS SINGLEseq');
268.         talisker_shutter(T,'close');
269.         disp('Fire PSO');
270.         aerotech_PSO(AT,'on');
271.
272.         % --- Set Camera Ready to Aquire Reference
273.
274.         handles.reference = handles.Holocam_sensor_1.Grab; %Sets iDS ccd
to ready and captures hologram on trigger
275.
276.         % --- Display Reference.
277.
278.         handles.reference_save = handles.reference;
279.         %imshow(handles.reference_save);
280.
281.         % axes(handles.image1_axes1);
282.         % imshow((handles.reference));
283.         %
284.         % axes(handles.image2_axes2);
285.         % imshow(fft2(handles.reference));
286.         % pause(0.5);
287.         disp('Captured Reference');
288.
289.         % --- Set Red Pitaya for Hologram Acq
290.
291.         fprintf(RedPitaya,'ACQ:RST');
292.         fprintf(RedPitaya,'ACQ:DEC 1');
293.         fprintf(RedPitaya,'ACQ:TRIG:LEV 800 mV');
294.         fprintf(RedPitaya,'ACQ:TRIG:DLY 13000'); %Set number of s
amples to delay the trigger by (moves signal left/right on graph)
295.         fprintf(RedPitaya,'ACQ:START');
296.         fprintf(RedPitaya,'ACQ:TRIG EXT_NE');
297.
298.         % --- Fire PSO with shutter open
299.
300.         disp('Waiting for Trigger for Hologram')
301.         fprintf(TekOsc, 'FPAnel:PRESS SINGLEseq');
302.         talisker_shutter(T,'open');
303.         aerotech_PSO(AT,'on');
304.
305.         % --- Set Camera Ready to Aquire Hologram
306.         % % %
307.         % % %         handles.hologram = handles.Holocam_sensor_1.Grab; %Sets iDS
ccd to ready and captures hologram on trigger
308.
309.         while 1

```



```

310.             %Insert iDS acquisition code here
311.             handles.hologram = handles.Holocam_sensor_1.Grab; %Sets iDS c
cd to ready and captures hologram on trigger
312.             trig_rsp=query(RedPitaya,'ACQ:TRIG:STAT?');
313.             if strcmp('TD',trig_rsp(1:2))
314.                 break
315.             end
316.         end
317.
318.         handles.hologram_save = handles.hologram;
319.         %imshow(handles.hologram_save);
320.
321.         % --- Acquire Timestamps
322.
323.         disp('Acquire Measurements for Scope')
324.         pause(15)
325.         fprintf(TekOsc, 'MEASUREMENT:MEAS1:VALUE? ');
326.         event_offset = fscanf(TekOsc);
327.         fprintf(TekOsc, 'MEASUREMENT:MEAS2:VALUE? ');
328.         delta_t = fscanf(TekOsc);
329.
330.         % --- Save Holograms and Time Stamps
331.
332.         hologram_save = handles.hologram_save;
333.         reference_save = handles.reference_save;
334.
335.         foldername = ['C:\Users\Anon\Desktop\Chris Test\' num2str(j)];
336.         mkdir(foldername);
337.
338.         filename = [foldername '\ ' xFL1_' num2str(i,'%05d') '.mat'];
339.         save (filename, 'hologram_save', 'reference_save', 'event_offset'
, 'delta_t');
340.
341.         %LOBE 1 procssing -----
-----
342.             handles.lobe_x_coordinate = -
920 ;
% VARIES depending on lobe position
343.             handles.lobe_y_coordinate = 230 ;
% VARIE
S depending on lobe position
344.             [handles.delta_phase_stetson_L1] = FL1_stetsonPhase(handles.holog
ram, handles.reference, handles.area_x_ROI, handles.area_y_ROI, handles.lobe_x_coord
inate, handles.lobe_y_coordinate, handles.o_padding);
345.             [handles.unwrapped_phase_L1] = Miguel_2D_unwrapper(handles.delta_
phase_stetson_L1);
346.             %[handles.unwrapped_phase_L1] = phase_unwrap(handles.delta_phase_
stetson_L1);
347.         %LOBE 2 procssing -----
-----
348.             handles.lobe_x_coordinate = -
485 ;
% VARIES depending on lobe position
349.             handles.lobe_y_coordinate = 615 ;
% VARIE
S depending on lobe position
350.             [handles.delta_phase_stetson_L2] = FL1_stetsonPhase(handles.holog
ram, handles.reference, handles.area_x_ROI, handles.area_y_ROI, handles.lobe_x_coord
inate, handles.lobe_y_coordinate, handles.o_padding);
351.             [handles.unwrapped_phase_L2] = Miguel_2D_unwrapper(handles.delta_
phase_stetson_L2);
352.             %[handles.unwrapped_phase_L2] = phase_unwrap(handles.delta_phase_
stetson_L2);
353.         %-----
-----
354.
355.         ax1 = subplot(1,2,1);
356.         axes(ax1);
357.         colormap(gray);
358.         imagesc(handles.unwrapped_phase_L1);
359.
360.         ax2 = subplot(1,2,2);
361.         axes(ax2);

```

```
362. colormap(gray);
363. imagesc(handles.unwrapped_phase_L2);
364.
365. talisker_shutter(T, 'close');
366.
367. %waitfor( msgbox('Move Sample'));
368.
369.     i = i + 1;
370. end
371.
372. end
```